UNIVERSIDADE DE SANTIAGO DE COMPOSTELA

FACULTADE DE FÍSICA

DEPARTAMENTO DE FÍSICA DE PARTÍCULAS

Instituto Galego de Física de Altas Enerxías

Study of Pionium Lifetime in pNi collisions at $p = 24\,GeV/c$

Oton Vázquez Doce

Bernardo Adeva Andany
Catedrático da área de Física atómica, molecular e nuclear

INFORMA

que a memoria titulada

Study of Pionium Lifetime in pNi collisions at $p = 24\ GeV/c$

foi realizada por D. Oton Vázquez Doce
no **Departamento de Física de Partículas**
da **Universidade de Santiago de Compostela**
baixo a sua dirección, e constitúe o traballo de tese que
presenta para optar o Grao de Doutor en Ciencias Físicas.

Santiago de Compostela, a 29 de Setembro de 2006.

Asdo. Bernardo Adeva Andany Asdo. Oton Vázquez Doce

A Pinkiña.

Agradecimientos

En primer lugar me gustaría agradecerle al director de esta tesis, Bernardo Adeva, la oportunidad que me brindó de trabajar en física de altas energías en un proyecto tan ambicioso como éste, y la de haber podido aprender trabajando codo con codo con él durante estos años algo de la muchísima física que sabe. Muchas gracias, como no, igualmente a Máximo Pló y a Faustino Gómez por los primeros consejos y guía, y en general a todos los que me ayudaron dentro del grupo de Santiago, especialmente a Juan Saborido y Manuel por el apoyo logístico.

Quiero agradecer también la ayuda que durante mis estancias en CERN me prestó la gente de la colaboración, especialmente a Claude Detraz en el inicio por ayudarme a poner a funcionar las MSGC, a Cibrán por todos los consejos durante estos años, y a Carlo Guaraldo por la templanza, y la oportunidad. Y como no, a Benja y a Oscar, por el apoyo técnico.

Por supuesto ni me haría falta nombrar aqui a mis compañeros desde el principio, empezando sin duda por Toño (ánimo, si lo intentas es muy fácil), y siguiendo por Cristina, Juan y Leticia. Gracias a los que han sido más que colegas, Javi y Lucía, esta tesis no hubiera sido posible sin vosotros...literalmente.

Gracias a los que nunca habéis entendido nada de esto, precisamente por no desesperaros con mis intentos de explicarlo, Gose, Ganty, Alberto, Fran, JosyAna, Juanitius, Pablo & Pablo y por suerte muchos más que harían la lista interminable.

Y gracias, simplemente por todo, aunque suene simple pero no lo sea, a Felisa, Mary, Jesús, Susi y Arantxa.

I dla Pinki, od początku do końca dziękuje, dziękuje że byłaś zawsze tam, kiedy tylko to co chciałem to być w twoich ramionach, dziękuje że pozwoliłaś odkryć mi ten skarb, a przede wszystkim dziękuje za to że "wszystko będzie dobrze".

Contents

Resúmen

La tesis aquí presentada se enmarca dentro del experimento DIRAC que se lleva a cabo en el Laboratorio Europeo de Física de Partículas (CERN) en Ginebra.

En el capítulo 1 se describe el objetivo del experimento DIRAC, que es la medida de la vida media del átomo piónico con un 10% de precisión. La vida media de éste átomo, formado por un pión positivo π^+ y un pión negativo π^- está relacionada directamente con la diferencia de longitudes de dispersión $\pi\pi$ en onda S $|a_0 - a_2|$. Estas longitudes de dispersión han sido calculadas en el marco de la Teoría de Perturbaciones Quiral (χPt) con gran precisión por medio de la creación de un Lagrangiano efectivo en términos de campos físicos. La medida de $|a_0 - a_2|$ constituye un importante test del conocimiento de la ruptura de simetría en la Cromodinámica Cuántica y las teorías efectivas a bajas energías.

Como la vida media del átomo piónico es tan pequeña que no puede ser medida directamente, el experimento DIRAC propone un método indirecto para su determinación. Basado en las secciones eficaces doblemente inclusivas de $\pi\pi$, la formación del pionium ha sido calculada en la interacción de un haz de protones de 24 GeV/c del acelerador PS del CERN con un núcleo de átomos de Niquel (en el caso del trabajo aquí expuesto, habiéndose usado diferentes materiales para el blanco a lo largo de las tomas de datos de DIRAC). Los átomos producidos en dichas interacciones pueden aniquilarse formando dos piones neutros π^0, ser excitados a niveles atómicos superiores (o análogamente bajar su nivel energético), o pueden ser ionizados tras interaccionar con los núcleos del blanco. La probabilidad de éste último pro-

ceso de ruptura está relacionada directamente con la vida media del átomo piónico. Dicha relación, que depende de la materia y grosor del blanco y del momento del átomo, es conocida con una precision del 1% (ver figura 1.1). DIRAC detecta los piones $\pi^+\pi^-$ producto de la ionización y obtiene la vida media del pionium por medio de la determinación de su probabilidad de ruptura.

En el capítulo 2 se describen las características generales, el diseño y el funcionamiento del espectrómetro usado por DIRAC para identificar y reconstruir las trazas de los piones resultantes de la ionización del átomo piónico. Para ello, el montaje experimental de DIRAC ha sido optimizado con el propósito de detectar pares con un bajo momento relativo en el centro de masas ($Q < 3\,MeV/c$), ángulos de apertura muy pequeños ($\theta < 3\,mrad$) y energías en el laboratorio casi idénticas. Los detectores que lo forman se describen con detalle en éste capítulo excepto en el caso de las MSGC/GEM que son tratadas en el capítulo 3. En la figura 2.1 se puede ver una recreación isométrica del montaje experimental instalado en la sala East Hall del CERN. Se trata de un espectrómetro de doble brazo que está dividido por un imán en dos partes. La primera de ellas, que comienza con las cámaras de micropistas de gas (MSGC/GEM) a 2.5 metros del blanco, es llamada parte *upstream* por estar situada antes del imán, mientras que la parte posterior a éste se denomina *downstream*.

La parte upstream está formada por los siguientes detectores:

- 4 planos de MSGC/GEM
- 2 planos de detectores de fibra (SFD)
- 4 planos de hodoscopios de ionización (IH)

Con este conjunto de detectores se realiza la reconstrucción de las trazas antes del imán con gran resolución espacial, siendo capaces de separar trazas a muy baja distancia y de evitar ambigüedades gracias a la doble amplitud de la señal registrada en el IH al paso de las partículas cercanas. La información temporal proporcionada por la fibra tambien se usa en el sistema de trigger.

Después del imán el espectrómetro se separa en dos brazos, uno para la partículas positivas y otro para las negativas, y ambos están formados por:

- Cámaras de deriva (DC)
- Hodoscopios verticales (VH)
- Hodoscopios horizontales (HH)
- Detectores Cerenkov (C)
- Pre-shower (PSH)
- Cámaras de muones (MU)

El conjunto de los tres últimos detectores elimina, tanto en la etapa de trigger como en la de análisis, la contaminación de electrones y muones en el espectro piónico. Las cámaras de deriva son el principal instrumento de reconstrucción de trazas tras el imán, mientras que los hodoscopios verticales nos proporcionan la información del tiempo de vuelo necesaria para reconocer los pares de piones formados en una misma interacción protón-núcleo (denominados sucesos "prompt").

El sistema de trigger de DIRAC reduce el número de sucesos por paquete de protones incidentes a una cantidad aceptable por el sistema de adquisición de datos del experimento. Dicho sistema, junto con el trigger del experimento, son tratados también en el segundo capítulo. DIRAC cuenta con un trigger multinivel con un última etapa de trigger neuronal (DNA), que acepta basicamente sucesos con $Q_L > 30\ MeV/c$ y $Q_T > 10\ MeV/c$, manteniendo al mismo tiempo la eficiencia para pares con momento relativo Q por debajo de esos valores.

Los detectores MSGC/GEM creados por la Universidade de Santiago se analizan con más detalle en el capítulo 3. En primer lugar se describen las tres placas que conforman la cadena electrónica del detector: la placa madre, donde la superficie activa de detección está implementada, la placa de control y finalmente la placa VME. Las cámaras de micropistas de DIRAC son 4 planos de detector gaseoso con una etapa intermedia de multiplicacion gracias al GEM (Gas Electron Multiplier) de unos $10 \times 10\ cm^2$ de superficie activa instrumentadas con micropistas de cobre, ánodos y cátodos sucesivamente dispuestos con una distancia entre los centros de los ánodos

de 200 μm, proporcionando una resolución espacial de 54 μm. En el año 2002, el autor de la tesis participó en la creación de dos nuevos planos de MSGC/GEM que fueron probados, reproduciendo todos los sistemas auxiliares (cadena electrónica completa, sistema de gas, cadena de alto voltaje, etc), en el laboratorio de la Universidad de Santiago.

Antes de su instalación en el espectrómetro se realizó un estudio sobre la uniformidad de la ganancia en los dos nuevos planos. Usando una fuente beta de Rutenio como radiación incidente, se estudiaron las diferencias relativas en la ganancia, expresada en cuentas de ADC, a lo largo de la superficie activa del detector. El montaje experimental, como se puede ver en la figura 3.14 incluía también un detector centelleador de INa(Tl) usado como creador del trigger. Los resultados se pueden observar en la figura 3.18 para ambos detectores, la cual revela una buena uniformidad en la ganancia a lo largo de la superficie de detección. Estos dos planos se instalaron en el espectrómetro en el CERN en mayo de 2002, formando parte de la toma de datos de los años 2002 y 2003.

El capítulo 4 describe el sistema de reconstrucción de trazas usando los detectores situados antes del imán. Está integrado dentro del paquete estándar del experimento (ARIANE), escrito en lenguaje de progración Fortran77. Este método permite obtener idénticos resultados para pares prompt y accidentales, constituyendo una enorme mejora en cuanto a resolución en la componente transversal de Q. Tiene además la ventaja de que la gran cantidad de partículas de fondo presentes en los detectores upstream puede ser reducida sin ambigüedad realizando un corte en las distribuciones de probabilidad de vértice de las trazas. Consta de tres fases:

- Reconocimento de trazas
- Ajuste de las trazas
- Asociación con las trazas reconstruídas por las cámaras de deriva

Durante el reconocimiento de las trazas las señales guardadas por los detectores upstream se analizan asociando las coordenadas de los centros de gravedad en cada plano. En un primer momento se buscan por separado

segmentos formados en la proyeccion X e Y para después añadir la información de los planos inclinados. Todas las trazas son ajustadas a una línea recta usando inicialmente una posición promedio del vértice y un momento promedio, dando las matrices de covariancia cuenta de la dispersión múltiple provocada por la materia del espectrómetro. Finalmente cada traza reconstruída tras el imán por las cámaras de deriva es extrapolada usando un mapa del campo magnético y la posición aproximada del vértice. Se usa el plano de la fibra X como plano de asociación, y la posición obtenida es comparada con la de las trazas upstream para asociarlas con un test χ^2.

La precisión requerida por el sistema de reconstrucción de trazas sólo puede ser obtenida tras un riguroso trabajo de alineamiento de los detectores. Dicho trabajo se describe en el capítulo 5. Los detectores situados antes del imán se alinearon entre sí en una primera fase iterativa, y después fueron alienados como bloque con la parte downstream. Los parámetros obtenidos se hicieron depender del número de run dentro de la toma de datos del 2001, que es la utilizada posteriormente en la determinación de la vida media del átomo piónico. La posición de la intersección del haz de protónes con el blanco también fue calibrada, de modo que tras el trabajo de alineamiento se obtuvieron los siguientes parámetros:

- 6 traslaciones individuales (una para cada plano upstream instalado en el año 2001) en la dirección perpendicular a la de las correspondientes micropistas o fibras (posición de la primera pista)
- 6 ángulos de Euler para cada dectector alrededor del eje Z (cálculo preciso de los ángulos θ_i)
- traslaciones y ángulos de Euler alrededor de los ejes Z e Y de la parte upstream como bloque con respecto a los brazos positivo y negativo de las cámaras de deriva
- posición promedio en X e Y del centro del haz de protónes con respecto a los detectores anteriores al imán

En el último apartado del capítulo 5 se describe también un método para obtener las eficiencias de los detectores MSGC/GEM durante su operación, basado en el cálculo de resíduos no correlacionados para cada plano.

En el análisis de la vida media del átomo piónico, para obtener la mayor precisión posbile en la extrapolación de la interacción de Coulomb en valores bajos de Q, se ha escogido la simulación Monte Carlo como método mas simple de análisis. La creación de dicho Monte Carlo se describe en el capítulo 6, así como su uso para determinar la resolución del método de reconstrucción de trazas en las componentes transversal y longitudinal del momento en el centro de masas Q_L y Q_T.

Aún con una excelente resolución en el tiempo de vuelo, un fondo de pares de piones no procedentes de la misma interacción protón-núcleo permanece bajo el pico de sucesos seleccionados con coincidencia temporal en los hodoscopios verticales (ver figura 8.1). Los diferentes tipos de pares presentes en dicho pico de sucesos prompt se crean usando generadores específicos que son pasados por el paquete de Monte Carlo GEANT adaptado al experimeto DIRAC. Junto con estos generadores, se ha creado tambien una simulación de pares atómicos procedentes de la ruptura del pionium. Se describe asimismo la digitalización de la señal producida en los detectores MSGC/GEM, basada en las distribuciones obtenidas con los datos reales, así como la simulación del fondo de partículas que no proceden del blanco. Se muestra la influencia de los parámetros de simulación de las MSGC/GEM sobre la resolución del vértice formado por ambos piones. Posteriormente se evalúa en detalle la resolucíon del método de reconstrucción en las distribuciones críticas Q_X, Q_Y, Q_T y Q_L, comparando los valores reconstruídos con los generados en el Monte Carlo, tanto para pares con interacción de Coulomb como para pares atómicos.

También en el sexto capítulo se comprueba el valor de la ineficiencia en la resolución de partículas a muy baja distancia. Debido a la granularidad de los detectores upstream, cuando éstos son atravesados por partículas muy cercanas en la proyección medida por el detector, existe un porcentaje de partículas q no pueden ser resueltas, comportandose el sistema de reconstrucción ineficientemente en estos casos. Conociendo las eficiencias de los detectores individuales dicho porcentaje puede ser conocido y comparado con el obtenido con Monte Carlo.

Se ha desarrollado un método para medir la resolución en el momento en el sistema de laboratorio δP con datos experimentales, basándose en los

sucesos recogidos por el trigger de Lambdas disponible en el experimento. La dependencia de $\delta P/P$ se parametriza con dos coeficientes, que son precisamente determinados con los datos de Niquel 2001, usando sucesos recogidos por el mencionado trigger, que registra pares pión-protón producidos en el decaimiento de dicha partícula. La idea es usar la determinación de la masa del lambda, a bajos ángulos de apertura, para realizar un detallado análisis cualitativo de la resolución del momento de las trazas individuales, en función de dicho momento. Tras la aproximación de bajo ángulo, la dispersión en la masa del lambda depende exclusivamente de la resolución en el momento del laboratorio. Tras la selección de sucesos el método usado es un ajuste por máxima verosimilitud a la expresión 7.3, usando un conjunto de sucesos que no sólo contienen la señal, sino tambien un fondo no resonante debido al ruido del trigger. La descripción por parte del ajuste de dicho fondo es de crucial importancia para tener una determinación lo más precisa posible de los parámetros A y B en la determinación de la resolución en el momento parametrizada de la forma:

$$(\delta P)^2 = (AP)^2 + (BP^2)^2$$

En el capítulo 8 se describe el método de extracción de la señal atómica y cómo se determina la probabilidad de ruptura del átomo piónico. Los sucesos son seleccionados de los datos tomados con blancos de Niquel de 94 y 98 μm de grosor durante la toma de datos del año 2001. Los pares accidentales, que no muestran coincidencia temporal en los hodoscopios verticales ya que proceden de diferentes interacciones protón-núcleo se usaron en el análisis para reproducir la aceptancia del trigger, corrigiendo así las distribuciones de Monte Carlo. Los sucesos prompt, que provienen de la misma interacción protón núcleo, son comparados en un ajuste bidimensional en las magnitudes Q_T y Q_L, con las siguientes distribuciones generadas por Monte Carlo:

- Pares con interacción coulombiana en el estado final, usando el factor de Sakharov.
- Pares accidentales que aún procediendo de diferentes interacciones protón-núcleo presentan coincidencia de tiempo en el detector de tiempo de vuelo.

- Monte Carlo de pares sin interacción coulombiana en el estado final.

- Modelo atómico de Monte Carlo que describe la señal de átomos piónicos sobre el fondo.

El ajuste se realiza minizando el χ^2 de la expresión 8.5 para determinar las fracciones de los distintos tipos de pares. La señal atómica se determina por substracción del fondo de los datos experimentales en la zona $Q_L < 2\ MeV$. En el capítulo 8 se describe también cómo a partir del número de átomos y de pares coulombianos obtenidos a través del ajuste se obtiene, usando los llamados factores K, la probabilidad de ruptura del átomo piónico.

Tal y como se describe en el capítulo 9, el ajuste se repitió en 10 intervalos de 600 MeV/c del momento de laboratorio en bines de $(0.5 \times 0.5)(MeV/c^2)$ de (Q_T, Q_L). De este modo se obtienen 10 valores de la probabilidad de ruptura del átomo, una para cada valor de p. La vida media se puede obtener por minimización con respecto a la predicción que relaciona dicha vida media con la probabilidad de ruptura del átomo dentro de un determinado blanco. Se muestra con propósito comparativo un ajuste global que contiene los 10 intervalos de p y que proporciona resultados similares. Se ha estudiado también la dependencia del resultado obtenido con los límites del valor de Q_L en la selección de sucesos, y con los de integración de la señal en Q_T y Q_L.

Al final del capítulo se evalúan los posibles errores sitemáticos, siendo los más significantivos:

- Conocimiento del ángulo medio de dispersión múltiple en los detectores anteriores al imán

- Corrección por la no uniformidad de la aceptancia del trigger en Q_L

- Simulación de las partículas de fondo en las MSGC/GEM

- Forma de las distribuciones atómicas

- Simulación del espectro de Q_T

- efectos del tamaño finito en la interacción coulombiana y contaminación de partículas η' y γ.

En el capítulo 10 se resumen los logros conseguidos, mostrando el resultado final para la vida media del átomo piónico:

$$\tau_{1S} = 2.58\ ^{+0.30}_{-0.26}$$

Por medio de la relación 1.5 se conoce también el valor para la diferencia de las longitudes de dispersion $|a_0 - a_2|$. Ambos resultados se presentan con un error procedente de la combinación del error sistemático explicado y del estadístico proporcionado por el ajuste, debido principalmente a la cantidad de sucesos prompt recogidos por el espectrómetro.

Chapter 1

Aim of DIRAC experiment and theoretical motivation

1.1 Introduction

Pionium is an hydrogen-like atom formed by a positive and a negative pion. Measuring its lifetime with a precision of 10%, provides in a model-independent way the difference between the isoscalar and isotensor strong S-wave $\pi\pi$ scattering lengths $|a_0 - a_2|$. These scattering lenghts have been calculated in the framework of Chiral Perturbation Theory (χPt) with high accuracy, and this measurement is a sensitive check of the understanding of chiral symmetry breaking in QCD, and effective theories at low energies.

Since pionium lifetime is so small that cannot be measured directly, DIRAC experiment proposes an indirect way to measure it. Based on the double differential two-pion production cross sections, pionium yields have been calculated for the interaction of the 24 GeV/c proton beam of PS accelerator at CERN with target atoms. Produced pionium pairs can break up into $\pi^+\pi^-$ after interaction with the Coulomb field of target nuclei, so that the breakup probability is uniquely linked to lifetime with precision of 1%.

1.2 QCD theory

Quantum Chromodynamics (QCD) has been succesfully tested in the high energy region. In processes with momentum transfer of $Q > 1\ GeV/c$, QCD is essentially a perturbation theory. Quarks are considered massles and the conservation of chiral symmetry in the perturbative regime allows to design the QCD lagrangian describing quarks and gluon interactions.

At low energies, due to the running coupling constant α_s, perturbative techniques are not aplicable. With momentum transfer $Q < 100\ MeV/c$ quarks cannot be considered massles, and the chiral symmetry must be spontaneosly broken. Under this scenario the three lightest hadrons, π^+, π^-, π^0, can be identified as the Goldstone bosons generated by this broken symmetry.

However, at low energies we can write an effective Lagrangian in terms of physical fields. For this Lagrangian, a perturbation theory, Chiral Perturbation Theory [1] was developed, that uses as expansion parameters the quark masses and the momenta. χPt is an effective theory in a sense that it operates with pion fields directly, as opposed to the quark and gluon degrees of freedom, and it can be used to calculate the strong S-wave $\pi\pi$ scattering lengths with a precision better than 2.5% [2].

1.3 Pion-pion scattering

Pionium is a Coulomb $\pi^+\pi^-$ bound state, with Bohr radius $r_B = 387\ fm$. It decays by strong interaction mainly into $\pi^0\pi^0$, its binding energy is 1.858 keV, and $J^{PC} = 0^{++}$.

The decay width can be written

$$\Gamma = \frac{1}{\tau} = \Gamma_{2\pi^0} + \Gamma_{\gamma\gamma} \tag{1.1}$$

however $\pi^0\pi^0$ channel largely exceeds the $\gamma\gamma$:

$$\frac{\Gamma_{\gamma\gamma}}{\Gamma_{2\pi^0}} \sim 4 \times 10^{-3} \tag{1.2}$$

so we can neglect the second decay channel and consider

$$\Gamma \approx \Gamma_{2\pi^0} \tag{1.3}$$

Pionium ground state (principal quantum number n=1, orbital quantum number l=0) lifetime τ_{1s} is therefore dominated by the short-range reaction

$$\pi^+\pi^- \rightarrow \pi^0\pi^0 \tag{1.4}$$

At lowest order in QCD and QED, the total width can be expressed as function of the S-wave I=0 (a_0) and I=2 (a_2) $\pi\pi$ scattering lengths [3] and the next-to-leading order in isospin symmetry breaking has been calculated:

$$\Gamma_{1s} = \frac{1}{\tau_{1s}} = \frac{2}{9}\alpha^3 P|a_0 - a_2|^2(1+\delta) \tag{1.5}$$

$$\text{where} \qquad P = \sqrt{M_{\pi^+}^2 - M_{\pi^0}^2 - \frac{1}{4}\alpha^2 M_\pi^2}$$

and α is the fine structure constant. A significant correction $\delta = (5.8 \pm 1.2)\times 10^{-2}$ arises with respect to lowest order, once a non-singular relativistic amplitude at threshold is built [4].

Therefore a 5% precision can be achieved in the measurement of $|a_0 - a_2|$ provided a 10% lifetime error is reached. Note should be taken that this method implies experimental access to the physical reaction threshold (Bohr momentum of the pionium $P_B \sim 0.5 MeV/c$).

The $\pi\pi$ scattering lengths have been calculated in the framework of χPt with small errors [2], by means of an effective lagrangian with a precision at the per cent level. These results, based on the assumption that the spontaneous chiral symmetry breaking is due to a strong quark condensate [5], implies a value for the difference of scattering lengths of

$$|a_0 - a_2| = (0.265 \pm 0.004)\ M_\pi^{-1} \tag{1.6}$$

which implies a lifetime prediction of $\tau_{1s} = 2.9 \pm 0.1 fs$ [2]. The alternative scheme with an arbitrary value of the quark condensate [6] (so-called generalised χPt) yields larger values for a_0 and a_2, with an arbitrary value of the quark condensate.

There exists an ample and detailed literature about the quiral expansion of $\pi\pi$ amplitudes, including error estimates from experimental threshold and low energy parameter uncertainties [7].

On the other hand,a self-consistent representation of $\pi\pi$ scattering lenghts also exists [8]. It is obtained by fitting experimental data in the low energy regime, and imposing standard Regge behaviour at higher energies. It allows for higher values of the difference $|a_0 - a_2|$.

We believe that a measurement of the scattering lengths will thus contribute in an importat way to the present understanding of chiral symmetry breaking in QCD and to constraint the magnitude of the quark condensate.

1.4 Pion production

Charged pions with opposite charge emerging from a high energy proton-nucleus collision are produced directly, or originated from strong short-lived $(\rho, \omega, K^*, ...)$ or electroweak long-lived $(\eta, \eta', K^0_s, ...)$ sources. Pion pairs from short-lived sources undergo Coulomb final state interaction and may therefore form atoms[1], since the region of production is very small as compared to the Bohr radius of the atom.

The differential production cross section of pionium atoms, with 4-momentum $p_A = (E_A, \vec{p}_A)$, only occurs in S-states [10], and can be expressed as:

$$\frac{d\sigma}{d\vec{p}_A} = (2\pi)^3 \frac{E_A}{2M_\pi} |\psi_n(0)|^2 \left(\frac{d\sigma^0_s}{d\vec{p}_1 d\vec{p}_2}\right)_{\vec{p}_1=\vec{p}_2=\vec{p}_A/2} \tag{1.7}$$

where M_π is the pion mass, $\psi_n(0)$ is the atomic wave function at the origin with principal quantum number n, and σ^0_s denotes the Coulomb uncorrected semi-inclusive $\pi^+\pi^-$ cross-section [11], which is enhanced by a high energy (24 GeV/c) and high intensity ($\sim 10^{11}$) proton beam colliding on a nuclear target foil [12]. A Nickel target was used specifically in the collected data used in the analysis presented here.

[1] the contribution to the pionium production of long-lived sources was neglected as it is under the 1% level [9].

1.5 Propagation inside the target

After production, the pionium atoms propagate (with an average Lorentz factor $\gamma \approx 17$ in DIRAC) inside the target foil [13], interacting mostly with the electromagnetic field of the target atoms. Therefore pionium can undergo one of the three following processes [16] [11], one mediated by strong forces, and the other two of electromagnetic nature:

- Annihilation [14] into $\pi^0\pi^0$
- Ionization (break up) by the target nuclei into $\pi^+\pi^-$
- Excitation/de-excitation to higher/lower principal quantum number levels

The relation

$$1 = P_{Br} + P_{ann} + P_{dsc} \tag{1.8}$$

is obviously satisfied being P_{Br} the pionium breakup probability, P_{ann} the annihilation probability, and P_{dsc} stands for the probability of the atom leaving the target in a discrete state.

Using a high-Z and thin target, the pionium ionization probability competes mainly [15] with the anihilation process, so that P_{dsc} is highly reduced.

The $\pi^+\pi^-$ pairs coming from pionium break-up (atomic pairs) exhibit specific kinematical features which allow to identify them experimentally. For thin targets ($10^{-3}X_0$), due to the very small momentum transfer induced by the electric field near the target nuclei, the signal of atomic pairs is detected by DIRAC spectrometer as an excess with respect to Coulomb-correlated pairs at very low center-of-mass momentum, $Q < 3\ MeV/c$, with a yield of $\sim 10\%$ in this Q interval.

1.6 Pionium lifetime

The breakup probability is a function of the atom momentum and depends on the dynamics of the pionium interaction with the target atoms and on

the pionium lifetime. For a given target atomic number and thickness, the theoretical breakup probability for pionium is calculated [16] with a relative error of less than 1% [17] thanks to the detailed knowledge of the cross-sections involved in the process, which is purely electromagnetic, in which Born and Glauber approximations are used [18][19][20].

This breakup probability is uniquely linked to the atom lifetime [10]. In Fig. 1.1 the P_{Br} as a function of the lifetime is displayed for a combination of Ni targets with 94 μm and 98 μm, which were the foil thicknesses installed in DIRAC during the 2001 data taking period.

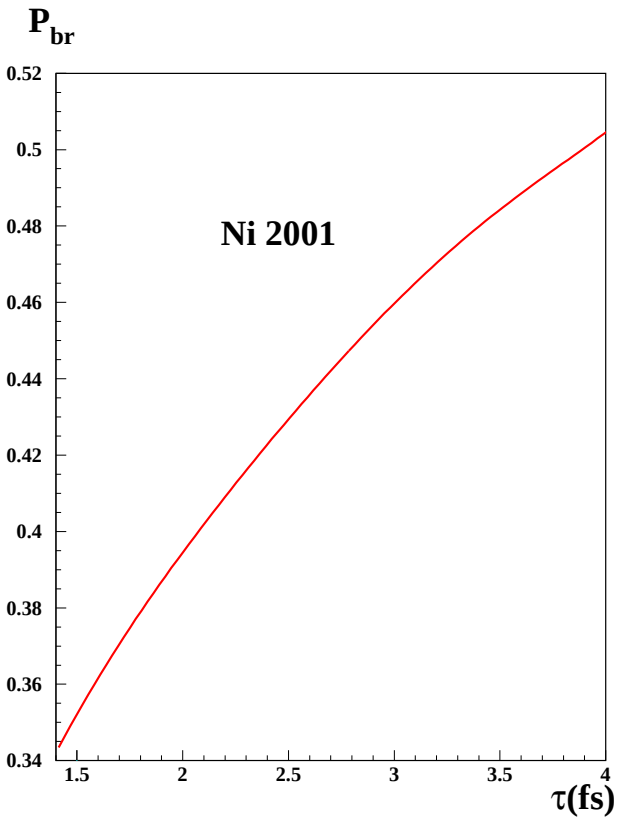

Figure 1.1: *Breakup probability as a function of pionium lifetime for a combination of Nickel targets with thicknesses of 94 μm and 98 μm*

Measuring P_{Br} thus allows to determine the lifetime of pionium. In DIRAC the breakup probability can be measured experimentally as the ratio of the detected number of atomic pairs (n_A) over the total number of produced atoms (N_A):

$$P_{Br} = \frac{n_A}{N_A} \tag{1.9}$$

The total number of produced $\pi^+\pi^-$ atoms (N_A) is related by an exact expression to the number of Coulomb correlated pion pairs (N_C) with low relative momenta, so that the breakup probability can be measured with DIRAC experimental method with the determination of the ratio between atomic and coulomb pairs in the desired Q range, as it will be seen.

Chapter 2

DIRAC setup

In this chapter, the general characteristics, design and working performances of the apparatus are explained and each detector is described in some detail, and the main lines of the trigger system and data-acquisition are also given. The MSGC/GEM system is more thouroughy described in the next chapter.

2.1 General apparatus description

Pion paris $\pi^+\pi^-$ emerging from break-up of pionium have a low relative momentum in their centre of mass system ($Q < 3\ MeV/c$), very small opening angle ($\theta < 3\ mrad$) and nearly identical energies in the laboratory frame. A high resolution magnetic spectrometer is then required [22] to split up the pairs and measure their relative momentum with sufficient precision to detect the pionium signal superimposed on the substantial background of "free" $\pi^+\pi^-$ pairs produced in inclusive proton-nucleus interactions.

The DIRAC experimental setup, located at the T8 proton beam line (with energy of 24 GeV/c) in the East Hall of the PS accelerator at CERN, became operational at the end of 1998 and has been collecting data since the middle of 1999. A general view of the spectrometer and a list of the setup components ordered along the proton beam direction are shown in Fig. 2.1, consisting of beam line, target station, secondary vacuum channel, spectrometer dipole magnet and detectors placed upstream and downstream of the magnet.

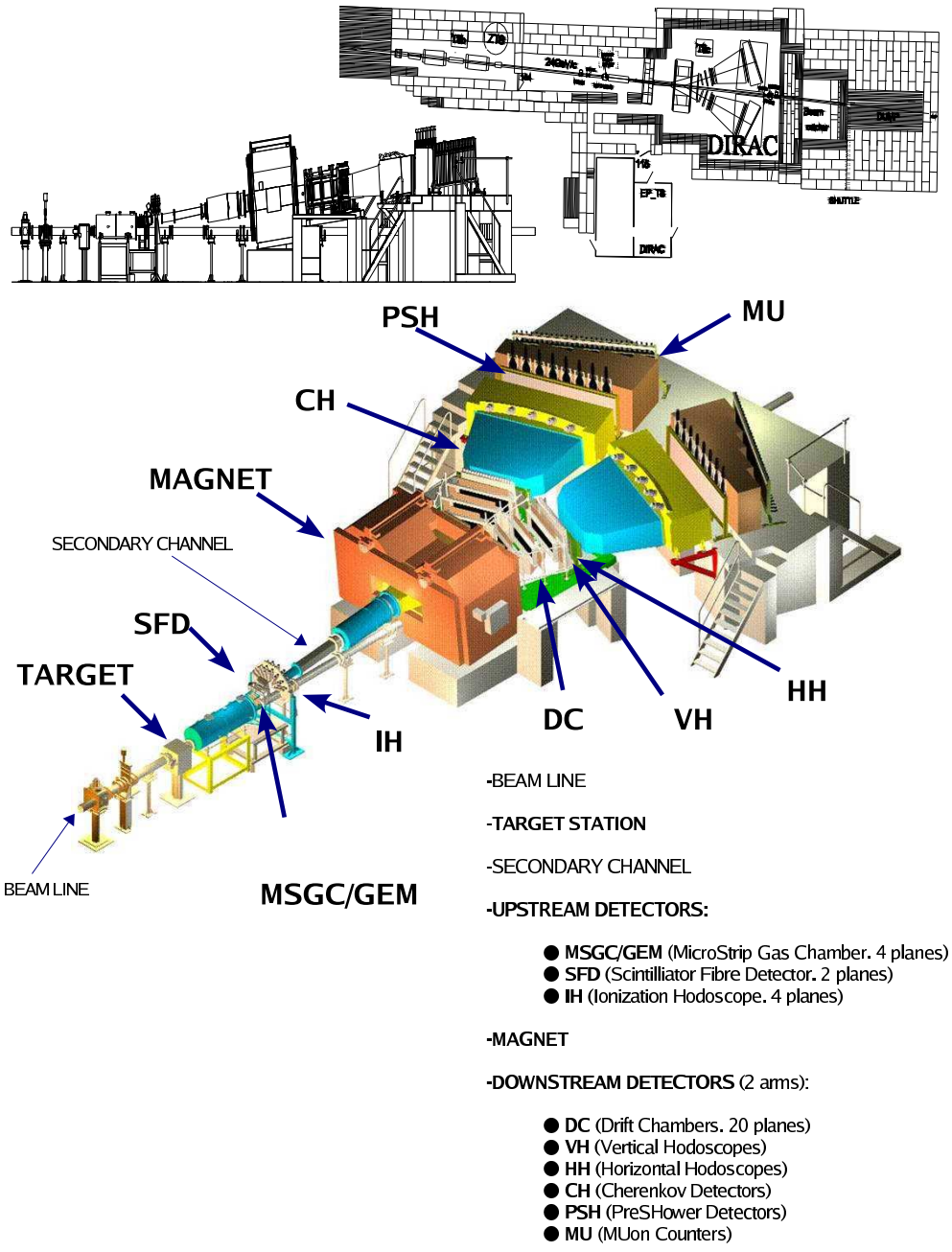

Figure 2.1: *Isometric view of the DIRAC setup.*

Protons are extracted in spills of $\sim 400 - 500\ ms$ duration from the PS to the T8 beam line using a slow ejection mode [23] . During data taking, between 1 to 5 cycles per PS super-cycle of $14.4 \div 19.2\ s$ duration are delivered to DIRAC. The proton beam intensity was set to $\sim 10^{11}$ protons per spill, depending on the target used.

The target station houses a device with 12 holders for the targets. The data analyzed in this work was mainly collected during 2001 data taking using two Ni targets with 94 μm and 98 μm thicknesses. The DIRAC experiment is sensitive to particles outside the beam core (halo), because the target is very thin and the upstream detectors are placed very close to the primary proton beam. Special optics has been designed to decrease the background halo to a negligible level. The ratio of detector counting rates with the target in place to those with an empty holder was measured to be ~ 25.

Free and atomic $\pi^+\pi^-$ pairs produced in the target enter a secondary particle channel which is tilted upwards by 5.7° with respect to the proton beam (as indicated in Fig. 2.1) to avoid background in the detectors. It consists of two vacuum cylindrical volumes, one immediately downstream the target station, and a second one located at $\sim 3.5\ m$ from the target between the spectrometer magnet poles. Secondary particles exit this tube through a 200 mm diameter window, made of 250 μm thick mylar film. The angular aperture of the secondary particle channel is determined by the collimator resulting in a solid angle acceptance of $1.2 \cdot 10^{-3}\ sr$.

Downstream the target the proton beam travels in a vacuum channel below the spectrometer. Before it is finally absorbed by a beam dump with a dedicated radiation shielding, in order to decrease the background gamma and neutron fluxes towards the detectors [24] . The downstream detectors are shielded in addition from background secondary particles produced at the primary proton beam pipe and surrounding elements by a 1 m thick iron wall that physically separates the upstream detector region from the rest. Collimators are inserted around the primary proton beam pipe and the secondary particle channel. A concrete radiation shielding encloses the whole DIRAC experimental apparatus to protect the surrounding East Hall in respect of the CERN safety regulations.

The secondary particle channel is endowed with a real spectrometer arm.

This upstream arm consists of two tracking devices, the microstrip gas chambers (MSGC/GEM) and the scintillating fibre detector (SFD). They are used to improve resolution on the longitudinal and transverse components of the relative momentum of pion pairs, by unambiguosly measuring the pair opening angle. The detection capability is increased for small angle tracks by an Ionization Hodoscope (IH) is located past the SFD following the proton beam direction. A real picture of the above-mentioned detectors, as they are installed between the first vacuum chamber and the secondary particle channel, can be seen in Fig. 2.2.

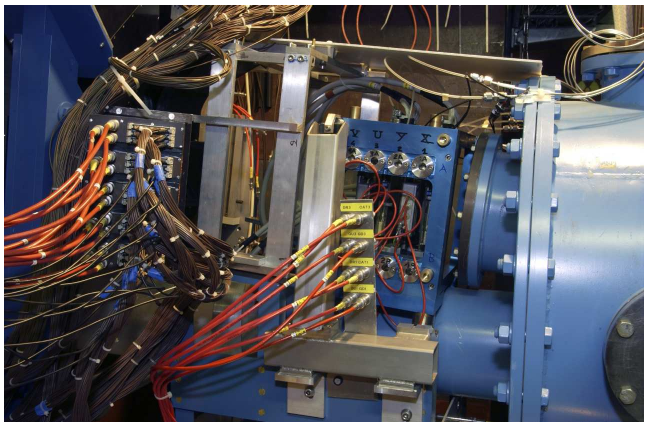

Figure 2.2: *Photography of the three detectors installed upstream the magnet, between the first vacuum chamber (right-hand side) and the secondary particle channel. From right to left, the MSGC/GEM, SFD and IH detectors can be found. The primary proton beam line can be appreciated at the bottom.*

Downstream the spectrometer magnet the setup splits into two identical arms for detection and identification of positive and negative charged particles. The half opening angle between the two arms is 19°. Along each arm the following detectors are located: drift chamber system (DC), vertical scintillation hodoscope (VH), horizontal scintillation hodoscope (HH), gas cherenkov counter (CH), preshower detector (PSH) and muon detector (MU).

2.2 The MSGC/GEM detector

It performs particle tracking at a distance of 2.4 m from the interaction point. In order to resolve two-particle ambiguities by means of stereo angles, four planes of a proportional gas detector with a single-hit space resolution of $\sim 50\ \mu m$ are installed. It achieves an experimental double track resolution better than 0.3 mm , limited by detector pitch and clustering. Because of its particular importance for upstream tracking, a more complete description of the MSGC/GEM will be done in the following chapters.

2.3 The Scintillating Fibre Detector

The Scintillating Fibre Detector (SFD) is used together with the MSGC/GEM detector, for upstream tracking, and it provides topological trigger capabilities [25] for rejection of pairs with relative distance larger than 9 mm. It also provides time information for upstream tracking.

The SFD consists of two perpendicular fibre planes to measure the X and Y coordinates of incident particles[1], as the deposited energy from the particles is transformed into light.

The SFD covers a $105 \times 105\ mm^2$ area. Each detector plane is composed of 240 column channels with 440 μm pitch, each consisting of a stack of 5 fibres in depth, measuring each one from 70 to 150 mm, as seen in Fig. 2.3. Fibres forming one sensitive column are connected via a light guide into one channel of position-sensitive photomultiplier (PSPM), with a total of 15 photomultipliers of 16 channels each.

A dedicated electronic circuit Peak Sensing Circuit (PSC) has been custom developed to provide signal discrimination with dynamic rejection of cross-talk in adjacent channels using the peak-sensing technique [26]. Discrimination of a channel is given by the condition $2A_i - A_{i-1} - A_{i+1} > A_{thr}$, where A_i are channel signal amplitudes and A_{thr} defines the threshold value.

For time correlated particle pairs (up to $\sim$ 5ns time difference) with

[1] A third upgraded SFD-U plane rotated 45° relative to X and Y was added for 2002 and 2003 periods.

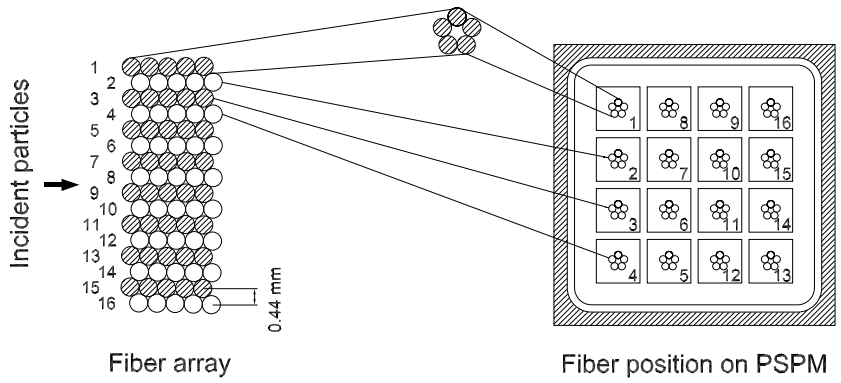

Figure 2.3: *The SFD principal structure. A 16-channel fragment is shown.*

distance more than one fibre pitch, the PSC algorithm provides efficient detection, avoiding cross-talk and rejecting noise. However, when adjacent fibre columns are crossed by two particles simultaneously, then the PSC algorithm leads to a suppression (with 50% probability) of the detected yield of double track events, and one of the hits is lost. For time difference greater than 5 ns the PSC behaves as an ordinary leading edge discriminator.

The performance of upstream detectors performance is compromised by the high particle flux originated by the proximity of the proton beam line and collimators.s Half the particles detected by SFD comes from secondary interactions in the channel [27].

The level of optical cross talk among the PSPM channels due to escape of ultraviolet light from one fibre column to the adjacent one, together with noise was found to be $\sim 2\%$. The detection efficiency is high (larger than 97% [28]) and the average hit multiplicity is near 5 in the 50 ns time window of TDC. Each detector fibre is equipped with a TDC channel which provides time tagging essential for upstream tracking.

Readout supplies time information in digital form TDC. The raw time spectra, obtained from e^+e^- and $\pi^+\pi^-$ events, are shown in Fig. 2.4 for two arbitrary SFD channels. After off-line deconvolution of the trigger time jitter the resolution of the SFD is found to be $\sigma = 0.8\ ns$. Single track resolution is defined by fibre column pitch of 440 μm.

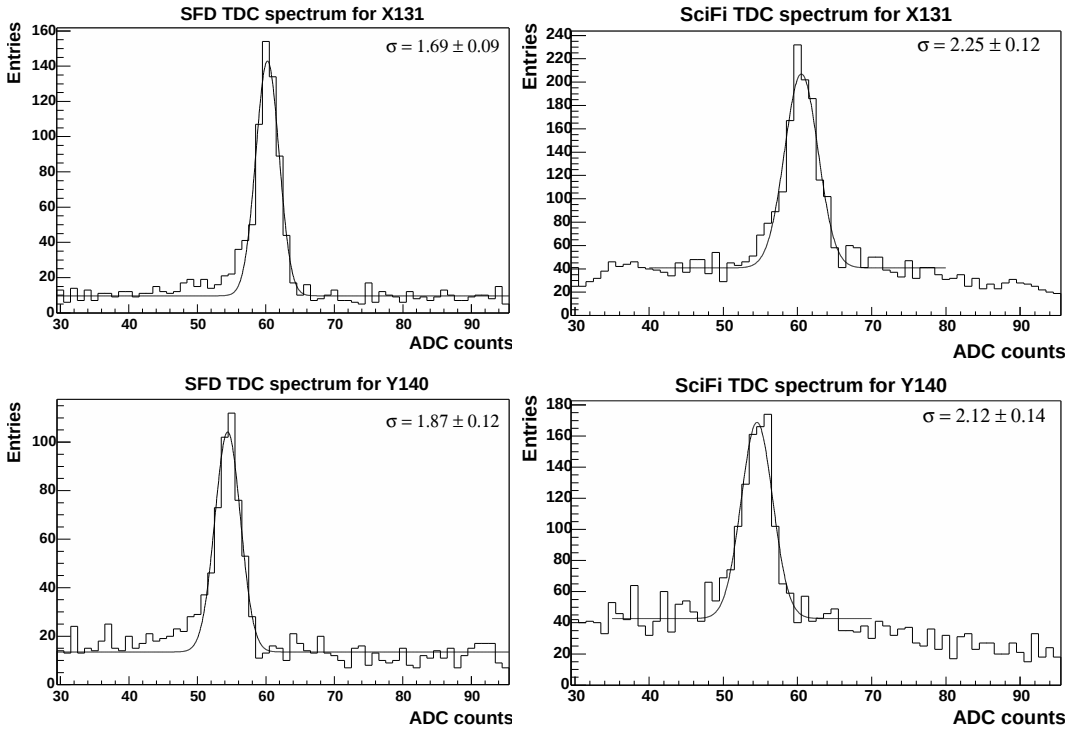

Figure 2.4: *SFD raw time spectra for e^+e^- (left) and for $\pi^+\pi^-$ (right) trigger data. The horizontal scale is in TDC channels, the channel width is 0.5 ns.*

2.4 The Ionization Hodoscope

Since charged pions originated from pionium breakup cross the upstream detectors at rather small relative distances, a dedicated Ionization Hodoscope [29] has been built to separate the double ionization signal produced by close pion pairs incident on the same scintillating slab, from single ionization signals produced by one particle. In this way, uncertainties resulting from pairs with relative distance less than the double track resolution are significantly reduced. In adittion, the IH takes part of the trigger system of DIRAC.

IH detector is a scintillation hodoscope [30] consisting of 4 planes of $11 \times 11\ cm^2$ sensitive area (Fig. 2.5) placed 3 m downstream the target. Two planes (X-A and X-B) vertically oriented, and the other two with horizontal slabs (Y-A and Y-B), being planes with the same slab orientation shifted by

a half-slab-width with respect to each other. Each plane is assembled from 16 plastic scintillating. The slabs are 11 cm long, 7 mm wide and 1 mm thick. They are connected to the PM photocathodes via 2 mm thick and 7 mm wide lucite light guides.

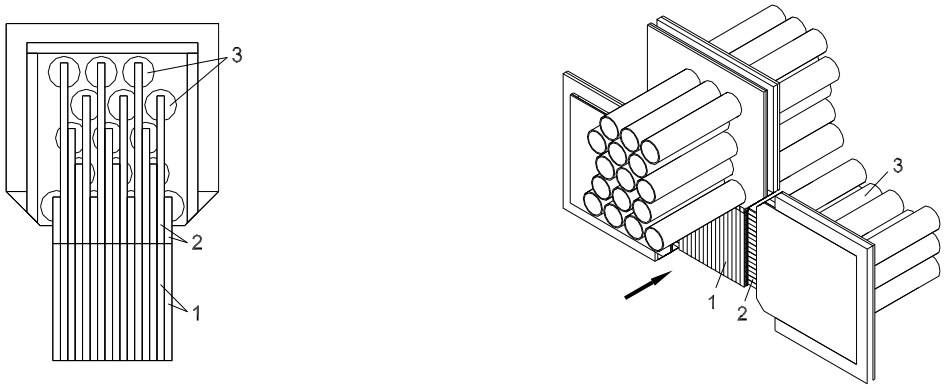

Figure 2.5: *Design and isomeric view of the IH scintillation plane (1 – scintillators, 2 – light-guides, 3 – photomultipliers).*

The front and rear surfaces of a slab are covered by a millipore film [31] for efficient light collection. At the lateral surface of the slab, light is reflected by a 30 μm mylar film in order to minimise the gaps between adjacent slabs, which is less than 70 μm wide.

Scintillation light is detected by photomultipliers Photocathodes are in optical contact with the wide side of a light guide instead of the traditional butt-end readout, improving the light collection efficiency.

Signal amplitude and time are digitised by ADC and TDC modules, respectively. The time resolution of the IH detector is better than 1 ns . The typical response of one IH channel to close particle pairs incident on one scintillating slab and to single particle is shown in Fig. 2.6. If a threshold is set to retain 95% of the double ionization signal from pairs, the contamination from single particle amplitudes is less than 15% (Fig. 2.7).

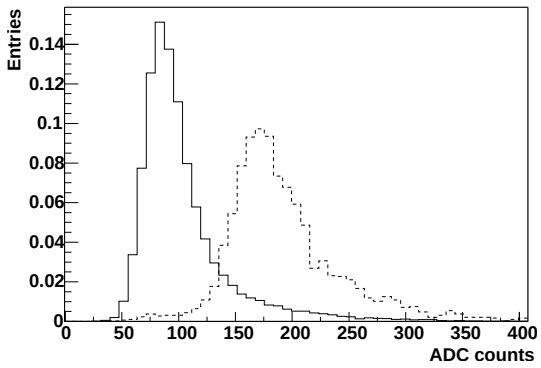

Figure 2.6: *Typical ADC spectra for single (solid line) and double (dashed line) ionization loss from particles crossing one IH scintillating slab.*

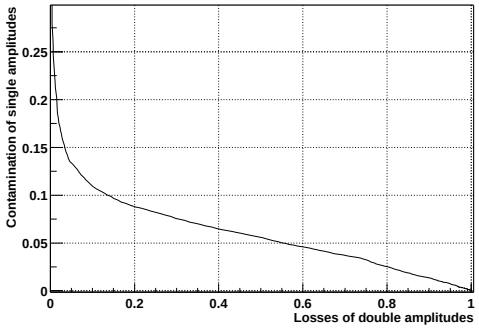

Figure 2.7: Contamination of single ionization amplitudes as a function of losses of double ionization as obtained from the analysis of the spectra of Fig. 2.6.

2.5 Magnet

The magnet separates positive and negative particles coming from upstream area, being the two downstream arms placed at arms $\pm 19^{\circ}$ relative to the central axis. Magnetic field ($B = 1.65\ T$, field integral $BL = 2.2\ T \cdot m$) has

been parametrized [32]. The dipole magnet has an aperture of $1.5 \times 0.50\ m^2$ ($W \times H$) and measures $0.5 \times 1.5 \times 1.1\ m$. To reduce the stray field, two magnetic screens are fixed near its entrance and exit.

2.6 Drift Chambers

The drift chamber system is used to perform particle tracking downstream the dipole magnet. These are gas detectors with periodic cell structure giving spatial and time (by means of the drift time) information, used in the T4 level trigger.

A two-arm solution has been chosen, except for the first chamber which is a single large module (DC-1) designed with two separated sensitive areas. This chamber provides 6 successive measurements of the particle trajectory along the coordinates X, Y, W, X, Y, W, where W is a stereo angle with inclination 11.3^0 with respect to the X-coordinate. Each of the two arms consists of 3 chamber modules, of identical design, measuring coordinates X,Y (DC-2), X,Y (DC-3) and X, Y, X, Y (DC-4) following the direction of the outgoing particle. The dimensions are $0.8 \times 0.4\ m^2$ for DC-1 sensitive areas, $0.8 \times 0.4\ m^2$ for DC-2, $1.12 \times 0.4\ m^2$ for DC-3, and DC-4 is $1.28 \times 0.4\ m^2$. DC-1 is instrumented with 800 electronic channels, and both arms together contain 1216 electronic channels.

The distance between the center of the first half of DC1 and the center of DC4 provides a lever-arm of 1.6 m along the average particle path, having uniform spacing of chambers DC-2 and DC-3 along this path. Six measurement points, together with a sufficiently long lever arm, allows to accurately reconstruct the downstream tracks.

A schematic drawing of the sensitive element is shown in Fig. 2.8. As seen in the figure, a sensitive area, corresponding to each anode wire and limited by the cathode planes and potential wires, has a square $(10 \times 10\ mm^2)$ shape. Cathode plane foils provide stable chamber operationand, being thin, add only small amount of material along the particle path. A rather large diameter of the anode wires has been chosen in order to operate the chambers at high current avalanche amplification mode.

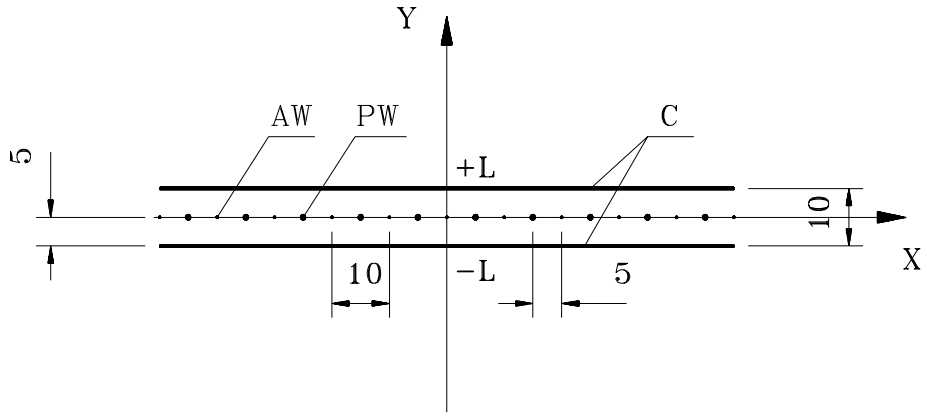

Figure 2.8: *Schematic view of the wire chamber electrodes: AW – anode wires, PW – potential wires, C – cathode foils. Dimensions are in mm.*

The chamber design is shown in Fig. 2.9 for the case of the DC-2 module. The module is a stack of aluminium and fibreglass frames fixed by screws with rubber o-rings glued to provide gas tightness. The design of module DC-1 differs from this description. The main difference, illustrated in Fig. 2.10, consists in the fact that DC-1 comprises, in a single gas volume, two sets of sensitive planes, placed symmetrically to the left and right hand side of the spectrometer axis. The middle zone, strongly irradiated , is made insensitive to the particle flux. The limiting edge of the sensitive zones can be varied. This design of the DC-1 module ensures little amount of material, by avoiding frames in the small angle region.

The readout electronics of the drift chambers, which is a custom-made system [33], provides data readout into the data collection memories and input to the trigger processor. The sensitive wire signals are digitised by TDC counters, which are plugged in the connectors mounted onto the chamber frames, and are connected to the Drift Chamber Proccessor (DCP) and VME buffer memory. This solution results in reduced number of electronic units, small number of cables and high noise immunity. The data of an event are stored in local data buffers until the higher level trigger decision is issued.

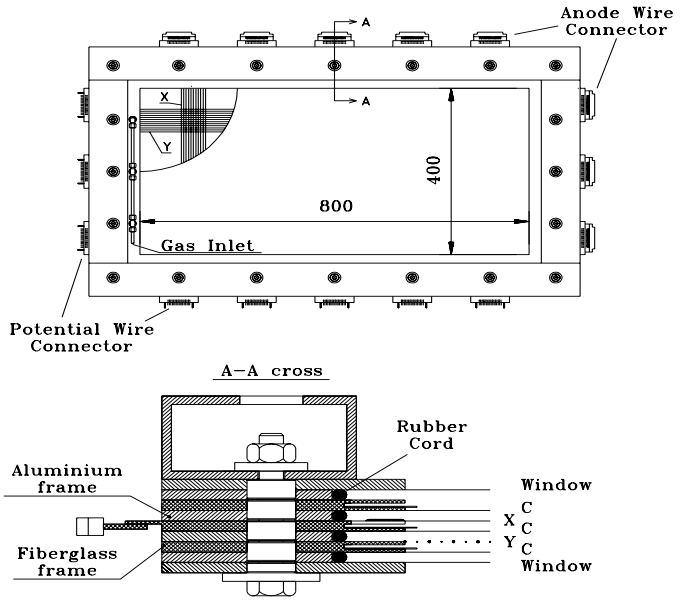

Figure 2.9: *Design of the DC-2 module. Top: general view. Bottom: structure of the frame stack; X – X-plane, Y – Y-plane, C – cathode foils.*

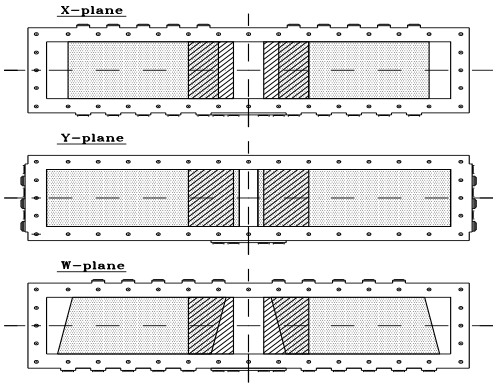

Figure 2.10: *Schematic view of the DC-1 module. Dotted areas show the sensitive regions of the X-, Y- and W-planes. Hatched areas mark the zones of the cathode strips which allow to change the width of the insensitive area in the central region.*

The drift chambers operate in a high current avalanche mode. The single hit efficiency is above 96% when the particle flux along the gas mixture $(Ar(\sim 50\%)+iC_4H_{10}(\sim 50\%)+H_2O(0.5\%))$ is about 10 kHz/cm^2. Tracking efficiency of the drift chamber system as a whole is about 99%, due to the requested number of hits per reconstructed track is less than the total number of sensitive planes crossed by a particle. A space-to-time relationship was extracted from the time spectrum and its integral distribution shown in Fig. 2.11, for a sample of clean events with a small amount of background hits. Study of the drift function parameters for different chamber planes at different beam intensities shows good stability of the above relation.

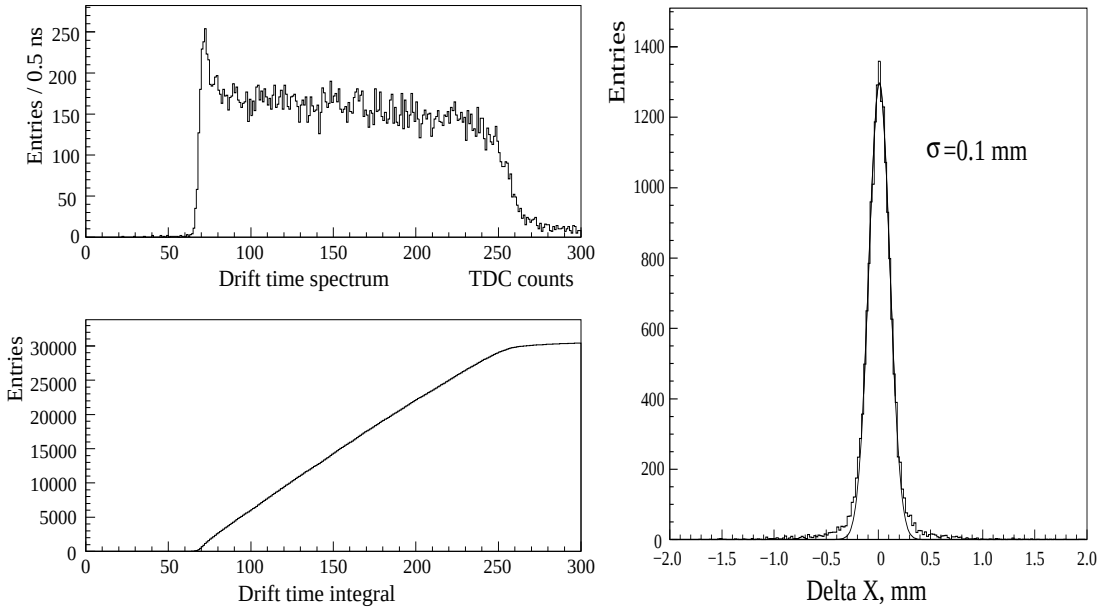

Figure 2.11: *Distribution of the drift time (left upper) and its integral spectrum (lower), horizontal scale is in TDC channels, bin width is* $0.5\ ns$*. On the right-hand side distribution of differences between the measured and predicted X-coordinate is displayed. Plots from* $X4$ *plane.*

Coordinate resolution of the DC system is illustrated too in Fig. 2.11,

where the distribution of differences between the predicted position and measured coordinates in one of the planes is shown ($X4$-plane right arm). The measured standard deviation, $\sigma = 100\ \mu m$, is defined not only by the intrinsic chamber plane resolution, but also by the accuracy of the predicted track coordinates. Taking the latter into account the measured intrinsic space resolution of one plane is better than 90 μm.

2.7 Time-of-Flight detector

A hodoscope system consisting of vertical and horizontal scintillation slabs has been placed downstream the drift chambers. It has the overall purpose of providing fast coincidence signals between both spectrometer arms, necessary for the first level trigger and for events selection.

The vertical array of scintillation counters is used, in correlation with other detectors, in the definition of dedicated triggers for calibration purposes and of a higher level trigger for the selection of low Q events (see trigger section). A key function of this detector, which motivated a special design, is to provide a very accurate time definition of pion pairs originated from the same proton interaction (**prompt** pairs), in order to perform a clean separation (in off-line analysis) with respect to pairs in which the pions are produced at different times (**accidental** pairs). Used as a time-of-flight detector it allows to identify $p\pi^-$ pairs in prompt events, as they might constitute a significant source of background to the $\pi^+\pi^-$ signal.

The TOF detector (also called VH) consists of two identical telescopes matching the acceptance of the DC system. Each telescope contains an array of 18 vertical scintillation counters. The slab dimensions are 40 cm length, 7 cm width and 2.2 cm thickness. Scintillation light is collected at both ends by two 12-dynode Hamamatsu R1828-01 photomultipliers coupled to fish-tail light guides. The front-end electronics was designed to minimise the time jitter, providing a position independent time measurement.

The VH single-hit detection efficiency is 99.5% for the positive, and 98.8% for the negative hodoscope arms. In Fig. 2.12 the distribution of the time difference between positive and negative pions in the spectrometer

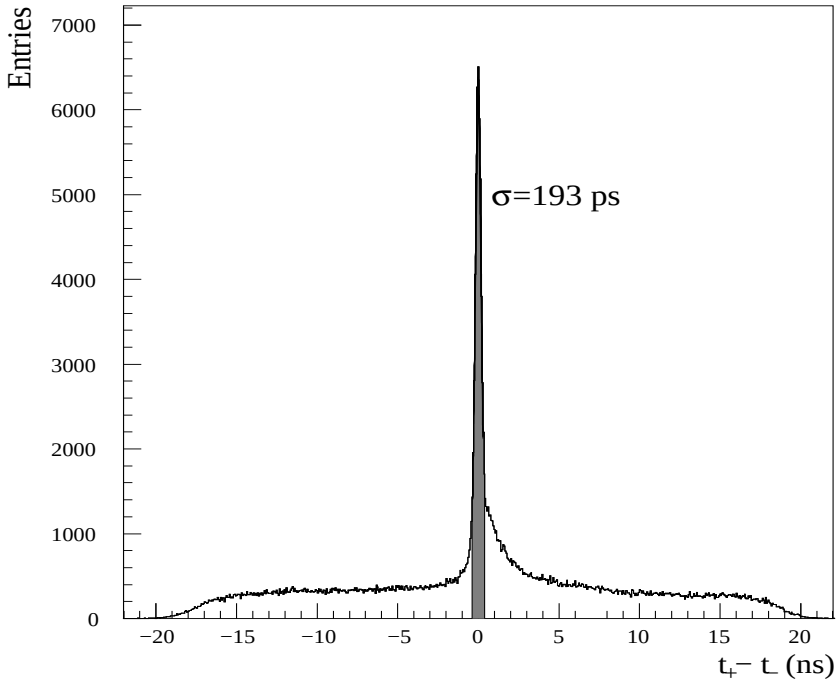

Figure 2.12: *Time difference between charged positive and negative particles obtained from standard hadron trigger data. The central peak has a gaussian width of 193 ps, and the shaded area represents a 2σ cut used to select prompt $\pi\pi$ events. The flat background is originated from accidental pairs, not belonging to the same beam interaction. Note the shoulder on the right-hand side of the peak, due to $\pi^- p$ prompt pairs.*

is shown. The observed ratio between prompt and accidental pairs in the 2σ cut region around the peak is about 16. The overall time resolution of the system has been measured with e^+e^- pairs to be 127 ps per counter [34], which corresponds to 174 ps accuracy for the time difference between positive and negative arms (time-of-flight resolution). The latter is shown in Fig. 2.13. The dedicated e^+e^- calibration trigger selects e^+e^- pairs from γ conversions and Dalitz decays of π^0 which are almost synchronous in time, as the time of flight of e^+e^- pairs is momentum independent in the available setup range of momenta.

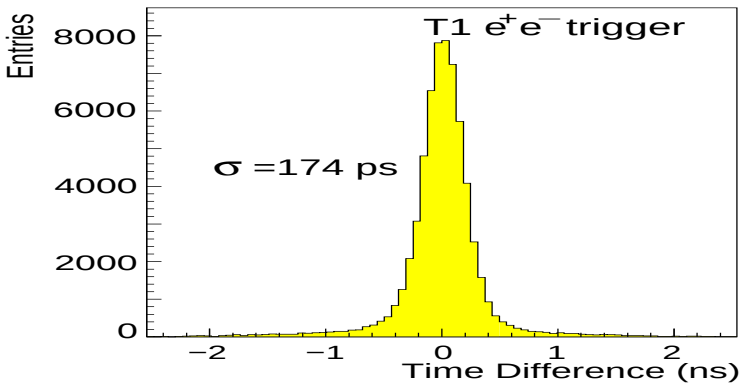

Figure 2.13: *Time difference spectrum for e^+e^- pairs detected by the vertical hodoscopes, after path length correction. Data come from e^+e^- triggers.*

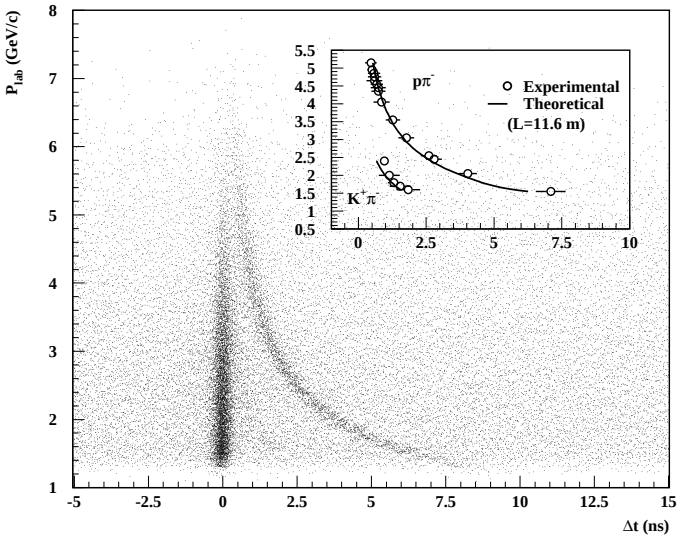

Figure 2.14: *Correlation between the measured momentum of the positive particle and the VH time difference between the positive and negative spectrometer arm, taking into account the correction for the difference in path length. The accumulation bands correspond to $\pi^-\pi^+$ (vertical band) and π^-p (curved band) pairs.*

This timing capability allows to separate $\pi^+\pi^-$ from π^-p pairs in the momentum range from 1 to 5 GeV/c, and from $\pi^\mp K^\pm$ pairs in the range from 1 to 2.5 GeV/c, as illustrated in Fig. 2.14.

2.8 The Horizontal Hodoscopes

The horizontal hodoscope system has a similar design and implication on the definition of the first level trigger as VH. Its response is used to apply a coplanarity criterion for triggering pairs hitting both detector arms. This trigger requirement selects oppositely charged particles with relative vertical displacement, Δy, less than 7.5 cm. Its response is used to select events with small relative angle in the Y direction, and to support the reconstruction with spatial track information.

It is also separated into two arms, each covering an area of $40\ times 130\ cm^2$. Each hodoscope consists of 16 horizontal extruded scintillating slabs of dimensions $130 \times 2.5\ cm^2$, with a thickness of 2.5 cm. Both ends of each slab are coupled to specially shaped light-guides as illustrated in Fig. 2.15.

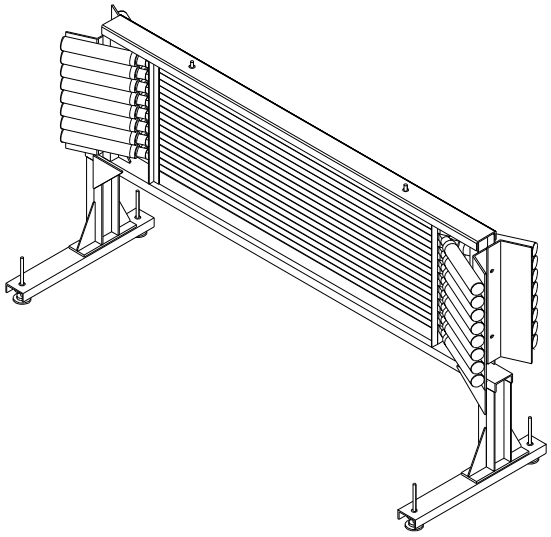

Figure 2.15: *General layout of the horizontal hodoscopes.*

Photomultipliers are equipped with a voltage divider allowing high counting rate capability. Front-end electronics system is the same as those for the vertical hodoscopes. The single hit detection efficiency of HH is greater than 96.6 % on both arms, and the time resolution is 320 ps.

2.9 The Cherenkov Counters

It provides the strong e/π separation capability needed by the experiment. This detector is essential for rejection of the main background of electron-positron pairs from photon conversion, Dalitz pairs, and to a minor extent from resonance decays. It is used in the first level $\pi^+\pi^-$ main trigger, in the calibration trigger to select e^+e^- pairs and its signals are available for offline analysis.

The cherenkov radiation occurs when the velocity of charged particle exceeds the velocity of light in a dielectric medium, and it polarizes atoms resulting in emission of coherent radiaton. DIRAC's cherenkov detector is structured in two identical threshold cherenkov counters [35], each covering one spectrometer arm (Fig. 2.16). The gas radiator is enclosed in a volume with dimensions 143×56 cm^2 and 336×96 cm^2, respectively. The chosen radiator is N_2 at normal temperature and pressure ($\theta_c = 1.4°$) and the counter length is 285 cm. Each counter is equipped with 20 mirrors and 10 photomultipliers on two rows. Cherenkov light reflected by pairs of adjacent mirrors is focused onto the same photomultiplier . The analog signals from PM are fed into two custom-made summing modules, discriminated and used for trigger purposes.

A single photoelectron peak is clearly observed in all channels and it is shown in Fig. 2.17, where we can see the ADC spectra from pions (a) and from single electrons (b). The number of photoelectrons detected by one counter arm is shown in Fig. 2.18, and from it we infer that both counters have an efficiency greater than 99.8 % when operated at a threshold slightly less than 2 photoelectrons. The pion contamination above the detection threshold is estimated to be less than 1.5 %. Such contamination arises from pions with momenta above the cherenkov threshold and from accidental

coincidences occurring within the trigger time-window.

A general picture of the installed detectors described so far, looking into the magnet from a distance close to that of the cherenkov counter, can be appreciated in Figure 2.19.

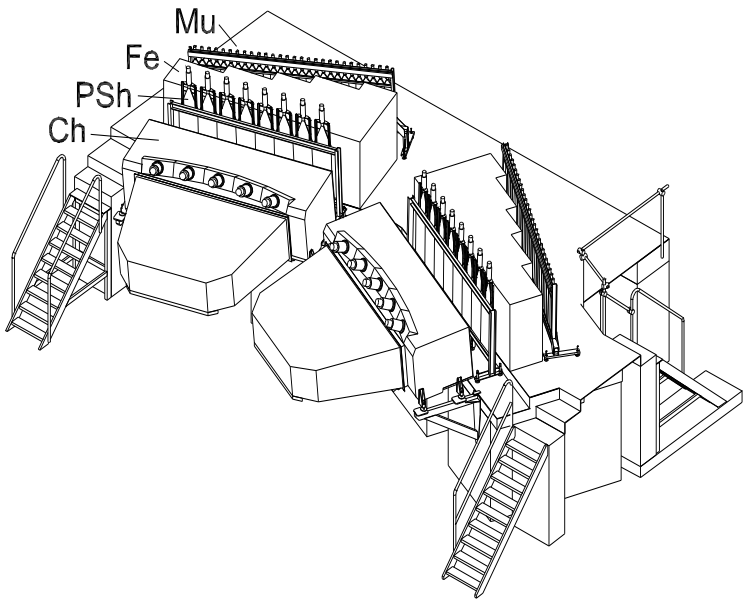

Figure 2.16: *The far end part of the DIRAC setup, comprising threshold cherenkov counters (Ch), preshower detector (PSh), iron absorber (Fe) and muon counters (Mu).*

2.10 The Preshower Detector

The purpose of the Preshower detector is two-fold: it provides additional electron/pion separation power in the off-line analysis and it is used in the trigger generating logic as well (T1).

The PSH is based on an array of lead converters followed by scintillation detectors [36]. Electrons (positrons) initiate in the converters electromagnetic showers which are sampled in the scintillation counters while pions be-

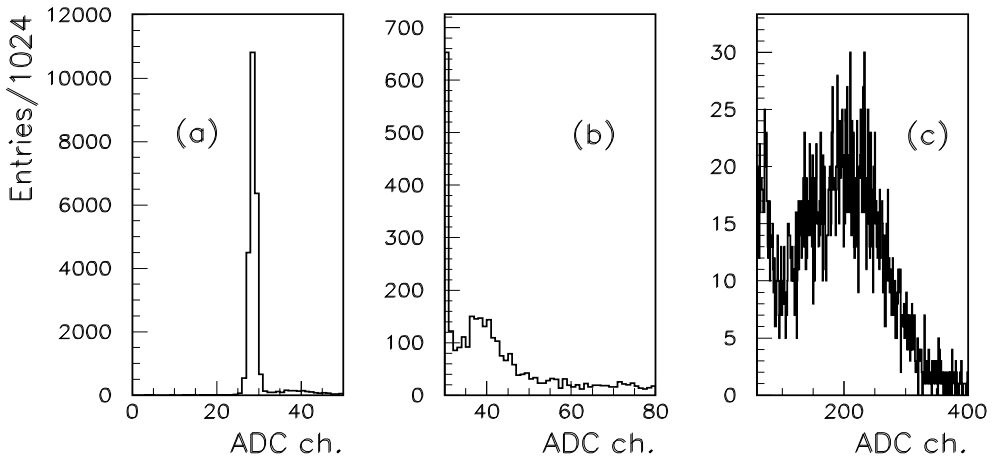

Figure 2.17: *ADC spectrum from one cherenkov photomultiplier: (a) spectrum from pions (practically equal to the ADC pedestal distribution), (b) amplitude signal from single photoelectron, (c) spectrum from electrons.*

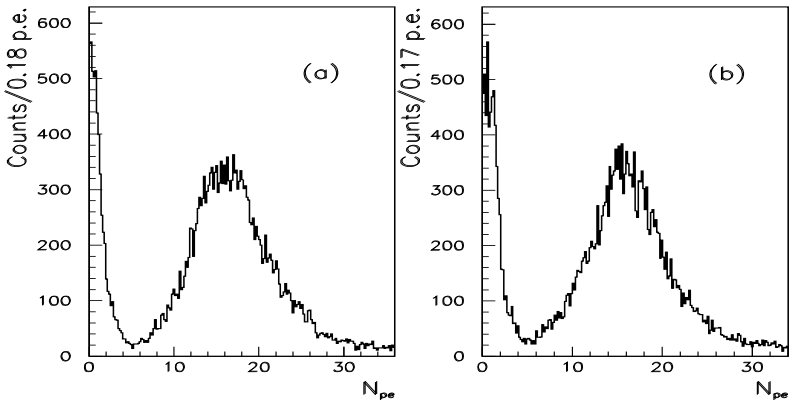

Figure 2.18: *Distribution of the number of photoelectrons detected from the (a) positive and (b) negative cherenkov detector arms.*

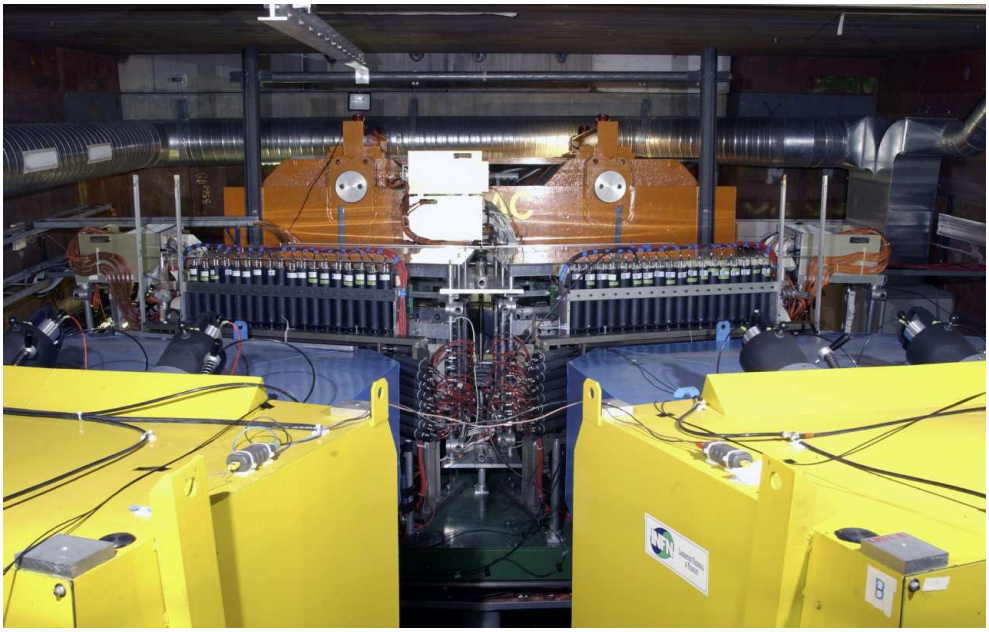

Figure 2.19: *General picture of the spectrometer installed downstream the magnet, taken from a reference plane close to the cherenkov counters, which can be appreciated in the bottom part of the picture. The magnet can be seen at the far end, and in between we see the vertical and horizontal hodoscope photomultiplier layout. The drift chamber system is installed behind it.*

have mainly as minimum ionizing particles. For trigger purposes, the signal has to be produced whether a pion or an electron cross a PSH counter.

The PSH consists of 16 detector elements placed symmetrically in two arms, as seen in Fig. 2.16. Each element has a Pb converter and a scintillation counter, Fig. 2.20. The converters of the two outermost elements of each arm (low momentum region) are 10 mm thick, whereas the rest are 25 mm thick (around 2 and 5 units of radiation length, respectively).The scintillator slab dimensions are $35 \times 75\ cm^2$ and 1 cm thickness. The detector signals are linearly split into two branches, one used for trigger purposes and another for ADC analysis. In the former, a leading edge discriminator is used with a threshold corresponding to efficient detection of minimum

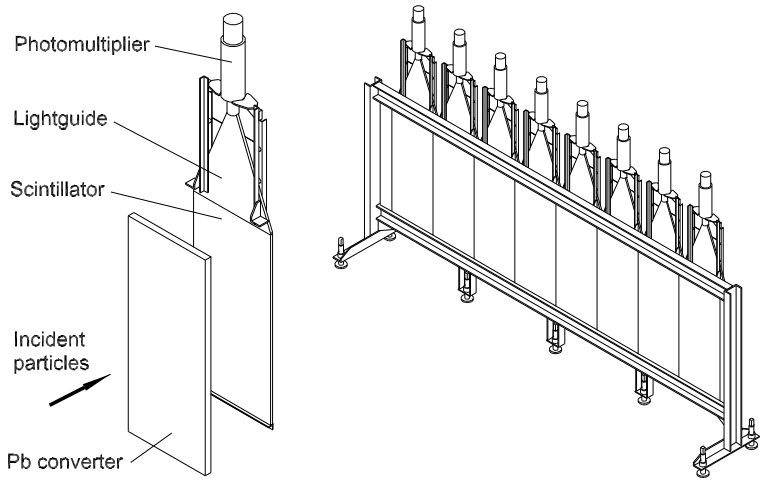

Figure 2.20: *PSH element and PSH array on one spectrometer arm.*

ionizing particles.

The single arm detector efficiency is 99.5% for pions. Fig. 2.21 shows the pulse-height spectra from one element of the PSH for pions and electrons selected by the trigger system (this selection is based on the cherenkov detector response). The pion spectrum has a tail (originating from nuclear interaction of pions in the converter) extending to the electron amplitude region. Off-line study showed that rejection of electrons reaches 85% with less than 5% losses of pions, what combined with cherenkov on-line identification yields almost 100% electron rejection (e/π ratio better than 10^{-4})

2.11 Muon detector

Admixture of decay muons in the $\pi\pi$ events can be a serious source of background. For this reason a muon detection system is implemented to provide efficient muon tagging in off-line analysis. Muons come almost entirely from pion decays with a small admixture from other decays and direct $\mu^+\mu^-$ pair production.

The muon detector consists of a double layer structure of scintillation

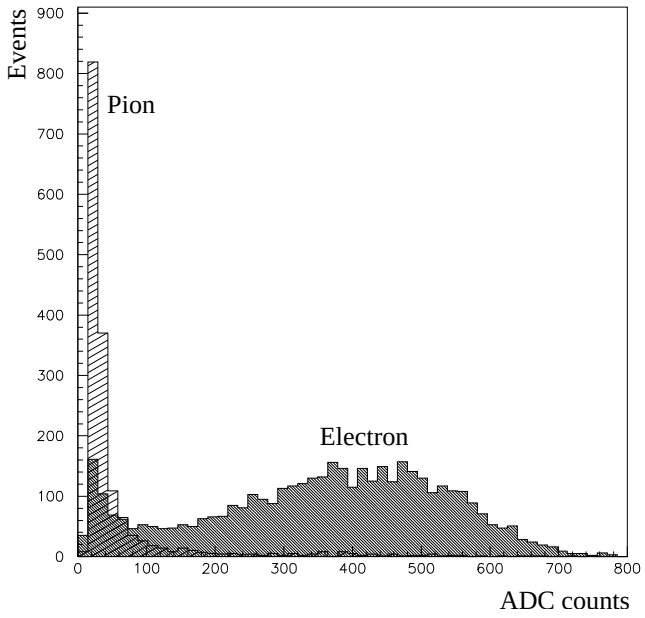

Figure 2.21: *Pulse-height spectra for pions and electrons in one element of PSH.*

counters (28 counters with equal scintillating slabs of $75 \times 12\ cm^2$ front area and 0.5 cm thickness per arm) placed behind a thick(from 60 to 140 cm, see Fig. 2.16) iron absorber which almost entirely absorbs hadrons and related hadronic showers. The thickness is larger in the region close to the spectrometer symmetry axis, in order to compensate for the harder pion momentum spectrum. This detector is placed at the downstream end of the DIRAC apparatus, few meters from the intense primary proton beam dump. As a result, the muon scintillation counters may undergo a high flux of background radiation from the beam dump area, which has required a special design of the counter arrays and electronics.

To reduce this background, data from muon detector are read out only if simultaneous signals from a pair of corresponding counters in the two layers are detected. In Fig. 2.23 the measured time difference between the signals of the muon detector and the VH is displayed for an individual muon element of the positive arm, showing a global time resolution of 1.3 ns.

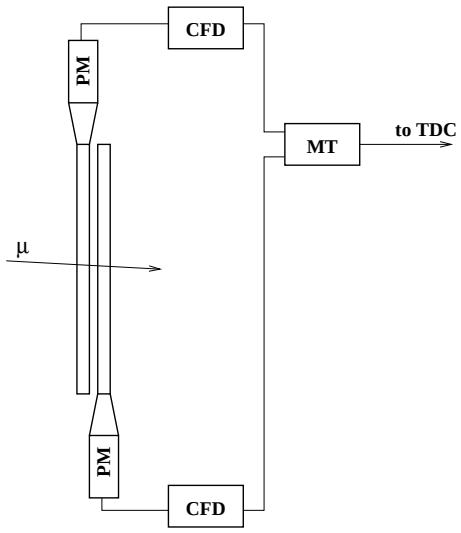

Figure 2.22: *Readout scheme of the muon detector element.*

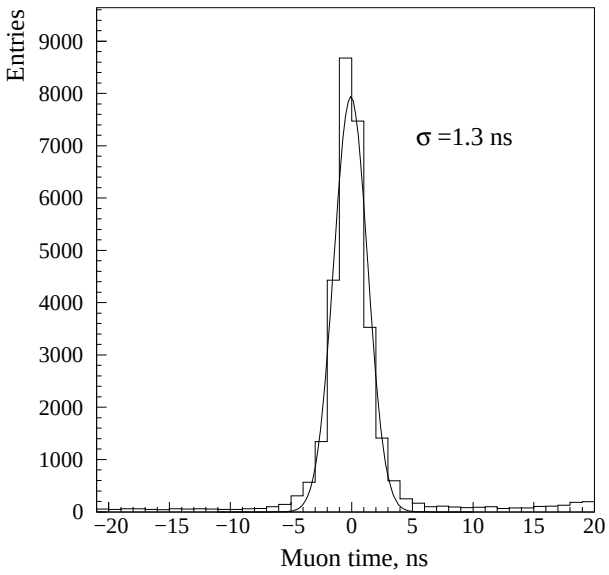

Figure 2.23: *Time difference between the signals of the muon detector and the vertical hodoscope.*

Off-line use of muon counters has been chosen to avoid suppression of useful pion events on-time with background signals in this detector. From experimental data we have inferred that the fraction of events containing at least one muon is about 10% [37].

2.12 Trigger system

The trigger system was designed to provide a reduction of the event rate to a level acceptable to the data acquisition system which is around 700 events/spill. Pion pairs are produced in the target mainly in a free state with a wide distribution over their relative momentum Q, whereas atomic pairs from $A_{2\pi}$ disintegration have very low Q, typically below 3 MeV/c. The on-line data selection rejects events with pion pairs having approximately $Q_L > 30\ MeV/c$ or $Q_T > 10\ MeV/c$, keeping at the same time high efficiency for detection of pairs with Q components below these values.

A sophisticated multilevel trigger is used in DIRAC [38]. It comprises a very fast first level trigger and two higher level trigger processors.

Due to the requirements of the data analysis procedure, to the on-line selection of time correlated (prompt) pion pairs, is added a large number of uncorrelated, accidental, pion pairs. The statistical error of the $A_{2\pi}$ lifetime measurement depends on the number of both prompt and accidental detected pairs so events are collected inside a coincidence time window ($\pm 20\ ns$) between the times measured in the left (VH1) and right (VH2) vertical hodoscopes, centered around the peak of prompt events

A block diagram of the trigger architecture is presented in Fig. 2.24. At first, pretrigger T0 starts DNA and the first level trigger T1 starts digitisation of the detector signals in the data acquisition (DAQ) modules (ADC, TDC, etc.). A positive response from T1 starts a powerful drift chamber trigger processor T4. At the next level the neural network trigger DNA/RNA rejects the events with high Q values, and a positive decision from it in coincidence with positive decision of T1 is used again in coincidence with T4 decision, which imposes additional constraints to the relative momentum and takes the final decision to accept or to reject the event, start the readout of all

electronics or clear the buffer.

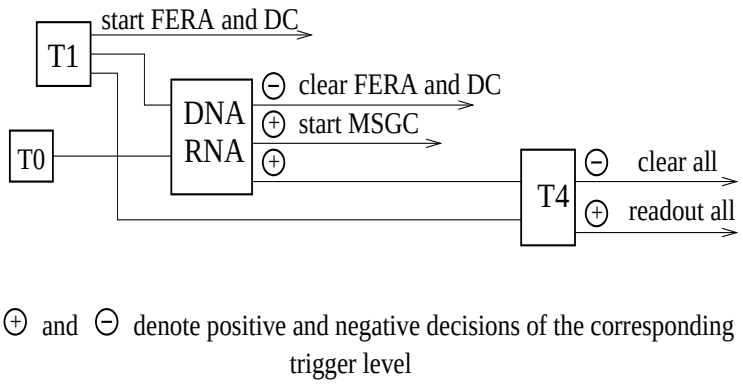

Figure 2.24: *General block diagram of the DIRAC multilevel trigger.*

In addition to the main trigger designed to detect pionic atoms, several calibration triggers are run in parallel.

2.12.1 First level trigger (T1)

The first level trigger (a detailed description is given in [40]) fulfils the following tasks:

- Selects events with signals in both detector arms.
- Classifies the particle in each arm as $\pi^{\pm}$ or $e^{\pm}$ depending on the presence of the cherenkov counter signal. Protons, kaons and muons are equally included in the "pion" class (the discrimination is done offline). For the pion signature $\pi^{+}\pi^{-}$ signature is needed a coincidence of a hit in VH, HH, no signal in Cherenkov counters and a signal coming form PSH in arm i:

$$(VH_i \cdot HH_i \cdot \overline{CH_i} \cdot PSH_i)$$

Meanwhile for $e^{+}e^{-}$ signal in Cherenkov is required:

$$(VH_i \cdot HH_i \cdot CH_i \cdot PSH_i)$$

The signal from both arms are combined to produce the final decision

- Arranges the coincidences between the signals detected in the two arms with a $\pm 20\ ns$ time window in Vertical Hodoscopes.

- Applies a coplanarity (Copl) criterion to particle pairs: the difference between the hit slab numbers in the horizontal hodoscopes in the two arms (HH_1 and HH_2) should be ≤ 2. This criterion forces a selection on the Q_y component of the relative momentum and provides a rate reduction by a factor of 2.

- Selects in parallel events from several physics processes needed for the setup calibration with desired rate: e^+e^- pairs, Λ decaying into a proton and a negative pion (see chapter 7), $K^{\pm}$ decays to three charged pions.

The electronics of T1 gives a decision within 120 ns. For Ni-2001 data physical pion trigger is set to (T1·$\pi^+\pi^-$·Copl).

2.12.2 Neural network trigger (DNA/RNA)

The DNA/RNA (Dirac Neural Atomic and Revised Neural Atomic triggers) is a processing system [41] [42] that uses a neural network algorithm.

Pretrigger T0 provides fast initial signal to DNA (coincidence of hit slab in VH1, VH2, PSH1 and PSH2). DNA/RNA receives (see Fig. 2.25) the hit patterns from VH1, VH2 and the X-planes of IH and the SFD, that are analyzed for the two arms, put in OR($\wedge$) relation with the following logic:

$$(VH_1 \cdot VH_2 \cdot IH_{x,1}) \wedge (VH_1 \cdot VH_2 \cdot IH_{x,2})$$

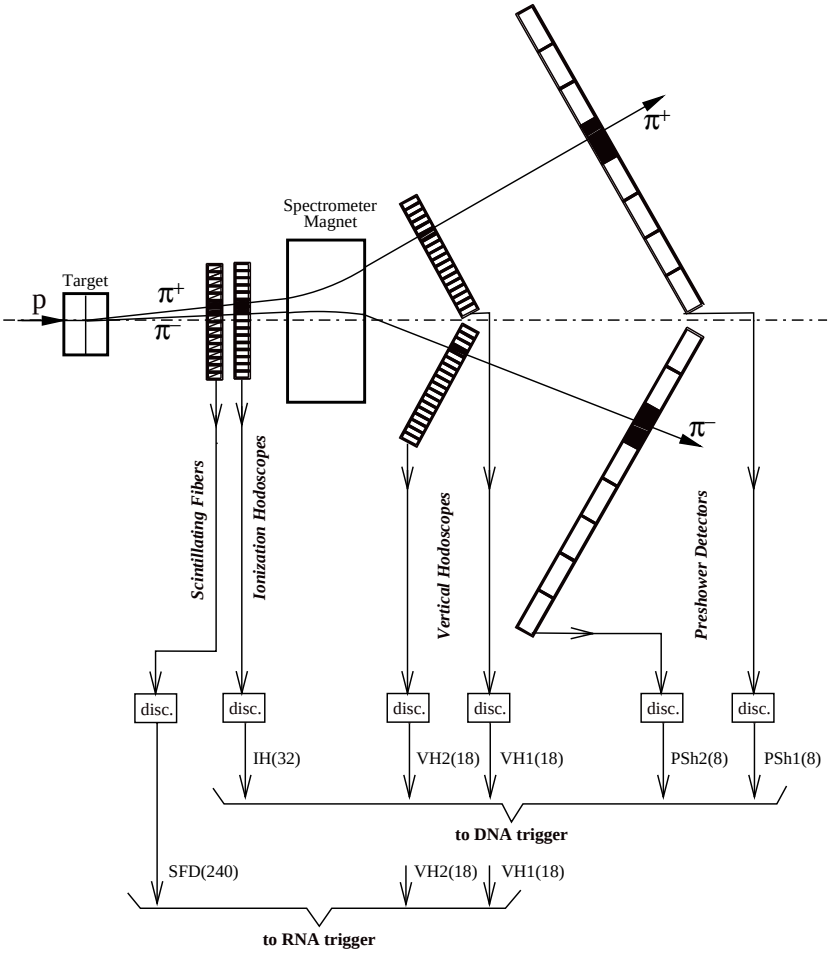

Figure 2.25: *DIRAC detectors used for the neural network triggers DNA and RNA. Numbers of signal channels from each detector are given in parentheses.*

The neural network was trained with Monte Carlo and real data to select particle pairs with low relative momenta: $Q_x < 3\ MeV/c$, $Q_y < 10\ MeV/c$ and $Q_L < 30\ MeV/c$. The events which do not satisfy any of those conditions are considered "bad" and rejected. DNA decision needs a positive decision from T1 for the event to be processed.

With DNA/RNA a rate reduction by a factor of 2.3 with respect to T1 is

achieved, and evaluates an event in 250 ns with an efficiency in low $\vec{Q}$ region of 94%.

2.12.3 Drift chamber processor (T4)

T4 is the final trigger stage and it requires DNA positive as input. T4 processor reconstructs straight tracks in the X-projection of the drift chambers which allows to select pairs with low relative momentum (the algorithm is described in [38]). The block diagram of the T4 operation is shown in Fig. 2.26. The drift chamber processor includes two stages: the track finder and the track analyzer.

The **track finder** the hit wires information from all DC X-planes (drift time values are not used in the T4 logic). For each combination of hits in two edge base planes defines hit windows for the intermediate planes and number of hits inside it are counted and required to be more than 4. An identical processor is used for each arm.

If tracks are found in both arms, the **track analyzer** continues the event evaluation. Track candidates are compared with a the contents of a look-up memory table obtained with Monte Carlo methods containing all possible combinations of track identifiers for pion pairs with $Q_L < 30\ MeV/c$ and $Q_x < 3\ MeV/c$ and allows the start of data transfer to VME if a coincidence is found.

The T4 decision time depends on the complexity of the event and is around 3.5 μs on average, being forced a positive response if time exceeds a limit in order to reduce dead-time [39]. The rejection factor of T4 is around 5 with respect to the T1 rate and around 2.5 with respect to DNA/RNA, and efficiency for $Q < 30\ MeV/c$ exceeds 99%.

The whole trigger system is fully computer controlled: no hardware intervention is needed in order to modify the trigger configuration. With all selection stages enabled the event rate at the typical experimental conditions is around 700 per spill, that is well below the limits of the DAQ rate

capability, calibration triggers being 7%.

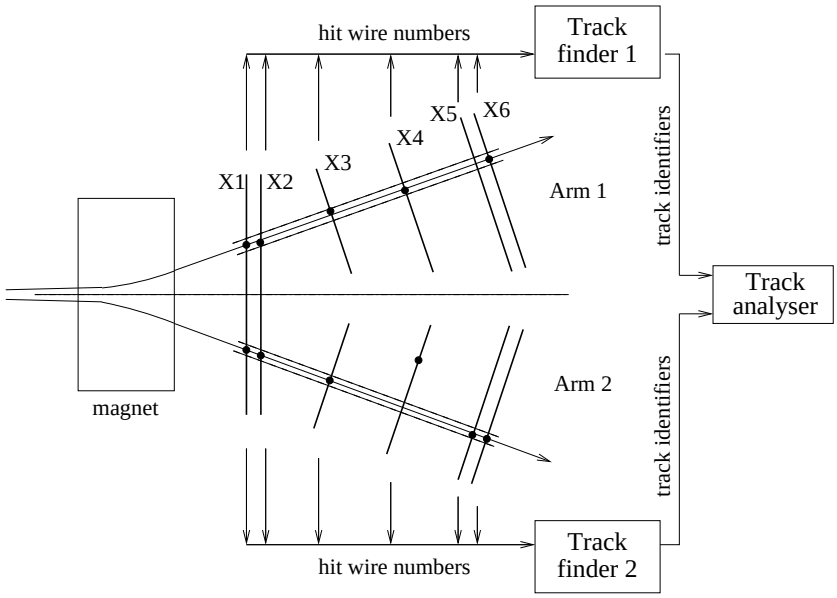

Figure 2.26: *T4 operation block diagram. Only the drift chamber X-planes involved in T4 are shown.*

2.12.4 Trigger performances

The performance of the trigger system as a whole in selecting low-Q events is illustrated in Fig. 2.27, where the magnitude of relative momentum of pion pairs Q is shown (in their center-of-mass frame), after DNA/RNA and T4 trigger selection (see trigger section). Trigger efficiency as function of Q is flat in the low-Q region, as illustrated in Fig. 2.27. This is considered an important figure of merit of the spectrometer, for a precision study of the $\pi^+\pi^-$ Coulomb interaction.

Pions from ionization of pionium entering the apparatus have momenta below 4 GeV/c. The apparatus momentum acceptance for time-correlated pairs is flat for pions with momenta between 1.6 GeV/c and 3 GeV/c, and it

decreases for higher momenta.

For the sake of completeness we also show the p and p_T distributions for a single π^- in Fig. 2.28, with superimposed a parameterisation of the inclusive yield based on the analytic representation [43], adapted to DIRAC center-of-mass energy ($\sqrt{s} = 6.84\ GeV$) [44].

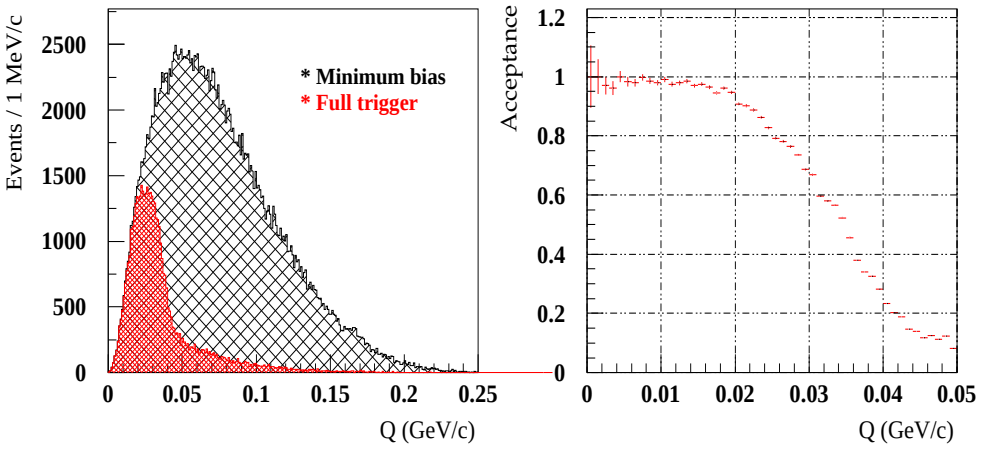

Figure 2.27: *Left: Distribution of Q for accepted $\pi^+\pi^-$ pairs after the full DIRAC trigger system, and for minimum bias pairs. Right: trigger acceptance, determined as the ratio between the previous two distributions.*

2.13 Data acquisition system

The architecture of hardware and software parts of the data acquisition system takes into account the time structure of the proton beam. During the accelerator burst the data from all detectors are read out into VME buffer memories (commercial and dedicated electronic modules) without any software intervention. The data transfer to VME processor boards, event building, data transfer to the main host computer and other relatively slow operations are performed during the pause between bursts. This provides the maximum operation rate of DAQ. The counting rates of all the detectors,

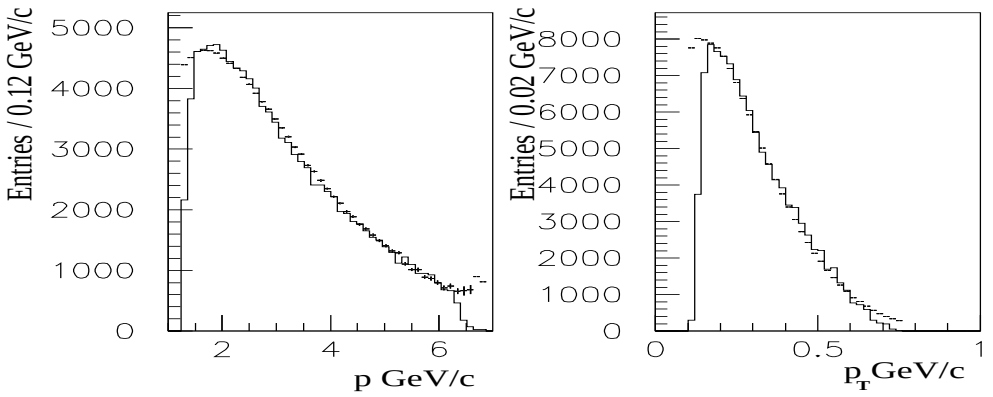

Figure 2.28: *Experimental p and p_T distributions of π^- corrected for apparatus acceptance (histogram) with superimposed the results of the parameterisation [43][44].*

trigger rates at different trigger levels and for different sub-trigger modes are recorded together with the value of the beam intensity provided by the PS complex.

The data readout [45] is arranged with 12 readout branches: 4 branches for MSGC/GEM [47], 3 branches for DC and 5 FERA [46] branches for all other detectors.

The logic of readout is the following. The first level trigger T1 starts digitisation in ADC and TDC of FERA and DC branches (see Fig. 2.24). If the T4 processor decides positively, the Inhibit Readout status is released and the converted event data are transferred to buffer memories. If the decision of DNA/RNA or T4 is negative, then a Fast Clear signal is generated [48] which discards the data in all FERA modules and DC registers. The processing of MSGC/GEM data is started by the next level DNA/RNA trigger. This reduces the dead time introduced by the Clear process which in MSGC/GEM electronics takes longer. Thus, the negative decisions of T4 only lead to clearing of the MSGC/GEM data. If no Clear signal is received, the converted data are transferred to buffer memories. The readout of the whole event takes 45 μs and is defined by a fixed acquisition time of MSGC which exceeds the

readout time in other branches.

The main part of the DAQ software [49] is running on two VME processor boards and on the main DAQ host. The main DAQ host performs event building, records the built data and distributes them to other computers for on-line monitoring and analysis. The DAQ software is written in C programming language and is running under UNIX-like operating systems.

The whole DAQ system is able to accept data from five consecutive bursts in one accelerator super-cycle with up to 2 MBytes per burst (this corresponds to 2000 triggers per burst) and to distribute events to all hosts participating in on-line data processing. The limitation comes from the capacity of the VME buffer memories.

An on-line monitoring program receives the data distributed by the main DAQ process. The program fulfils accumulation of several hundred histograms, including all raw signal spectra from any detector as well as spectra obtained after a fast preliminary data handling. The software is written in the frame of ROOT software package. Apart from the common program, there are dedicated monitoring programs developed for more detailed control of individual detectors.

Chapter 3

Microstrips Gas Detectors in DIRAC

MSGC/GEM detectors were chosen for the first set of active planes at the secondary particle channel. Their tracking principles, geometry, and construction technique are described in this chapter. In the last section, results from the study of relative gain done by the author for the two last installed planes, are presented.

3.1 The MSGC/GEM and GEM detector principles

MSGC (Micro Strip Gas Chambers) are proportional detectors, conceptually inspired by the Multi Wire Proportional Chambers (MWPC) developed in the 60's [50]. The wires of the MWPC are replaced by meta micro-strips implanted on a dielectric substrate, in order to improve space resolution and reduce occupancy and ion collection time. MSGC came as a natural improvement of MWPC when in 1988 Anton Oed [51] built the first prototype.

In a high radiation experiment like DIRAC, it allowed to resolve the problem of installin a tracking detector upstream the magnet that could stand particle fluences at the level $10^3 mm^{-2} s^{-1}$

Microstrips gas chambers showed however some problems due to the

presence of discharges inside the gas. This usually produced damages in the strips, so it forced to decrease the applied electric field, reducing the gain. A new amplification element was introduced by Fabio Sauli in 1996 [55], the Gas Electron Multpilier (GEM), a perforated metalic electrode film acting as amplifier of the proportional charge [53]. Using MSGC with GEM allows to reduce (by values higher than 100 mV) the voltage applied to the strips, providing a more secure operation. GEM implementation even allowed non parallel-plane geometries, and the use of several GEM layers could be combined as amplification stages.

3.2 MSGC/GEM of DIRAC experiment

The University of Santiago de Compostela has been responsible for the conception [11] and full construction of this detector. The author of this thesis participated actively in its upgrade in 2002, and was responsible for the installation in the beam of 2 new planes before the 2002 experimental period.

The MSGCs detectors of DIRAC are the first active planes of the spectrometer, at a distance of 2.4 m from the target foil. The four planes take part of the upstream tracking procedure of the experiment, developing the main task of direct measurement of particle trajectories upstream the magnet. Its excellent spatial resolution allows to improve the double track resolution for close lying tracks.

Four MSGC/GEM parallel planes are installed in the DIRAC spectrometer in first position from the interaction point (2.4 m), in order to reduce the multiple scattering in front to the minimun implied by the target foil. It performs the real measurement of the transverse momentum (Q_T) by measuring the distance between π^+ and π^-. Together ith SFD it also allows to improve the resolution of the longitudinal component Q_L, by providing the impact point at the magnet entrance. Because of its standalone tracking capability with stereo angles, it also monitors the beam position coordinates. MSGC's allows to resolve tracks with the same hit in SFD, improving double track resolution from 4 mrad to 0.6 mrad. The precise spatial resolution from MSGC together with TDC information from SFD allows an effective

rejection of background particles crossing the detectors from secondary interactions or particle decays along the channel. As a additional merit, they do not affect negatively to the global setup, adding a low quantity of matter and being practically transparents to the radiation.

The MSGC's measure particle coordinates in 4 planes along the direction of the incoming particle: X, Y, XP, YP, with orientations 0, 90, 5, 85 degrees, respectively, where the 0 degrees are defined by microstrips running vertically (X-coordinate). The distances to the target plane in Z coordinate are 2.338, 2.246, 2.464, 2.502 m. The stereo angles allow resolution of ghost ambiguities for two or more particles. With a single-hit space resolution close to 50 μm, this detector provides a precise measurement of the pion pair opening angle, ultimately limited by multiple scattering in the thin target. The four planes installed in DIRAC spectrometer can be seen in Fig. 3.1.

The DIRAC MSGC chambers are gas detectors working in proportional mode based on the principle of the Gas Electron Amplifier (GEM) [53] [52], complemented with a second amplification and readout stage provided by Micro Strip Gas Chambers. Each chamber has active area $10.24 \times 10.24\, cm^2$, and its active gas volume is limited by two planes, a drift electrode and a microstrip sensor plane. An additional GEM foil is placed between them, evenly spaced from the other two with a uniform gap of 3 mm, as indicated in Fig. 3.2.

The drift electrode is made of a Chromium-coated thin glass (200 μm) methalized in one side connected to a negative voltage. GEM is a kaptom film of 50 μm double-sided methalized with 4 μm of Cu. It presents a perforated pattern with 80 μm diameter wholes, 140 μm apart from each other. The microstrip plane consists of alternating Chromium strips mounted over a subtract DESAG D263 of 300 μm thick ionic glass. Anodes are 9 μm wide, catodes 100 μm and pitch between anodes is 200 μm. In the bottom side of microstrips plane a methalic film is used as electrode (backplane).

Planes are mounted on a Stesalit frame chemically inert with respect to the gas mixture. Detector gas used for operation is a mixture with Argon and Di-metil-eter (DME, C_2H_6O) in the 60/40 proportion. The entrance hole in the frame of the detector has a diameter greater that the output one, ensuring a light overpressure neccesary for detector working.

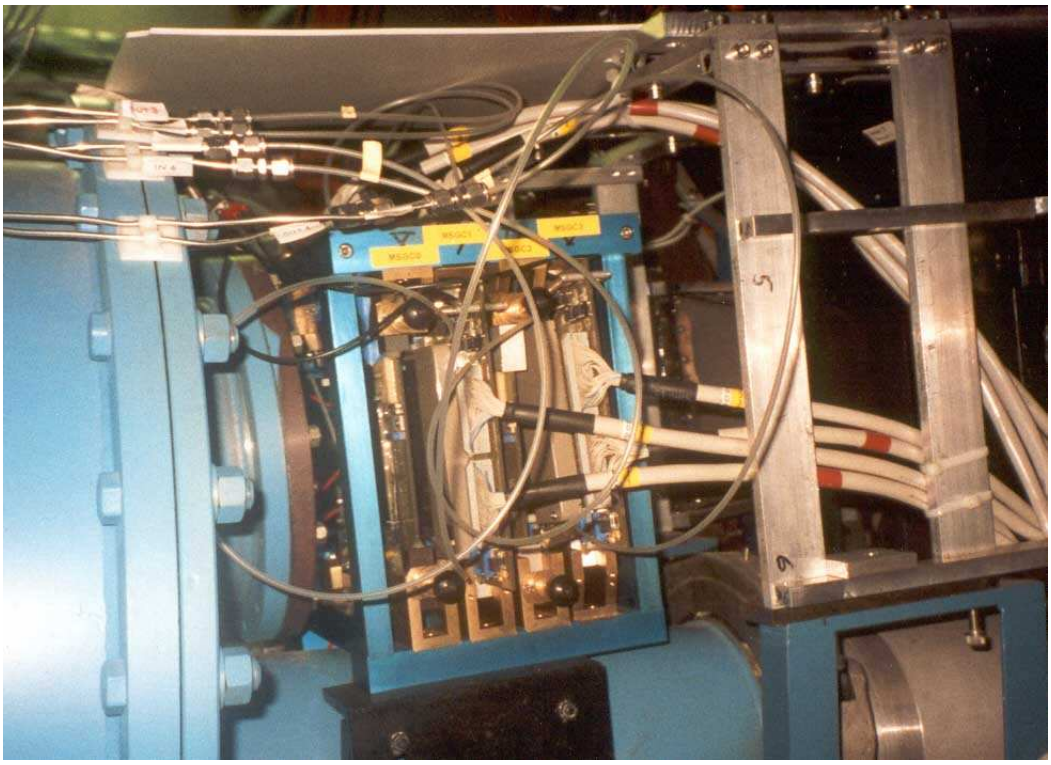

Figure 3.1: *The four MSGC/GEM planes installed in DIRAC spectrometer, between the vacuum chamber (left) and the SFD (right).*

With the implementation of GEM foil, applying a potential difference of $\sim 400\ V$ between the two metal layers (amplification by a factor of 30), primary electrons signal becomes doubly amplified, allowing lower values of High Voltage (HV) and so a more stable operational mode. A primary electron produced in the first gas volume, defined by the drift plane (with applied voltage of $\sim -400\ V$) and GEM, will ionize the atoms of the gas producing an initial electron avalanche when entering the GEM electric field. At a later stage, a new multiplication takes place in the region next to the microstrips. The electrons produced in the avalanche are collected by the anode (ground) nearest to the position of original electron. Electrons are attracted by the positive strips electric field developing a second avalanche

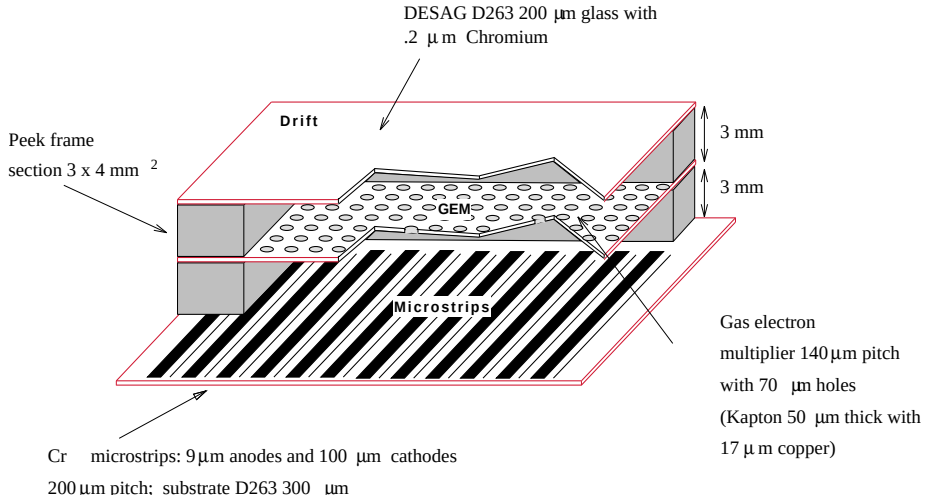

Figure 3.2: *Layout of the GEM/MSGC detector.*

so electron signal becomes doubly amplified. The cloud of postivie ions tends to cluster around adjacent cathodes, with applied voltage of $\sim -3000\ V$. An overall detector gain of approximately 3000 is achieved.

HV values are limited by sparks inside the gas volume, that may occur when charge collected by the strips is over a threshold value, usually produced under high particle flux conditions.

3.3 Electronics

For each plane, the electronics chain consists of three distinct parts:

- the Mother Board, which contains the front-end amplification and pipeline and it also serves as mechanical support for the detector active area.

- the Control Board that stores digital control sequence needed for APC chips and performs fast digital conversion of analog signals.

- the VME modules, to handle the trigger signal and perform real time pedestal subtraction and zero suppression [54].

3.3.1 Mother Board

Front-end electronics and active surface of the detector are mounted over this 4-level circuit board. 16 Analog Pipeline Chips (APC) are bounded on a multi-layer hybrid in order to perform the readout of microstrips signal. Cable connectors allows to receive the control sequence needed for APC chips, and to send analog ouptut with microstrip charge information. In Fig. 3.3 two MSGC planes ready for installation are shown, whereas a scheme of mother board can be seen in next figure (Fig. 3.4).

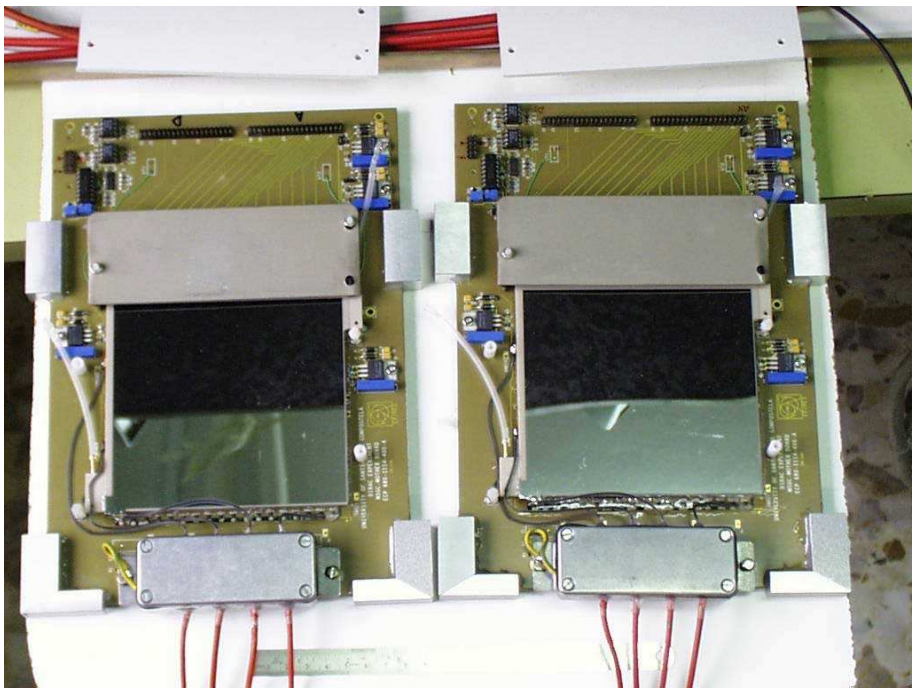

Figure 3.3: *Two MSGC/GEM mother boards before their installation at the DIRAC spectrometer. Hybrids with APC ASICs are covered to protect bondings.*

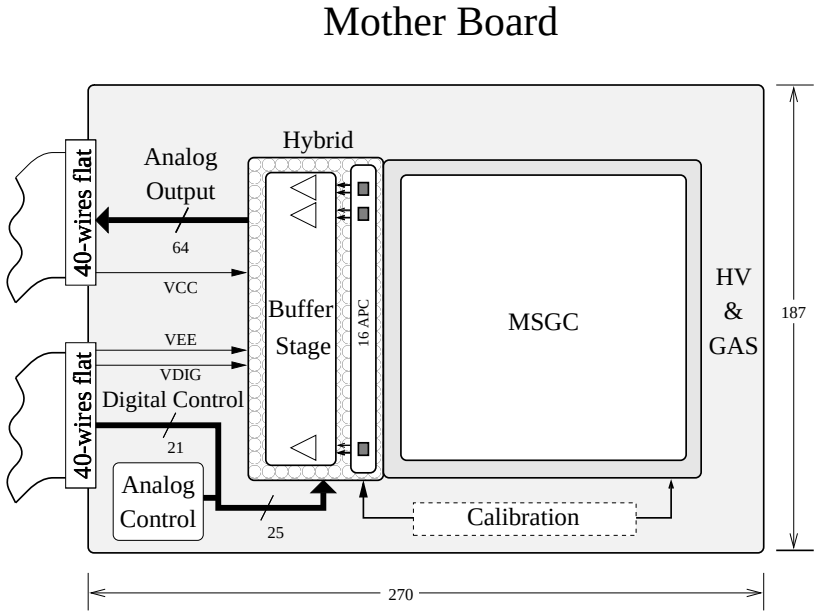

Figure 3.4: *Mother board scheme.*

APC ASICs

Designed by R.Horisberger [56], 16 ASICs are mounted on an hybrid layer sitting on the mother board, bonded with special design to the anode endings. ASIC is endowed wit 64 channels , each one with a charge sensitive preamplifier followed by analog programming memory (pipeline), run at 10 MHz, built by 32 capacitors and an edge-operation capacitor. Access to the channels is performed sequencially during the readout of cathodes signals, so in order to reduce dead-time only 32 of them are instrumented from the same ASIC (which allows to avoid the first noisy channel).

The analog pulse is formed by charge subtraction from consecutive capacitors, at positions given by the delayed trigger signal, following an specific protocol defined by APC control sequences [54]. The final ASIC output is 32 analog signals from the instrumented channels driven in parallel to the control board. This robust procedure, which allows easy integration of a large number of channels, limits however the time resolution of the readout

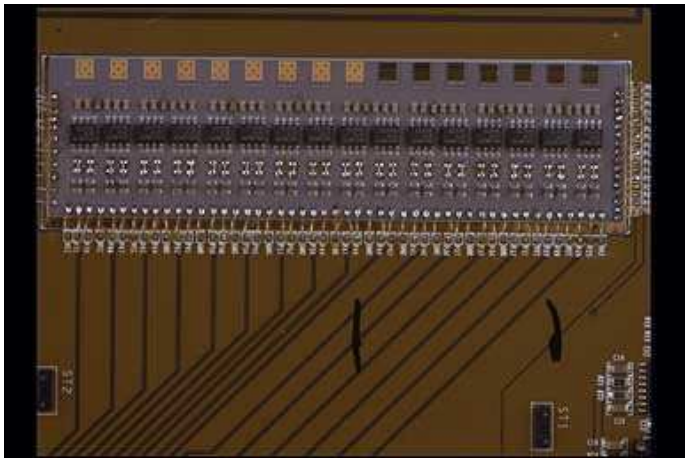

Figure 3.5: *Hybrid with y APC ASICs.*

to a window of approximately 200 ns, due to the 10 MHz frequency of the pipeline. In Fig. 3.5 we see several APC ASICs installed in the hybrid.

3.3.2 Control board

Control board was designed and built at CIEMAT (Madrid). It is placed inside the experimental area, past the magnet, behing the 1 m thick iron wall for radiation shielding. This board is equiped with a Fast Programmable Gate Array (FPGA) and develops two main tasks, namely:

- It stores the digital control sequence needed for APC ASICs, written in available memories at a first operation stage.

- Digitizes analog signal received from channel readout. Signals are multiplexed by means of 8 ADC ASICs and transferred to the VME board.

It receives from coaxial cables the trigger and fast clear signals needed for detector performance.

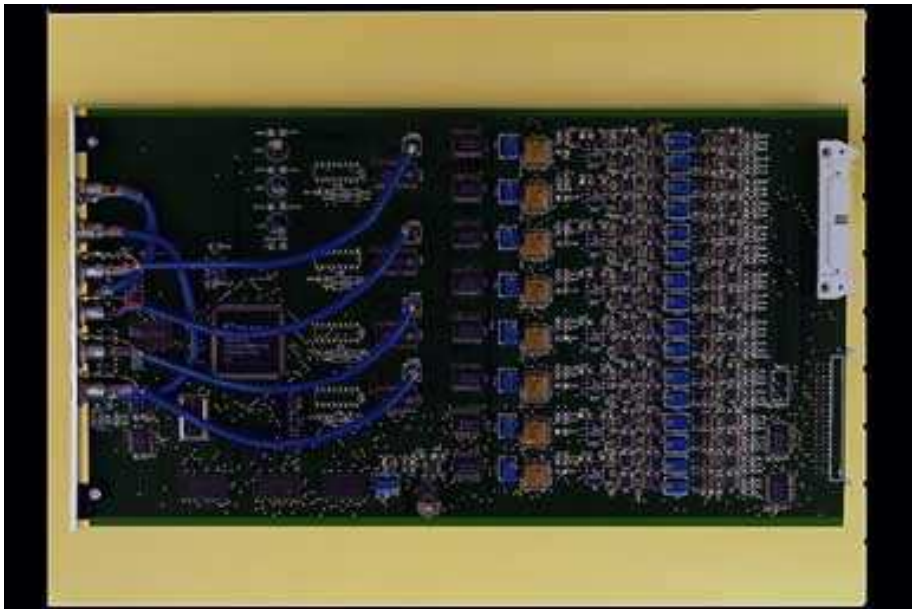

Control Board

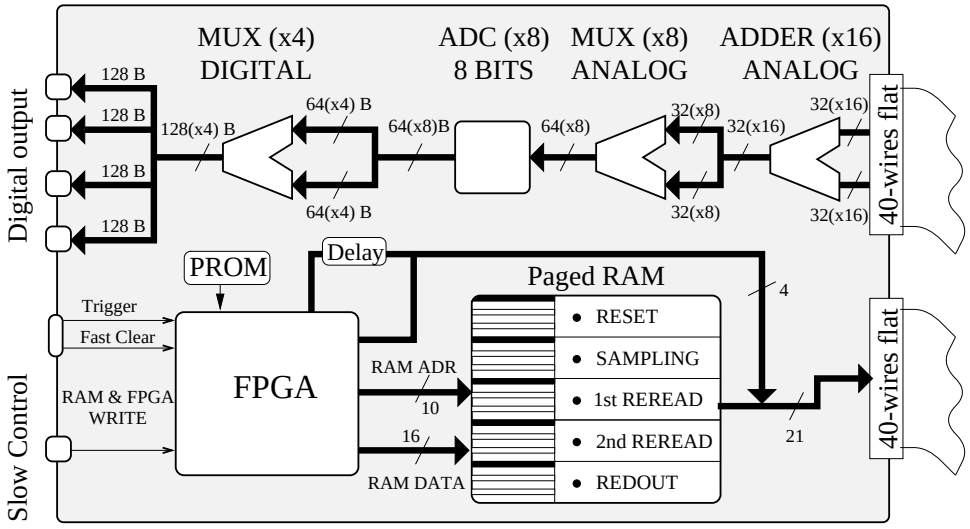

Figure 3.6: *Control board and its scheme*

3.3.3 VME module

The VME module, a joint design between CIEMAT and USC, is the last card of MSGC/GEM electronic chain, providing readout information to the DAQ system of the experiment. It is divided into 4 segments, each controlled by an independent FPGA.

This board receives multiplexed digitized signal from microstrip charge readout and performs real time pedestal subtraction and zero suppression. It handles trigger and Fast Clear[1] signals, and transfers APC control sequence to the control board.

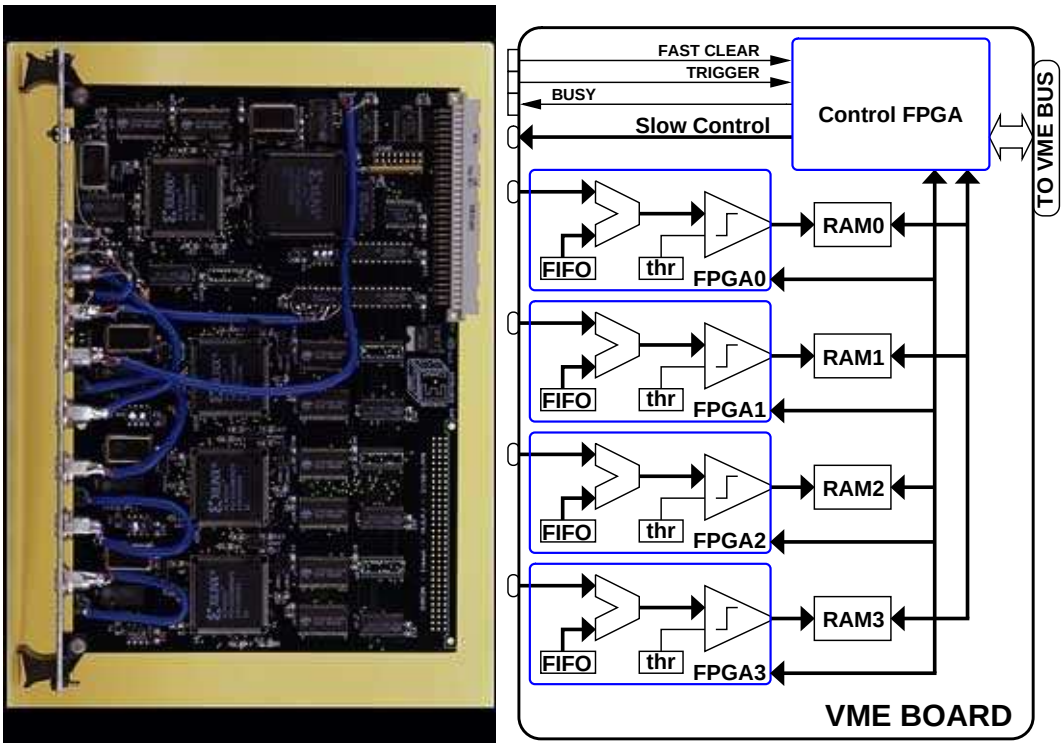

Figure 3.7: *Picture and schematized diagram of VME module of MSGC/GEM detectors.*

[1]This signal, implemented in the highest level trigger, stops the readout of current event and enables the system for new triggers.

3.4 Detector performance

Consecutive micro-strips with pulse above threshold are pattern-recognised as clusters (also called hits hereafter). Pulse height information is used to determine a center-of-gravity coordinate for each hit. We call hit multiplicity the number of microstrips fired in the cluster.

The hit multiplicity per cluster (a), and the number of cluster per plane (b) are shown in Fig. 3.9.

In Fig. 3.8 we can see how when two particles cross the detector plane at very small distance a special configuration is produced, where two clusters are separated by one lower microstrip pulse height. In this case, the two clusters are split, and the strip with minimun pulse height is divided in two halves.

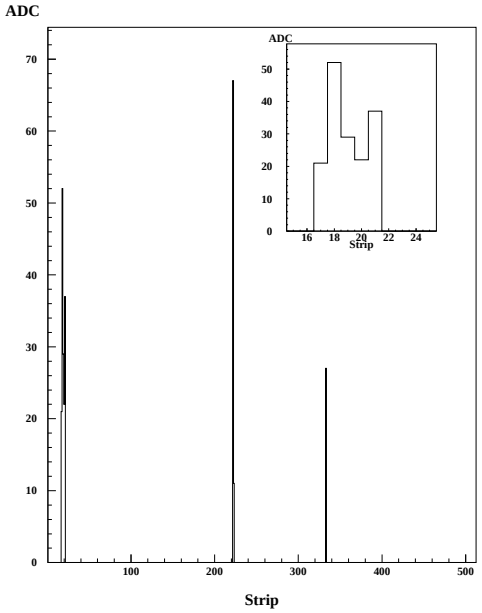

Figure 3.8: *ADC counts registered from a single event in one MSGC/GEM detector. First strips are shown in detail in upper-right part. Two clusters are identified and charge of strip 20 is split.*

For clusters with multiplicity greater than one single strip, associated coordinate is determined with a center-of-gravity algorithm, considering the pulse height of strips belonging to the cluster. The strip multiplicity per cluster made (a), and the cluster multiplicity per plane (b) are illustrated in Fig. 3.9.

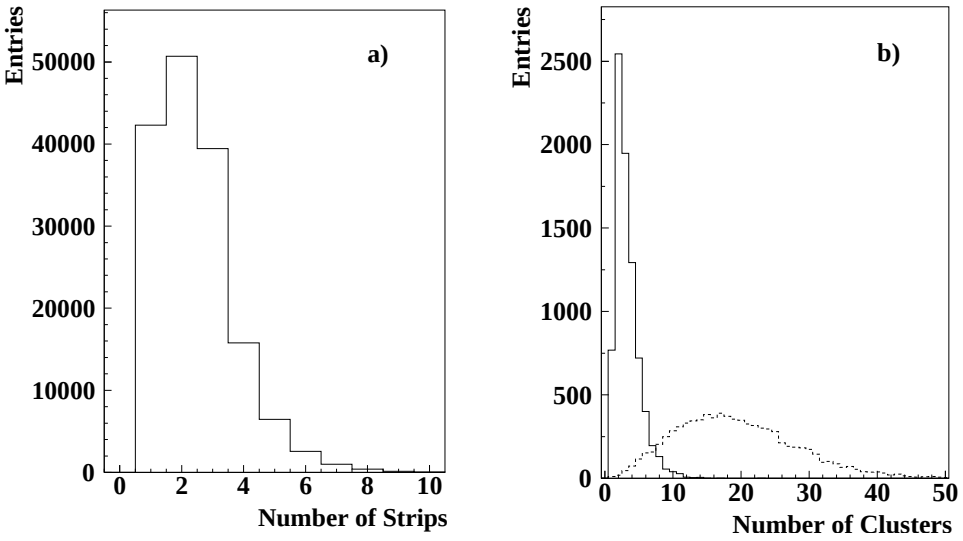

Figure 3.9: *a) MSGC strip multiplicity per hit-cluster b) cluster multiplicity per event in one plane (X). The dotted line shows all clusters registered by the data acquisition, whereas the continuous line shows only those having a time tag, established when the cluster has a corresponding hit in the SFD aligned with the interaction point.*

Single hit resolution was determined during the commissioning run in April 2000 by setting 4 MSGC planes parallel to each other, all measuring the some coordinate. The resolution was defined using in each case 3 detectors to define the track, and typical vales of 54 μm were found, as shown in Fig. 3.10. The average efficiency for a standard detector is 90%. When at least 4 signals among 6 detectors are required to construct a track, this is sufficient to provide 97% overall tracking efficiency upstream the magnet.

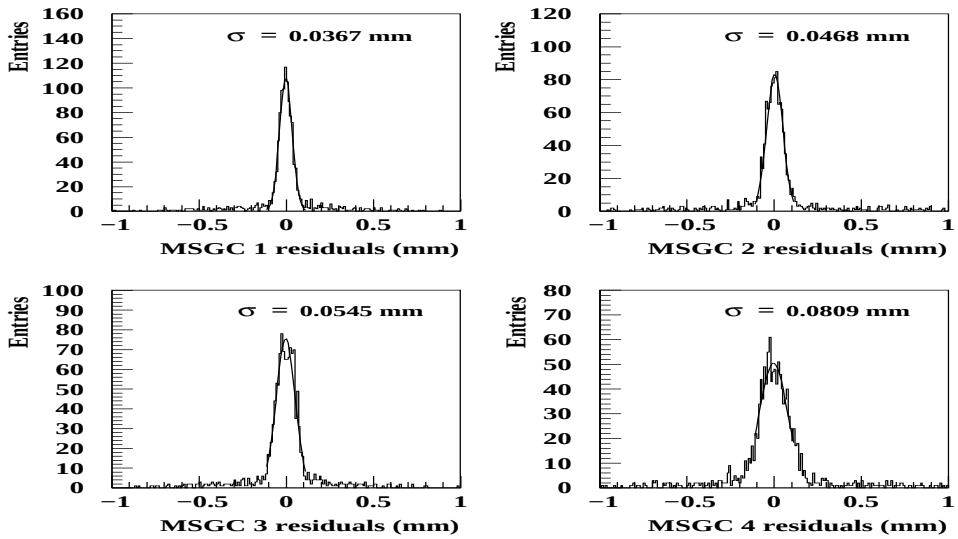

Figure 3.10: *Space resolution of the GEM/MSGC detector measured in a dedicated beam-test with 4 planes parallel to each other.*

Two detector planes were installed in 1999 and the full set of four planes was installed in 2001. In order to improve the gain performance and prevent ageing, two new planes were installed in 2002, which replaced the ones installed in 1999. The author of this thesis contributed to the construction and installation of the latter in the 2002 DIRAC run.

3.5 New MSGC/GEM detectors.

From the last months of 2001 to the end of April 2002, two new MSGC/GEM planes were constructed and fully tested in the Santiago laboratory prior to their the installation in the DIRAC spectrometer.

The whole MSGC/GEM setup, including the three main boards and auxiliary systems were reproduced and checked in Santiago. The electronics chain was mounted on a rack with VME, CAMAC and NIM crates and controlled via PC with LabVIEW software (see Fig. 3.11). The control and trigger signals were created by two dual timers, NIM-TTL and NIM-ECL convert-

ers. For high voltage a CAEN N471A source was used meanwhile for gas system Bronkhorst control unities were mounted over the two gas lines of Ar (30 cc/min) and DME (20 cc/min) with presures of 1-2 bar, and 10 mbar overpressure for the mixture.

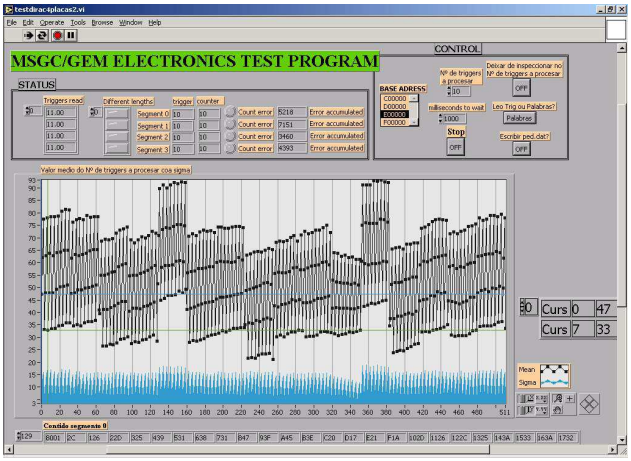

Figure 3.11: *Calibration signal shape used to test APC chips of new MSGC/GEM planes with LabView.*

The two new planes had two distinct features as compared to replaced MSGCs:

- Cathodes that collect ions from the multiplication were now powered in groups of 32 throught a decoupling resistor of 1 MΩ, while groups of 16 consecutive cathodes were used in the old planes. This scheme avoids that induced current in the anothes could mask the signal. With 32 coupled cathodes this effect is minimized (3% of signal reduction) and strips still have an effective protection for possible streamers[2].

- New implementation of HV distribution. A methalic box with 4 lemo cables at each side was mounted on the mother board. Cables provide high voltage from the HV source to the 4 electrodes. The setup consumes a maximun of 2 nA with standard HV values.

[2]anomalous avalanche with a large charge ouput from ionized atoms.

The 2nd of May 2002 the planes were installed in the DIRAC spectrometer to take part of the MSGC/GEM data taking periods. X and YP planes (placed at the two edges of the setup) were replaced. This choice was based upon the observed performance, efficiencies, and specially the number of dead strips in the old planes, which was over 1% of the total number of instrumented channels. Laboratory test previous to its installation at CERN revealed an amount of 0.6% and 0.2% dead channels for the new planes, due to imperfections or shortcuts in the microstrips plane, some of them shown in Fig. 3.12.

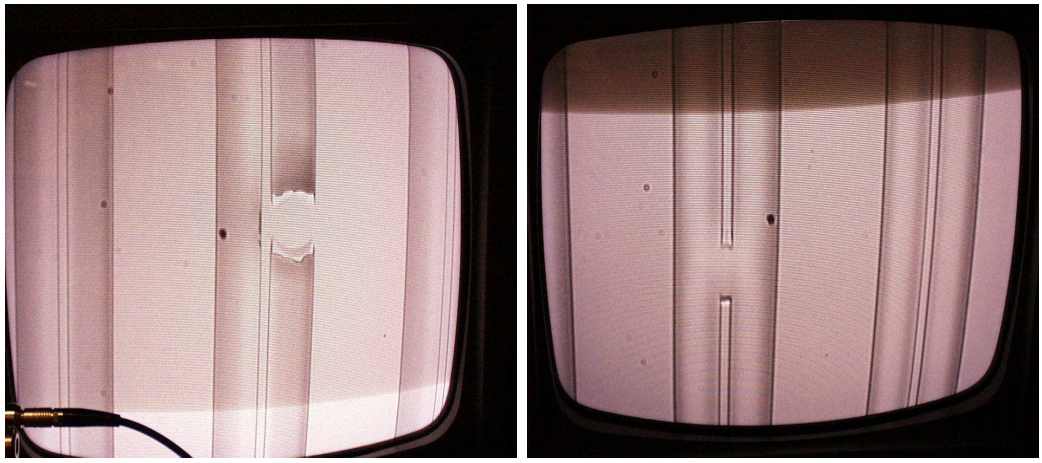

Figure 3.12: *Strips number 121 and 415 of one of the two new detectors. A shortcut (left) and a broken strip (right) as viewed with microscope.*

3.6 Uniformity of gain

To finalize the checks after the production of the two new detectors, the whole MSGC/GEM electronics, HV and gas setup was tested in the laboratory. A detailed study to evaluate the uniformity of the gain across the active area of the detectors ended the calibration job.

Uniformity of the multiplication gain is a key factor when searching for pulse height signal over a threshold during the clustering procedure, and precision center of the gravity of the clusters relies on a constant microstrip

gain.

Beta source of Ru-106, with characteristics summarized in table 3.1 and decay scheme as seen in Fig. 3.13, was used as radiation source. Due to the low thickness of microstrips detectors, decays of Rh to their fundamental state are negligible, coming detected radiation from beta decay of Rh (Ru $\rightarrow$ Rh has too low energy).

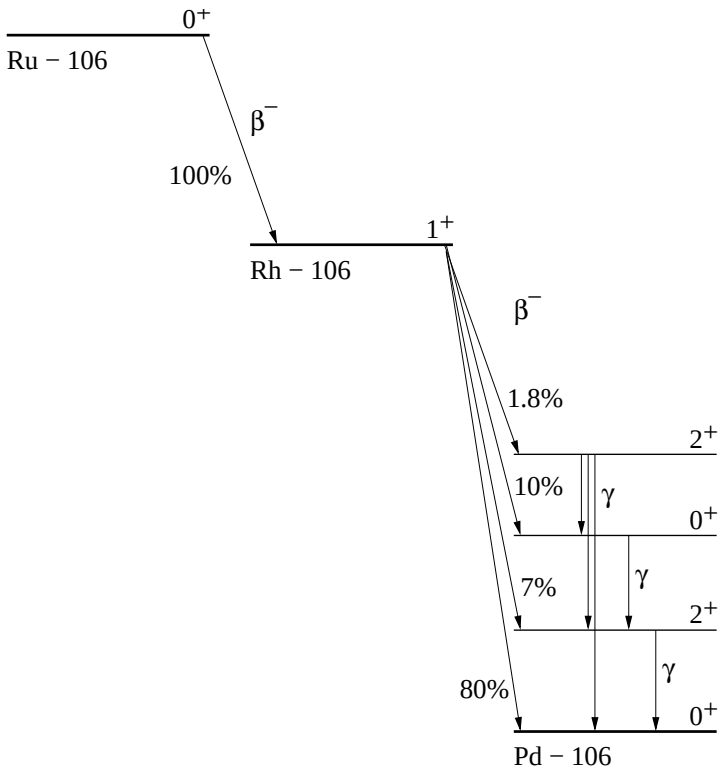

Figure 3.13: *Decay scheme of Rr^{106} beta source.*

We can consider our gas detector as a thin material layer where the energy of electrons is being degradated. Electrons, starting from a very low energy, behaves as minimiun ionizing particles, as pions does in DIRAC. The possibility of a great energy transfer in an unique collision is limited by half the initial energy, being this type of reactions very unfrequent as compared with other interations less energetic. The distribution of energy loss probability is

Table 3.1: *Characteristics of Rr^{106} beta source.*

Element	**Ruthenium**	**Rodium**
Atomic number	106	106
Lifetime	367 d	29.8 s
Maximun Energy	39.4 KeV	3.55 MeV
Activity(April/2002)	0.034 μCi	
Diameter	25.4 mm	
Active diameter	22 mm	
Window (0.9 mg/cm^2)	Aluminized Mylar	

assimetric, with a large tail following Landau distribution.

3.6.1 Experimental setup

With triggering purpose a INa(Tl) scintilliator detector was put in coincidence with studied MSGC/GEM planes. The scintillator, of $10 \times 20\ cm^2$, is placed over the microstrip chamber. With this setup, when a particle passes throught the scintillator generates a signal which will serve as trigger appling the convenient delay in corcondance with the algorithm of APC chips.

Experimental setup can be seen in Fig. 3.14, with the beta source hidden under the MSGC plane, and the scintillator over the drift electrode overlapping the whole active zone of the microstrips.

To set the detection threshold for the scintillator, the ratio of beta decay signal from Ru source and radiation background in the laboratory is evaluated using LabView software. A threshold of 170 mV was required for the scintilliator signal to send a trigger signal (see Fig. 3.15). Moving beta source along the MSGC plane in a perpendicular direction to the strips, 80000 triggers were registered at each position (~ 70 strips bin) for one detector and 50000 for the other. The Fig. 3.11 shows the aspect of labView program used, with a typical pulse height sum distribution along the detector strips (wiremap).

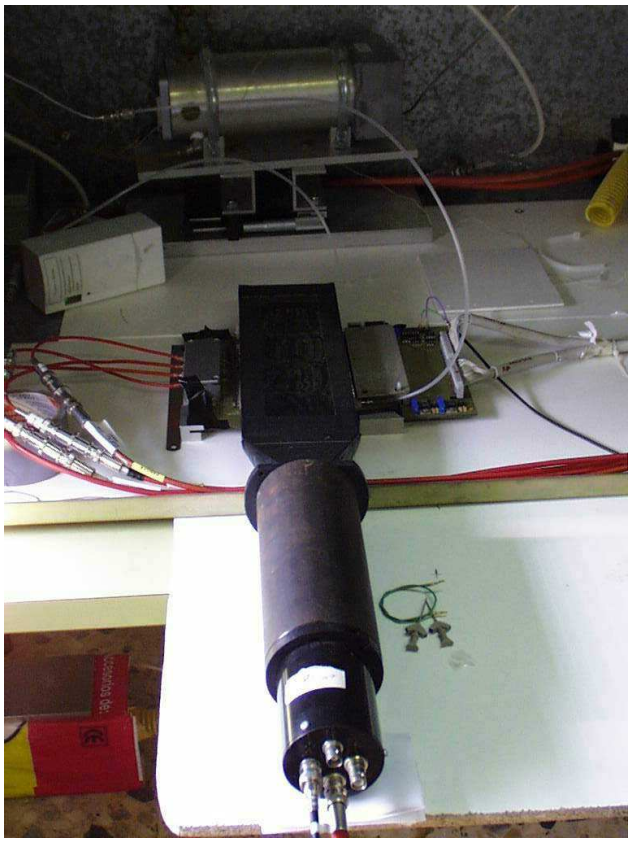

Figure 3.14: *Experimental setup in Santiago laboratory.* Ru^{106} *source is hidden under MSGC studied plane. INa(Tl) scintilliator is seen at front.*

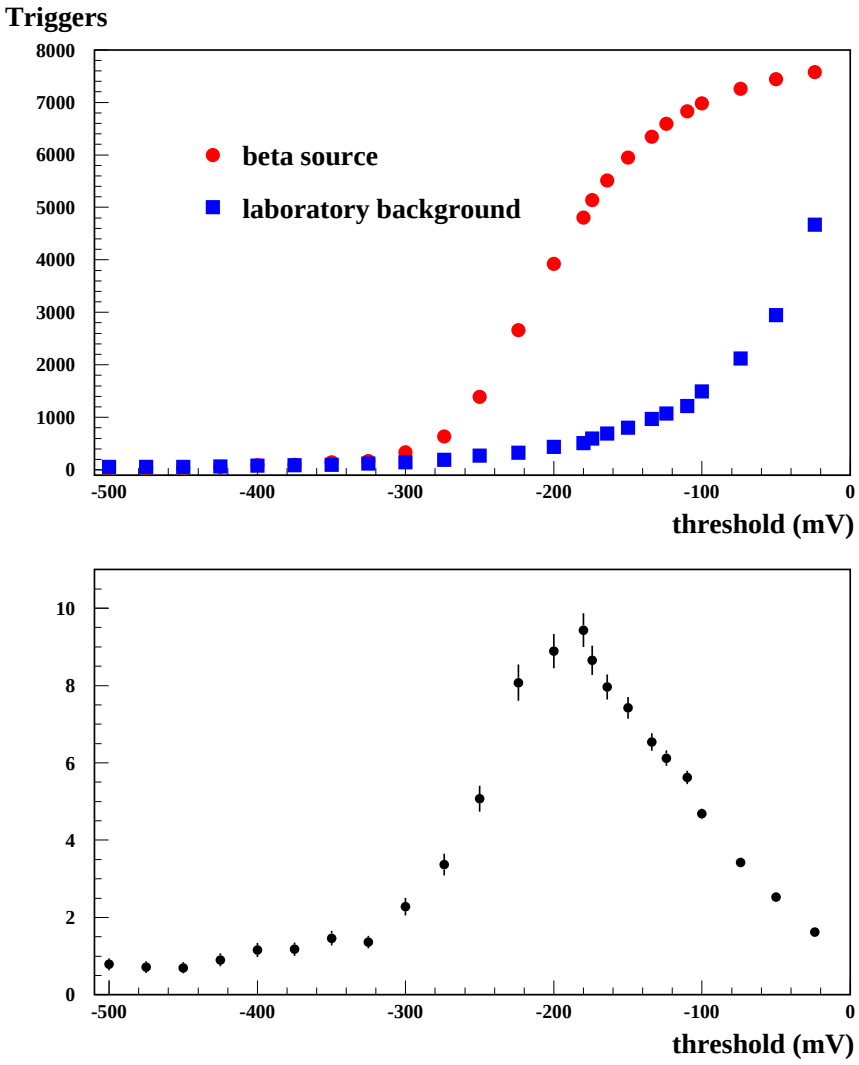

Figure 3.15: *Scintillator trigger threshold is shown (top) in presence of the beta source and only with laboratory background. At bottom the ratio between the two measurements is displayed. Threshold was set to 170 mV.*

3.6.2 Pedestals

Pedestals are defined as the characteristic voltage of each channel, considering the whole electronic chain, in absence of charge over the detector. During DIRAC data taking periods, a specially designed trigger is used to collect 1000 events to evaluate pedestals. Pedestal triggers may be in coincidence with proton spills crossing the detector, as proton beam is not interrupted. The value of pedestal is the average of the 1000 events, with addition of the root mean square, in order to detect broken strips or noisy APC channels. Calculated values are written to memory at the beggining of each run, and substracted by VME modules making use of the Fifo memories.

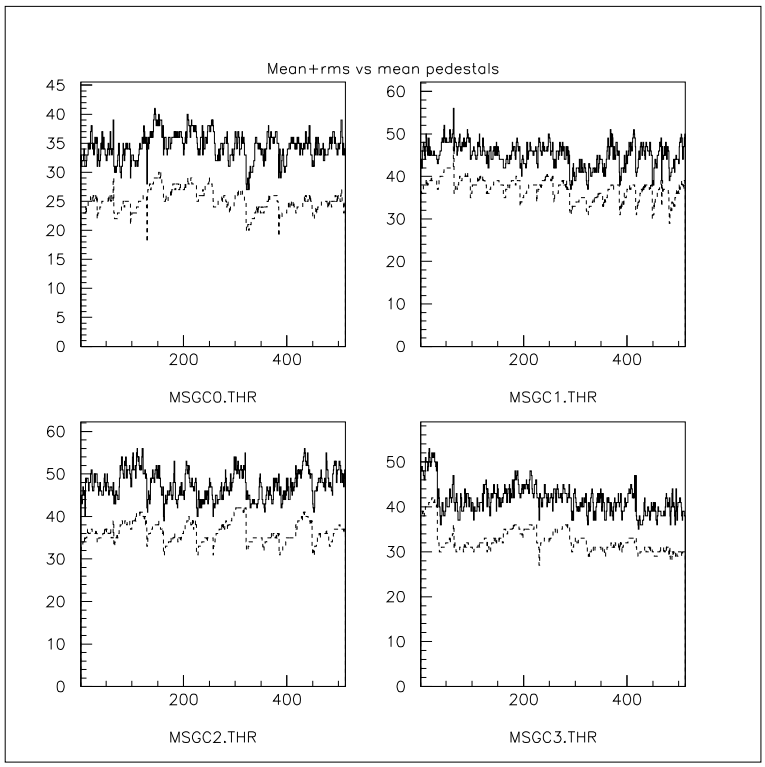

Figure 3.16: *Obtained pedestals as seen in DIRAC monitoring system. Dotted line corresponds to mean value of pedestals for each channel, and continuous line takes into account the corresponding rms.*

Pedestal subtraction is applied in the study of multiplication gain, subtracting signal in the channels from charge collected in absence of beta source. A hundred of events without beta radiation are written to VME memories with this purpose.

3.6.3 Results

A gaussian fit is performed to the added wiremap for each position of the beta source. The closest strip to the mean value of the fit is used as estimator of the beta source central position.

The interest resides only in particles crossing the detector with angles closer to 90° with the detector planes, rejecting inclined tracks. We apply a cut over the central strip equivalent to $\sim 2.2\ cm$, active diameter of the beta source (29 microstrips). Coming from the center of the beta source, tracks with angles $> 5°$ are rejected, decreasing the mean value of the cluster multiplicity distribution, as seen in Fig. 3.17 (d). Inclined tracks would add bigger tails to landau pulse height distributions, since crossing detector the particle produces low signal in a row of several strips, and so producing clusters with low strip multiplicity and low values of the collected charge.

Pulse height sum distribution is used to evaluate relative differences in the gain along the detector, in ADC counts. A study of absolute gain would require a dedicated calibration of electronic chain with a known signal of momoenergetic source (like X-ray), to extract relationship between the collected charge in the anodes and the corresponding ADC counts, and so knowledge of the number of electrons produced in the avalanche.

The pulse height sum distribution after the cuts, see Fig. 3.17 (b), is fitted to a landau-like function for each source position [57]. Most probable values obtained from the fit serve us for evaluation of the gain uniformity along the active area of the MSGC planes. The Fig. 3.18 displays obtainded results in ADC counts in function of the beta source position (in strip number) for the two detectors. Top differences do not reach 10% over the mean values, corresponding to dead-strips regions. The rms of the distribution is 1.8 ADC counts with mean value of 24.8 for the first detector and 1.7 and 22.2 values for the second one.

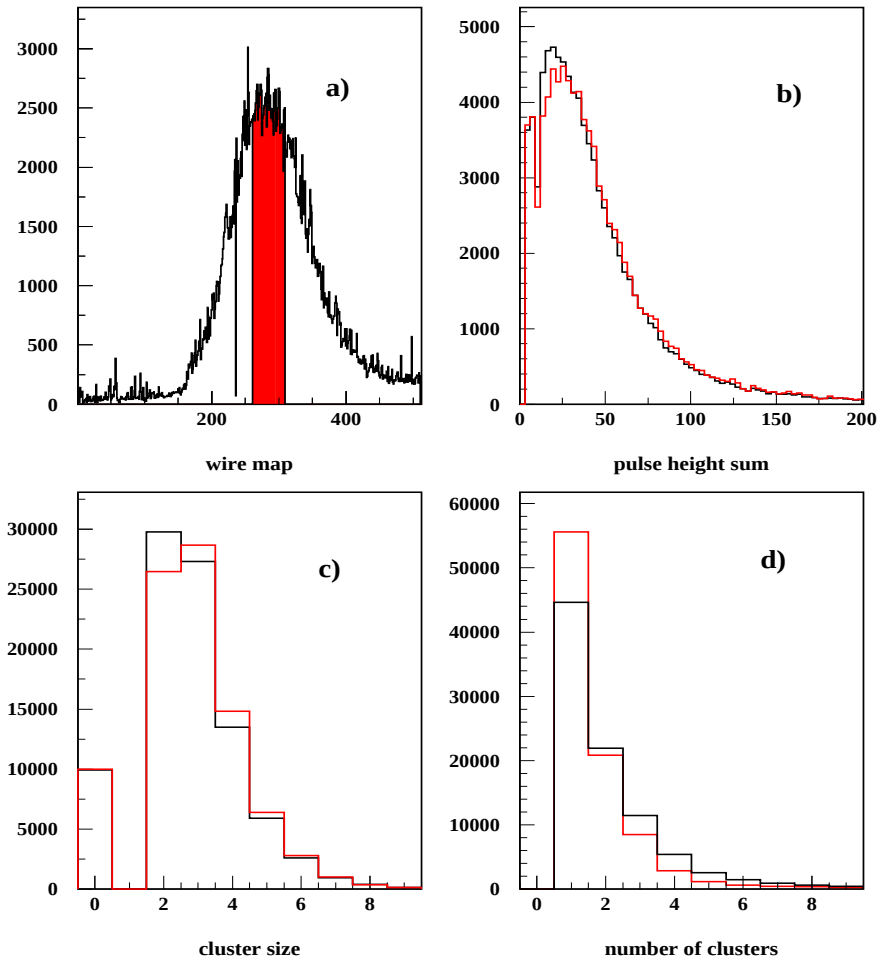

Figure 3.17: *Wiremap (a), pulse height sum (b) (in ADC counts), cluster size (c) and cluster multiplicity (d) plotted for one position of beta source. Normalized (except for wire map) distributions after the cut explained in the text are shown in red.*

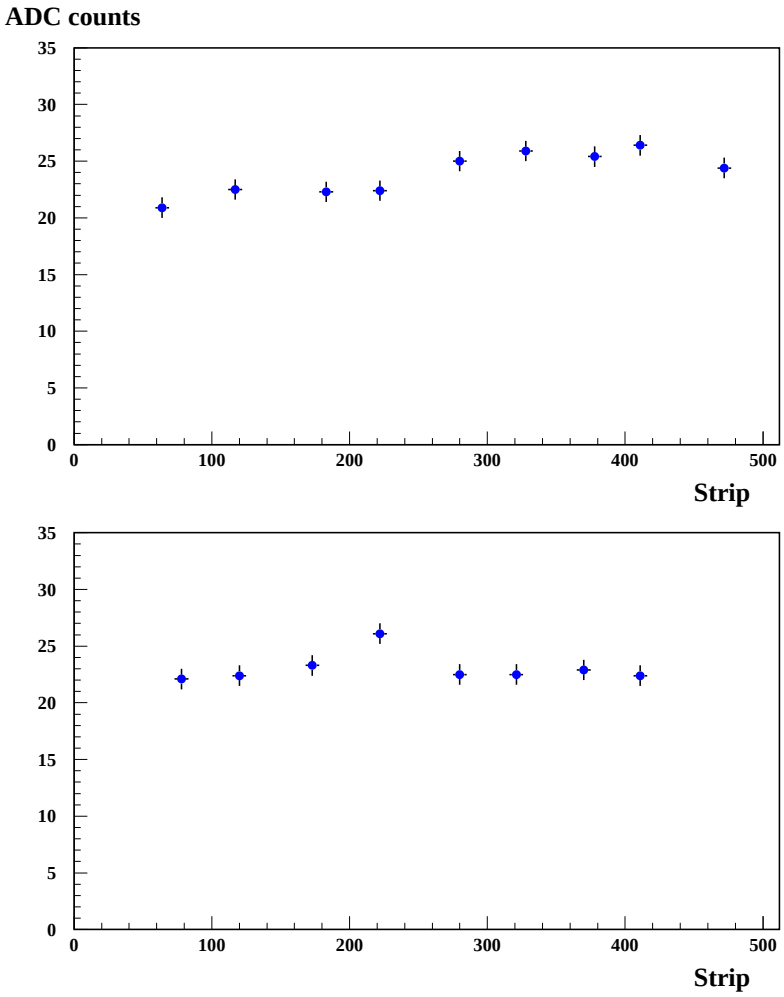

Figure 3.18: *The relative gain expressed in ADC counts for each position of beta source (expressed in strip number) for the two studied detectors.*

Chapter 4

Tracking system for upstream detectors

This chapter describes method that was developed in DIRAC to perform track reconstruction, using all available information from the spectrometer. In the following chapters it will be shown how Monte Carlo simulation has clearly indicated the goodness of the method for describing atom and background pairs, achieving the best resolution in Q_X and Q_Y.

Because resolution in $\vec{Q}$ components is ultimately limited by multiple scattering in the target foil and detector materials, special effort has been devoted to a precise mathematical description of correlations between coordinates measured by different detector layers, and to event-by-event covariance matrix calculation.

The results obtained allow identical resolution for prompt and accidental pairs in the analysis. The performance checks presented in this chapter only use real data from the spectrometer.

4.1 Introduction

The method described here is present in the standard ARIANE package. ARIANE program [68] is the DIRAC reconstruction software, written in Fortran77

programming language[1]. The reconstruction method based upon upstream tracking was already described conceptually in coincidence with the first operational version of the software [36]. Several upgrades have been added since them in the handling of multiple scattering, real stereo angles, and other setup parameters.

The method counts with a first stage of pattern recognition of particle tracks using 10 detectors[2] upstream the magnet, followed by the matching of upstream tracks with drift chamber tracks to determine the first order correction to pion momentum. Reconstruction of the longitudinal and transverse components of $\vec{Q}$ in the center-of-mass frame, as well as their precision errors, is finally achieved.

Apart from the very significant improvement in resolution offered, the method has the additional advantage that the copious background hits present in upstream detectors, due to the high beam intensity, can be unambiguously reduced by selection of only those that show a well defined probability to belong to a particle track. Moreover, the redundancy of particle trackers before the magnet allows to circumvent possible systematic effects in detector response[3], that might be extremely difficult to simulate by Monte Carlo.

4.2 Pattern recognition

A program has been developed to perform standalone pattern recognition of stereo upstream tracks pointing to the beam intersection with the target. The calibrated mean central position of the beam at the target plane is used in this procedure (althought insignificant with Monte Carlo, a great effort has been devoted for this calibration).

The essential ingredient is the use of the stereo angles XP (+5°) and YP (-5°) of MSGC, and of the U-plane (45°) of SFD, only available from 2002 onwards. A second feature is the utilisation of the time markers provided by the TDC channels of SFD. This is a key task due to the intrinsic bandwidth

[1] more than 125000 code lines

[2] 11 detectors from 2002 data due to the presence of new SFD-U plane.

[3] such as the PSC response in SFD detector.

limitation of MSGC electronics, which records all hits in a 250 ns time window. The time tag for each track will be matched later with that provided by the TOF counters, associated with DC tracks.

The pattern recognition has two steps:

- **identification** of X and Y segments (hit pairs) in each projection separately, pointing to the estimated beam intersection with the target. Single hits are also accepted (slope defined by the interaction point)

- **association** of X and Y segments to form a stereo track, when a corresponding hit is found in the extrapolation to one of the tilted planes XP, YP (or U).

In order to minimise noise contributions while keeping efficiency close to maximum, a momentum-dependent space search window of 3σ in particle extrapolation (interpolation) from detector to detector is applied at each combination tried.

The calculation of the search window receives contributions from two sources in quadrature: multiple scattering and angle subtended by the beam spot at detector i. For $i < j$, the former is determined by the expression:

$$\Delta r^2_{MS} = V_{MS}(i,i)\left(\frac{z_{i+1} - z_i}{z_i - z_T}\right)^2 + |V_{MS}(j,j) - V_{MS}(i,i)| \qquad (4.1)$$

where $V_{MS}(i,i)$ are the diagonal elements of the matter component of covariance matrix defined in next section, and z_T is the Z-coordinate of the target.

In order to define a track, a minimum of 4 hits is required among the 6 detectors (7 detectors, from 2002 onwards). Alternatively, upstream tracks are built when they have at least two hits in each projection, among the sets (X, XP, SFD-X) and (Y, YP, SFD-Y)

In Fig. 4.1 we show the distribution of the number of tracks found per event by the pattern recognition, as well as the hit multiplicity per track.

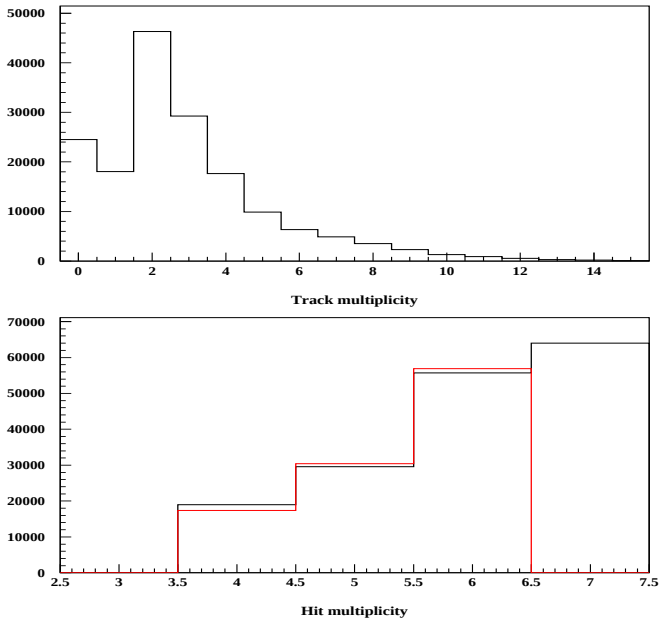

Figure 4.1: *The top histogram shows the number of tracks found per event by the pattern recognition, and the bottom one the hit multiplicity (number of fired detectors) per track. Red line stands for Ni-2001 data, and black for 2002, with SFD-U plane.*

4.3 Track Fitting

Once identified, the hits that belong to the track are fitted to a straight-line hypothesis A in order to determine the two slopes (x' and y') and intercepts (x_0 and y_0) of the particle trajectory at a given longitudinal coordinate z_0:

$$A = \begin{pmatrix} x_0 \\ x' \\ y_0 \\ y' \end{pmatrix} \tag{4.2}$$

The χ^2 and fit probability for A is also determined,as well as the 4×4 co-

variance matrix, which, due to the relatively small pion momenta, takes into account Coulomb multiple scattering, including detector-to-detector correlations.

A particle momentum based upon the nominal beam position is used at a first iteration, which is later improved in successive re-fits. Full precision is achieved when particle momentum is re-determined after matching with DC tracks.

The procedure we shall describe is implemented in general form, in order to cope with $i = 1, N$ detectors located at Z-coordinates z_i and measuring at arbitrary stereo angles θ_i. This geometrical information for upstream detectors is encoded by the matrix:

$$H = \begin{pmatrix} \cos\theta_1 & z_1\cos\theta_1 & \sin\theta_1 & z_1\sin\theta_1 \\ \cos\theta_2 & z_2\cos\theta_2 & \sin\theta_2 & z_2\sin\theta_2 \\ \cdot & \cdot & \cdot & \cdot \\ \cdot & \cdot & \cdot & \cdot \\ \cos\theta_N & z_N\cos\theta_N & \sin\theta_N & z_N\sin\theta_N \end{pmatrix} \tag{4.3}$$

The N measurements t_i for $i = 1, N$ are stored in the vertical array T in local coordinates of the corresponding detector. The χ^2 to be minimised is then given by the expression:

$$\chi^2 = (T - HA)^T (V_{det} + V_{MS})^{-1} (T - HA) \tag{4.4}$$

where $V = V_{det} + V_{MS}$ is the $N \times N$ detector covariance matrix. V_{det} is the diagonal matrix which describes intrinsic detector resolutions squared in each detector plane:

$$V_{det} = diag\ \left(\sigma_1^2, \sigma_2^2, \ldots, \sigma_N^2\right) \tag{4.5}$$

We assume N thin detectors $i = 1, N$ (4 MSGC + 2 SFD) numbered in ascending order from the interaction point, M_1 thin dummy layers before detector 1 (it allows for target layers and membranes) and M_2 layers located after detector N (allows for IH detectors). The total number of scatterers is therefore $M = N + M_1 + M_2$. The V_{MS} matrix encodes the information of the matter distribution seen by the particle which is observed by detectors i

and j, and has traversed material thicknesses s_k of average radiation length X_{0k} each, located at coordinates z_k. For $i \leq j$ it is given by:

$$V_{MS}(i,j) = \sum_{k=1-M_1}^{i-1} \theta_{0k}^2 (z_i - z_k)(z_j - z_k) \cos(\theta_i - \theta_j) \qquad (4.6)$$

The sum extends over all material planes k seen by the particle from the interaction point up to the preceeding plane to detector i. The average multiple scattering angle θ_{0k} in each layer depends on the particle momentum p (and velocity β) according to the expression:

$$\theta_{0k} = \frac{13.6MeV}{p\beta c}\sqrt{\frac{s_k}{X_{0k}}}\left[1 + 0.038\ ln\left(\frac{s_k}{X_{0k}}\right)\right] \qquad (4.7)$$

This matrix is symmetrised by construction: $V_{MS}(j,i) = V_{MS}(i,j)\ \forall\ i \leq j$. The relative orientation $\theta_i - \theta_j$ between detector planes i, j determines proper correlation between their respective measurements.

Note that, whereas V_{MS} is defined only for (active) detectors i, j, the sum in (4.6) runs over all material planes k present in the setup, including in particular the target and vaccuum chamber membrane thicknesses.

The minimum χ^2 fit A is obtained[4] by matrix inversion :

$$A = \left(H^T(V_{det} + V_{MS})^{-1}H\right)^{-1}\left(H^T(V_{det} + V_{MS})^{-1}T\right) \qquad (4.8)$$

where $V(A) = \left(H^T(V_{det} + V_{MS})^{-1}H\right)^{-1}$ is the 4×4 covariance matrix for the measurement of A.

It is to be noted that whereas unhit detectors i (according to individual detector efficiencies) do not contribute directly to the calculation of χ^2 they do contribute to the correlation matrix of the active ones.

The previous fit is intended to provide the best measurement of the particle trajectory at the proton interaction point with the target. However, maximum resolution in the momentum determination requires the measurement be optimised at the magnet entrance, when used as input for the transfer

[4] Calculations are performed in double precision using standard CERNLIB routines for matrix manipulation.

function of the DIRAC dipole magnet. For this purpose, a calculation $\tilde{V}_{MS}$ for $i \leq j$ is performed in the following way:

$$\tilde{V}_{MS}(i,j) = \sum_{k=j+1}^{M+M_2} \theta_{0k}^2 (z_i - z_k)(z_j - z_k)\cos(\theta_i - \theta_j) \tag{4.9}$$

where k now runs over material planes located after detector j. As compared to V_{MS}, the matrix $\tilde{V}_{MS}$ actually describes the particle propagation over the M layers in reverse order, as if it propagated backwards in time. The probability track distribution from the described method is shown at the top part of figure 4.2.

4.4 Matching with Drift Chamber Tracks

For every opposite-charge pair, each track reconstructed in drift chambers is extrapolated backwards by means of the transfer function of the DIRAC dipole magnet, using a first order momentum hypothesis based upon the calibrated X-coordinate of the beam. The extrapolated coordinates (x_1^{dc}, y_1^{dc}) and (x_2^{dc}, y_2^{dc}) obtained at a given reference plane (chosen to be SFD-X detector) are then compared with those extrapolated forward for every pair of upstream tracks (x_1^{up}, y_1^{up}) and (x_2^{up}, y_2^{up}). A minimum χ^2 test is used to select the pair of upstream tracks which provides best matching , according to the expression:

$$\chi^2 = \left(\frac{x_1^{up} - x_1^{dc}}{\Delta x_1}\right)^2 + \left(\frac{y_1^{up} - y_1^{dc}}{\Delta y_1}\right)^2 + \left(\frac{x_2^{up} - x_2^{dc}}{\Delta x_2}\right)^2 + \left(\frac{y_2^{up} - y_2^{dc}}{\Delta y_2}\right)^2 \tag{4.10}$$

The values used for Δx_i and Δy_i are functions of momentum, given by parametrisations of the form $A + B/p$, determined by fitting the dependence of the sigma values (gaussian fit) of the observed distances between DC and upstream tracks, for X and Y, and for the two downstream arms of the spectrometer separately.

Time cuts are applied for each track association prior to the χ^2 test, in order to ensure consistent time between corresponding upstream (t_{up}),

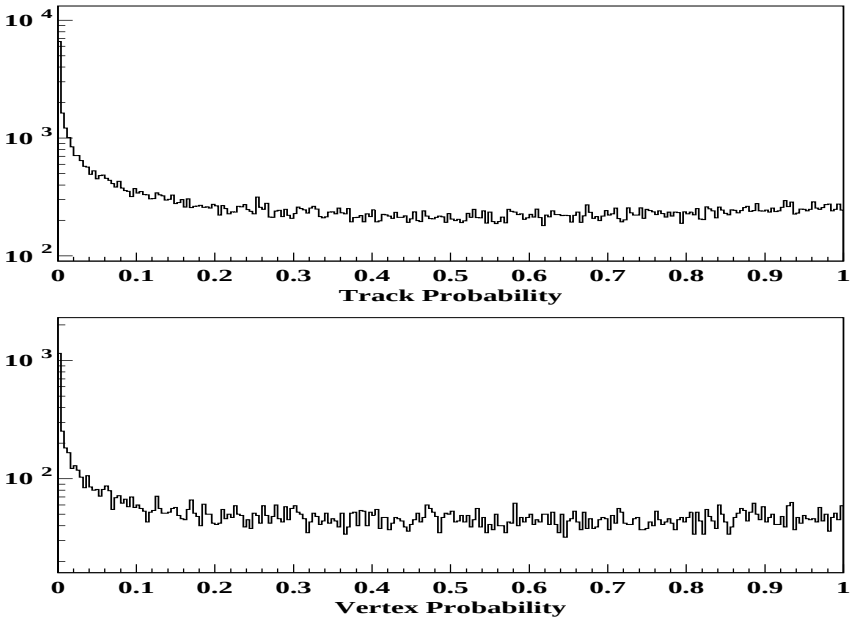

Figure 4.2: *The top histogram shows the probability that the 6 (7) hits found by the pattern recognition actually belong to a particle track, propagating with multiple scattering theory as described. No beam constraint is imposed by this fit. The bottom distribution corresponds to the probability that two tracks in a prompt pair, each with an arbitrary number of hits, have a common intersection at the target plane.*

measured by SFD TDC hits present, and downstream (t_{dc}) tracks, defined by the TOF counters: $|t_{up} - t_{dc}| < \Delta t$, both for real and accidental pairs. Cuts are also chosen according to the observed time-difference distributions. Application of such time cuts produces a suppresion of the low-momentum proton background.

The differences between extrapolated coordinates and time from both sides of the magnet are shown in Fig. 4.3, while Fig. 4.4 displays the momentum dependence according to the parametrisations used for positive arm. Matching efficiency, defined as the fraction of DC tracks that found

correspondance with upstream detectors, is illustrated in Fig. 4.5 both for single tracks and for track pairs.

Cases in which the pair of DC tracks can only be associated with a single (unresolved) upstream track, sufficiently close to both, are retained by the matching procedure. A double ionization test will be applied to the track, based upon the observed pulses in Ionization Hodoscope layers and the time cuts are relaxed, in order to make acceptance for unresolved real and accidental pairs as close as possible.

4.5 Beam constraint and vertex fit

Once the track originally found by the pattern-recognition has been matched with a DC track and the magnitude of its momentum is improved with respect to the first-order approximation, its charge sign will be determined.

Knowledge of momentum allows a better description of multiple scattering in the covariance matrix, so a new track fit is performed. In addition, a general procedure is implemented to re-assign the original hits that belong to the track. Individual hits found to be more than 3σ away from the track are dropped, and track parameters are re-defined.

Track fitting based only upon measuring detectors provides in general a sufficient level of precision. However in those cases in which the track is left with only 4 hits, the fit has no degrees of freedom, and it becomes more vulnerable to noise hits. Here again we are going to take advantage of the effort devoted to alignment and calibration which allows an accurate determination of the beam intersection at the Z target coordinate. Two constraints are then introduced at the pattern-recognition level, requiring the center of the beam intersection with the target (X and Y coordinates) to lie on the particle trajectory, within a given probability cut. Mathematically, this is achieved by extending the detector covariance matrix dimension by two units. A tolerance at 1σ level is specified, corresponding to the observed beam spot size projections.

When individual tracks are subject to the beam-constrained fit, the target radiation length needs to be taken into account, in addition to the estimated

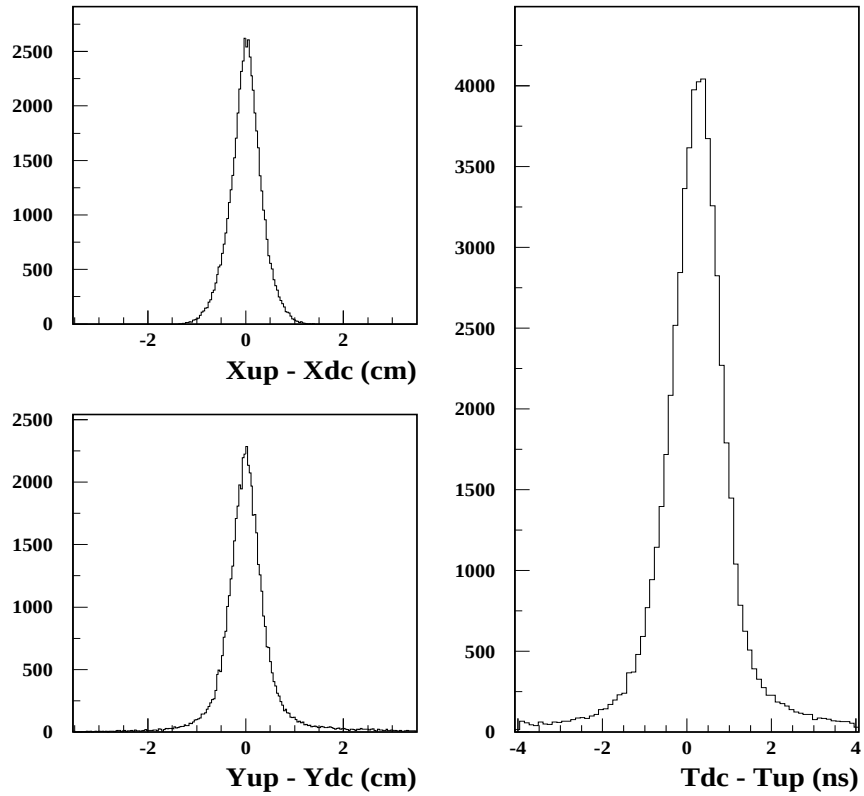

Figure 4.3: *Top (bottom) left show the difference in X-coordinate (Y-coordinate) between backward-propagated DC tracks (using first-order momentum by the magnet transfer function), and uptracks extrapolated to the matching plane. The right-hand histogram shows the time difference between DC tracks (as measured by the TOF counters, t_{dc}), and associated upstream tracks (t_{up}), as defined in section 2.*

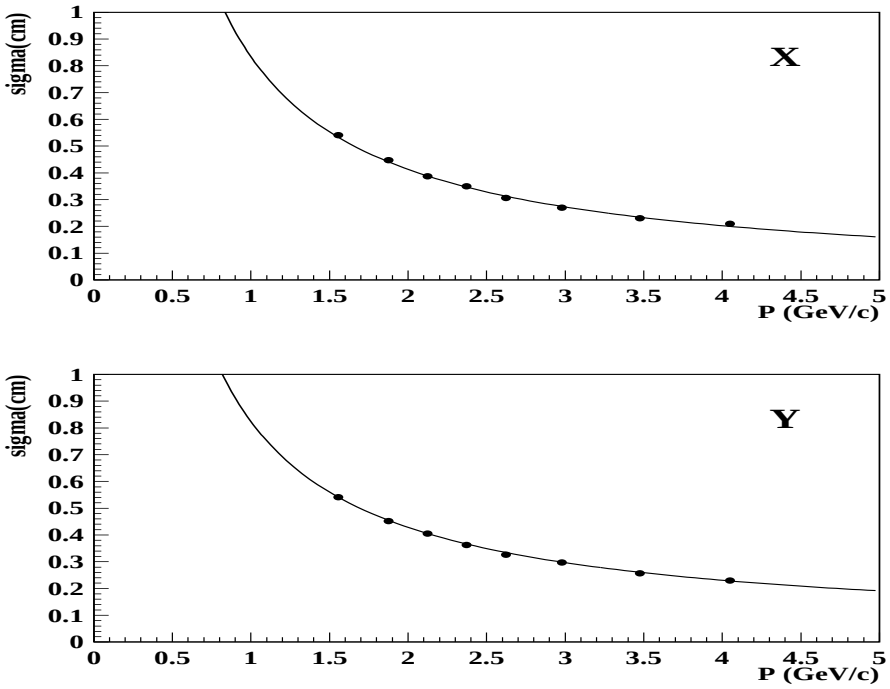

Figure 4.4: *Top (bottom) figure shows the positive arm momentum dependence of the fitted sigma values to the matching distances in X-coordinate (Y-coordinate) as shown in average in figure 4.3. The corresponding parametrisations* $A + B/p$ *are drawn in each case.*

beamspot size in X and Y projections. This input allows to extend the 7×7 detector correlation matrix $V = V_{det} + V_{MS}$ (as defined in section 3) to dimension 9×9. The track covariance matrix $V(A)$ then obtained trully represents the particle propagation at the target interaction point.

Moreover, to improve precision and minimize the effect of multiple scattering and SFD cross-talk, only the signals from MSGC information are used in this final track re-fit.

In order to illustrate the correctness of the error description provided by this procedure, we show in the left part of Fig. 4.6 the measured distribu-

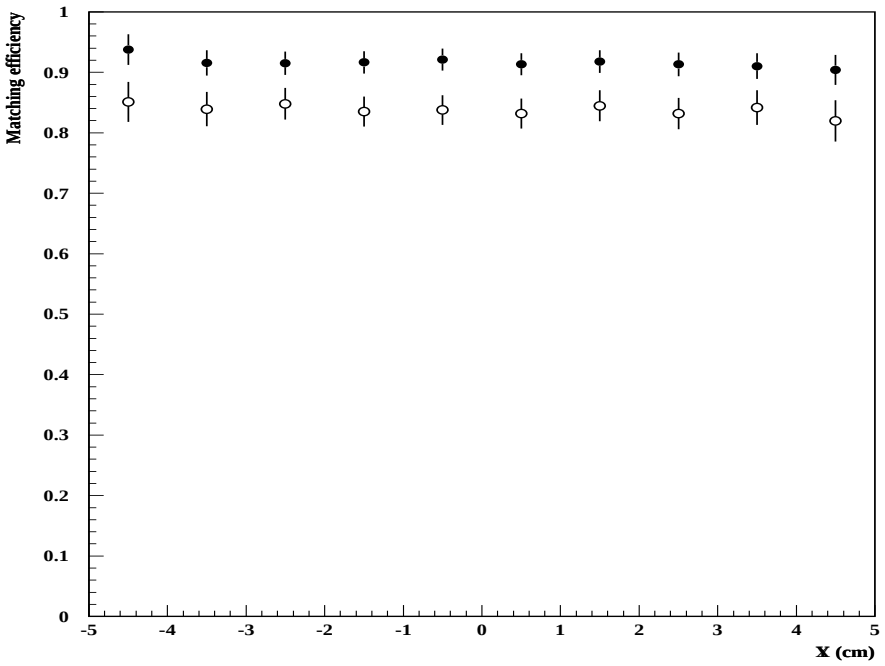

Figure 4.5: *Fraction of drift chamber tracks which found a corresponding upstream track (black circles), as function of X-coordinate measured at the matching plane (SFD-X). Open circles show the fraction of opposite-charge pairs which found a corresponding pair of upstream tracks.*

tion of the differences between extrapolated track coordinates at the target plane, normalised to their calculated error (given by the diagonal elements of $V(A)$). It can be appreciated that there is perfect agreement between the calculated errors and the measured ones. Clearly this beam constraint is in better agreement with the hypothesis that both particles come from the same interaction point, as in the case of prompt pairs. Accidental pairs, on the other hand, are only approximately described by this hypothesis so we obtain a good error match by artificially decreasing the nominal beamsize constraints in the fit by 10% in X (20% in Y). When this is done, we ob-

tain the distributions shown in the right part of Fig. 4.6. This prescription ensures equally precise error handling for real and accidental pairs, in the determination of Q_X,Q_Y and Q_L.

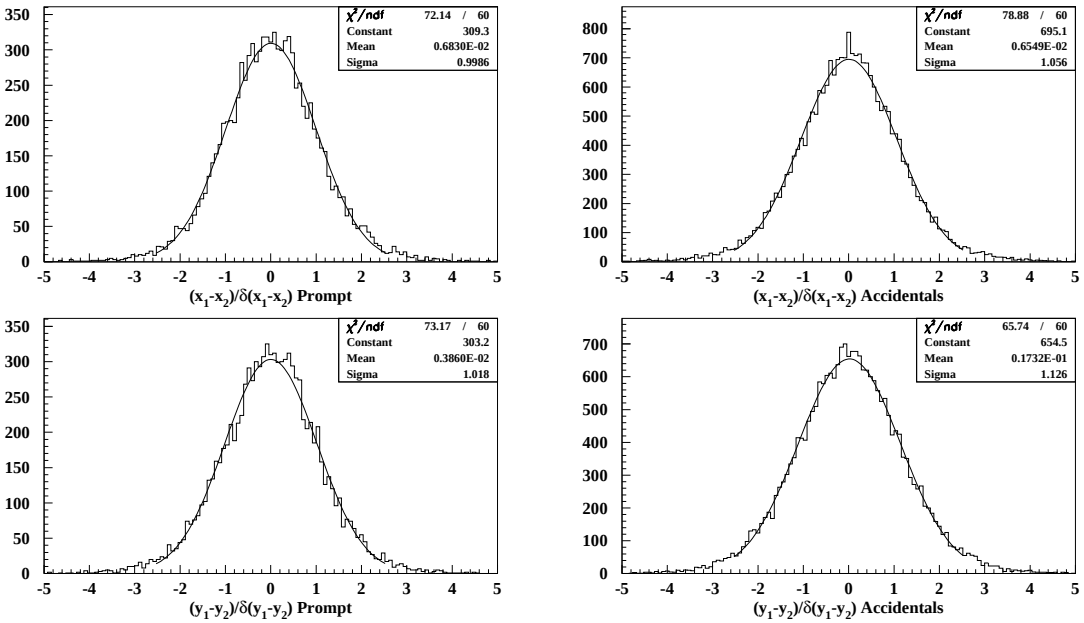

Figure 4.6: *The top (bottom) histogram shows the distribution of measured values of $x_1 - x_2$ ($y_1 - y_2$) divided by its error, where x_1 and x_2 (y) are the X (Y)-coordinates of the positive and negative track intersections with the target plane. Prompt pairs are selected in the left histograms and accidental pairs in the right ones. The error was determined event-by-event by the beam-constrained fit.*

The beamsize dimensions that provide optimal description of the errors 1.0 mm and 1.7 mm in the X and Y projections (consistent with reported in [37]) , respectively. More direct evidence for the observed difference between real and accidental pairs can be obtained by comparing the measured sigma values of $x_1 - x_2$ ($y_1 - y_2$) They significantly differ by 6.5% (10.5%).

4.6 Double ionization in IH from low angle pairs

Straight-line tracks reconstructed in the upstream detectors are extrapolated to the IH in order to determine the slab numbers intersected by the particle at each detector plane. Pulse-height (ADC) and TDC information are incorporated to the track, after application of various corrections following reference [29], some of which depend upon the longitudinal coordinate along the counters.

Special attention is devoted at this point to single unresolved tracks that can be matched to two DC tracks. It is neccesary to look for a double ionization signal in IH detector in order to establish or not their two-particle nature. We say there is double ionization in one track when at least one of the two intersected slabs of IH shows calibrated pulse above threshold ($\sim$150 counts), in a given projection (X or Y). Null pulses are excluded from the test.

When both tracks share the same SFD hit, additional MSGC signals close to the track are searched for, and incorporated to either one of the two tracks. Wide MSGC clusters (strip multiplicity larger than 3) that are found in this procedure, are subsequently broken into two, before they get associated to the tracks. Double ionization is required for this close-pair configuration, before it is accepted.

The algorithm applied consists of excluding the maximum and the minimum pulses among those found in IH layers, and then require $A > A_{cut}$ with A being the average of the remaining ones. The cut value A_{cut} is optimised according to the fitted curves obtained for single and double track intersections on individual counters. It is remarkable that practically no background from single ionization is observed, when two-track crossings are required on individual slabs, as it can be seen in the right-side peak of Fig. 2.6 (chapter 2).

The above analysis for close-angle pairs still allows that unbroken MSGC clusters are shared by both tracks. In this case, clusters are split into two, under the assumption that they were produced by two particles. Splitting

takes place then by means of a simple algorithm that takes the RMS of the strip-pulse distribution as most likely distance. In the case of one-strip clusters, it is necessary to add two small pulses at adjacent microstrips, in order to compensate partially for the effect of pedestal substraction.

Chapter 5

Upstream alignment and MSGC/GEM efficiencies

High precision in relative pion momentum components in the two-particle center-or-mass frame (Q_L, Q_X, Q_Y) can only be achieved after proper alignment between detector elements of the upstream detectors, the beam, and the drift chambers. In particular, a good description of track probabilities, multiple scattering correlations, and intrinsic detector resolutions requires this as a first step.

The detector alignment procedures are described in this chapter, together with an estimation of the operation efficiencies for the 4 MSGC/GEM planes present in the 2001 year.

5.1 Alignment

First a rigurous iteractive method of alignment of upstream detectors and beam position is performed. The alignment program can be carried out almost entirely using properly selected upstream tracks. For the precise measurement of transverse and longitudinal components of pions relative momentum in the center-of-mass system the alignment is performed as run-dependent. DIRAC standard experimental files (runs) correspond to 8 hours periods of data collection. Geometry files used by ARIANE reconstruction

code allows to change detector configuration from run to run. Missalignment due to night-day temperature effects, or changes produced by interventions in the spectrometer are corrected with the parameters specified in geometry files. As a first step it is performed the alignment of MSGC/GEM with SFD, and upstream detectors are used together as a block for geometrical correspondence with DC positions in order to assure a high matching efficiency.

The following parameters have been determined as output of the calibration procedure:

- 6 offsets of individual detector planes (for 2001) in the direction perpendicular to the corresponding strips or fibres (position of the first strip).
- 6 Euler rotations of each detector plane about the Z-axis (precision tunning of the θ_i angles).
- offsets and overall Euler rotations about the Z and Y axis of uptream detectors as a whole with respect to positive and negative arm of drift chambers.
- mean position in X and Y of the beam center, with respect to the upstream detectors.

5.1.1 Upstream detectors

A precise alignment of upstream detectors is required for a correct behaviour of track recognition procedure, as well as for the MSGC/GEM background rejection with TDC information from SFD hits.

In order to obtain the spatial residual distributions for the 6 studied planes, the same sample of 2001 data as for lifetime analysis is used, selecting tracks according to the following criteria:

- Tracks formed by 6 upstream hits (4 MSGC/GEM + 2 SFD).
- Track probability greater than 5% in the straight line fitting.
- Prompt time correlated pairs.

- Events matched with DC tracks after the magnet.

In order to evaluate the upstream detectors parameters (offsets and Euler angles) we base on the non-correlated residuals of each MSGC/GEM and SFD plane. Residuals are calculated as the difference between track extrapolation to the desired plane and the coordinate of closest registered hit. Althought in data selection and track recognition all available information is used, a non-correlated residual distribution is determined by dropping individual detector hits from the track fitting, avoiding biases from the studied detector information. This is schematized in Fig. 5.1.

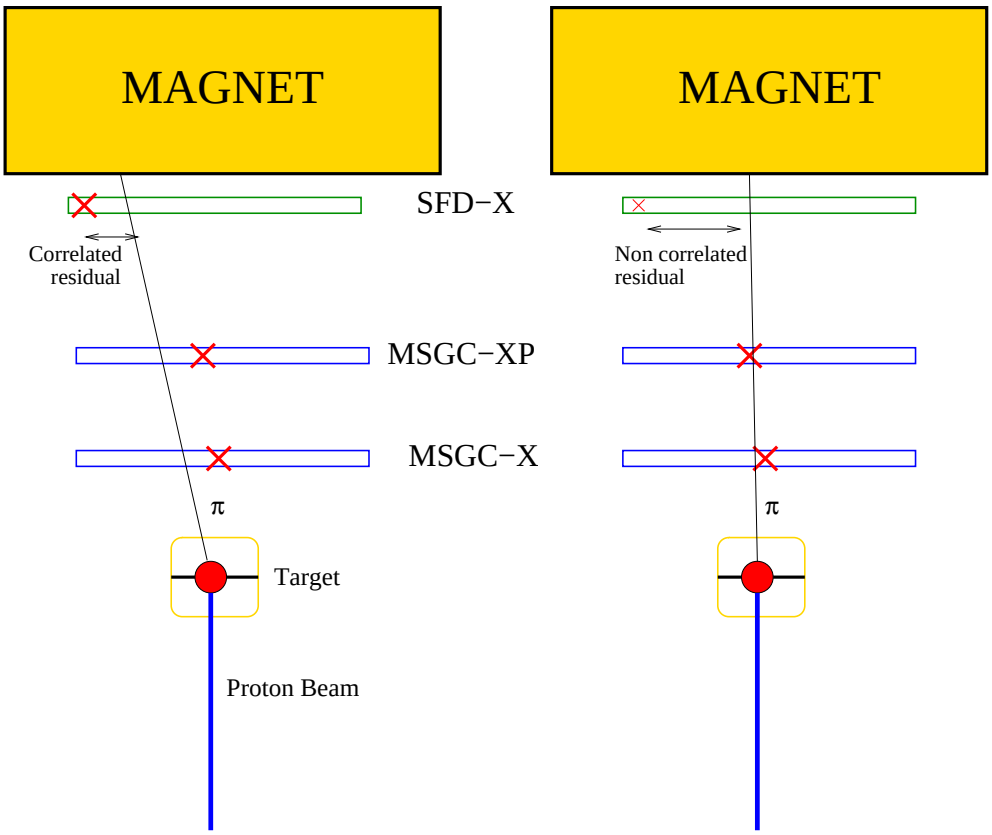

Figure 5.1: *Excluding associated hit of current studied detector, a non correlated residual is obtained (right).*

Residuals distributions calculated with the described method for MSGC and SFD, are fitted with a gaussian distribution, and mean value is used as estimator of the offset position for the detector with respect to the upstream block.

With standard geometry files from DIRAC collaboration, offsets obtained for the 6 upstream planes in function of the run number for 2001 data is presented in Fig. 5.2. Taking into account the status of initial alignment, Ni-2001 data was divided in 6 main segments (A-E). We found in some cases coincidence with interventions in the experimental area between segments:

- A segment. Runs from 3447 to 3491.
- B segment. Runs from 3493 to 3913. After this run an IH intervention was performed.
- C segment. Runs from 3914 to 4072. Data taking stop after 4072 run for the installation of two new targets (Nickel and Titanium).
- D segment. Runs from 4075 to 4277.
- E segment. Runs from 4280 to 4301.

An iterative procedure is then defined to correct geometry files for the six segments. Alignment is considered finished when offsets are under 10 μm for MSGC/GEM and 50 μm for SFD. After alignment jobs, characteristic residual distributions (for segment D) are displayed in Fig. 5.3, meanwhile offsets are plotted in Fig. 5.4 again for comparison purpose.

For Euler angles, dependence of mean fitted value of the residuals with orthogonal coordinate to the strips (or fibre) orientation is calculated. The slope of the fitted straight line to this dependency gives us, in radians, the angle between the strips of the plane and its desired orientation. The same segments with iteractive method again are corrected for this angle by means of the geometry files.

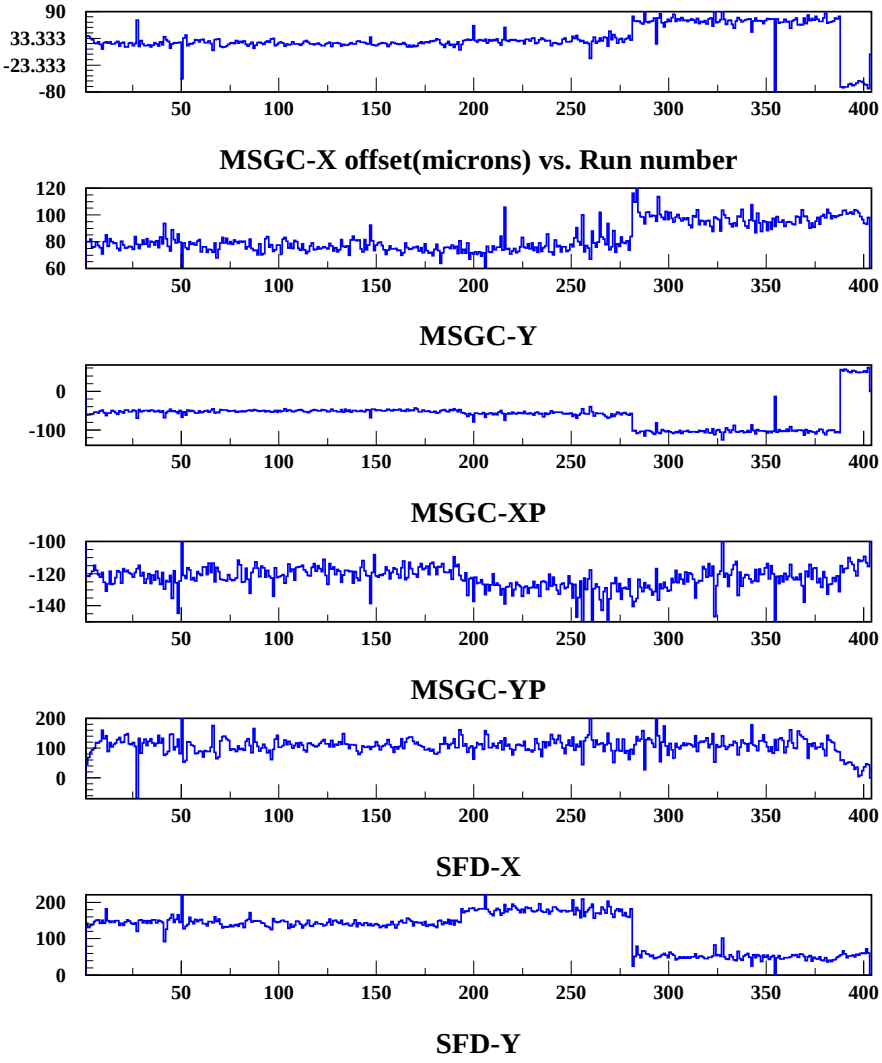

Figure 5.2: *Original residual offsets for upstream planes in 2001. Offsets are in μm displayed in function of the run number.*

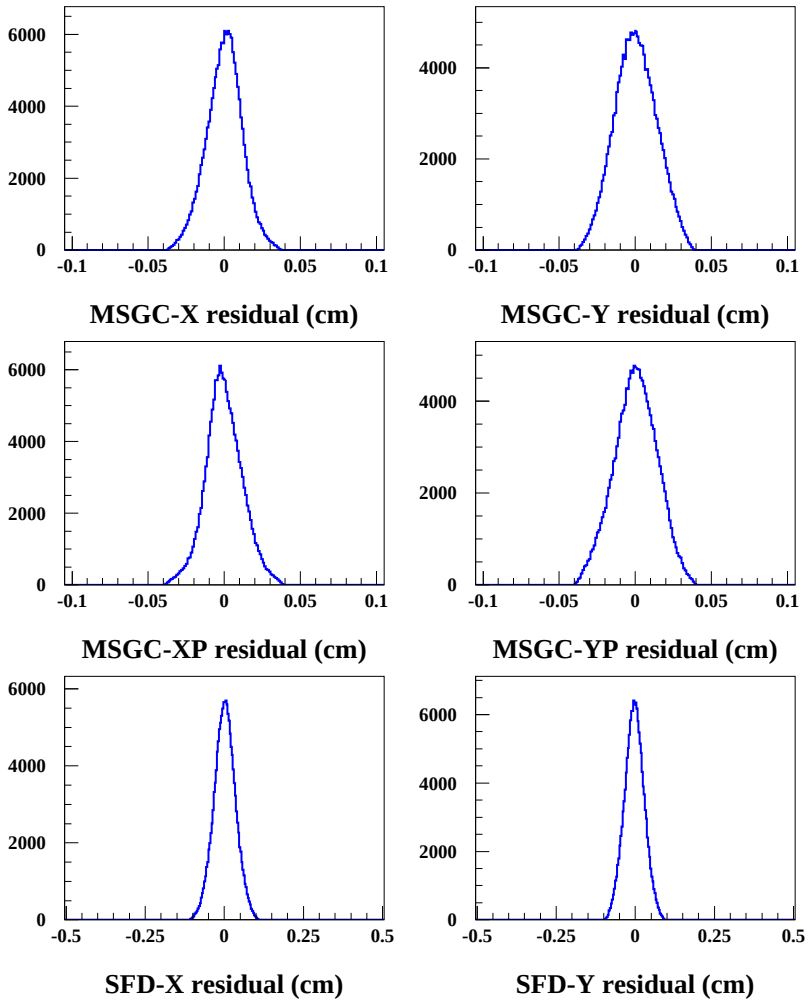

Figure 5.3: *Residuals for the 6 upstream planes (D segment). X (Y) detectors are displayed at left (right) side.*

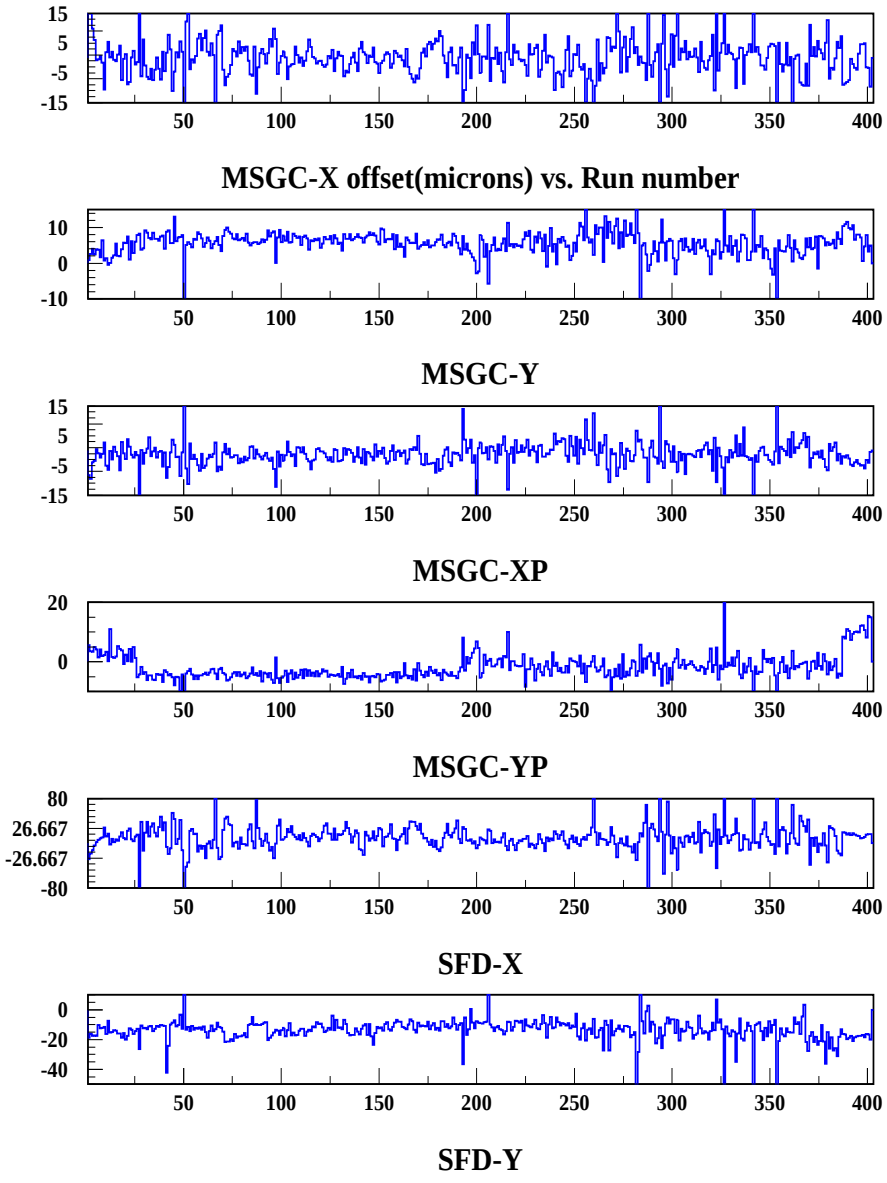

Figure 5.4: *Offset residuals for 2001 data period after alignment.*

5.1.2 Alignment with downstream detectors

Considering upstream part of spectrometer as a block, alignment of its global position relative to DC chambers is done, in order to improve matching efficiency between upstream and downstream reconstructed tracks.

In addition to the previous selection criteria, events are required to have only one reconstructed track for each DC arm.

The comparison of tracks extrapolations from two sides of magnet as shown in the previous chapter (see Fig. 4.3) is fitted with a gaussian distribution to extract the offset estimation, which will be again the mean position of the fit. This offset is included at the matching stage in the ARIANE reconstruction code. Upstream extrapolation to the matching plane is corrected before performing the χ^2 test (see equation 4.10).

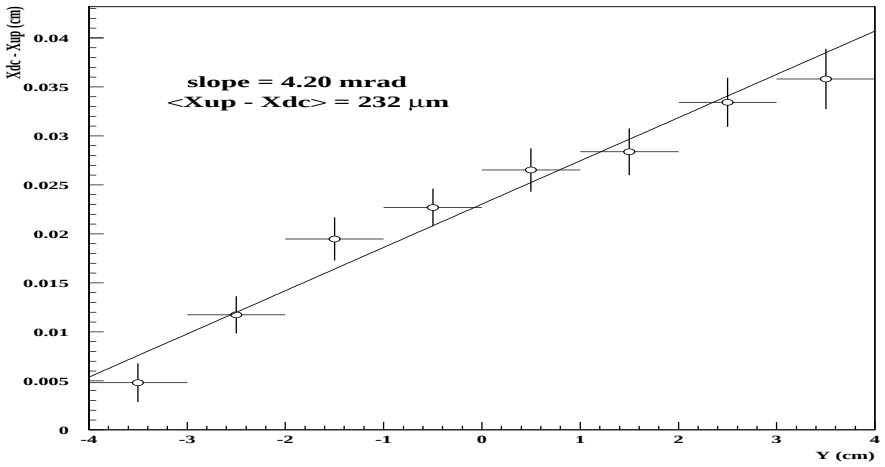

Figure 5.5: *Measured offset in X-coordinate between drift chamber and upstream tracks at the matching plane, as function of Y-coordinate. Observed slope and intercept are indicated.*

Relative angle rotation between the two spectrometer parts are included in the calibration. As illustration we show in Fig. 5.5 the measured offset in X-coordinate between the drift chamber and the upstream tracks at the

matching plane, as function of Y-coordinate. The observed slope of 4.2 mrad, determines an overall Euler rotation about the Z-axis between the upstream detectors and the average of positive and negative arms.

To ensure that the Q_L distribution are accurately simmetric and centered at zero, another alignment procedure is developed in lab-frame momentum intervals. It is based on the correction of the first-order track momentum approximation from DC measurement, performed when matching with upstream tracks. Results obtained are reported in chapter 8, section 2.

5.1.3 Beam position

Coordinates of proton beam intersection with the target plane, plays an important role in the hit identification for tracks during the pattern recognition procedure allowing a rigurous probability cut for the tracks, and to get a good description of lab-frame momenta of particles.

The beam spot coordinates are obtained for each run by making a gaussian fit to the unconstrained intersection of fitted tracks with the target plane.

In figures 5.6 and 5.7 the X and Y coordinates of this instersection are displayed. They are shown in function of the run number, and a beamspot position estimation using only DC information is displayed for comparison.

5.2 MSGC/GEM efficiencies

The knowledge of the detection efficiency of MSGC/GEM planes under experimental data collection conditions is strictly needed for a good Monte Carlo simulation of MSGCs response (which will be described in the next chapter), and allows a better knowledge of detector features.

Cluster multiplicities distribution of figures 6.4 and 6.5 in the next chapter, can only be well reproduced in the first bins (rate between 0 and 1 cluster bins) by Monte Carlo simulation with detailed knowledge of planes efficiency. The same stands for the description of two-track inefficiency of upstream part, described in detail in section 6.2.1.

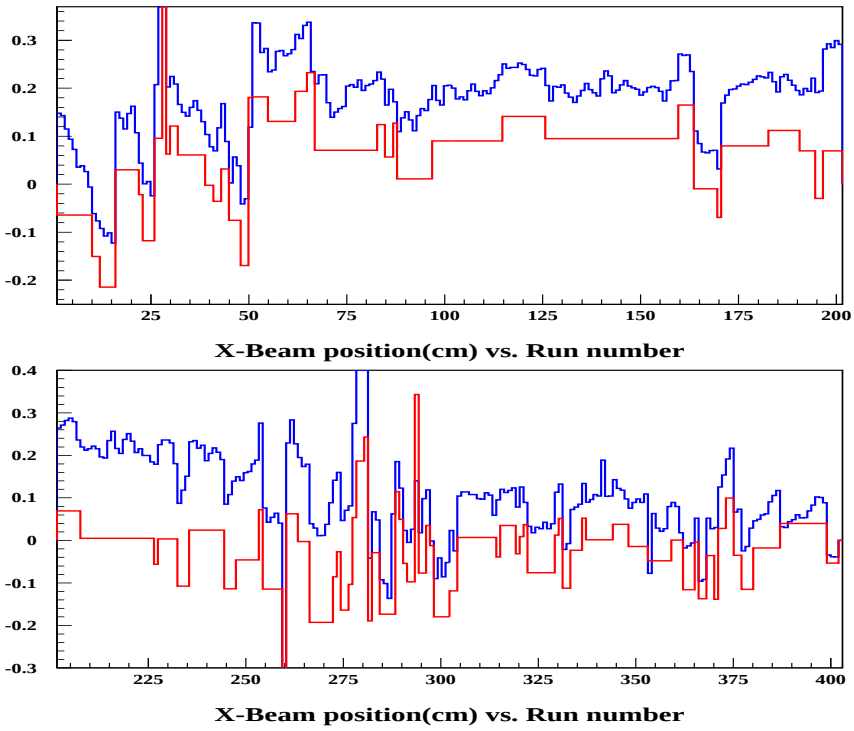

Figure 5.6: *Beam intersection with target plane (X coordinate) determined with upstream detectors (blue) as function of the 2001 run number. In red a beam position estimation using only information from the drift chambers.*

An specific event selection for the evaluation of each studied plane is performed, with three basic items, namely:

- Laboratory frame momentum of tracks is required to be $p_{+,-} > 2.75\, GeV/c$ in order to select events with low dispersion angle due to multiple scattering in the detectors.

- To evaluate efficiency of X-coordinated detectors (MSGC-X, MSGC-XP and SFD-X), events with $Q_X > 1.75\ MeV/c$ are selected in order to avoid not resolved close-lying tracks. Values of Q_Y over 1.75 MeV/c

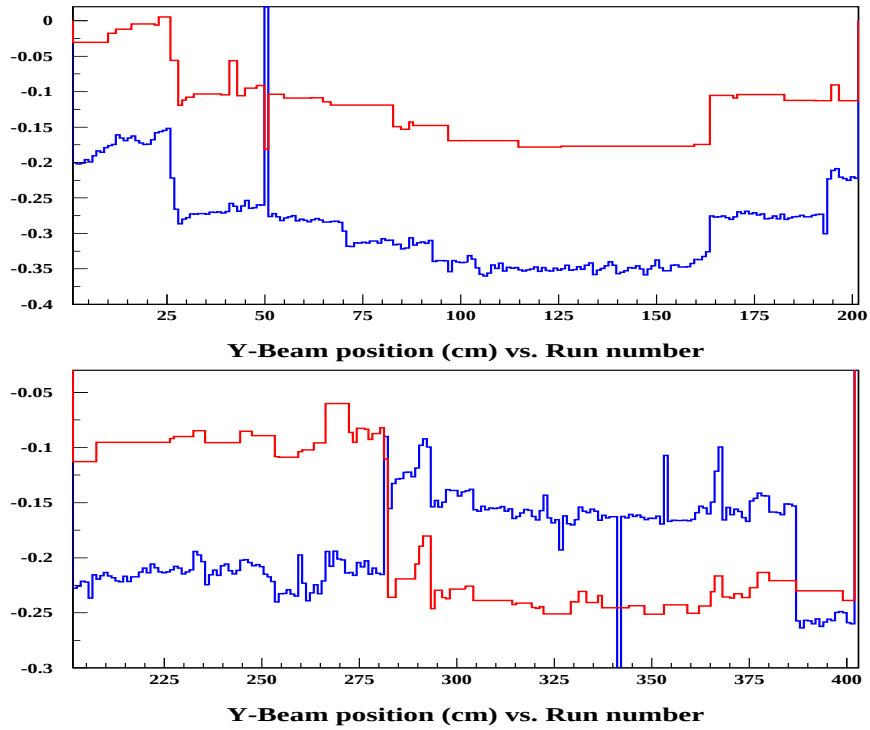

Figure 5.7: *Beam position for Y coordinate obtained with upstream detectors (blue) and drift chambers (red).*

are required for the measurement of Y detectors (MSGC-Y, MSGC-YP and SFD-Y).

- Tracks with at least 5 hits (independently of the currently studied plane) are used. For each plane, well-defined tracks are formed by hits in the other 5 upstream detectors.

Efficiency of plane i is defined as

$$\epsilon_i = \frac{N_{5+1}}{N_5^*} \tag{5.1}$$

with

$$N_{5+1} = \text{Number of selected tracks with 6 upstream hits}$$

$$N_5^* = \text{Number of tracks with avobe selection criteria}$$

This is basically the ratio of selected tracks where the plane under evaluation has been efficient. For Ni-2001 data, obtained efficiencies displayed in table 5.1.

Table 5.1: *Overall efficiency values as defined in the text obtained for MSGC/GEM planes present at Ni-2001 period.*

Plane	Efficiency
MSGC-X	0.893 ± 0.002
MSGC-Y	0.910 ± 0.002
MSGC-XP	0.906 ± 0.002
MSGC-YP	0.823 ± 0.002

Alternative calculation with the same sample of selected tracks was made using the described non-correlated residuals. The gaussian fit to the residual distributions was used to define a 3σ window around the mean value coordinate for each detector. Efficiency was then defined as the ratio of events with a residual value inside the window. The efficiencies obtained with this method did not differ from the presented in table 5.1.

Chapter 6

Evaluation of $\vec{Q}$ resolution with Monte Carlo

Apart from collecting time correlated pairs (prompt events), the DAQ system also collected a relatively large fraction ($\sim$ 60%) of accidental pairs, which will be used in the analysis. In addition to this samples, and in order to extract the pionium lifetime from the $\vec{Q}$ spectra, a Monte Carlo simulation of the different types of pion pairs collected by the spectrometer has been developed. We are going to use it first for evaluating the $\vec{Q}$ resolution of the reconstruction method.

6.1 DIRAC Monte Carlo

For the analysis of pionium lifetime, in order to achieve the most accurate extrapolation of Coulomb interaction down to very small values of Q, we have chosen Monte Carlo simulation as the simplest analysis procedure.

Even with the excellent time-of-flight resolution of the spectrometer, a non-Coulomb background remains in prompt-pair event selection. It consists of accidental pairs and also pion pairs from long-lifetime decays, which we will call non-Coulomb correlated pairs.

All the components of Q spectrum present in the prompt peak of time coincidence are created by specific generators and passed through the Monte

Carlo Package GEANT adapted to DIRAC experiment [58]. Together with this generators, a simulation of atom pairs form pionium breakup, and special accidental pairs with time coincidence in the TOF detectors are created. The digitization of the detectors and the simulation of the background noise is made by ARIANE program just before the Monte Carlo reconstruction takes place.

A concatenated-script system has been developed to handle the Monte Carlo generation and reconstruction. It has been implemented over the queue system of the SVGD [59] cluster of CESGA[1], allowing to send an (almost) infinite number of generation or reconstruction jobs using only one command line, handling more than 80 processors and 2 Tb of data.

In this chapter we will make use of this Monte Carlo simulation to evaluate in detail the resolution of the reconstruction method in the critical distributions for the lifetime measurement, Q_X, Q_Y, Q_T and Q_L.

6.1.1 Monte Carlo generators

It should be understood that the use of Monte Carlo is entirely restricted to the description of experimental resolution, and by no means it implies specific model assumptions about proton-nucleus physics.

The input files for GEANT are produced with a specific $\pi^+\pi^-$ generator, with different features according to the corresponding distributions of atomic, Coulomb, non-Coulomb or accidental pairs. GEANT input contains initial momentum vectors of the pion pairs as well as coordinates of the production point. It is needed to specify $\vec{p}$ and $\vec{Q}$ distributions by means of two vectors in polar coordinates $(|\vec{p}|, \theta, \phi)$ and $(|\vec{Q}|, \theta', \phi')$. In the case of accidental pairs two different production coordinates were produced, due to their uncorrelated origin in proton-nucleus collision.

For **atoms**, the $\vec{Q}$ distribution was parametrized in order to simulate the breakup cross-section [65]. The pionium dissociation point is generated according to the dependence of breakup probability with propagation distance inside the target, using a GEANT-like step procedure [60].

[1] Centro de Supercomputacion de Galicia

Meanwhile **accidental** and **non-Coulomb pairs**, due to their uncorrelated nature, are defined purely by phase space $Q^2 sin\ \theta$.

Coulomb interaction [61] is described by the Gamow enhancement of their Q-space wavefunctions, $A_C(Q)Q^2 sin\ \theta$, with

$$A_C(Q) = \frac{2\pi M_\pi \alpha / Q}{1 - e^{-2\pi M_\pi \alpha / Q}} \tag{6.1}$$

The input lab-frame pion momentum spectrum p is actually taken from real spectrometer data. For this purpose, a de-convolution of the reconstructed prompt pair spectrum E as function of p and θ (angle with respect to the proton beam) is performed, according to the expression:

$$G_1(p,\theta) = \frac{E(p,\theta)}{\epsilon(p,\theta)} \frac{1}{A_C(Q)} \tag{6.2}$$

where $A_C(Q)$ is the Coulomb factor and the acceptance function ϵ is evaluated by Monte Carlo as follows :

$$\epsilon(p,\theta) = \frac{R(p,\theta)}{G_0(p,\theta)} \tag{6.3}$$

where R is the Monte Carlo reconstructed output for a given generator input G_0. The procedure was iterated only once, and G_1 taken as final generator input. The acceptance function matrix $\epsilon(p,\theta)$ does not appear to depend significantly on G_0. Two different G_1 functions were determined, one for prompt events and another for accidental pairs. The latter (obtained with $A_C(Q) = 1$), is used for simulation of the accidental pair background in prompt events. Their corresponding spectra $E(p,\theta)$ do differ significantly, mainly due to the proton background which is present in accidental pairs. In fact, this point has been verified following the procedure outlined in reference [67] for 2001 data. For atomic and non-Coulomb pairs the same initial $\vec{p}$ vs θ dependence is used. p and θ input spectras are shown in figures 6.1 and 6.2 for prompt and Accidental pairs respectively.

With these distributions as input files, tracking is performed by the GEANT-DIRAC program [58] using standard geometry and detector files. Pion pairs are propagated through the detector materials and resulting spatial detector hits and time-of-flight are written into the output file. This

information is in a subsequent step digitized by ARIANE which describes the specific response of each detector.

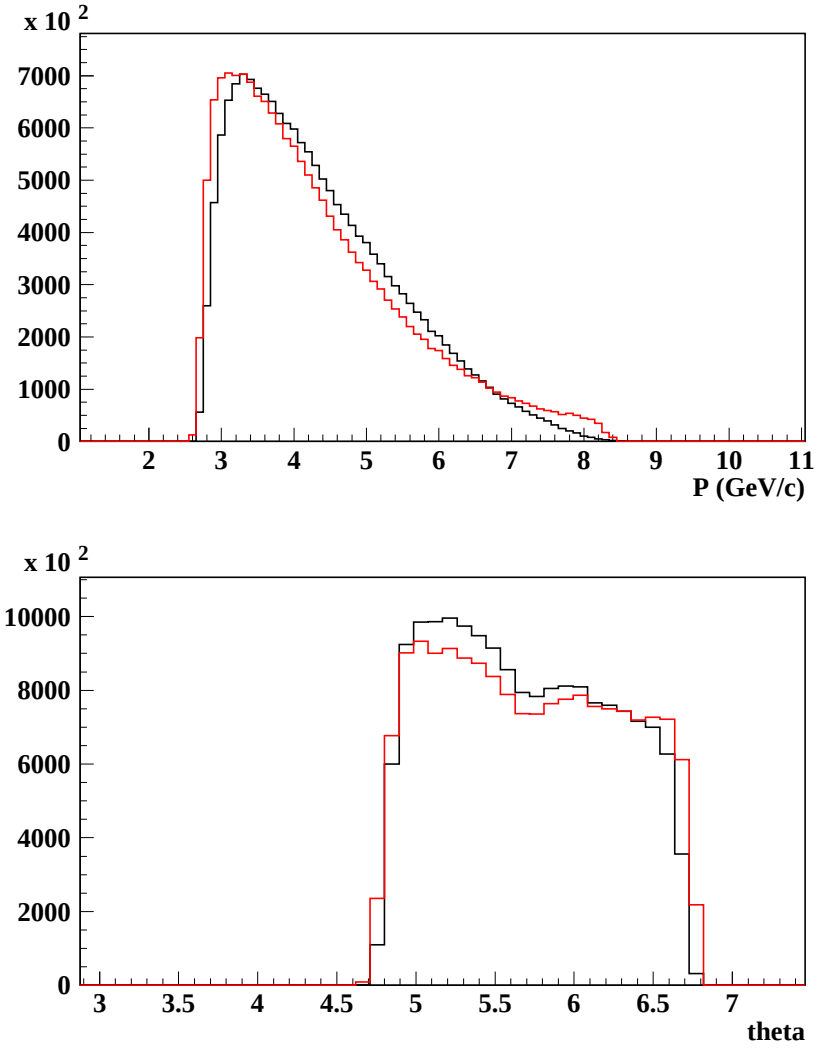

Figure 6.1: *p and θ distributions obtained from experimental prompt pairs (after subtraction of accidental pairs) are shown in black. Red lines correspond to de-convoluted input spectrum for Monte Carlo, as explained in the text.*

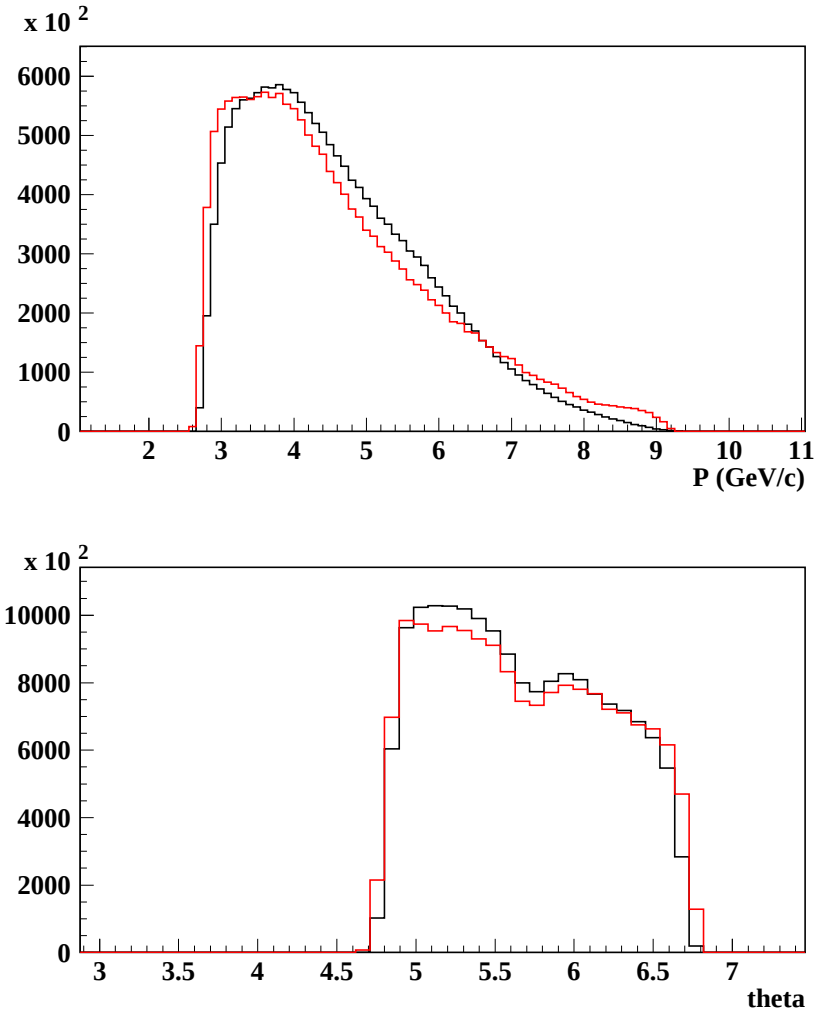

Figure 6.2: p and θ distributions for accidental pairs. Red lines correspond again to de-convoluted input spectrum for Monte Carlo.

6.1.2 MSGC/GEM simulation

The detector hits digitizations are performed by ARIANE program [68] when running over Monte Carlo files (output files from GEANT) at a lower level before reconstructing them in the same way as real data. Special care was done for simulating the response of MSGC/GEM detector according to the experimental measurements.

The procedure for MSGC/GEM cluster patterning uses real data input to describe correlations between cluster total charge, micro-strip multiplicity and differential charge. An average of all Ni data spectrometer runs from 2001 was used as input for the simulation code.

Monte Carlo simulation takes into account the following aspects, where the MSGC/GEM clusters (or hits) are defined as a continuous set of strips above threshold:

1) overal charge collected by the strips of each MSGC/GEM plane

2) cluster strip-multiplicity and pulse-height pattern within a cluster

3) efficiencies of the 4 MSGC/GEM planes

4) Number and position of dead strips in the 4 planes along the data collection period

5) detector-correlated hit multiplicity

6) space correlations within the same detector (pair production, showers)

7) absence of space correlations between different detectors (when trigger particles are removed)

8) finally, clusterisation algorithm (the same ARIANE code as for experimental data is used)

For the first and second item, all information is encoded from real data under the form of dedicated input histograms initialised by ARIANE. For each hit an individual amount of charge is assigned based in the overall

charge distributions. Figure 6.3 shows microstrip multiplicity (cluster size) of MSGC/GEM hits.

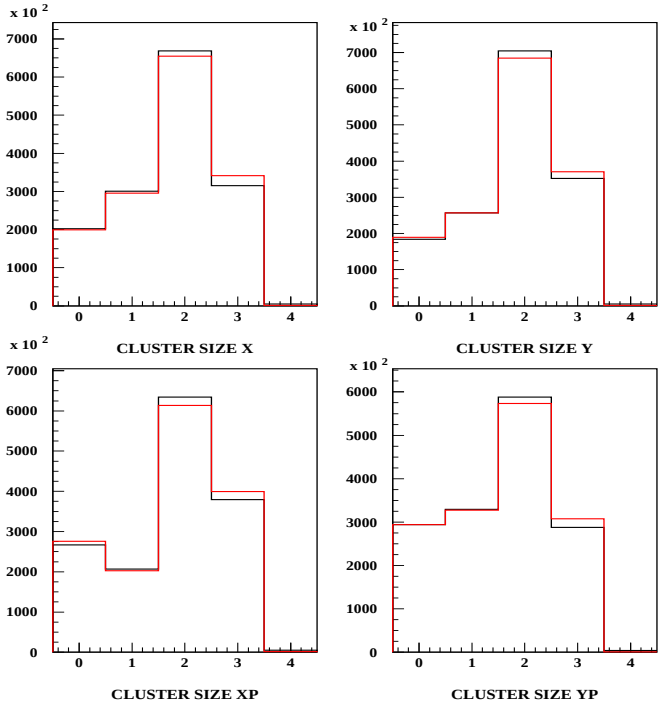

Figure 6.3: *Distribution of microstrip multiplicity (cluster size) of MSGC/GEM hits in real 2001 data including background hits for real (black line) and Monte Carlo (red) data.*

For MSGC/GEM efficiency, the simulation parameters were cross-checked with real data, and they are adjusted to the values quoted in chapter 4.

Concerning detector-correlated hit multiplicity, these are also input from experimental data, but under the form of 4-fold correlation matrices, so that 4 multiplicities for X, Y, XP, YP detectors are generated jointly.

As far as item 6 is concerned, it is observed that a fraction of close-hit pairs are produced near the detector frames, outside the acceptance of the drift chambers. Therefore we focus our simulation for those MSGC/GEM

hits that actually lie on the path of the extrapolated drift chamber tracks. So we define a hit multiplicity N_h as the sum of all hits found within a 3σ cut around the extrapolated coordinates of positive and negative tracks to all MSGC/GEM detectors. The same momentum-dependent σ is used here as for the matching procedure in ARIANE reconstruction.

The observation mentioned in item 7 was demonstrated by showing that events with one-sided activity in X-coordinate did not have corresponding activity in XP (likewise for Y and YP), when hits from real trigger tracks were removed. Therefore simulation of space correlations appeared to be unnecessary.

Let us take a closer look at the simulation of this MSGC particle background in the next subsection.

6.1.3 Background noise simulation

The source of MSGC/GEM background is real particles that cross the detector outside the trigger gating time. Pipeline delay was adjusted at installation time so that maximum pulse-hight is obtained within the experiment trigger gate, and it decreases by approximately a factor two at the borders of the 250 ns time acceptance.

Simulation of out-of-time noise hits in MSGC/GEM detectors is done by reproducing the experimentally observed characteristics of this background. When the two $\pi^+\pi^-$ triggering tracks (available from the matching) are removed, no evidence of space correlations between different planes, thus indicating this background essentially originates from wide angle tracks with respect to the beam direction.

We should mention that, because of the non-linear response of the clusterisation routine, which combines nearby particles together at large particle densities, the simulation procedure generally requires several iterations to converge.

It is important to note that this simulation is totally constrained by the observed hit multiplicities. The full 2001 data sample was included in our analysis, in order to account for possible run-to-run variations.

The final results for simulated MSGC/GEM hit multiplicities are illus-

trated in Fig. 6.4, where the number of MSGC hits found within a 3σ road around drift chamber tracks, for each detector plane, is compared for real data and Monte Carlo simulation. The same distributions in logharitmic scale are plotted too (Fig. 6.5), so the excellent simulation quality can be appreciated. Not only average values are described, but also multiplicity shape is correctly reproduced. Please note that the peak observed in the first bin (value=0) of plot corresponding to MSCC-XP is due to the fact that this plane was not opperational during some 2001 data runs.

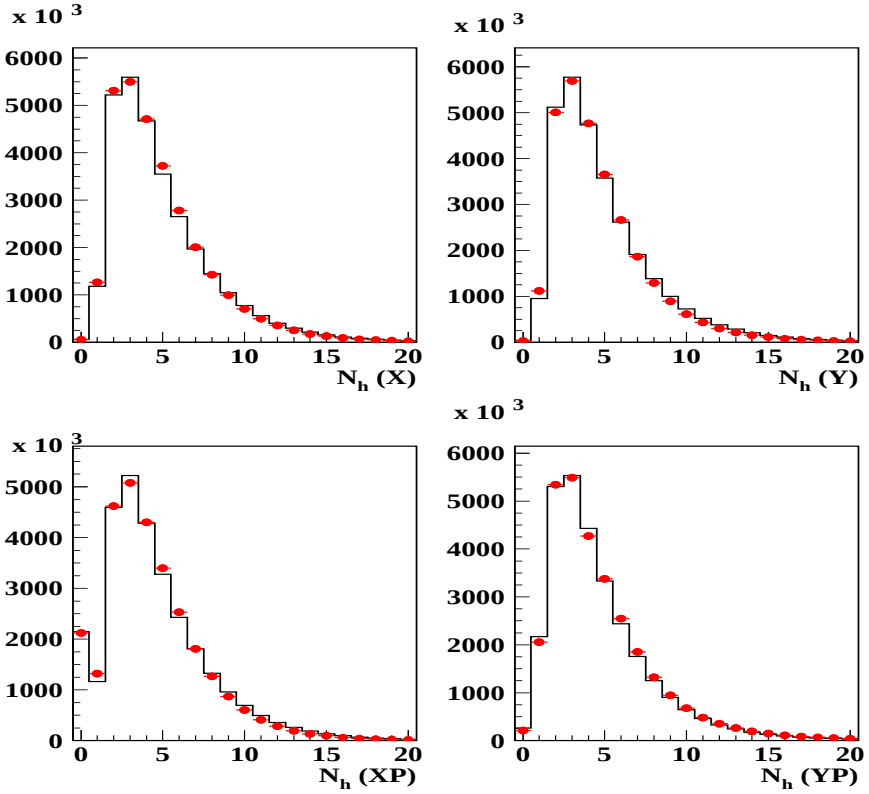

Figure 6.4: *Number of MSGC clusters found close to any of the drift chamber tracks, including the real signal pairs (dots), compared to Monte Carlo simulation (line). Detector ordering is X/Y (top left/right) and XP / YP (bottom left/right). All data runs used in lifetime analysis were included.*

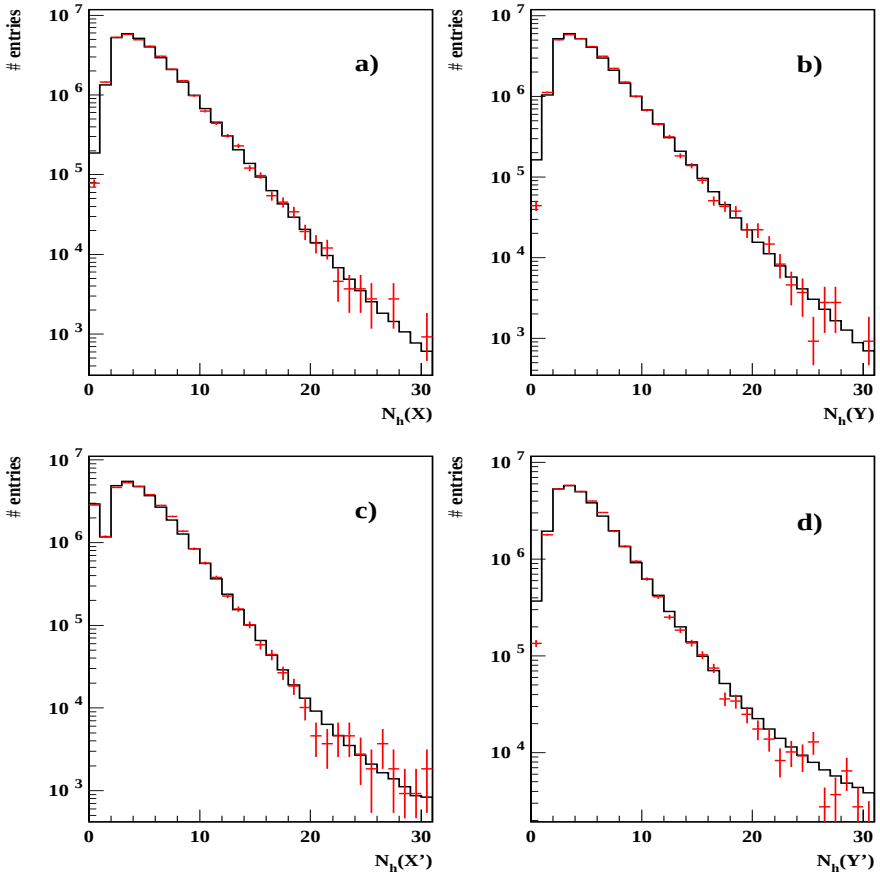

Figure 6.5: *Continuous lines represent observed hit multiplicity in MSGC X (a) ,Y (b) , XP (c) and YP (d) detectors for 2001 data runs, as described in the text. Coloured crosses are the Monte Carlo simulations described in the text, for each detector.*

6.1.4 Influence of simulation on vertex resolution

We have analyzed in detail whether MSGC/GEM parameters in ARIANE simulation might influence the results of vertex resolution.

Vertex resolution is defined as the sigma from a gaussian fit to the distribution of the relative difference between the extrapolated coordinates of the two tracks at the target plane. Only tracks with registered hits in all upstream detectors are used for this issue. Histograms were fitted to a gauss function in different slices of p, and sigma values in each proyection (σ_x and σ_y) were compared, using a sensible parametrization $a + b/p$.

The resolution in determining the vertex of the two reconstructed particles is directly related to Q_T resolution and it was used [62] [28] to determine the amount of upstream matter for the Monte Carlo used in pionium lifetime, by achieving a correct description in θ resolution.

Here is analyzed the role that the described digitizations play concerning this item. It is quite clear that with a single-hit resolution of 50 μm this influence is bound to be small as compared to multiple scattering, given the detector geometry.

The prediction for vertex resolution is shown in Fig. 6.6 under the assumption that all cluster sizes were equal to one microstrip and that all were equal to two microstrips with standard Monte Carlo. From Fig. 6.3 it is clear that both asumptions are extreme, in relation with the precision of the digitization code. However, the changes induced are very small, hardly changing Monte Carlo prediction.

Noise level is quite strong in both MSGC/GEM and SFD detectors. Because the vertex resolution relies mostly on the MSGC, we have studied the influence of changing the MSGC/GEM background conditions on the previous results. We show in Fig. 6.7 the vertex resolution obtained after $\pm$ 10% variation of average hit multiplicity, as compared with the observed average values. For reference, we also show the prediction for null MSGC/GEM background. It is clear that significant changes on noise conditions hardly change the result. The extreme hypothesis of null background clearly illustrates the effect of noise. At low momentum (where search windows are larger for multiple scattering), the probability for noise hits to enter the track is higher,

given the fact that pattern recognition uses the calibrated beam spot center. We conclude that a wrong simulation of MSGC/GEM background does not significantly the results.

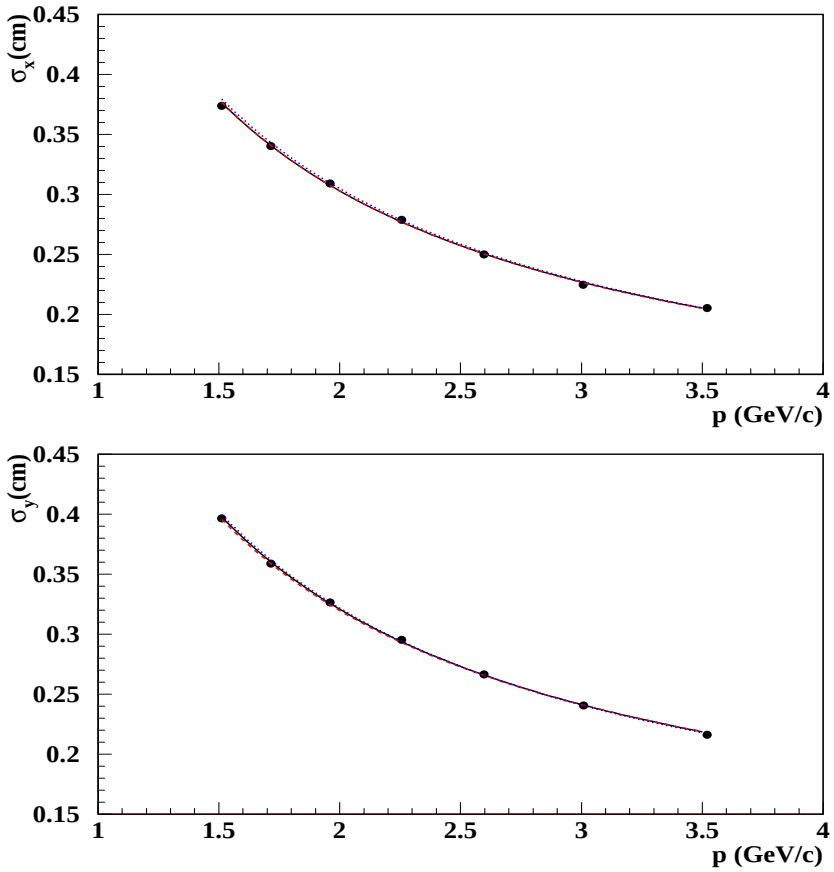

Figure 6.6: *Comparison between vertex resolution obtained after variation of the MSGC/GEM cluster size shown in figure 6.3. The full circles and line correspond to the standard digitization, where real multiplicity is simulated. Dotted/dashed lines are obtained with all clusters having one/two microstrips only.*

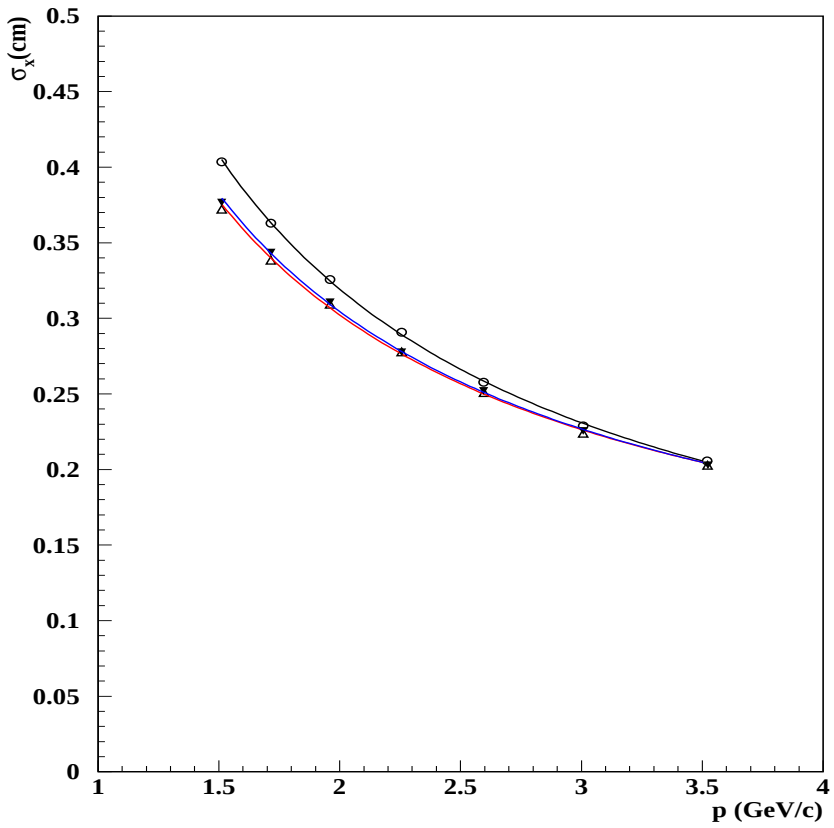

Figure 6.7: *Comparison between vertex resolution (X-projection) obtained after variation of MSGC/GEM background level. Open/full triangles indicate +/- 10% variation of MSGC average hit multiplicity, with respect to the observed (standard) values in figure 6.4. Open circles show the case where MSGC/GEM background is totally removed (lines are also shown in all cases, following a fit to* $a + b/p$ *parametrisation).*

In figure 6.8 we show the vertex resolution obtained with SFD background removed, as compared with the one with nominal parameters. Although the background level in SFD is high, its influence is negligible (both in X and Y). This is understood, since noise SFD hits will not be followed by MSGC/GEM

hits in front, and the track will not be reconstructed since 6 upstream hit tracks were selected in this analysis.

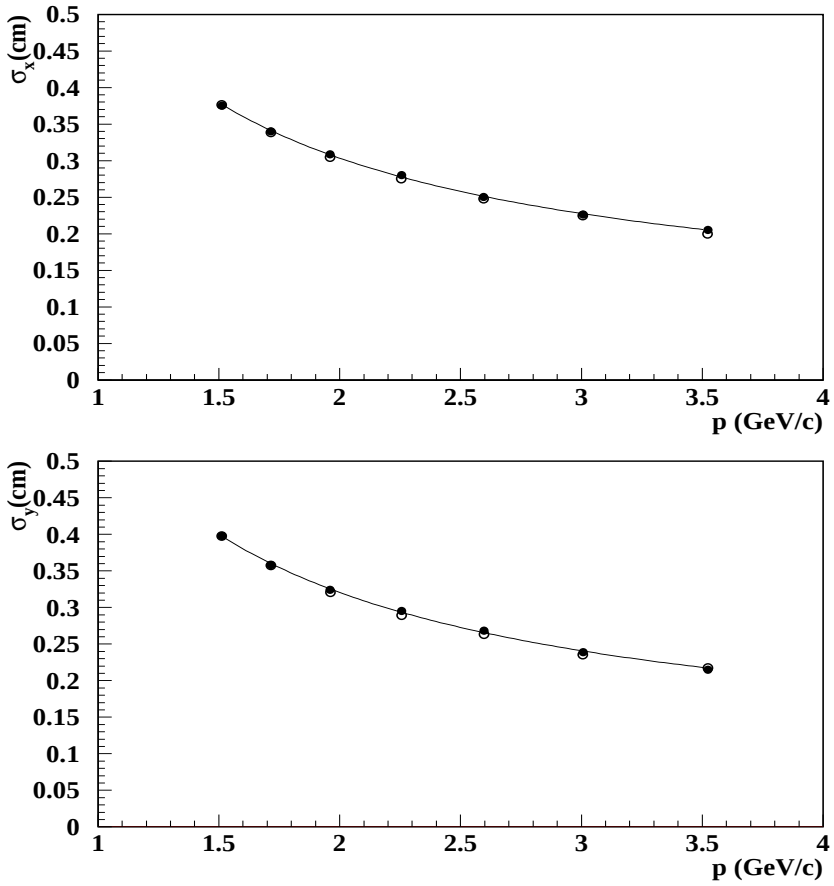

Figure 6.8: *Comparison between vertex resolution in X (top) and Y (bottom) obtained from standard simulation (full circles) and simulation with SFD background removed.*

6.1.5 Monte Carlo event selection

Buffer files (which contain GEANT-DIRAC output) were created after generator cuts $Q_T < 8\ MeV/c$ and $|Q_L| < 24\ MeV/c$.

During reconstruction a simplified pre-selection pass is done, which performs the essential functions of the standard pre-selection [69] used with real data (wich will be described in next chapters). Particularly a veto on large ($> 6\ MeV/c$) Q_X or Q_Y estimated values, in the presence of SFD background is applied.

GEANT-DIRAC is used with modified average multiple scattering angle according to reference [62]. Average radiation length of upstream detectors, which correlates with resolution performance, has been the subject of variations at the level of 15% with respect to standard GEANT-DIRAC values. For the sake of concreteness, the choice made in this work corresponds to the values optimised in [62] with real data. Lower values would of course mean better resolution, in all transverse momentum quantities which will be evaluated.

6.2 $\vec{Q}$ resolution.

In this second part of chapter 6, it is going to be made a complete evaluation of reconstruction efficiency and resolution of the tracking method in DIRAC.

The 10 upstream detectors account for a sizable amount of radiation length and the background conditions are extremely high in all of them and Monte Carlo simulation is used to evaluate in detail the critical distributions for the lifetime measurement, namely Q_X, Q_Y, Q_T and Q_L. Conditions of 2001 spectrometer data were chosen for this analysis.

The real advantage of the upstream arm relies on its capability for maximal reduction of detector backgrounds and decays. This point is essential for determination of pionium lifetime with a high intensity proton beam, because when the atom signal is mapped into the (Q_T, Q_L) plane, background will be reflected into uncertainty in Q_T, and therefore into systematic error. Dropping the Q_T projection from the analysis would result, on the other hand, in reduced (statistical) precision with respect to the 2D fit described

in the upcoming chapter 8.

Special care is made in the analysis of the rate of pion pairs leading to a very small value of $Q_{X,Y}$ due to single-hit inefficiency of SFD. It can be noticed a relatively large enhancement in the reconstructed Coulomb pairs at Q_X and Q_Y close to zero, clearly related to the single-hit inefficiency of SFD, in conjunction with unability of MSGC's to resolve these pairs. A delicate challenge to the DIRAC simulation and reconstruction procedure arises from the response of PSC electronics of the fibre detector when two low-angle pulses arrive in strict time coincidence suppresion of one of the pulses occurs with a significant probability, The distorsion caused by this effect is largely diminished when the the track is measured by MSGC/GEM hits having stereo angles.

With experimental knowledge of the average single-hit efficiencies of MSGC's and SFD's (see [71]), we are able to calculate the probability that, under certain conditions, a wide-angle pion pair looses the experimental information necessary to measure the track separation, due to combined SFD and MSGC/GEM inefficiency. We call this probability *two-track inefficiency* r_0. A comparison of the tracking results with this calculation, allows to make a precise tune of the reconstruction in order to reduce the two-track inefficiency for Coulomb pairs (and therefore the enhancement at $Q_{X,Y}$ close to zero), minimizing sources of track inefficiency.

During this tunning with Monte Carlo simulation, time cuts between SFD and VH were optimized, as well as the following aditional constraints needed for tracking procedure was introduced:

- In cases where the pair contains only one hit in X, one hit in XP and two hits in SFD-X (likewise in the other projection), MSGC/GEM hits are newly searched for in the vicinity of existing ones, that may have escaped pattern recognition or have been dropped earlier. They are then assigned to closest track. This improves the quality of low Q_X and Q_Y spectra.

- Charge division of common microstrip in double MSGC/GEM clusters is done proportional to pulse-height, rather than by 1/2. It slightly improves $Q_{X,Y}$ spectrum.

- In the same way, under specific track configurations, splitting into two of MSGC/GEM clusters is done.

Attempts were also made to use MSGC/GEM pulse-height information in available hits, in order to improve further the spurious contribution to single-track pairs by providing appropriate veto, defined by the absence of double MSGC/GEM pulse. The fine granularity of the MSGC's would overcome the limitation originated by the 6 mm slab width of IH detector. However, Landau tails did not allow further improvement.

6.2.1 Cross-check of two-track inefficiency

In absence of detector backgrounds, the wide-angle (distance larger than 1.5 mm) two-track inefficiency r_0 , multiplied by the integrated Coulomb pair rate (up to the maximum Q_T values that emerge from the trigger system), gives us the excess number of events that will be erroneously found by the reconstruction at Q_X and Q_Y close to zero, because one track has been lost. The presence of backgrounds can only decrease this event rate artificially, and the exact calculation must of course be made by Monte Carlo. Independently, the utilisation of IH detector will also decrease this rate (this time not artificially) to the real value r_H, after application of suitable pulse-hight cuts on the extrapolated IH slabs of each candidate track, in A and B layers. Let us recall here that each track is required to have at least two hits in each projection (either SFD or MSGC/GEM), and that the pair can be vetoed in absence of single pulses in IH (two tracks) or double pulse (single track). Here again, the exact calculation of r_H can be made by Monte Carlo. The ratio $f_H = r_H/r_0$ has been determined to be 0.50 ± 0.03.

In order to cross-check the tracking performance, we have removed detector backgrounds from the simulation, and inhibited the application of IH cuts. In this simple situation, the observed two-track inefficiency can be compared with the following calculation:

$$\begin{aligned} r_0^{th} = 2\epsilon_F(1-\epsilon_F)\Big(2\epsilon_M^3(1-\epsilon_M) + 2\epsilon_M^2(1-\epsilon_M)^2\Big) \\ +2\ \epsilon_F^2\epsilon_M(1-\epsilon_M)^3 + 2\epsilon_F^2\epsilon_M^2(1-\epsilon_M)^2 \end{aligned} \qquad (6.4)$$

where ϵ_F and ϵ_M are the single-hit efficiencies of SFD and MSGC/GEM. We obtain from the tracking the (measured) value $r_H^{ms} = f_H \cdot r_0^{ms} = 1.71 \pm 0.03\ \%$, to be compared with the calculated value, in terms of pure Gaussian efficiencies of MSGC/GEM and SFD, $r_H^{th} = f_H \cdot r_0^{th} = 1.28\ \%$. In both cases detector backgrounds were removed. We find there is acceptable agreement between the two, after checking that the discrepancy can be explained by adjustable track requirements (beam impact parameter for MSGC-only track projections and DC matching distance, 55%), Molière tails of multiple scattering at track pattern recognition (30%), and other rare geometrical effects (15%).

Therefore, we consider that the performance of the tracking is close to its expected value. Certainly, the two-track inefficiency r_H^{ms} can still be reduced by less stringent cuts, but then background level would be compromised. Please note that the efficiency values ϵ_F and ϵ_M in the Monte Carlo have been determined from the entire experimental data sample in 2001, and are subject to very little uncertainty. Moreover, we know that single-hit efficiencies do not depend essentially on track separation, except for very small distances (due to the PSC effect) [71].

6.2.2 Resolution study

In order to illustrate the general performance of the tracking procedure, a comparison is made between the input center-of-mass momentum components and the reconstructed output. Input is defined as the Q_i values for GEANT $\pi^+\pi^-$ pairs that emerge from the target foil [2]. These are considered as $true$ values for the reconstruction procedure, and we denote them by Q_i^{gen} (generator pairs). As for the index i is concerned , we will discuss here the quantities Q_X, Q_Y , $|Q_X|$, $|Q_Y|$, $Q_T = \sqrt{Q_X^2 + Q_Y^2}$ and $|Q_L|$, as most representative. Only the last four are actually measurable by the experiment, because the charge sign becomes random at small opening angles, due to multiple scattering. Nevertheless we also include the first two, for

[2] technically it is achieved by a GEANT cut at 1.15 cm away from the target foil position, since the maximun aim of our reconstruction must be describe the $\vec{Q}$ at this point, we can not go back and disable multiple scattering inside the target.

the sake of illustration of tracking properties. In any case, let us mention that the alignment procedures include the charge conjugation symmetry as a constraint, and that the precise determination of pionium lifetime does not require any measurement of the charge sign.

It is required that the generated event passes the trigger and that the drift chambers produce one positive and one negative track, with standard χ^2 cuts. The ensemble of these pairs (N_0) is considered as the reference normalisation, for overall efficiency studies. Generic distributions of Q_i^{gen} in N_0 will be denoted by G_0 in the following. A subset $N_1 \subset N_0$ is defined by reconstructed pairs. For every matched pair (between downstream and upstream arms) there will be a reconstructed (measured) value Q_i^{rec} and a generator (true) value Q_i^{gen}. In the next section we analyze the difference $|Q_i^{gen}| - |Q_i^{rec}|$ (which we call $resolution$), as well as the correlation between Q_i^{gen} and Q_i^{rec}, for atom pairs and for Coulomb pairs separately. We will be calling, generically, G_1 and R_1 the distributions of Q_i^{gen} and Q_i^{rec}, respectively, for pairs that belong to N_1.

The following results are presented after a cut $Q_T^{gen} < 6\ MeV/c$, where the generator value Q_T^{gen} is defined past the target foil.

6.2.3 Atom pairs

In figure 6.9 the reconstructed Q_X distribution (R_1) is shown for atom pairs, and it is compared with generator (true) values G_1. The effects of statistical bias and efficiency, on the one hand, and distortion caused by the measurement, on the other hand, can be reasonably decoupled by showing the ratios G_1/G_0 and R_1/G_1, separately, which is done in figure 6.10 (top).

Figures 6.11 and 6.12 show exactly the same histograms as figures 6.9 and 6.10, but applied to Q_Y. According to these results, the following general features of $Q_{X,Y}$ reconstruction for atom pairs can be extracted:

a) there is a small overall inefficiency (less than 1%). It is attributed to double-pulse broadning in IH, inefficiency of SFD and MSGC/GEM detectors and to multiple scattering tails. The central region of Q_X shows a small additional depletion of 2%, which depends on the actual double ionization cut used.

b) the measurement of $Q_{X,Y}$ reproduces the true spectrum (G_1) rather closely. There is however a small widening due to the entangled effect of detector backgrounds and detector inefficiency (SFD, MSGC ,IH). In fact this explanation takes sense exactly for the slight deep at low Q_X values.

Correlation between Q_X^{gen} versus Q_X^{rec} is shown in figure 6.15 (top), for atom pairs. We see that besides the correct same-sign correlation, there is an orthogonal one due to charge confusion originated from multiple scattering in the overall spectrometer. This charge confusion is irrelevant for the lifetime measurement, which is based upon Q_T analysis. In addition, we see small horizontal and vertical lines. The former is due to atom pairs which have lost a SFD hit due to detector inefficiency. The vertical one originates mostly from background hits in SFD (apart from a very small component due to large-angle Coulomb scatters) that cause artificial opening of the atom pair. In both cases, what is seen in the plot corresponds to the remainder of what the MSGC/GEM detector could not resolve, due to its own inefficiency. A limited number of events has been run to produce this plot, in order to appreciate more clearly the proportion of vertical and horizontal lines. Figures 6.13 and 6.14 (top) are structured in the same way as figures 6.9 and 6.10, but now applied to the transverse momentum Q_T, for atom pairs. The general features previously discussed for $Q_{X,Y}$ certainly apply for Q_T too. The resolution function R_1/G_1 for atom pairs (figure 6.14, top) now shows a slight depletion at small Q_T values, with a corresponding enhancement at the distribution tail. This effect is essentially due to MSGC/GEM background hits. Event-by-event resolution for atom pairs, defined by $|Q_i^{gen}| - |Q_i^{rec}|$, is analyzed in figure 6.16 (top) for $|Q_X|$, $|Q_Y|$, and Q_T. It can be described by a gaussian fit with some tails, which are different on the positive and negative sides. These tails are evaluated as the fraction of events measured with $|\Delta Q_i| > 2\ MeV/c$, in each case. Results, together with the σ values from the gaussian fit, are given in table 6.1

The resolution tails observed in figure 6.16 are asymmetric in all cases, due to the distinct effect of detector (SFD and MSGC) backgrounds (left side), which open up the pair, and inefficiency (right side), with the opposite

trend. The effect of inefficiency is more severe for Coulomb pairs than it is for atom pairs, because of the larger transverse momentum span of the former.

Special attention has been devoted to the tail of reconstructed Q_T distribution for atom pairs, due to the fact that lifetime analysis will require a cut $Q_T < 5\ MeV/c$ (maximum allowed by unbiased pre-selection procedure). The fractional integral for $Q_T > 5\ MeV/c$ is given in table 6.2 for reconstructed atoms, together with the fraction obtained under the same cut for generator values, which also contribute to this region due to multiple scattering in the target foil. The difference between the previous two quantities (indicated in the last column of table 6.2) evaluates the fraction of lost pairs after $Q_T > 5\ MeV/c$ cut. Results are also indicated for an interesting 4 MeV/c cut.

Finally in figure 6.17 we also show $|Q_L|$ spectrum and in figure 6.18 the corresponding ratios and resolution plots for atom pairs, following the same line as for the previous discussion of other quantities.

Table 6.1: *Gaussian resolution σ and fraction of events where $|Q_i^{gen}| - |Q_i^{rec}|$ is larger than 2 MeV/c, for atom pairs. Positive and negative tails are given separately.*

	σ (MeV/c)	Tail (+) (%)	Tail (-) (%)
$\|Q_X\|$	0.10	0.10	2.42
$\|Q_Y\|$	0.11	0.09	2.45
Q_T	0.12	0.08	4.10
Q_L	0.52	2.66	2.56

Table 6.2: *Fraction of atom pairs reconstructed with two different Q_T cuts, the corresponding fraction for the original generator values (after multiple scattering in the target foil), and the difference between the two.*

	tail (%)	generator (%)	loss (%)
$Q_T^{rec} > 4$ MeV/c	3.73	1.09	2.65
$Q_T^{rec} > 5$ MeV/c	2.12	0.31	1.80

6.2.4 Coulomb pairs

Reconstruction of Coulomb pairs reveals sufficiently different properties so that they need be reported separately. Needless to say that the reconstruction package must be exactly the same in both cases. However, the Q_i span is much wider than for atom pairs, and that implies specific features that are presented in figures 6.9-6.18. We follow exactly the same exposure as previously done for atom pairs, and the results are presented at the bottom of each figure.

Table 6.3: *Gaussian resolution σ and fraction of events where $|Q_i^{gen}| - |Q_i^{rec}|$ is larger than 2 MeV/c, for Coulomb pairs. Positive and negative tails are given separately.*

	σ (MeV/c)	Tail (+) (%)	Tail (-) (%)
$\|Q_X\|$	0.10	1.11	1.13
$\|Q_Y\|$	0.11	1.21	1.19
Q_T	0.12	1.15	1.51
Q_L	0.52	2.77	2.66

If we now review the general properties previously observed for atom pairs in $Q_{X,Y}$ reconstruction, we see that here too overall inefficiency does

not exceed 3%. The resolution function defined by R_1/G_1 ratio has however a different shape. A narrow enhancement is observed at small $Q_{X,Y}$, which is actually the effect of SFD inefficiency. As a matter of fact, well separated track pairs will be reconstructed with a very small $Q_{X,Y}$ when one of the SFD hits is lost, and the MSGC is not able to recover the pair due to its own inefficiency [3]. The strong background of single-to-double ionization in IH detector (at the level of 40%), and the fact that most pairs actually cross the same IH slab (standard reconstruction cut is $Q_T < 5$ MeV/c), makes the double ionization cut rather inefficient to avoid this configuration. In $Q_T = \sqrt{Q_X^2 + Q_Y^2}$ spectrum this effect produces a smooth increase towards Q_T=0.

It is interesting to understand how the Q_X reconstruction performs for different number of MSGC+SFD hits in each track separately. There are 6 categories in total, namely 6-6, 6-5, 6-4, 5-5, 5-4 and 4-4. We show in figure 6.19 the reconstructed Q_X spectrum in each category, as compared with the original generator values, in each case. Like in the case of atom pairs, very short distances can be resolved by the MSGC/GEM in all categories, including 6-6. However, for the latter a bias exists against very small opening angles, due to the SFD double track resolution. The excess at zero Q_X corresponds to the fake pairs with one SFD hit missing, discussed in previous paragraph.

[3] note that $2\epsilon_s(1-\epsilon_s) + (1-\epsilon_s)^2 = 0.19$ for $\epsilon_s = 0.90$ being the single plane MSGC/GEM efficiency, and that two planes are required in this case.

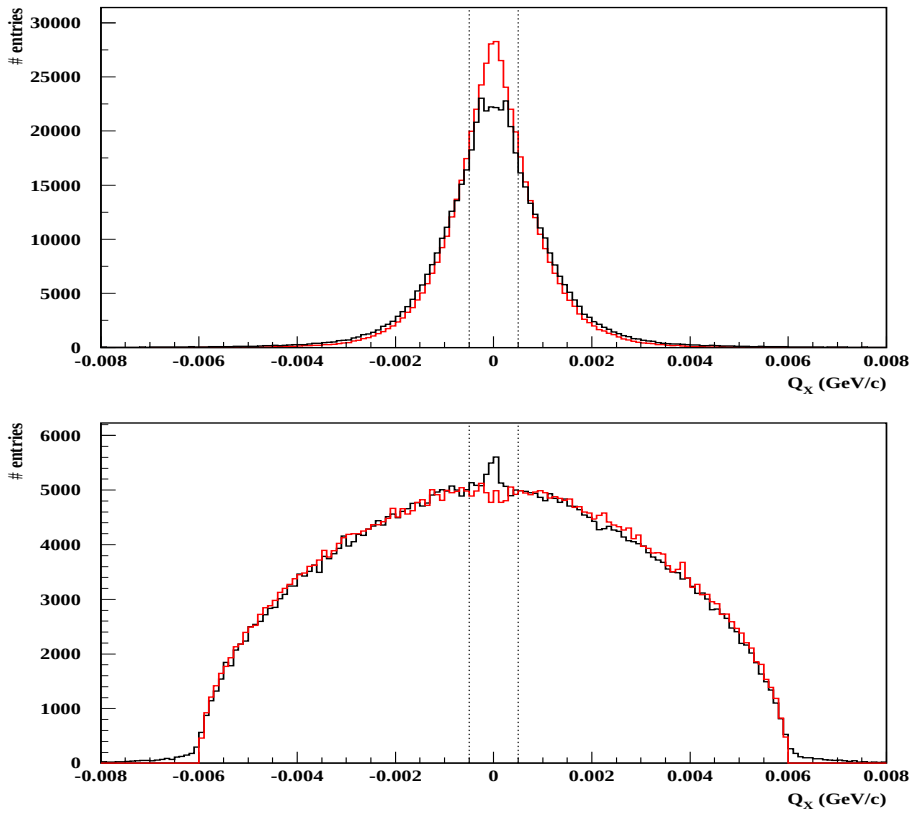

Figure 6.9: *Comparison between generated Q_X spectrum G_1 (red), and reconstructed spectrum R_1 (black) for atom pairs (top), and for Coulomb pairs (bottom). See the text for more detail.*

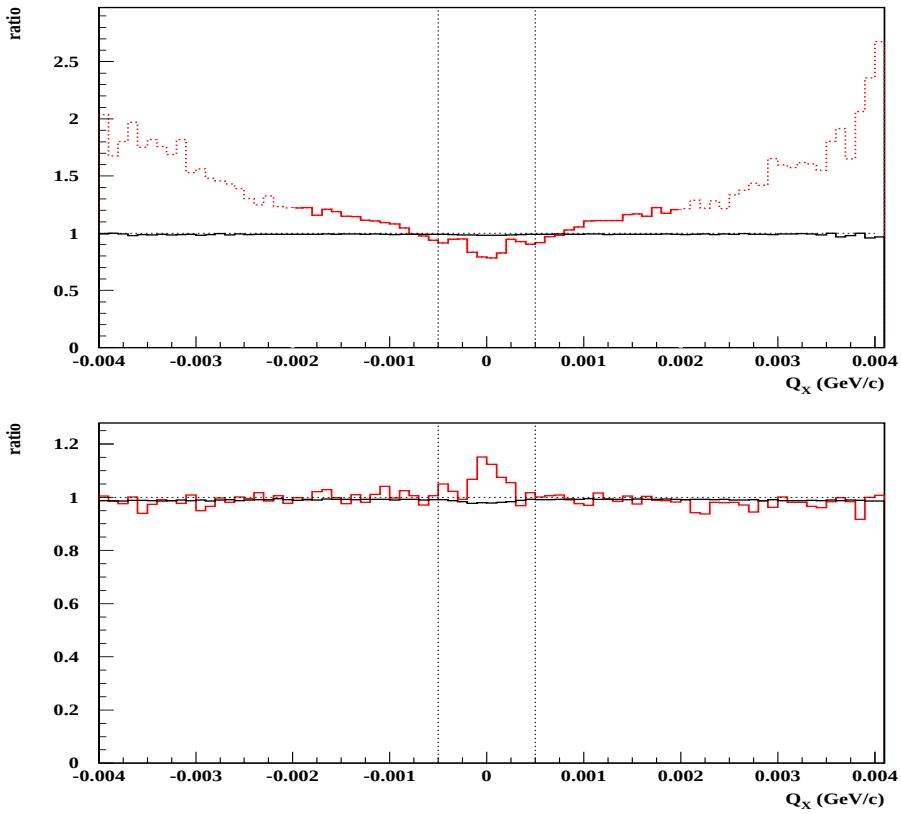

Figure 6.10: *Ratios G_1/G_0 (black) and R_1/G_1 (red) for the lines shown in figure 6.9 for Q_X of atom pairs (top). Corresponding ratios are also given for Coulomb pairs (bottom). See text for more details.*

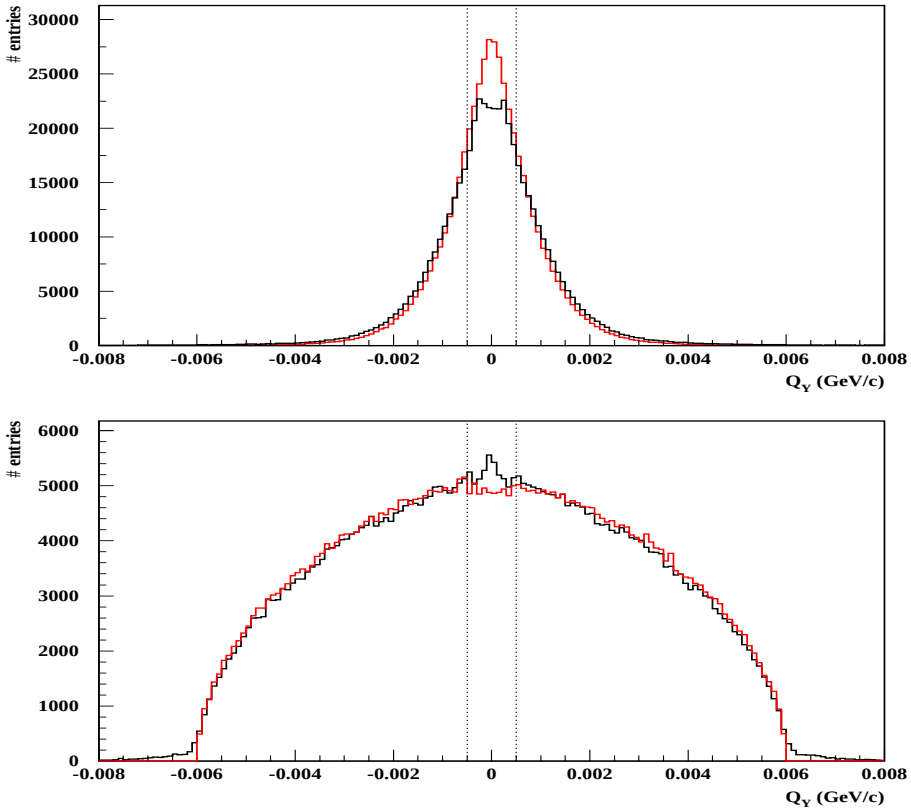

Figure 6.11: *Comparison between generated values G_1 (red), and reconstructed (R_1) values (black) of Q_Y for atoms pairs (top), and for Coulomb pairs (bottom). See the text for more detail.*

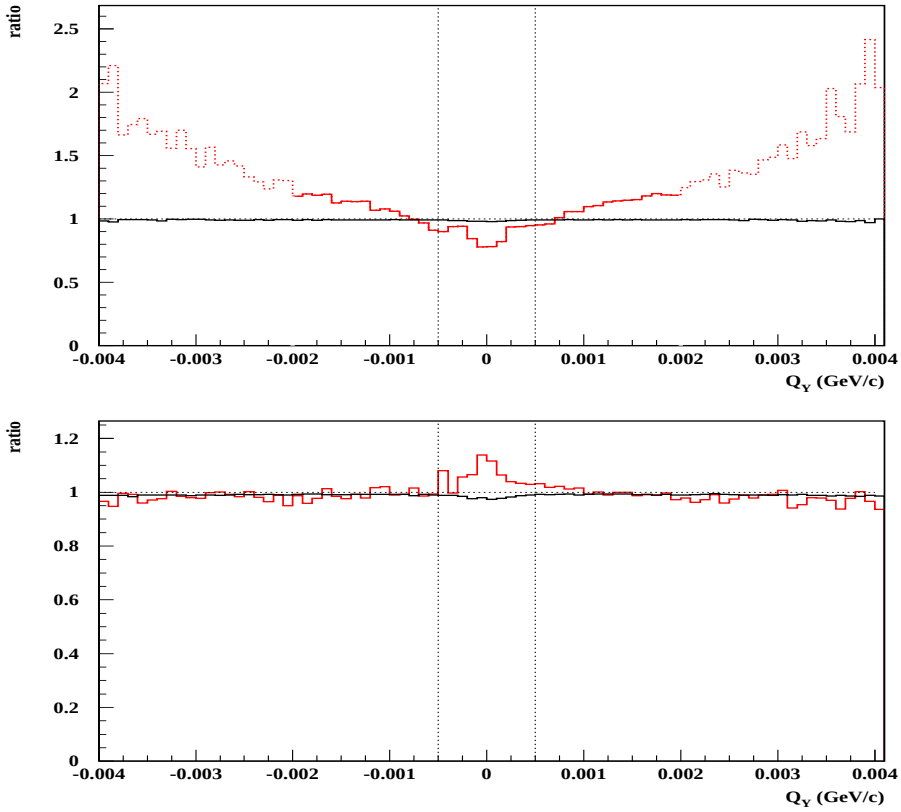

Figure 6.12: *Ratios G_1/G_0 (black) and R_1/G_1 (red) for the lines shown in figure 6.11 for Q_Y of atom pairs (top). Corresponding ratios are also given for Coulomb pairs (bottom). See text for more details.*

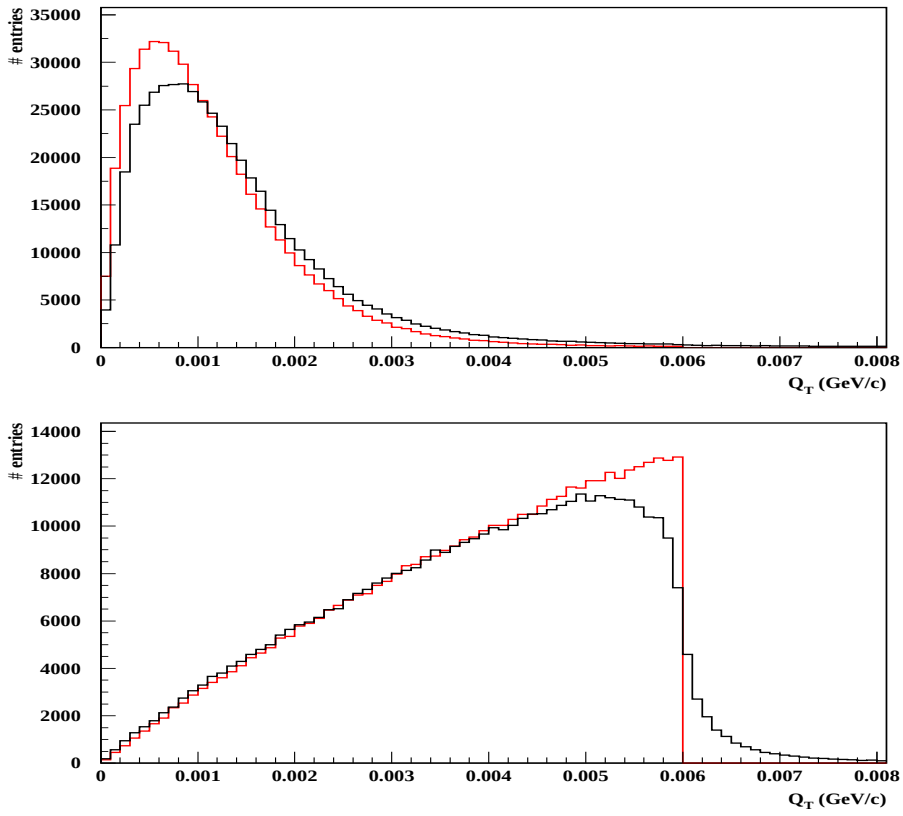

Figure 6.13: *Comparison between generated Q_T spectrum G_1 (red), and reconstructed spectrum R_1 (black) for atom pairs (top), and for Coulonb pairs (bottom). See the text for more detail.*

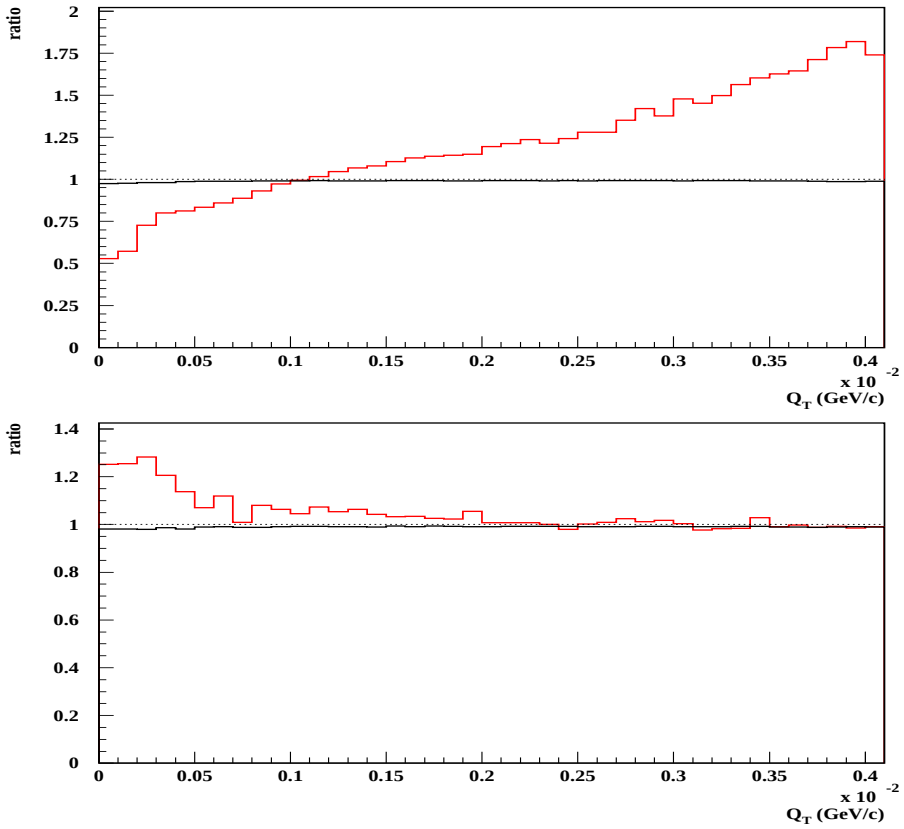

Figure 6.14: *Ratios G_1/G_0 (black) and R_1/G_1 (red) for the lines shown in figure 6.13 for Q_T of atom pairs (top). Corresponding ratios are also given for Coulomb pairs (bottom).*

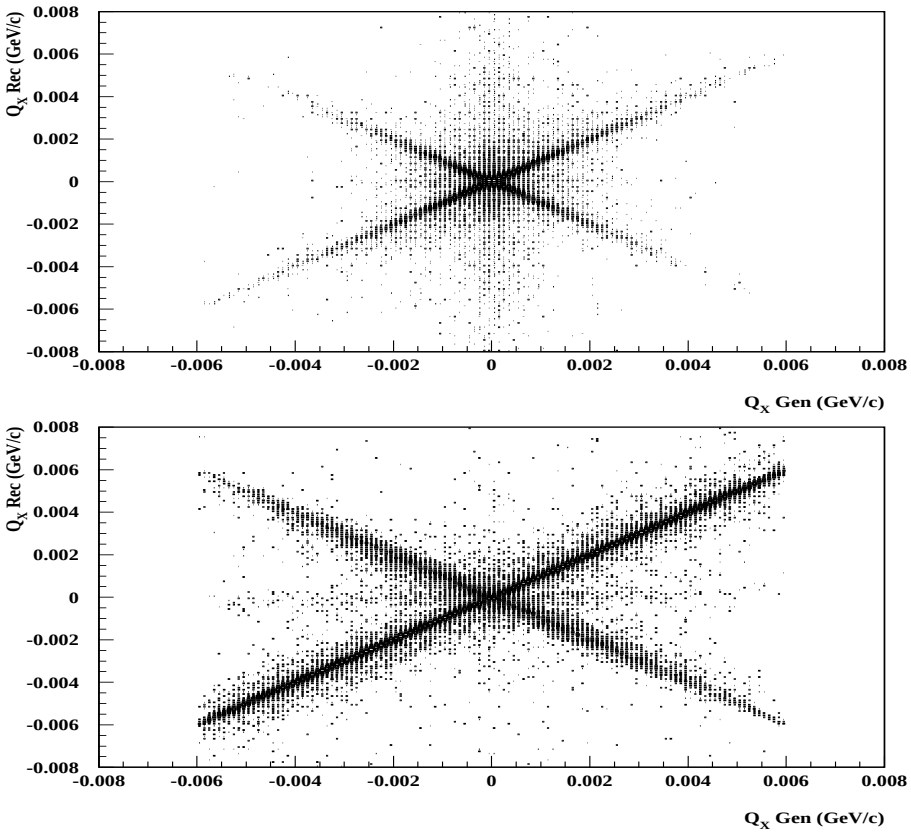

Figure 6.15: *Correlation between generated and reconstructed Q_X for atoms pairs (top) and Coulomb pairs (bottom).*

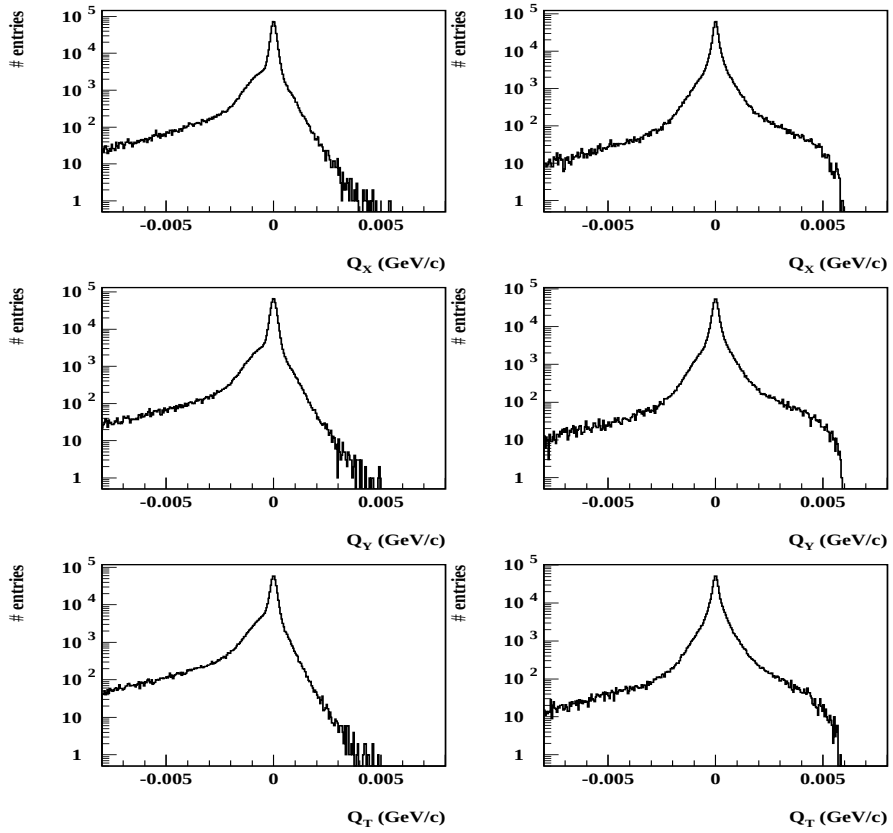

Figure 6.16: *Resolution defined as $|Q_i^{gen}| - |Q_i^{rec}|$ for $|Q_X|$ (top) , $|Q_Y|$ (center) and Q_T (bottom). Atoms pairs are shown at the left, and Coulomb pairs at the right hand side.*

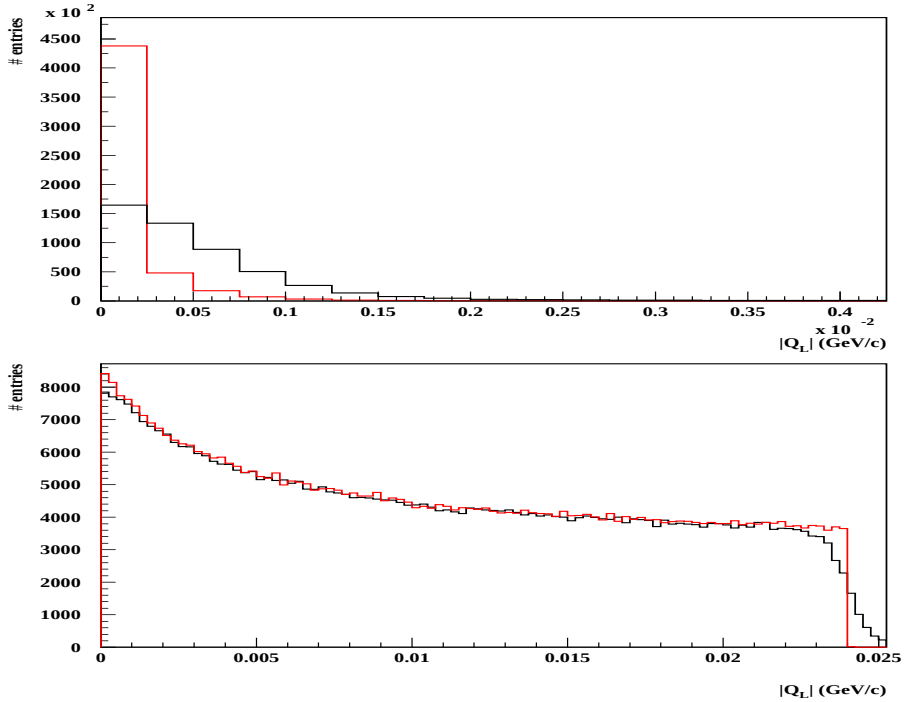

Figure 6.17: *Comparison between generated $|Q_L|$ spectrum G_1 (red), and reconstructed spectrum R_1 (black) for atom pairs (top), and for Coulomb pairs (bottom).*

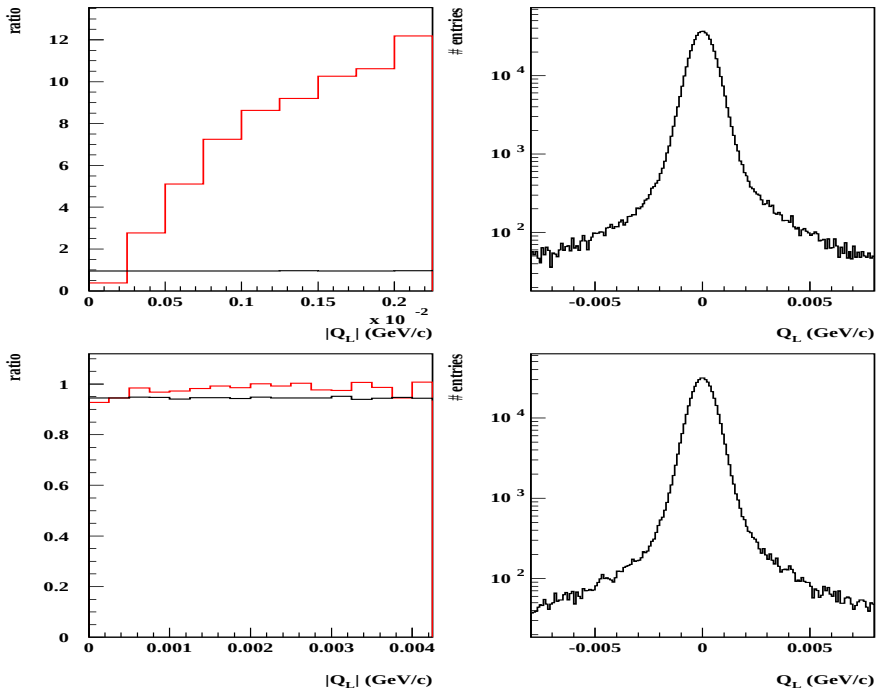

Figure 6.18: *Ratios G_1/G_0 (black) and R_1/G_1 (red) for the lines shown in figure 6.17 for $|Q_L|$ of atom pairs (top left). and for Coulomb pairs (bottom left). Resolution plots for Q_L are also shown at the right hand side.*

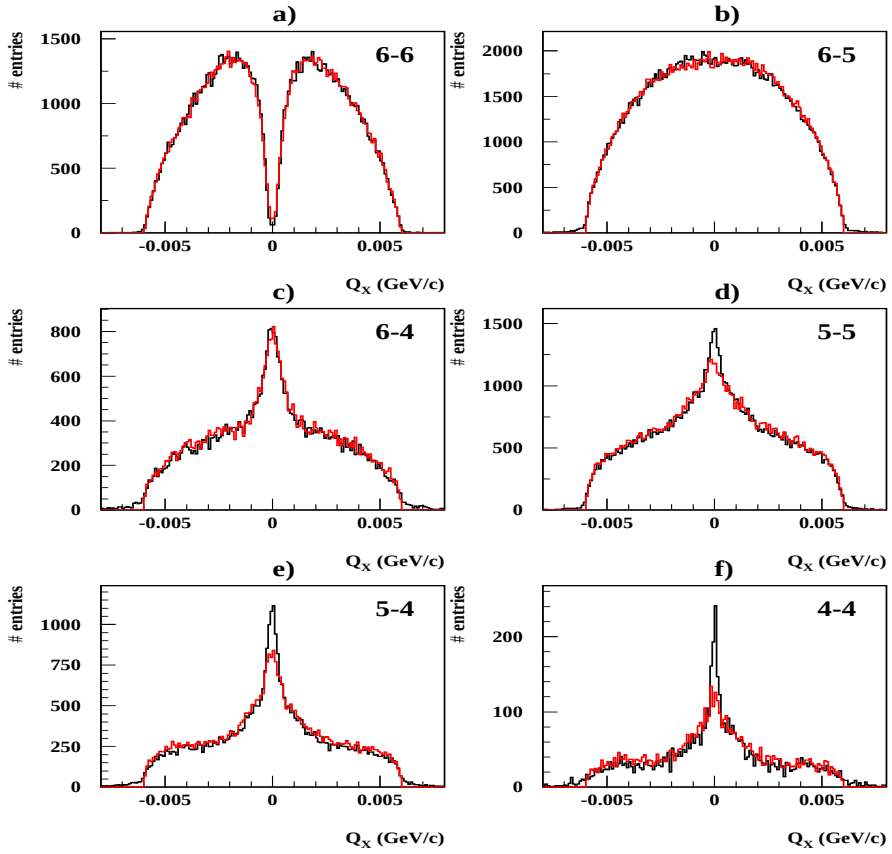

Figure 6.19: Q_X *spectrum of the reconstructed Coulomb pairs shown in figure 6.9 (bottom) separated into 6 categories according to the number of hits in each track, namely : 6-6 , 6-5 , 6-4 , 5-5 , 5-4 , 4-4.*

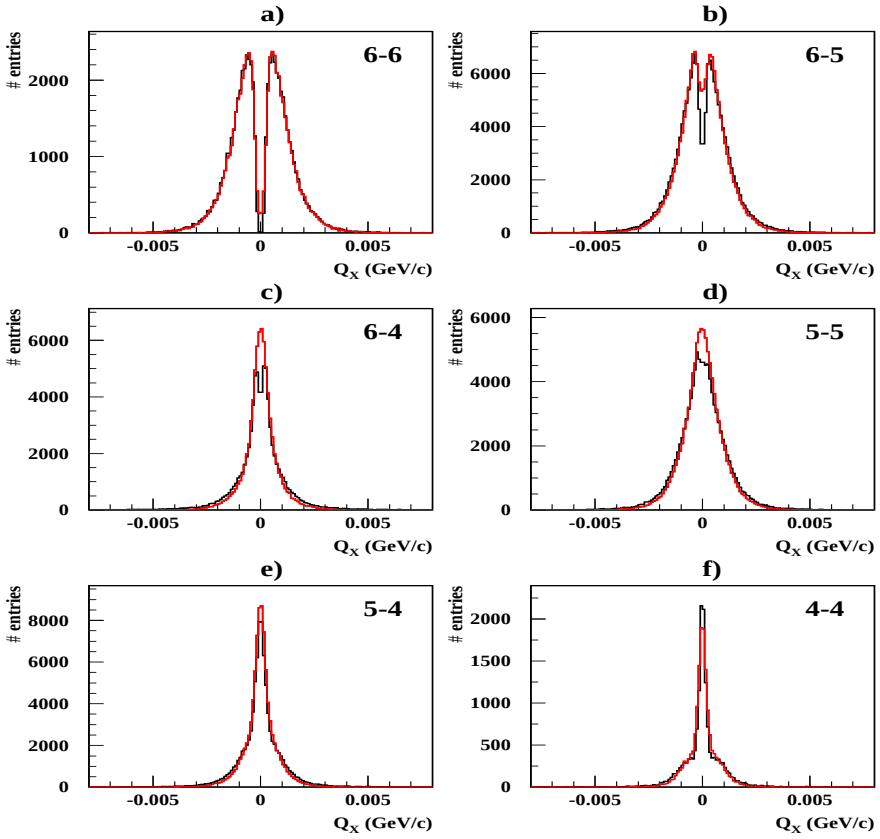

Figure 6.20: Q_X *spectrum of reconstructed atom pairs shown in figure 6.9 (top) , separated into 6 categories according to the number of hits in each track, namely : 6-6, 6-5 , 6-4 , 5-5 , 5-4 , and 4-4.*

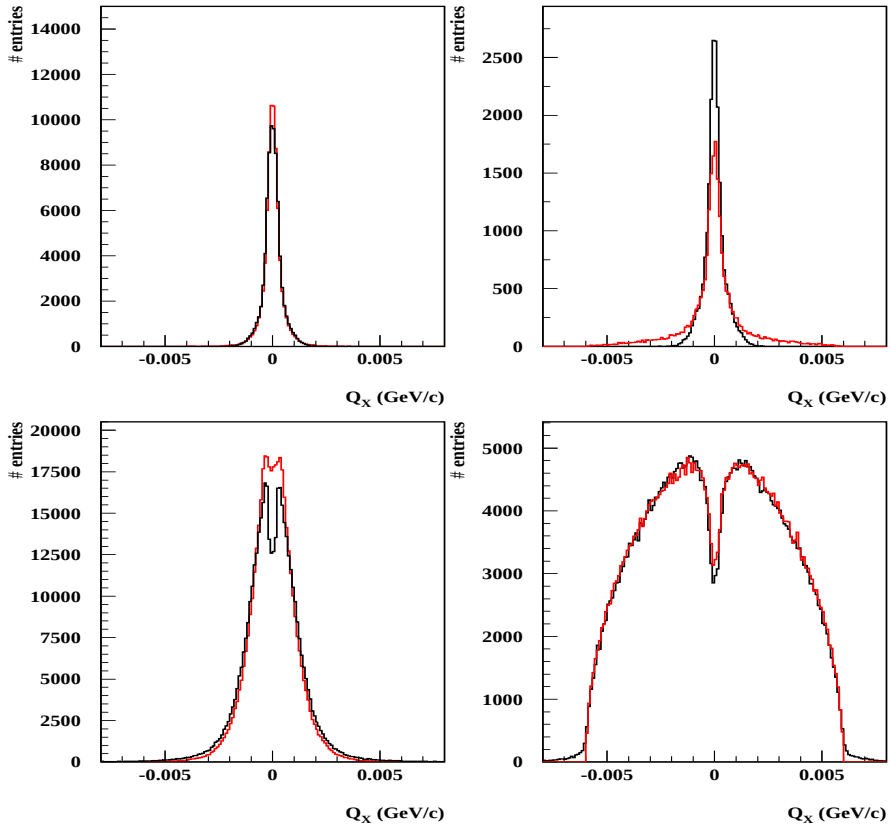

Figure 6.21: *Reconstructed Q_X (black) along with generated G_1 spectrum (red) for events with a single SFD hit shared by both tracks (top), and for the remainder (bottom). Left hand side for atom pairs, right for Coulomb pairs.*

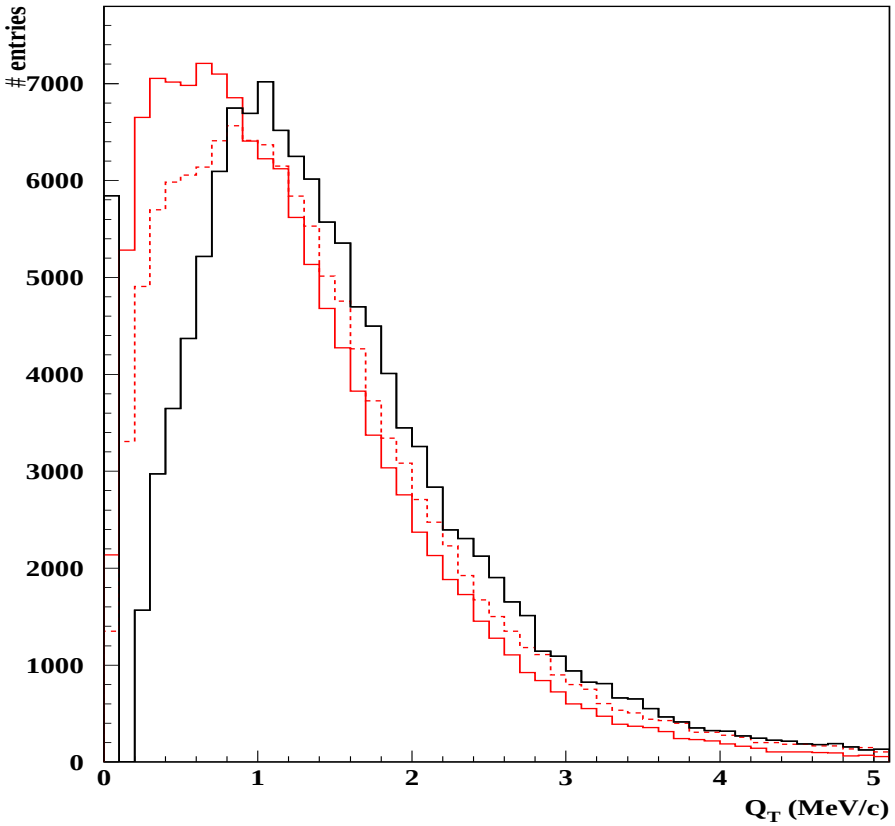

Figure 6.22: *Reconstructed Q_T spectrum for atom pairs when only SFD hits are used in the final vertex fit (black). Upstream tracking reconstruction is shown as dotted red line, and the true spectrum (G_1) is shown as a red line. The spike at zero corresponds to identical SFD hits.*

6.2.5 Conclusions

The effort made in achieving an accurate Monte Carlo simulation of upstream detectors response and background levels using real data has allowed us us to evaluate in detail the tracking method for DIRAC in this chapter. The tracking method provides excellent resolution and performance for indistinct reconstruction of atom pairs and Coulomb pairs, and it is well suited for accurate determination of pionium lifetime. Variation of detectors background and efficiencies within acceptable limits do not produce essential changes of the performance parameters analyzed.

The results can be summarised as follows:

- The tracking is efficient for atoms and Coulomb pairs (maximum 3% overall inefficiency) and the original $Q_{X,Y}$ and Q_T spectra are well reconstructed in shape.
- The overall acceptance for pionium pairs and for Coulomb pairs are equal to each other as function of Q_T.
- The two-track inefficiency for wide-angle pairs is small, thus making expected enhancement at very low Q_X and Q_Y nearly disappear.
- resolution tails in all relevant transverse and longitudinal quantities have been determined, and they are all small (largest 3% for Coulomb correlated pairs).
- Pionium signal reconstruction is, on the other hand, less prompt than the generator, due to a corresponding increase of the effect of detector backgrounds. Atom loss at $Q_T < 5\ MeV/c$ cut is however very small (1.80%).

Chapter 7

Experimental determination of momentum resolution using Lambda events

A method to determine the momentum resolution δp of DIRAC spectrometer using only experimental data is described in this chapter. The momentum dependence of $\delta p/p$ is parametrised with two coefficients, which are accurately determined for Ni 2001 data, using lambda events at low decay angle. As a result, a Monte Carlo simulation is constructed where resolution in longitudinal (Q_L) compoment of Q exactly matches the experimental data.

7.1 Single track momentum resolution

In the DIRAC experiment, the detection of pionium signal over the background Coulomb pairs relies directly on having a sufficiently good momentum resolution in the $\pi^+\pi^-$ center-of-mass frame , both in the longitudinal(Q_L) and transvers (Q_T) components. At very low pair opening angle θ, Q_L depends entirely on the magnitude of pion momenta (p) in the laboratory frame. At larger values of θ, an accurate measurement of Q_T relies on both θ and p resolution. Therefore resolution in p plays an essential role for atom pair detection. As a consequence of that, it needs to be known precisely in

order to perform an accurate convolution of the Coulomb correlation function with experimental resolution , whenever Monte Carlo simulation is used for the analysis of pionium signal.

Because of the low Q acceptance of the experiment trigger, we cannot easily use meson resonances as calibration tools, and the best option has been to setup a simple lambda trigger. This is achieved by using an extra vertical hodoscope slab close to the beam, in order to catch the fast proton track [22]. This trigger has a more detailed description in the next section.

The idea is to use the analysis of lambda mass, at low opening angles, to perform a detailed quantitative assesment of momentum resolution of individual charged tracks, as function of track momentum. This resolution can be compared with the one obtained from $\pi^+\pi^-$ Monte Carlo, in order to make sure they are in perfect agreement.

Lambda mass M_Λ is determined exactly from measured decay π^- (x) and proton (y) momenta and opening angle θ, as :

$$M_\Lambda^2 = m_p^2 + m_\pi^2 + 2\sqrt{m_\pi^2 + x^2}\sqrt{m_p^2 + y^2} - 2xy\cos\theta \qquad (7.1)$$

By squaring both sides of this equation, one realises it represents a rotated hyperbola with a physical branch in the positive quadrant of (x, y) plane :

$$m_p^2 x^2 + m_\pi^2 y^2 + x^2 y^2 sin^2\theta - \Delta^2 xycos\theta = K^2 \qquad (7.2)$$

where $\Delta^2 = M_\Lambda^2 - m_p^2 - m_\pi^2$ and $K^2 = \left(\Delta^2/2\right)^2 - m_p^2 m_\pi^2$. For each positive value of π^- momentum x, there are two positive solutions for proton momentum y.

It is easy to show from the previous expressions that, in the low-angle approximation ($\theta^2/2 \ll 1$), the lambda mass error δM_Λ is given by:

$$M_\Lambda{}^2(\delta M_\Lambda)^2 = \left(\frac{x}{x_0} - \frac{y}{y_0}\right)^2 \left(y_0^2(\delta x)^2 + x_0^2(\delta y)^2\right) \qquad (7.3)$$

where $x_0 = \sqrt{m_\pi^2 + x^2}$ and $y_0 = \sqrt{m_p^2 + y^2}$. δx and δy are the π^- and proton momentum errors, respectively. The lowest order finite angle correction to this expression arises from a term $+x^2y^2\theta^2(\delta\theta)^2$. In order to make sure that (7.3) is exact to the percent level, a suitable upper cut on

Q_T (actually a θ cut) must be done on lambda selection. Effectively this is achieved by $Q_T < 20MeV$, as we shall see later. As expected, formula (7.3) depends only on the magnitude of lab-frame momenta x and y.

7.2 Λ trigger.

Let us start with a deeper explanation of the lambda trigger available in DIRAC.

The barion Λ is one of the products that overcomes from the interaction between proton spill and target nucleus. This resonance is part of what we call in DIRAC long lived sources, when we refer to the creation ways of pion accidental pairs. From PDG we get a mass of $1115.683 \pm 0.006\ MeV/c^2$ [72], decaying with ratio 63,9% into

$$\Lambda \longrightarrow p + \pi^- \tag{7.4}$$

A diagram of lambda trigger, which is part of T1 trigger described in chapter 2, is displayed in Fig. 7.1, and it can be expressed as:

(VH_1[17] HH_1 $\overline{CH_1}$ PSH_1) $\rightarrow p$
(VH_2[1-16] HH_2 $\overline{CH_2}$ PSH_2) $\rightarrow \pi$

This trigger is very similar to the physics pion trigger in its basic version, but with additional restriction in the use of vertical hodoscopes. Only slab 17 is used in the positive arm, meanwhile the first 16 slabs (of 18) are used in the negative one. This tries to take advantage of the kinematics of lambda decays, which gives a very different horizontal boost for proton and negative pion.

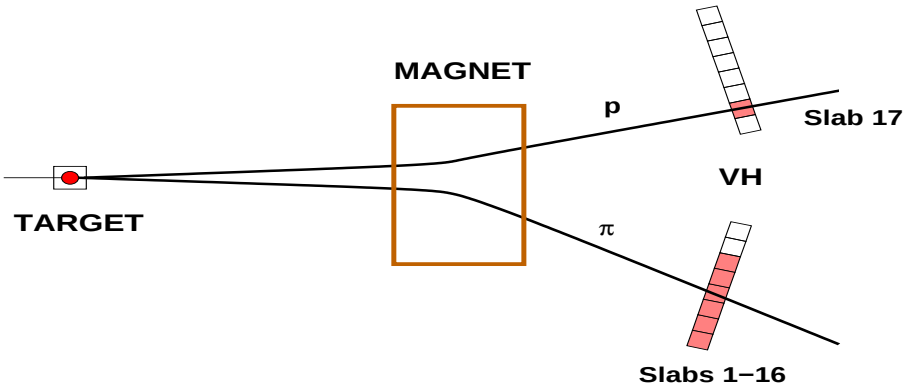

Figure 7.1: *Lambda trigger diagram. Different slabs are used in the positive and negative arm of Vertical Hodoscopes due to the kinematics of Λ decay.*

7.3 Maximun likelyhood method description.

We assume that momentum error δp (for both pion and proton tracks) arises from the quadrature of two components, according to expression:

$$(\delta p)^2 = (Ap)^2 + (Bp^2)^2 \tag{7.5}$$

the first term, proportional to p, receives contribution from the average material thicknesses of detector elements upstream and downstream the magnet. The second term, proportional to p^2, depends on intrinsic tracking detector resolutions at both sides of the dipole (drift chambers, MSGC/GEM and SFD). The previous momentum scaling arises from the assumption that multiple scattering error scales as $1/p$, whereas intrinsic detector resolutions are assumed to be momentum independent.

As explained before, because of the kinematics of lambda decays, the negative pion acquires a momentum lower than the average $\pi^+\pi^-$ prompt tracks in DIRAC physics triggers, whereas the proton momentum is higher than this average, as it can be appreciated in Fig. 7.2. This is the ideal situation to perform a momentum analysis of the spectrometer resolution, specially if we use low angle pairs, with topology as close as possible to that

of the Coulomb $\pi^+\pi^-$ pairs.

The method used is then a maximum likelihood fit to expression (7.3), using a sample of lambda triggers which contains not only the signal, but also the non-resonant background, due to trigger noise. The description of the latter by the likelyhood function is important if we want to have a precise determination of the A and B coefficients in (7.5).

For each event i, a two-dimensional likelyhood function was defined as a function of lambda mass M_i (under the $p\pi^-$ hypothesis) and the magnitude p_i of total lab-frame momentum of the pair. It reads as follows:

$$\mathcal{L}_i = \alpha \frac{\mathcal{P}_N(p_i)}{S_N}\frac{G(M_i)}{S_G} + (1-\alpha)\frac{\mathcal{P}_N(p_i)}{S_N}\frac{\mathcal{P}_B(p_i, M_i)}{S_B} \tag{7.6}$$

where $\mathcal{P}_N(p) = 1 + a_1 p + a_2 p^2 + \ldots$ is an Nth order polynomial in p and $G(M)$ is a gaussian function describing the resonance:

$$G(M_i) = \exp\left(-\frac{(M_i - M_\Lambda)^2}{2(\delta M_i(A,B))^2}\right) \tag{7.7}$$

where the error $\delta M_i(A,B)$ is given by expression (7.3) evaluated at π^- (x_i) and proton (y_i) momenta of event i. The momentum error δp is given by (7.5) as function of momentum, with identical A and B parameters for both particle types. The polynomial $\mathcal{P}_B(p, M)$ describes a linear mass dependence of the background: $\mathcal{P}_B(p, M) = 1 + b_1 M + b_2 p$. The corresponding normalisation integrals S_N,S_G and S_B must be calculated for each parameter choice, so that the likelyhood function is normalised to unity in the domain $(p_1, p_2) \times (M_1, M_2)$, where $p_{1,2}$ are the lower and upper total momentum cuts (similarly $M_{1,2}$ for the invariant mass).

The maximum likelyhood parameters are found to minimise the function:

$$-\ln\mathcal{L} = -\sum_{i=1}^{N} \ln\mathcal{L}_i(A, B, M_\Lambda, \alpha, a_k, b_l) \tag{7.8}$$

where N stands for the number of lambda triggers selected for the fit, and $\mathcal{L}_i$ is the likelyhood function evaluated for event i characterised by measured values x_i,y_i,M_i and p_i.

The overall likelyhood $\mathcal{L}$ for N lambda events significantly increases when each measured proton momentum y_i is replaced, in expression (7.3) for δM_i, by one of the hyperbolic solutions of equation (7.2), corresponding to the measured π^- momentum x_i. This is equivalent to take advantage of the lambda mass constraint in momentum scaling of δp (7.5), together with the fact that π^- momentum has allways the smallest error.

A straightforward procedure is to determine first the a_k and b_l coefficients of the polynomials, by performing a fit to the background only. Once these parameters are fixed, M_Λ,α,A and B can be left free in the final fit. All minimisations were performed by MINUIT program [73].

7.4 Selection of lambda events

We have applied the analysis described in the previous sections to the DIRAC 2001 Ni target data sample, Lambda triggers are routinely taken at constant fraction of total spill rate during normal physics runs, and they have been subject to the standard calibrations for 2001 data periods. Reconstruction was done as explained for pion pairs in chapter 4.

The upstream track pattern recognition was run with the standard parameters used for $\pi^+\pi^-$ prompt pair selection, which implies that only tracks pointing to the beam intersection with the target plane within 3 σ will be reconstructed, σ being track resolution in the transvers (XY) plane. No attempt has been made to enlarge these pattern recognition windows in the present analysis. Admittedly, this causes a bias in lambda selection which has the general trend to enhance the signal at short decay path. We have prefered this option in order to keep the tracking performance as close as possible to that with $\pi^+\pi^-$ pairs, which we want to evaluate.

Aditional constraints for lambda events are required, namely:

- Time difference $t_2 - t_1$ between positive and negative tracks in vertical hodoscope TDCs is restricted to the interval $0 < t_2 - t_1 < 1.3\ ns$.

- A decay vertex is determined by finding the point of closest approach between both tracks, and the probability of track intersection at that

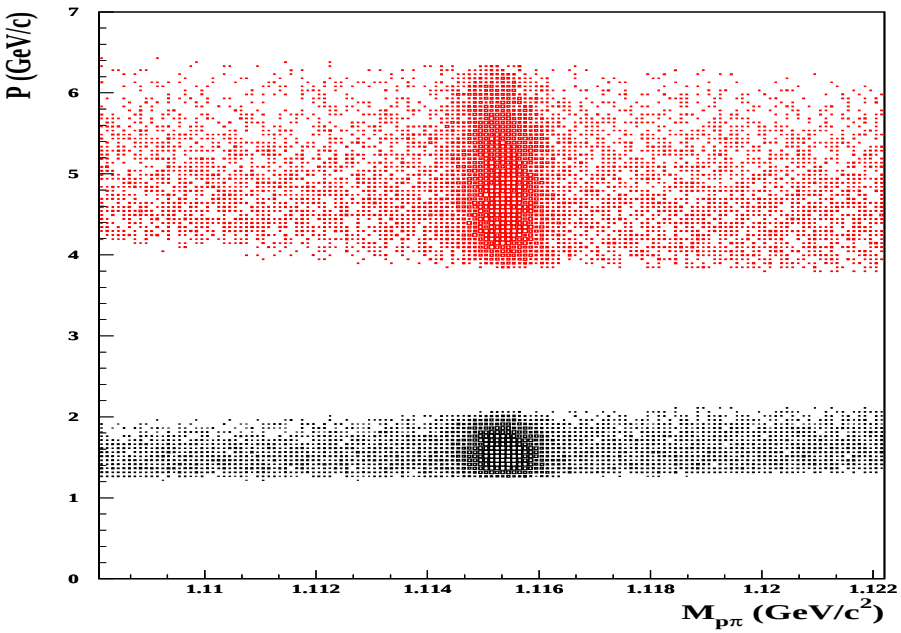

Figure 7.2: *Scatter plot representing the measured invariant mass (under $p\pi^-$ hypothesis) versus positive (red colour) and negative (black) track momenta, for lambda triggers of 2001 run. A clear momentum gap can be appreciated, due to lambda decay kinematics and vertical hodoscope time cuts.*

particular point $(\mathcal{P}_v)$ is then calculated. Events with $(\mathcal{P}_v) > 1\%$ are selected.

- Also a joint track probability $(\mathcal{P}_t)$ is defined as the one corresponding to $\chi^2 = \chi^2_1 + \chi^2_2$, where $\chi^2_{1,2}$ are the fit χ^2 for each individual track. $\mathcal{P}_t$ are required to be larger than 1% too.

The invariant mass is calculated according to expression 7.1, taking into account the parallax error in θ due to displaced vertex.

In Fig. 7.2 we see a scatter plot of individual track momenta (π^- and proton) versus reconstructed invariant mass, showing the momentum range covered by this analysis. The mass projection from previous plot is better

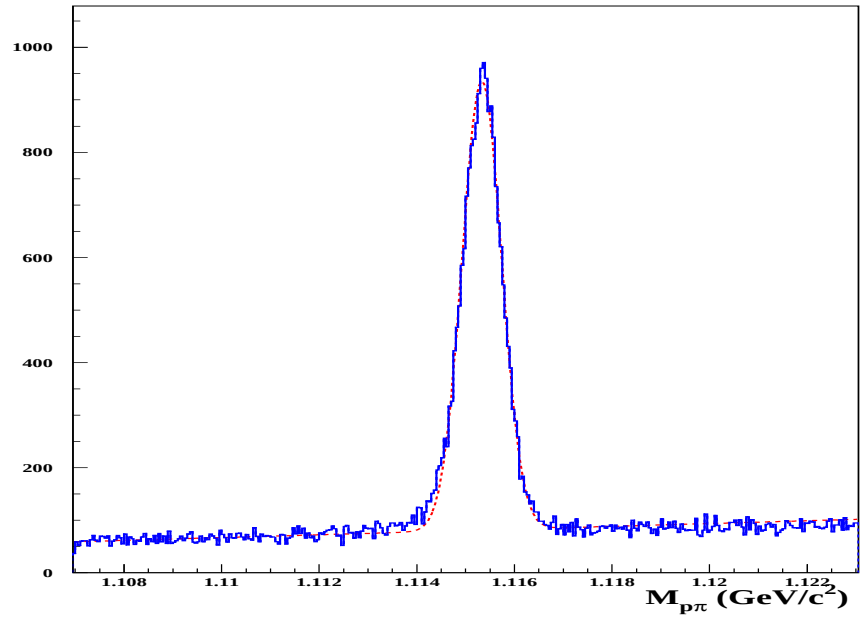

Figure 7.3: *Invariant mass spectrum obtained from the projection of scatter plot in figure 7.2. A gaussian fit with linear background is also shown for reference, with* $\sigma = 0.395 MeV/c^2$, *and* $M_{p\pi} = 1115.4 MeV/c^2$.

appreciated in Fig. 7.3, from where we extract an average mass resolution of 0.395 MeV/c^2.

In Fig. 7.4 selected lambda events are mapped onto the (Q_L,Q_T) plane. As expected, they lie on a circular coronna whose width is determined by our mass resolution. It can be appreciated that a cut $Q_T < 20\ MeV$ is enough to ensure that mass resolution is determined by Q_L resolution only, and therefore relation (7.3) is fulfilled. In Fig. 7.5 we show the lambda momentum and opening angle distributions.

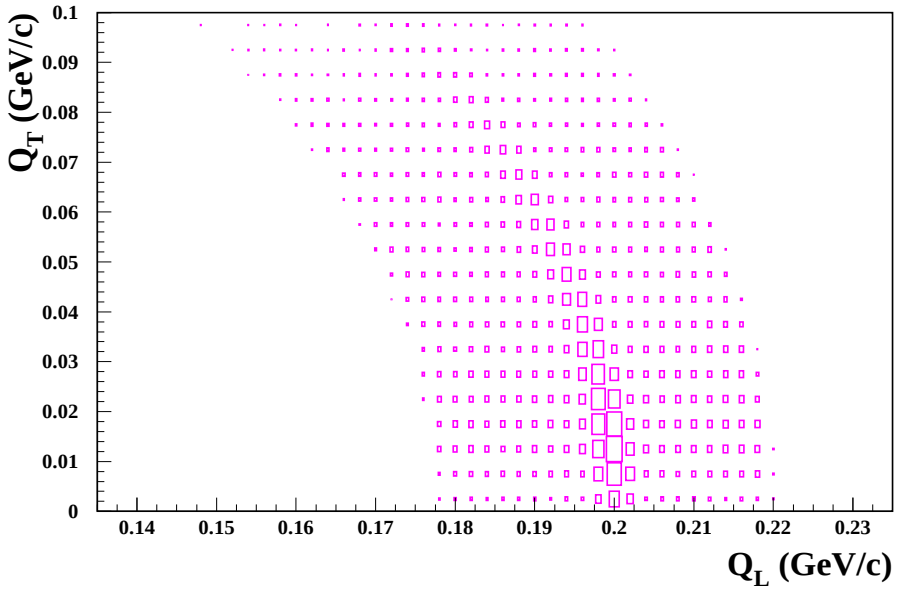

Figure 7.4: *Longitudinal (Q_L) versus transvers (Q_T) momentum in the lambda center-of-mass frame, with respect to its direction of flight. Lorentz transformation is done under $p\pi^-$ hypothesis. A mass cut $1114.0 < M_{p\pi}(MeV/c^2) < 1116.5$ has been applied.*

7.5 Results and comparison with Monte Carlo.

The maximun likelyhood fit procedure described before was applied for Ni 2001 data, and table 7.1 gives the output parameters found. Errors are given by variation of $-ln\mathcal{L}$ by 0.5 units, on positive and negative side of the minimum. We can summarise the result by plotting the relative momentum error $\delta p/p$ as function of momentum, according to the expression $\delta p/p = \sqrt{A^2 + B^2p^2}$, with A and B as determined by the fit. This is shown by the red line in Fig. 7.6, where a yellow coloured band represents the $\pm 1\sigma$ error variation taken simultaneously in both parameters. The fact that $\delta p/p$ is found to be nearly constant indicates that spectrometer resolution

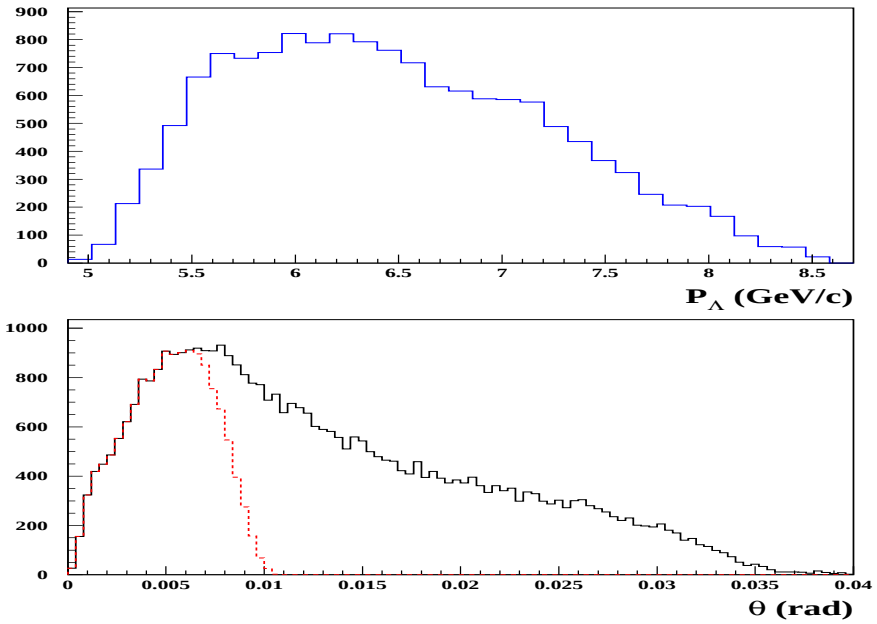

Figure 7.5: *For lambda events defined by the mass cut used in figure 7.2, (a) shows the magnitude of vector sum of proton and π^- momenta for lambda events, and (b) the opening angle θ between the two tracks. The dotted red line shows the effect of the $Q_T > 20MeV/c$ cut.*

is dominated by multiple scattering, rather than by intrinsic detector resolution. At $p = 2.5GeV/c$, the relative momentum error is 0.281 % , for the overall 2001 data taking period analyzed. The B parameter is small, $2.0^{+0.3}_{-0.4} \times 10^{-4}GeV^{-1}$, but significantly away from zero. Introduction of the finite angle correction term $+x^2y^2\theta^2(\delta\theta)^2$ (see first section of this chapter) with $\delta\theta = 5 \times 10^{-4}$ estimated from Monte Carlo, resulted in a negligible change in the previous parameter values and likelyhood function.

The fit results can be visualised using a weighing procedure according to the $\mathcal{L}$ function at maximum, applied to random values in the domain $(p_1, p_2) \times (M_1, M_2)$. This is represented in Fig. 7.7, where the mass spectrum is shown in four slices of lambda momentum, with a superimposed

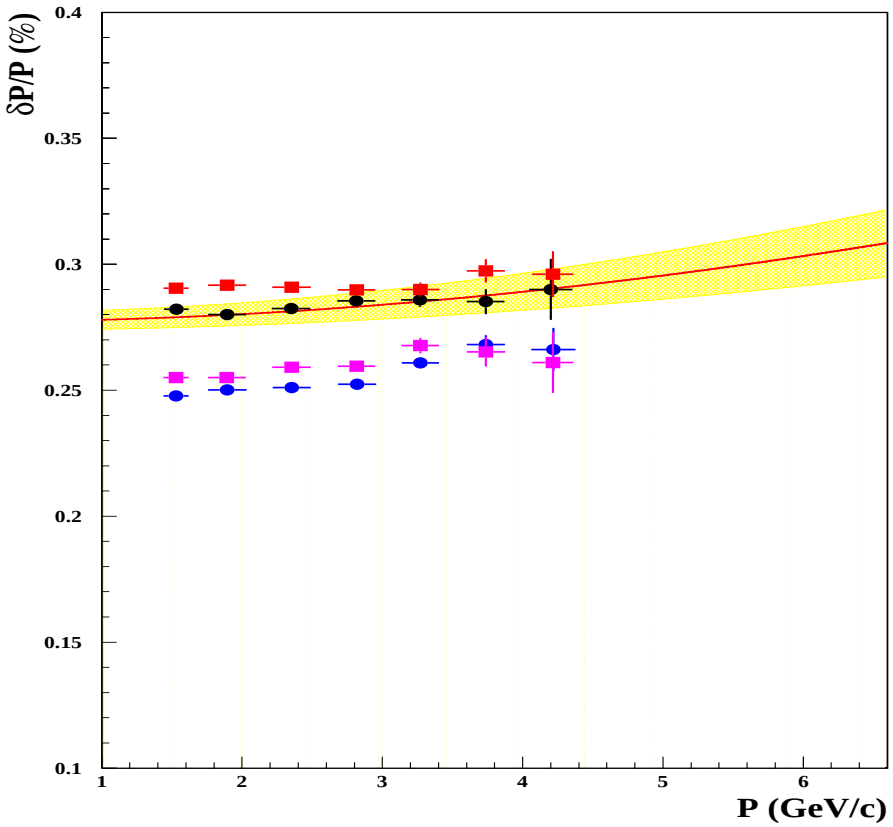

Figure 7.6: *Relative momentum error $\delta p/p$ as function of track momentum. The red continuous line represents the parametrisation $\sqrt{A^2 + B^2 p^2}$ fitted to experimental lambda data. The yelow band represents $\pm 1\sigma$ variation of the parameters. Blue dots indicate resolution of standard $\pi^+\pi^-$ Monte Carlo, according to input generator information. Purple squares correspond to a Monte Carlo simulation with upstream scattering angle increased 15%, and black dots to Monte Carlo where multiple scattering angle has been increased in downstream detectors (10%). Red rectangles show the same option as before for upstream arm, but 18% multiple scaterring increase downstream.*

Table 7.1: *Parameters obtained for the maximum likelyhood fit to the experimental lambda sample of 2001, as defined in the text. Quoted errors correspond to variation of 0.5 units of the likelyhood function.*

A	$(0.277 \pm 0.003) \times 10^{-2}$
B	$0.205^{+0.033}_{-0.038} \times 10^{-3}\ GeV^{-1}$
M_Λ	$1115.410 \pm 0.005\ MeV/c^2$
α	0.529 ± 0.005
b_1	12.8 ± 1.9
b_2	-0.047 ± 0.009

a_1	-66.014 ± 0.048
a_2	36.205 ± 0.007
a_3	-7.3399 ± 0.0009
a_4	0.65470 ± 0.00002
a_5	-0.02176 ± 0.00001

coloured line representing the fit results. Note the fit parameters are unique, in particular the mass, as given by table 7.1. The fit projection onto the p spectrum is shown in Fig. 7.8. The fit quality appears to be good in both projections.

Now we can compare the previous results with Monte Carlo data [74]. In Monte Carlo, the original track momentum p_g [65] is of course known "a priori" from the generator, therefore by performing the ARIANE reconstruction we can determine $\delta p/p$ as function of p for individual tracks. This is done by means of a gaussian fit to the distribution of observed differences of inverse momenta $1/p - 1/p_g$. There are two possibilities open, as far as the generator is concerned:

- to use a lambda production Monte Carlo
- a standard $\pi^+\pi^-$ generator with Coulomb correlated pairs

Within the first case, we still have two different ways to determine momentum resolution, namely:

a) to proceed as explained before, using knowledge of original track momentum

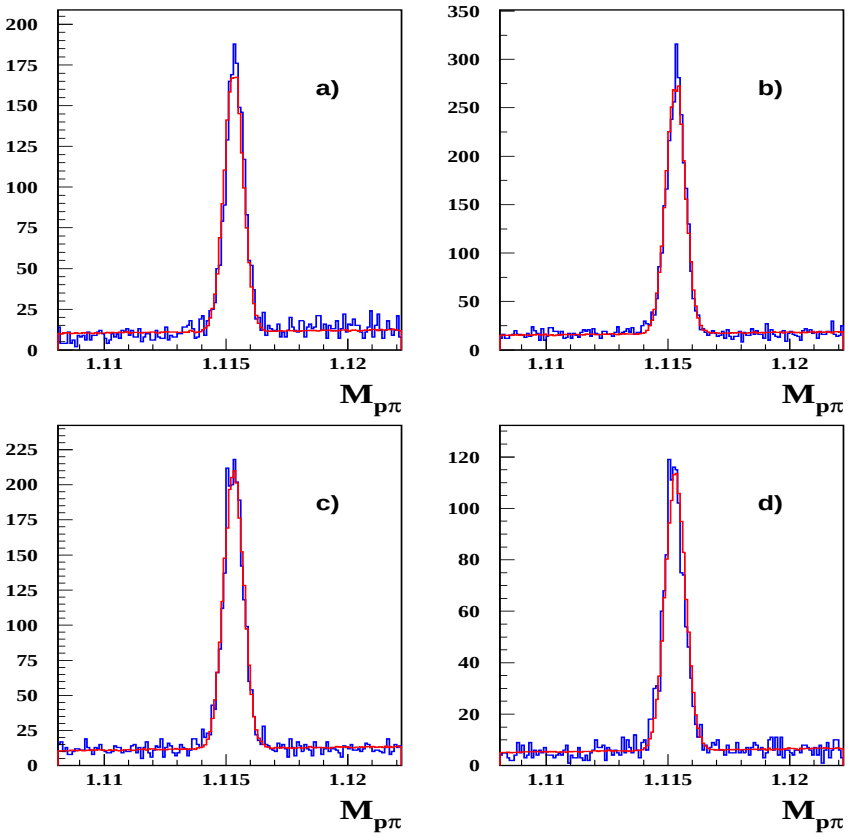

Figure 7.7: *Visualisation of maximum likekyhood fit quality. Invariant mass spectra are shown in four slices of lambda momentum, namely a)* $5 < p(GeV) < 5.75$, *b)* $5.75 < p(GeV) < 6.5$, *c)* $6.5 < p(GeV) < 7.25$, *d)* $7.25 < p(GeV) < 8$. *The fit results, with parameters given in table 2, are indicated by the red coloured line.*

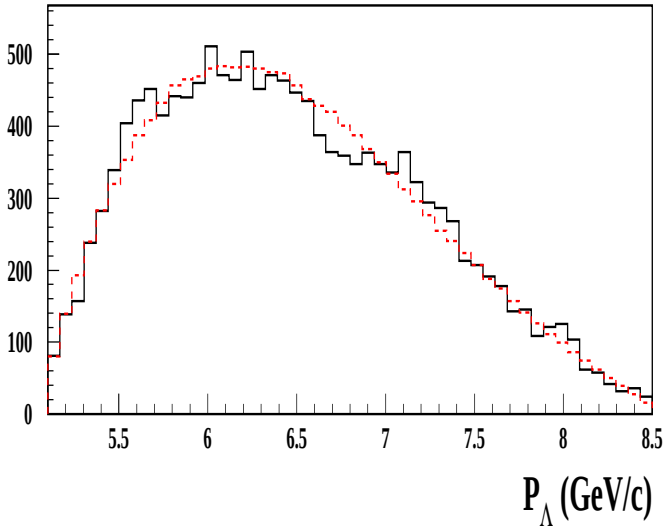

Figure 7.8: *Visualisation of maximum likekyhood fit quality, projected into the spectrum of total momentum p. Coloured line is constructed according to parameters in table 7.1.*

b) to treat the lambda Monte Carlo data as if they were real events, and apply to them the maximum likelyhood analysis described in section 4. Null background ($\alpha = 1$) should be assumed in this case.

A detailed comparison between methods a) and b) above provides an important consistency check for the low decay angle method described in section 3, and approximation made in section 1. The results should coincide. A confirmation that this indeed happens is given in Fig. 7.9.

Now a comparison between the resolution obtained with $\pi^+\pi^-$ Monte Carlo and the one from lambda method (b) above, tells us whether the hypothesis that the proton in lambda decay behaves like a pion with identical momentum is a good approximation or not, in terms of momentum reso-

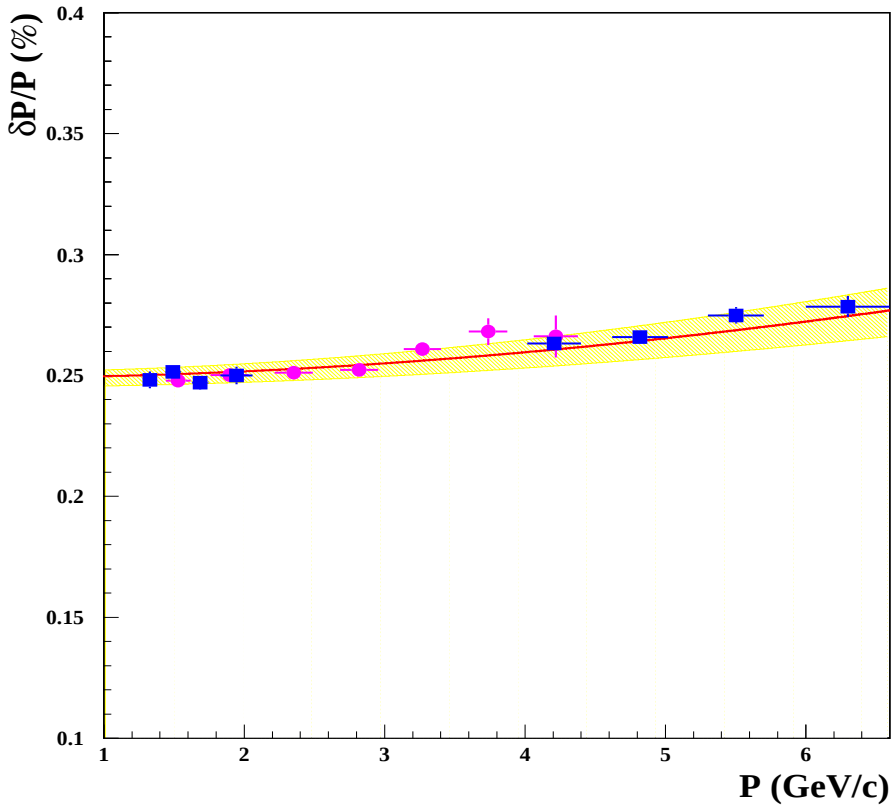

Figure 7.9: *Relative momentum error $\delta p/p$ as function of track momentum. The red continuous line represents the parametrisation $\sqrt{A^2 + B^2 p^2}$, with A and B determined from a maximum likelyhood fit to lambda Monte Carlo. The yellow band represents $\pm 1\sigma$ simultaneous variation of the parameters. Blue squares indicate Monte Carlo resolution determined from the generator input information. Purple dots indicate resolution of standard $\pi^+\pi^-$ Coulomb pairs Monte Carlo.*

lution. The results from $\pi^+\pi^-$ have been overlayed to the lambda decay ones in Fig. 7.9 with purple coloured dots. We can see that they are well compatible, within errors.

Needless to say that all of the above comparisons require the Monte Carlo simulations to be performed at exactly the same conditions of material thicknesses and detector resolutions, in order to make sense. The standard materials file was used in all cases, with default detector resolution parameters.

Once the previous cross-checks have been made, we can turn back to the main objective, namely to find out whether the momentum resolution in the $\pi^+\pi^-$ Coulomb correlated Monte Carlo is correctly described or not. In other words, we want to determine accurately what changes need to be made to the standard Monte Carlo in order to achieve a perfect description of momentum resolution, and at the same time of vertex resolution according to the discussion made. Only then we can fully trust the Monte Carlo as normalisation reference for the Coulomb pair background, in our search for pionium breakup signal.

In Fig. 7.6 we show again the curve of $\delta p/p$ determined from the data (red line), along with the resolution obtained from $\pi^+\pi^-$ Monte Carlo for three different options, namely:

a) the standard version with default values of material budget and detector resolution parameters (blue).

b) An improved version with upstream matter increased 15% [62].

c) the upstream part as before, but downstream multiple scattering increased by 10% (black), with standard drift chamber resolution.

7.6 Conclusions

DIRAC spectrometer, by means of its upstream detector arm, provides a precise and reliable instrument for analysis of pionium breakup signal. Momentum resolution is analyzed in detail using experimental data from 2001 run. These results are used to constrain sensitive parameters of the Monte

Carlo simulation, like material budget and intrinsic detector resolutions, for downstream part. A final Monte Carlo simulation is found which exactly matches the experimental data. Momentum resolution in DIRAC is found to be accurately described by a parametrisation $(\delta p/p)^2 = A^2 + B^2 p^2$ with $A = 0.277 \pm 0.003$ % and $B = (2.0^{+0.3}_{-0.4}) \times 10^{-4} GeV^{-1}$.

Chapter 8

Analysis of (Q_L, Q_T) spectrum

Below we are going to describe the extraction of pionium signal and the determination of the breakup probability. Events are selected from available data to take part of the final lifetime analysis before applying tracking procedure.

A fundamental task is going to be done by accidental pairs, which will be used in the analysis to perform trigger acceptance corrections to Monte Carlo Q_L spectrum.

A 2-dimensional fit procedure using the Monte Carlo distributions previously presented is explained, from which we obtain the number of atomic and Coulomb correlated pairs. The measured breakup probability is obtained with the relation between this two quantities using the concept of K-factor.

8.1 Data selection

The analysis presented in this study has used the standard pre-selection procedure described in reference [69], for 2001 Ni target events before applying the previously described track reconstruction.

8.1.1 Pre-selected events

In a level-zero processing, files of experimental data sample are significantly reduced by means of a pre-selection job. The main features of this work can be summarized as follows:

- The presence of at least 1 and maximun of 2 tracks in the Drift Chambers is required.
- For these tracks a spatial (momentum dependent) and time window over their extrapolation to SFD is opened and events with more than 1 hit (up to 4) in these windows are selected.
- In the same way a selection is made by requiring a spatial and probabilistic tolerance over the track extrapolations (via Kalman filter) to the target.
- For each couple of DC-tracks, events with al least one combination that matches $|Q_x| < 6\ MeV/c^2$, $|Q_y| < 6\ MeV/c^2$ and $|Q_L| < 45\ MeV/c^2$ are kept for further analysis.

The cuts introduced in this filtering procedure do not produce any significant bias in the shape of two-pion Coulomb interaction spectrum, further than shrinking the Q_T distribution to the approximate cut of $Q_T < 6\ MeV/c$. In particular, they are sufficiently general not to introduce bias in upstream detector multiplicities.

The main use of this pre-selection items from the strong data reduction, which facilitates data processing through multiple iterations. This is of course at the cost of having slightly reduced experimental constraints in the description of the Q_T spectrum of Coulomb interaction background. As we shall see, the Q_L spectrum will effectively provide such constraint.

8.1.2 Analysis reconstruction criteria

Pions are reconstructed according to the method described and evaluated in previous chapters, using the whole spectrometer capabilities, and particullary the 10 upstream detectors available in 2001. Straightline fitting in conjuntion

with TDC information from SFD hits allows unambiguous reconstruction of pion pairs upstream the magnet, matching with DC tracks is performed and double ionization pulse in IH required for non resolved pairs. In order to improve precision and minimize the effect of multiple scattering in the break-up probability measurement, only the signals from MSGC/GEM detector are used in the final track re-fit.

For the pionium lifetime analysis an aditional set of constraints and reconstruction cuts are applied, the same for Monte Carlo as well as for experimental data:

- Relative transverse momentum cut is applied: $Q_T < 5\ MeV/c$ and $|Q_L| < 22\ MeV/c$. The chosen value is high enough to contain all pionium signal events below, and low enough to assure the absence of any bias from pre-selection cuts or from top Q_T value in the generation of Monte Carlo files.

- Longitudinal momentum is cut under $|Q_L| < 20\ MeV/c$. Such a broad value allows to have lever-arm enough to provide an accurate description of Coulomb correlation in the background fit. The stability of the simulation at high $|Q_L|$ values is assured by the use of experimental accidentals pairs in the description of the trigger behaviour.

- Only positive particles with laboratory momentum $p < 4\ GeV/c$ are analyzed to remove time-corrlated protons (see Fig. 2.14).

- Thanks to the high time resolution of the VH we can easily have an accurate definition of pion pairs originated from the same proton interaction, performing a clean separation with respect to uncorrelated pairs in which pions are produced at different interactions. **Prompt** time correlated pairs are selected within a $-0.5 < \Delta t < 0.5$ ns time difference between the negative and positive arm of VH. For **Accidental** uncorrelated pairs time window is $[-14, 4]$ and $[11, 14]$ ns (Fig. 8.1)

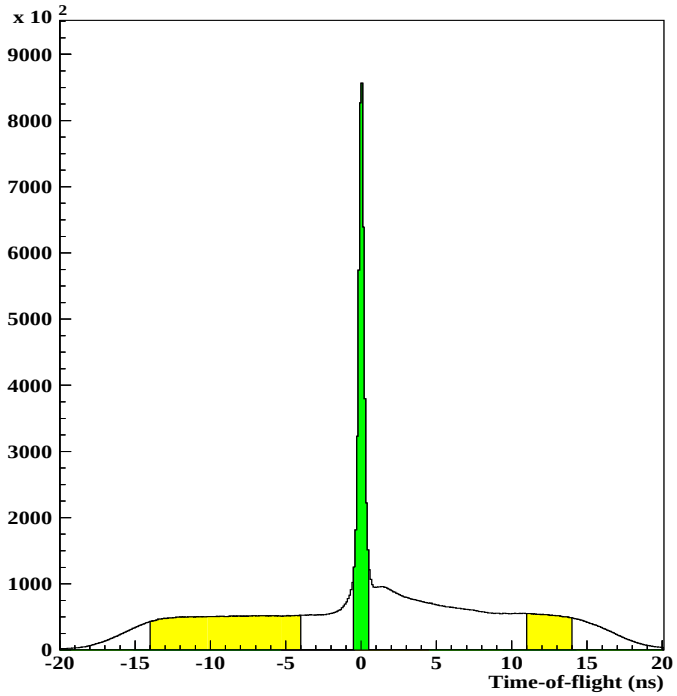

Figure 8.1: *Time difference between positive and negative particles from VH measurement. Prompt events are defined inside the [-0.5,0.5] ns window (green), and accidentals are selected from yellow coloured window in order to remove proton and kaon contamination ([-14,-4] and [11,14] ns).*

- For unresolved tracks, double ionization signal in IH is optimized in 10 laboratory momentum intervals. Fraction of tracks with only one SFD hit in the X and Y projections are used as calibration for both experimental and Monte Carlo data. Minimun pulse height value is chosen to be p-dependent to assure a perfect concordance of unresolved tracks fraction between Monte Carlo and real data (Fig. 8.2)
- Standard cuts for muon background rejection using muon counters and pre-shower detector are applied, and PSH pulses have been analyzed to cross-check and improve Cherenkov veto efficiency.

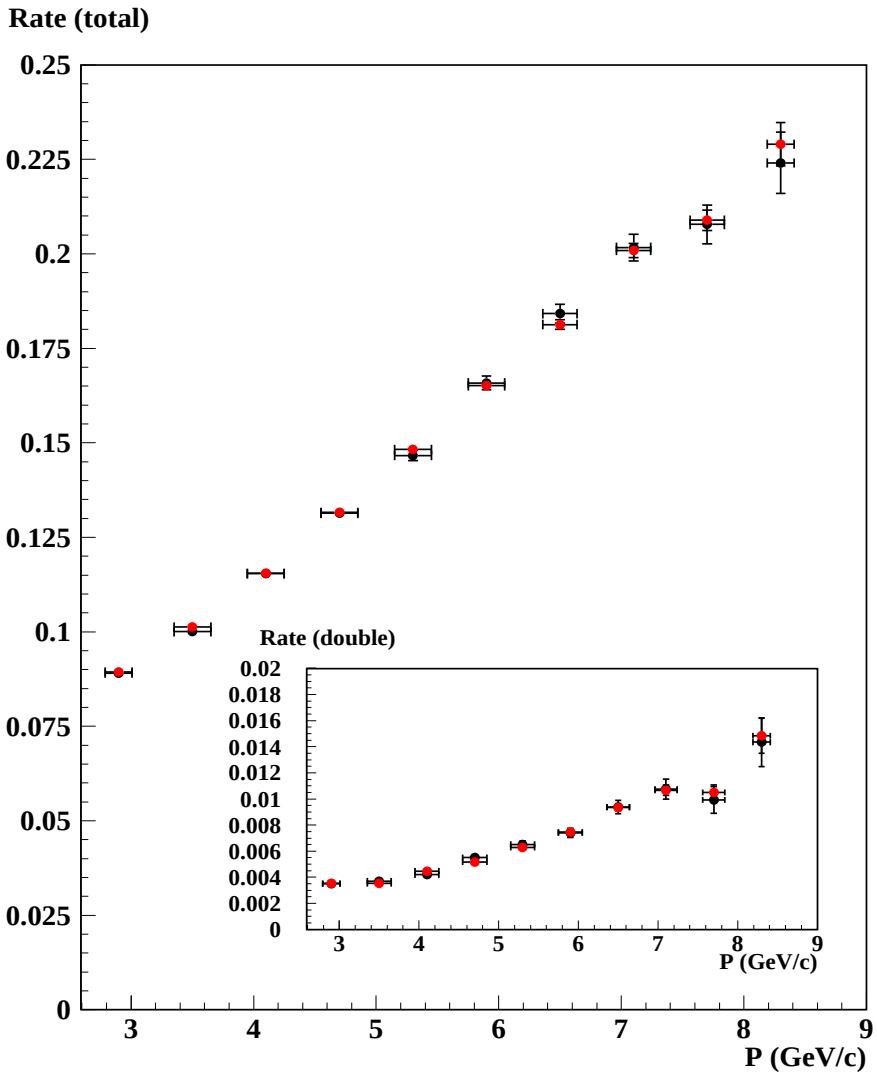

Figure 8.2: *Rate of tracks with only one SFD hit in X or Y projection for real data (black dots) and Monte Carlo (black dots) after optimization of double ionization signal in IH. At right-bottom rate of unresolved events in both projections is shown.*

8.2 Use of accidental pairs and detector alignment for Q_L spectrum

Accidental pairs have been used to calibrate the spectrometer acceptance as function of Q_L, due to non-uniform trigger efficiency. The ratio R between Monte Carlo simulated non-Coulomb Q_L spectrum and that obtained from accidental pairs has been observed to be slightly non uniform. Since accidental triggers have undergone the same electronics readout chain as the prompt data, this ratio has been used as a correction factor to the Monte Carlo, in the analysis of Q_L spectrum. As it will be seen below, this is supported by the fact that the corrected results are in very good agreement with the analytical prediction based on the Sakharov factor for Coulomb pairs. This ratio R has been determined not only globally but also in each individual momentum interval that can be read in table 8.1. The correction has been smoothed by making linear or polynomial fits in the region $|Q_L| > 10\ MeV/c$, with results indicated in figure 8.3.

A precision analysis of Q_L spectrum further requires alignment of DC coordinates with respect to upstream detectors in the bending (X) projection, separately for positive and negative arms. This is achieved by ensuring that the Q_L distributions are accurately centered at zero in each momentum interval. Small shifts are observed with respect to the original calibration, which was based upon momentum-averaged deviations. As an illustration of the quality of the calibrated data, the asymmetry values around zero

$$A = (F - B)/(F + B) \tag{8.1}$$

are given in table 8.1 at every momentum bin, where

$$F = \int_{-X}^{0} (d\sigma/dQ_L) dQ_L \tag{8.2}$$

and

$$B = \int_{0}^{X} (d\sigma/dQ_L) dQ_L \tag{8.3}$$

with $X = 2\ MeV/c$.

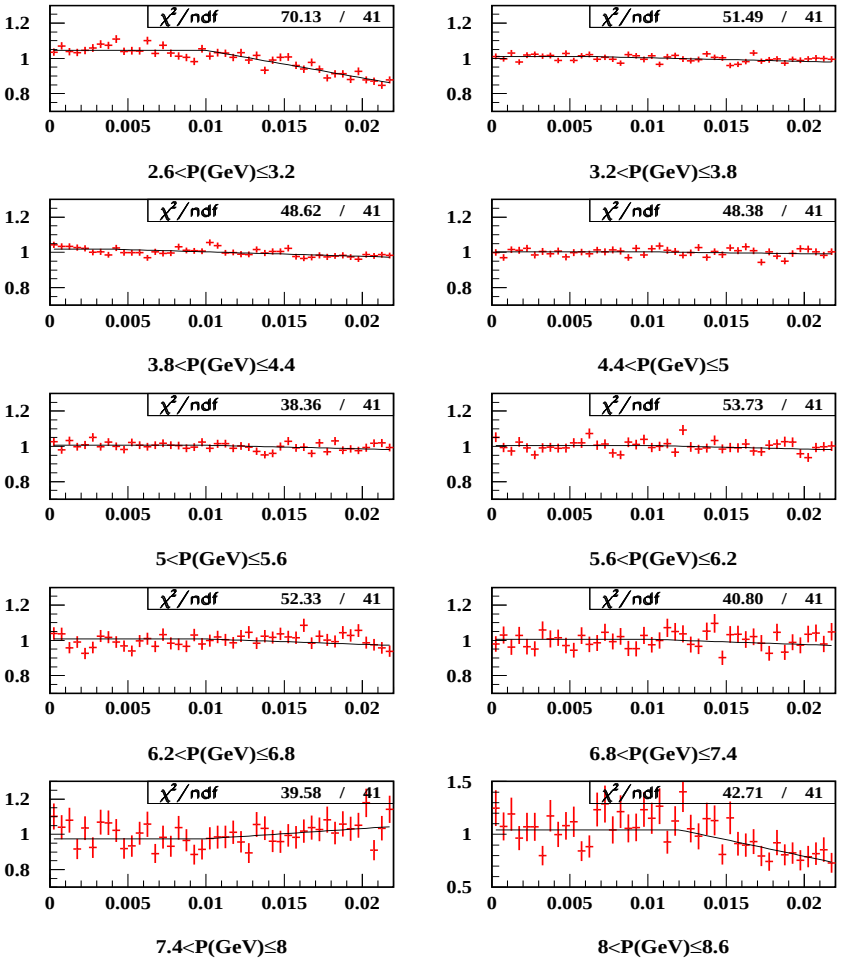

Figure 8.3: *Ratio between non-Coulomb Monte Carlo and observed accidental Q_L spectrum in 10 different intervals of lab-frame momentum p*

Table 8.1: Q_L *asymmetry values around zero within* $\pm 2MeV/c$*, after calibration at each momentum bin.*

p interval (GeV/c)	asymmetry (error)
2.6-3.2	0.0058 $\pm$ 0.0066
3.2-3.8	-0.00005 $\pm$ 0.0053
3.8-4.4	0.0056 $\pm$ 0.0057
4.4-5.0	0.000017 $\pm$ 0.0065
5.0-5.6	-0.0013 $\pm$ 0.0076
5.6-6.2	-0.0043 $\pm$ 0.0091
6.2-6.8	0.0018 $\pm$ 0.0119
6.8-7.4	0. $\pm$ 0.0165
7.4-8.0	-0.0021 $\pm$ 0.0230
8.0-8.6	0.0201 $\pm$ 0.0344

8.3 Analysis of Q-spectrum with 2-dimensional fit

The experimentally measured time-correlated spectrum (NP) consists [70] of pion pairs (labelled AA) from the ionization of pionium, Coulomb correlated pions (CC), non-Coulomb pairs from long lived sources (NC), and the extrapolation of the accidental background in time coincidence (AC):

$$NP = \alpha_1 CC + \alpha_2 AC + \alpha_3 NC + \gamma AA \tag{8.4}$$

where α_1, α_2, α_3 and γ are the relative share in the total measured spectrum.

A two-dimensional analysis of $\pi^+\pi^-$ spectrum in the center-of-mass frame has been carried out, choosing the transverse $Q_T = \sqrt{Q_X^2 + Q_Y^2}$ and longitudinal (from now $Q_L \equiv |Q_Z|$) components (with respect to the pair direction of flight Z) as independent variables.

This analysis has been done independently at ten individual $600MeV/c$

bins of the laboratory-frame momentum p (magnitude of 3-vector sum of pion momenta p_1 and p_2) , and also globally including all values of p in the same fit. Results will be presented in the next chapter.

Irrespective of the parameter variation strategy, or of the momentum definition followed in each case, the prompt two-pion spectrum in (Q_T, Q_L) plane has been χ^2-analyzed by comparison with the outlined input spectra, generated for both 94 μm and 98 μm Ni target thicknesses with the same ratio as experimentally collected data:

- Monte Carlo describing the Coulomb final-state interaction by means of the Sakharov-Gamow-Sommerfeld factor, using single pion laboratory-frame momentum from de-convoluted prompt spectrometer data (see chapter 6). The effect of the η' and ω large-size resonances is taken into account separately as a small correction.

- Monte Carlo describing accidental coincidences taken by the spectrometer. It represents the uncorrelated non-Coulomb background in prompt events. They have a strictly isotropical distribution in their center-of-mass frame, being its laboratory momentum spectrum generated according to that of true accidental pairs taken by the spectrometer, after de-convolution of detector acceptance.

- Monte Carlo describing Coulomb non-interacting $\pi^+\pi^-$. It simulates any additional fraction of non-Coulomb events where one of the pions originates from decay of long-lifetime resonances (up to ns scale). Such events are still detected as time-correlated by the precision coincidence of the spectrometer. In practice it differs from the previous one very slightly, only from the different lab-frame pion momentum distribution. Their lab-frame momentum spectrum (entirely decoupled from Q-space) is also taken from spectrometer data.

- Pionium atom Monte Carlo model [65], which is used to fit the observed deviation with respect to the continuum Coulomb background spectrum constructed from the previous input, and to cross-check the substracted signal shape.

Accidental contamination is extracted, the fraction of accidental pairs has been determined experimentally from the time-of-flight (TOF) spectrum in each momentum bin and in the whole data sample. It is done by a simple straight line extrapolation of accidentals in the interval [-12,-4] ns over the prompt region. Obtained values are given in table 8.2. The increasing fraction of accidental pairs can be noticed from figure 8.4.

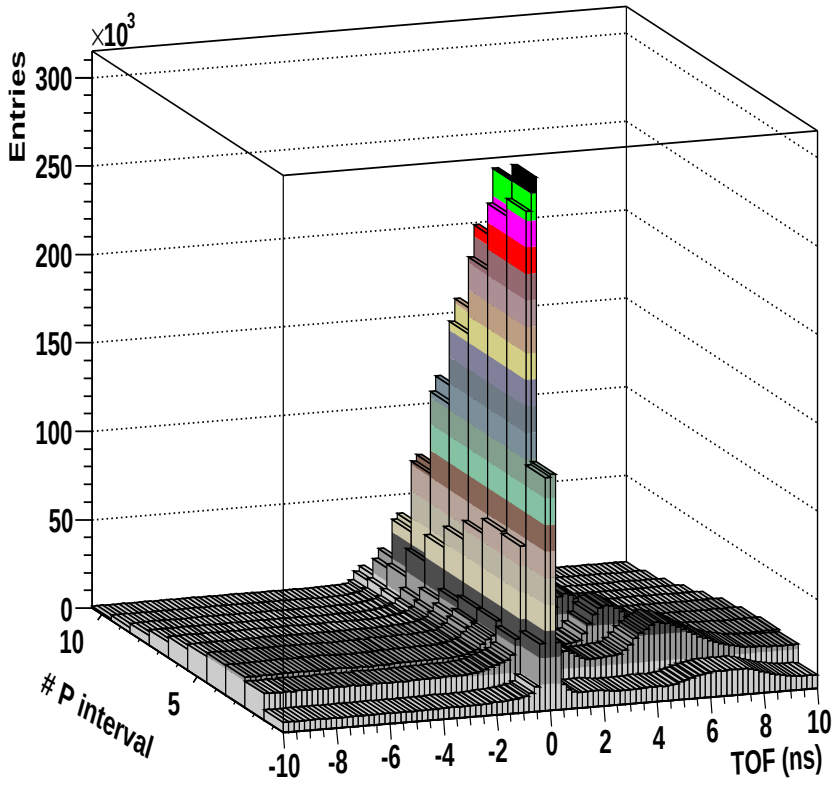

Figure 8.4: *TOF spectrum in function of lab frame momentum interval as defined in table 8.1. It can be noticed how accidental pairs contamination in the prompt peak increases with p.*

Table 8.2: *Fraction of accidental pairs determined from TOF spectrum at individual lab-frame momentum bins with $Q_L < 20MeV/c$.*

p interval (GeV/c)	α_2
2.6-3.2	0.0773 ± 0.0002
3.2-3.8	0.0876 ± 0.0001
3.8-4.4	0.1038 ± 0.0001
4.4-5.0	0.1139 ± 0.0001
5.0-5.6	0.1203 ± 0.0002
5.6-6.2	0.1269 ± 0.0002
6.2-6.8	0.1348 ± 0.0003
6.8-7.4	0.1440 ± 0.0004
7.4-8.0	0.1531 ± 0.0008
8.0-8.6	0.1602 ± 0.0018
Overall (2.6-8.6)	0.0975 ± 0.0001

The total number of events used from the above samples are denoted by N_{CC}, N_{AC}, N_{NC} and N_{AA} respectively, whereas N_p represents the total number of prompt events in the analysis, under the quoted cuts $Q_T < 5MeV/c$ and $Q_L < 20MeV/c$. Index k runs over all (i, j) bins of the (Q_T, Q_L) histograms, and we denote by N^k_{CC} the number of Coulomb events observed in each particular bin (i, j). Similarly for the other input spectra, namely N^k_{AC}, N^k_{NC} and N^k_{AA}. Normalised spectra are used to fit the data, and we denote them by small letters, $n^k_{CC} = N^k_{CC}/N_{CC}$ and likewise for the rest. The ratios $x_{CC} = N_{CC}/N_p$, $x_{AC} = N_{AC}/N_p$, $x_{NC} = N_{NC}/N_p$ and $x_{AA} = N_{AA}/N_p$ help to define the statistical errors. The χ^2 analysis is based upon the expression:

$$\chi^2 = \sum_k \frac{\left(N^k_p - \beta\alpha_1 n^k_{CC} - \beta\alpha_2 n^k_{AC} - \beta\alpha_3 n^k_{NC} - \beta\gamma n^k_{AA}\right)^2}{\beta\left(n^k_p + n^k_{CC}(\frac{\alpha_1^2}{x_{CC}}) + n^k_{AC}(\frac{\alpha_2^2}{x_{AC}}) + n^k_{NC}(\frac{\alpha_3^2}{x_{NC}}) + n^k_{AA}(\frac{\gamma^2}{x_{AA}})\right)} \quad (8.5)$$

where α_i and γ are the respective Monte Carlo type fractions (according to $\alpha_1 + \alpha_2 + \alpha_3 + \gamma = 1$). A **control region** is defined by the cut $Q_L > 2\ MeV/c$, where we do not expect deviations with respect to the continuum Coulomb interaction background. We call $Q_L < 2\ MeV/c$ the **extrapolation region** in which the atom signal is contained.

Subtraction of accidental pairs is performed by blocking the α_2 parameter to the experimentally observed fraction under the prompt peak. Minimisation of the above χ^2 over the entire (Q_T, Q_L) plane determines the non-Coulomb fraction α_3, and the atom fraction γ as free parameters. The β parameter, which represents the overall Monte Carlo normalisation, is actually determined by the number of prompt events, and it is fixed according to the expresion:

$$\beta = \frac{\sum_{Q_L>2MeV/c} n_p}{\sum_{Q_L>2MeV/c}(\alpha_1 n_{CC} + \alpha_2 n_{AC} + \alpha_3 n_{NC} + \gamma n_{AA})} \tag{8.6}$$

to ensure that the Monte Carlo normalization equals the number of prompt in the control region.

Once the previous fit has converged, the atom signal is defined in each (i, j) bin as the difference between the prompt spectrum and the Monte Carlo with the pionium component (AA) removed. This 2D signal, which reveals the excess with respect to the calculated Coulomb interaction enhancement, is analyzed in detail in the next chapter, where it is compared with the Monte Carlo prediction for atom production. Further χ^2 tests are performed both in the $Q_L > 2\ MeV/c$ (control region, where pionium Monte Carlo does not contribute) and in the $Q_L < 2\ MeV/c$ (extrapolation region) separately.

8.4 K-factors and break-up probability

The conversion from integrated atom production signal to break-up probability is done by means of the so-called theoretical K-factor , which are defined as follows. Using generated Monte Carlo we can apply the correction needed due to the spectrometer acceptance and reconstruction effects, obtaining as a result the experimental K-factor.

The break-up probability has been defined as the ratio of the number of broken up atoms n_A over the initially produced number N_A of pionium pairs:

$$P_{Br} = \frac{n_A}{N_A} \tag{8.7}$$

The number of atoms N_A produced in a given phase-space volume is analytically calculated in quantum mechanics [75] and can be related by means of the theoretical K-factor to the number N_C of produced Coulomb pairs [66], both observed in the same kinematical region Ω of the (Q_T, Q_L) plane:

$$K^{th} = \frac{N_A}{N_C} = 8\pi^2 Q_0^2 \frac{\sum_1^\infty \frac{1}{n^3}}{\int A_C(Q) d^3Q} \tag{8.8}$$

where the integral in the denominator extends over the desired Q-space volume. $Q_0 = \alpha M_\pi$ is two times the atom Bohr momentum p_B, and n its principal quantum number. For the sphere of radius $Q < Q_c$ the following expression is obtained:

$$K^{th}(Q_c) = \frac{N_A}{N_C} = \frac{\sum_1^\infty \frac{1}{n^3}}{\int_0^{Q_c/2p_B} \frac{kdk}{1-exp(-2\pi/k)}} \tag{8.9}$$

For a rectangular domain Ω in the (Q_T, Q_L) plane, integration of (8.8) in cylindrical coordinates provides the values given in table 8.3.

Now we can return to the break-up probability and redefine it with the theroretical K-factor as:

$$P_{Br} = \frac{n_A}{N_A} = \frac{n_A}{N_C K^{th}(\Omega)} \tag{8.10}$$

However the measurement obtained in DIRAC for n_A and N_C has been influenced by several reconstruction biases, namely multiple scattering in the target and in the detector layers, geometrical acceptance of the spectrometer, trigger, and detector and tracking innefficiencies. In fact the influence is not the same for atom than for Coulomb pairs, specially if in the election of the domain Ω we don't choose Q_T and Q_L values high enough to assure that the

whole atom spectrum is contained into Ω. The more we reduce the domain Ω "entering" the atom spectrum, the more reconstruction biases differ for atoms and Coulomb pairs.

The break-up probability is then determined as:

$$P_{Br} = \frac{n_A}{N_C K^{exp}(\Omega)} \tag{8.11}$$

with the experimental K-factor defined in the following way:

$$K^{exp}(\Omega) = K^{th}(\Omega)\frac{\epsilon_A(\Omega)}{\epsilon_C(\Omega)} \tag{8.12}$$

where:

$$\epsilon_A(\Omega) = \frac{n_A^{rec}(\Omega)}{n_A^{gen}(\Omega)} \qquad \text{and} \qquad \epsilon_C(\Omega) = \frac{n_C^{rec}(\Omega)}{n_C^{gen}(\Omega)}$$

define the efficiency of the reconstruction method as a whole for atoms and Coulomb pairs, respectively, in a given kinematical region Ω. The factors ϵ_A and ϵ_C are determined with high precision using separate Monte Carlo inputs, after processing the full simulation/digitization/reconstruction chain. They are ratios between reconstructed output and generated input. For the Nickel 2001 data K^{exp} has been evaluated using Monte Carlo files with two different target thicknesses (94 and 98 μm), in the same proportion as the sample of experimental data that will be used for lifetime analysis.

For a given momentum interval, the measured values of P_{Br} should not depend on the actual domain Ω which is chosen to perform the measurement, and this particular point will be studied in the following chapter.

The experimental K-factor values do however exhibit a laboratory-frame momentum dependence (due to the terms ϵ_A and ϵ_C) which has been analyzed in detail, and it is indicated in table 8.4. These values and its dependence have been taken into account in the determination of break-up probability.

Table 8.3: *Numerical values of K^{th} and K^{exp} as defined in the text. Each raw corresponds to a given rectangular cut in (Q_T, Q_L) plane , with $Q_T^c = 5\ MeV/c$ and $Q_L^c = 20\ MeV/c$ being the reference cut values. K^{th} values are obtained by integration of (8.8) in cylindrical coordinates.*

$Q_L^{cut}(MeV/c)$	K^{theo}	K^{exp}
0.5	0.4372	0.3017 ± 0.0010
1.0	0.2389	0.2193 ± 0.0005
1.5	0.1669	0.1618 ± 0.0003
2.0	0.1300	0.1274 ± 0.0002
$Q_T^{cut}(MeV/c)$	K^{theo}	K^{exp}
0.5	3.2457	0.8457 ± 0.0083
1.0	1.2382	0.6681 ± 0.0038
1.5	0.6995	0.5206 ± 0.0021
2.0	0.4674	0.4027 ± 0.0013
2.5	0.3426	0.3137 ± 0.0009
3.0	0.2660	0.2505 ± 0.0006
3.5	0.2147	0.2054 ± 0.0005
4.0	0.1781	0.1720 ± 0.0004
4.5	0.1509	0.1468 ± 0.0003
5.0	0.1300	0.1274 ± 0.0002

Table 8.4: *K-factors determined in 10 intervals of laboratory-frame momentum for standard* (Q_T, Q_L) *cut:* $Q_T^c = 5\ MeV/c$ *and* $Q_L^c = 20\ MeV/c$.

p interval (GeV/c)	K^{exp}
2.6-3.2	0.1140 $\pm$ 0.0005
3.2-3.8	0.1196 $\pm$ 0.0004
3.8-4.4	0.1267 $\pm$ 0.0005
4.4-5.0	0.1316 $\pm$ 0.0005
5.0-5.6	0.1368 $\pm$ 0.0007
5.6-6.2	0.1407 $\pm$ 0.0008
6.2-6.8	0.1431 $\pm$ 0.0011
6.8-7.4	0.1474 $\pm$ 0.0015
7.4-8.0	0.1451 $\pm$ 0.0021
8.0-8.6	0.1490 $\pm$ 0.0043

Chapter 9

Pionium lifetime

Data taken with DIRAC spectrometer in 2001 with two Nickel targets of 94 and 98 μm thickness is analyzed to obtain pionium lifetime. Standard DIRAC radiations lenghts in Monte Carlo were increased by 15% upstream the magnet in concordance with conclusions from specific studies [62].

With the 2-dimensional fit described previously, the number of ionized atoms and Coulomb correlated pairs in the same kinematical region are obtained, using Monte Carlo distributions from simulated pionium signal to guide the fit, and suppressing gamma term in equation 8.5 to build the linear combination of Monte Carlo, which will be subtracted from real collected data to obtain experimental atom signal.

The fit is repeated 10 times in referred p intervals. A global fit with added statistics from all intervals is done, and only for the sake of comparison the results from the 10 p bins are statistically promediated.

After the selection explained in the previous chapter, a total number of 907796 prompt events is used in this analysis. Generated Monte Carlo sample of Coulomb correlated pairs reaches 3434049 events applying the same cuts.

At the latter step of the analysis, the defined K-factor is used to extract breakup probability of the pionium, and by means of the unique target-dependent $\tau - P_{Br}$ relationship, lifetime of pionic atoms is obtained. In the last section of the chapter, an evaluation of main systematic errors is done to get final result.

9.1 Momentum-dependent fit results

Ten independent fits are performed in 600 MeV/c lab-frame $\pi^+\pi^-$ momentum bins, starting from 2.6 MeV/c. By choosing a momentum-dependent fit in narrow bins, the Q-dependence of the efficiency of $\pi^+\pi^-$ detection is weakened [76].

Minimisation of χ^2 in expression (8.5) was carried out in $(0.5\times0.5)(MeV/c)^2$ bins of (Q_T, Q_L) space, independently in each of the ten $\pi^+\pi^-$ momentum intervals indicated in table 8.4 leaving α_1 and γ as free parameters. The α_2 parameter (fraction of accidental pairs) was blocked to the values experimentally observed from TOF, which were indicated in table 8.2. The $\alpha_3 = 1 - \alpha_1 - \alpha_2 - \gamma$ fraction then measures the long-lifetime non-Coulomb component. Fit range is defined by standard cuts of $Q_T < 5\ Mev/c^2$ and $|Q_L| < 20\ Mev/c^2$.

The extrapolation method can thus be applied to the region $Q_L < 2\ MeV/c$, in such a way that an atom signal is defined in each (i, j) bin of (Q_T, Q_L) space by the difference between the prompt spectrum and the Monte Carlo prediction with pionium component removed.

The fit quality is indicated by the χ^2-values obtained in each momentum bin. In table 9.1 those χ^2-values are given separately for the control ($Q_L > 2\ Mev/c^2$) and extrapolation ($Q_L > 2\ Mev/c^2$) region. Although the pionium atom Monte Carlo has been used to guide the fit, the restriction of the χ^2 to the domain $Q_L > 2\ MeV/c$ (where their contribution is very small) is equally good when the γ component is suppressed. The number of extracted atoms, α_1 parameter, and the obtained breakup probability are displayed too for the then momentum intervals.

The atom spectra are shown at the end of this chapter in figures 9.15 to 9.23 as function of Q_T and Q_L, and compared to the pionium Monte Carlo prediction in each case. The estimator of fit quality is provided by the χ^2 value extended over the extrapolation domain $(0, Q_T^c) \times (0, Q_L^c)$ with $Q_T^c = 5\ MeV/c$ and $Q_L^c = 2\ MeV/c$, with one degree of freedom used by the γ parameter. Those are given in last column of table 9.1. When the fit procedure is applied to the control region $Q_L > 2\ MeV/c$, small deviations are still observed in Q_T spectrum, despite the acceptable values of χ^2. We

attribute those to a remaining imperfection of the simulation of double-track resolution, and we actually improve the extrapolated spectrum by correcting for those deviations (observed in the control region) and projecting them them onto individual Q_T bins at $Q_L < 2\ MeV/c$. One degree of freedom is subtracted for every corrected Q_T bin.

Table 9.1: *The main results of the fit concerning number of atom pairs N_A, α_1 and χ^2 over the control (χ^2_c) and extrapolation (χ^2_e) region are indicated in this table, for every 600 MeV/c momentum interval p_i as defined in table 8.4.*

	N_A	α_1	χ^2_c / ndf	χ^2_e / ndf
p_1	839 ± 80	0.866 ± 0.016	320.6 / 350	45.8 / 40
p_2	1260 ± 113	0.814 ± 0.011	360.9 / 350	45.7 / 40
p_3	1333 ± 106	0.802 ± 0.012	355.1 / 350	25.5 / 40
p_4	1135 ± 92	0.842 ± 0.014	337.3 / 350	30.5 / 40
p_5	784 ± 85	0.853 ± 0.016	306.7 / 350	25.4 / 40
p_6	577 ± 78	0.848 ± 0.021	335.1 / 350	46.8/ 40
p_7	427 ± 62	0.794 ± 0.026	335.1 / 350	43.4 / 40
p_8	214 ± 43	0.809 ± 0.037	333.3 / 350	66.8 / 40
p_9	174 ± 43	0.804 ± 0.066	395.9 / 350	44.6 / 40
p_{10}	32 ± 24	0.863 ± 0.199	344.1 / 350	54.1 / 40

The number of atom pairs n_A determined as function of p is plotted in figure 9.2 along with the number of Coulomb pairs given by the fit in each case. Errors in N_A are given by MINOS variation of γ parameter. It is seen that atom production follows rather closely the spectrum of semi-inclusive $\pi^+\pi^-$ differential cross-section, as expected from bound state production. Please note that both of these spectra are uncorrected for spectrometer acceptance.

In figure 9.4 we plot the remaining number of non-Coulomb pairs determined by the fit as function of p, after subtraction of accidentals according

to table 8.2, and we compare the spectrum with that previously determined for Coulomb pairs (see figure 9.2). We attribute this reminder to a long-lived component in $\pi\pi$ prompt triggers, in a much shorter timescale than the TOF detector can appreciate ($\sim 170\ ps$). Although we have not attempted a detailed comparison with Monte Carlo models (with specific resonances), the observed softer spectrum is qualitatively well understood.

9.1.1 Breakup probability and lifetime.

Pionium break-up probabilities can now be determined by using the momentum-dependent K-factors calculated in table 8.4, and they are shown in figure 9.1. Errors were propagated from those provided by the fit for n_A and N_C. P_{Br} values, shown in table 9.2 are compatible with a smooth increase with increasing atom momentum, as predicted by Monte Carlo tracking inside the target foil [65][17]. The $1s$ pionium lifetime (τ_{1s}) can then be determined by χ^2 minimization with respect to the latter prediction, having τ_{1s} as only free parameter, using the relationship explained in chapter 1. Alternatively, P_{Br} measurements can be combined with independent statistical errors, and Monte Carlo tracking applied with a given atom momentum spectrum.

At bottom in figures 9.15 to 9.23, P_{Br} values are shown as function of integration limits in Q_T and Q_L. Expanding equation 8.11 in all its terms for a given kinematical region Ω we obtain

$$P_{Br} = \frac{n_A}{N_C K^{exp}} = \frac{n_A}{N_C}\frac{1}{K^{theo}}\frac{\epsilon_C}{\epsilon_A} = \frac{n_A}{N_C}\frac{1}{K^{theo}}\frac{n_C^{rec} n_A^{gen}}{n_C^{gen} n_A^{rec}} \tag{9.1}$$

and fading away constants we left with

$$P_{Br} \propto \frac{n_A}{N_C}\frac{n_C^{rec}}{n_A^{rec}} \tag{9.2}$$

since both n_C^{rec} and N_C has the same shape (of the reconstructed distribution of Coulomb pairs from Monte Carlo input), we finally get:

$$P_{Br} \propto \frac{n_A}{n_A^{rec}} \tag{9.3}$$

Table 9.2: *Breakup probabilities values obtained from the fit in p slices.*

	P_{Br}
p_1	0.417 $\pm$ 0.041
p_2	0.385 $\pm$ 0.035
p_3	0.451 $\pm$ 0.036
p_4	0.459 $\pm$ 0.038
p_5	0.407 $\pm$ 0.045
p_6	0.424 $\pm$ 0.058
p_7	0.564 $\pm$ 0.084
p_8	0.502 $\pm$ 0.103
p_9	0.841 $\pm$ 0.220
p_{10}	0.301 $\pm$ 0.231

so it is seen how the breakup probability values will show a dependence on the integration limits (in Q_T and Q_L) as far as the experimentally subtracted atom spectra n_A differs from reconstructed Monte Carlo atoms shape (n_A^{rec}). We see in mentioned figures how we get an asymptotic vale as integration region is increased and so containing the whole atom spectra and avoiding the fluctuations caused by not having a perfect description of it.

Provided there is good agreement between Monte Carlo and prompt data in Q_L projection, the measured values of the P_{Br} should not depend on the upper limit Q_L^c chosen for the fit. We have tested the stability of P_{Br} at each momentum bin, and the good behaviour is illustrated in figures 9.11 and 9.10. We have safely chosen $Q_L^c = 20\ MeV/c$ for reference, in view of the fact that statistical errors from the fit are not improved anymore beyond this limit. Note that these results reveal good performance of the acceptance corrections shown in figure 8.3, based on the accidental spectrum.

The fitted values of α_1 parameter (fraction of Coulomb pairs) are also shown in figure 9.3 as function of p. They show little variation, compatible with a small linear increase.

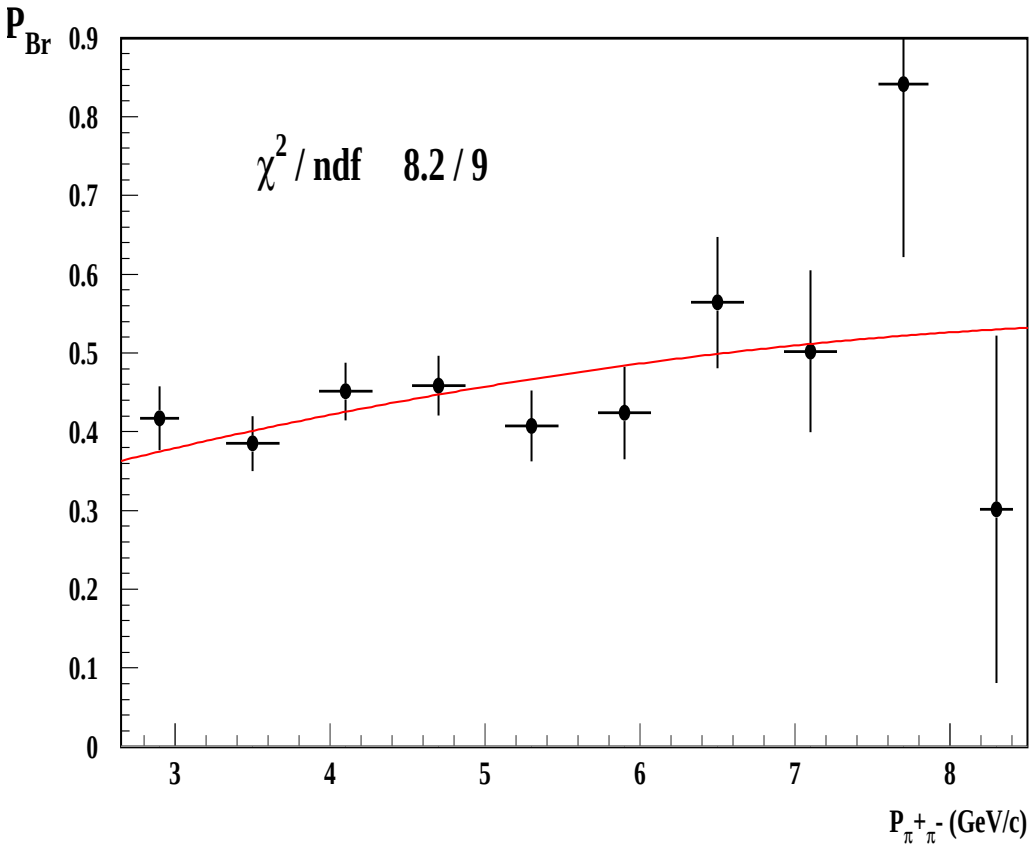

Figure 9.1: *Pionium break-up probabilities as function of atom momentum, as compared to best fit Monte Carlo prediction with average Ni foil thickness* ($\tau_{1s} = 2.58 fs$).

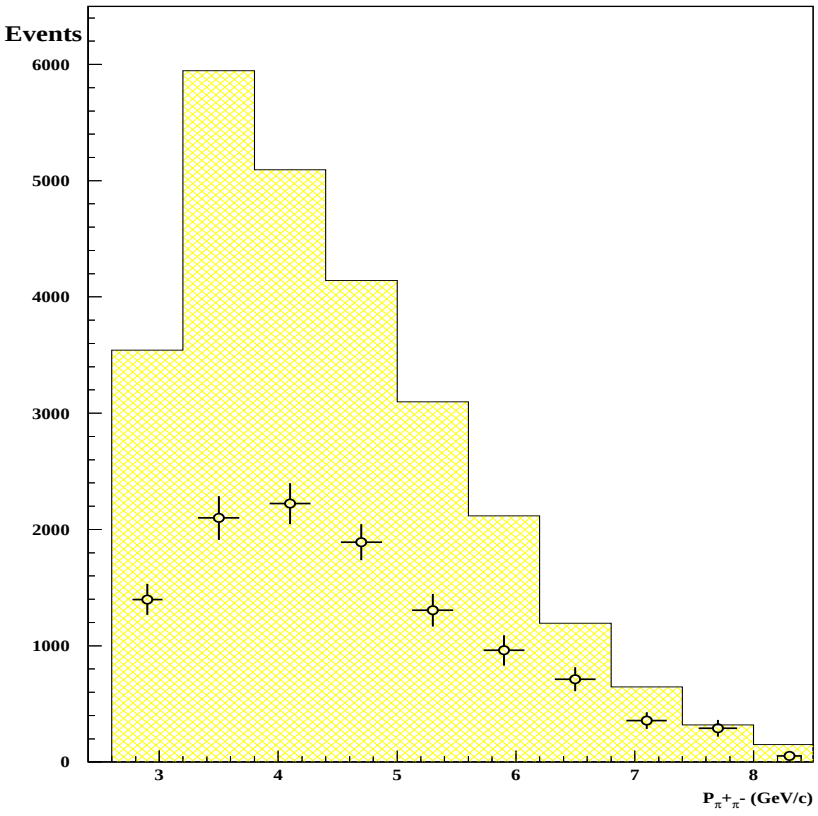

Figure 9.2: *Fitted number of atom pairs as function of their lab-frame momentum (coloured) , as compared to the fitted number of Coulomb pais for $Q_L > 2\ MeV/c$ (black). The latter has been normalized to the same area, to avoid the large difference in actual scale.*

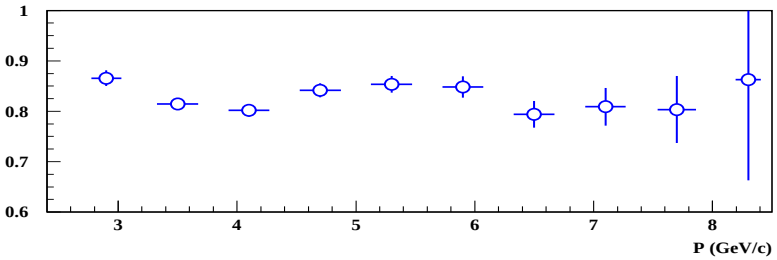

Figure 9.3: *Fitted values of α_1 parameter as function of $\pi^+\pi^-$ momentum.*

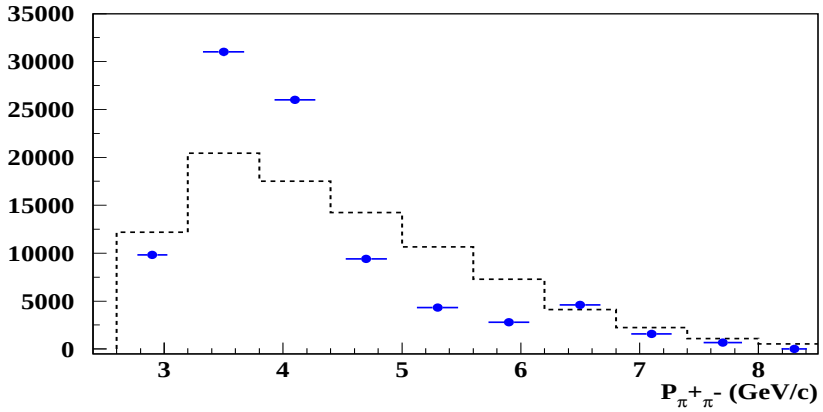

Figure 9.4: *Fitted number of long-lifetime pairs (coloured), determined from α_3 parameter, as function of $\pi^+\pi^-$ momentum. It is compared with the number of Coulomb pairs shown in figure 9.2, normalized to the same area.*

9.2 Global fit results

In addition to the previous (momentum-dependent) analysis, we have also performed a global fit to the data, in which single parameters α_i, β and γ are left free to minimize the χ^2 defined in the momentum-integrated (Q_T, Q_L) plane by expression (8.5). Bin width can be decreased to $0.25 \times 0.25\ (MeV/c)^2$ in the mapped 2-dimensional (Q_T, Q_L) plane due to the increased amount of statistics. The fit results are indicated in table 9.3. Certainly the procedure allows a determination of a total number of atom pairs $\bar{n}_A$ and a mean break-up probability $\bar{P}_{Br}$ after taking into account the momentum-averaged K-factors shown in table 8.3.

These results are compared in table 9.3 with those obtained for n_A and P_{Br} by explicit sum and statistical averaging of the 10 values at individual momentum bins, respectively. χ^2-values and numbers of degrees of freedom have also been summed in these case. Their restriction to the control and extrapolation regions separately are shown in table 9.4. Fit results seem to be rather close, although we believe the momentum-dependent fit in narrow bins is more rigorous in view of possible acceptance correlations and will be used for giving the pionium lifetime value.

For visualization of the global atom signal projections, both methods provide nearly identical results. We show in figure 9.5 the Q_T spectrum, with the atom signal obtained by subtraction of Monte Carlo with pionium component removed. The prompt data are shown separately for the region $Q_L < 2\ MeV/c$ and $Q_L > 2\ MeV/c$. The longitudinal spectrum is shown in 9.6, and the relative momentum magnitude Q in figure 9.7.

A 2D lego plot of the atom signal is shown in figures 9.8 and 9.9, where in the latter a signed transverse component Q_{xy} has been defined by projecting the measured value of Q_T over a randomly selected azimuth ϕ ($Q_{xy} = Q_T\ cos\phi$).

As in previous section, P_{Br} values are shown as function of integration limits in Q_T and Q_L, now in 0.25 MeV/c bins for the global fit (see Fig. 9.12), as well as the stability of the measured values of P_{Br} with respect to the upper limit Q_L^c chosen (Fig. 9.11).

The fit procedure implies a correlation between α_1 and γ (proportional

to N_A) which is displayed in figure 9.13 for the global fit. This correlation is taken into account in the statistical errors given in every momentum bin.

Table 9.3: *Comparison of fit results with α_1 and γ as global fit parameters and superposition of 10 independent fits at different 600 MeV/c momentum bins.*

	α_2	P_{Br}	n_A	N_C
Global fit	0.815 $\pm$ 0.006	0.438 $\pm$ 0.016	6738 $\pm$ 190	120611 $\pm$ 812
p-dependent fit	0.823 $\pm$ 0.015	0.432 $\pm$ 0.016	6775 $\pm$ 244	121323 $\pm$ 821

Table 9.4: *Comparison of the χ^2-values in the whole region, as well as in extrapolation ($Q_L < 2\ MeV/c$) and control ($Q_L > 2\ MeV/c$) regions for the fits indicated in table 9.3.*

	χ^2 / ndf	χ^2_e / ndf	χ^2_c / ndf
Global fit	1516.7 / 1600	147.7 / 160	1368.9 / 1440
p-dependent fit	3853.2 / 3900	428.7 / 400	3424.4 / 3500

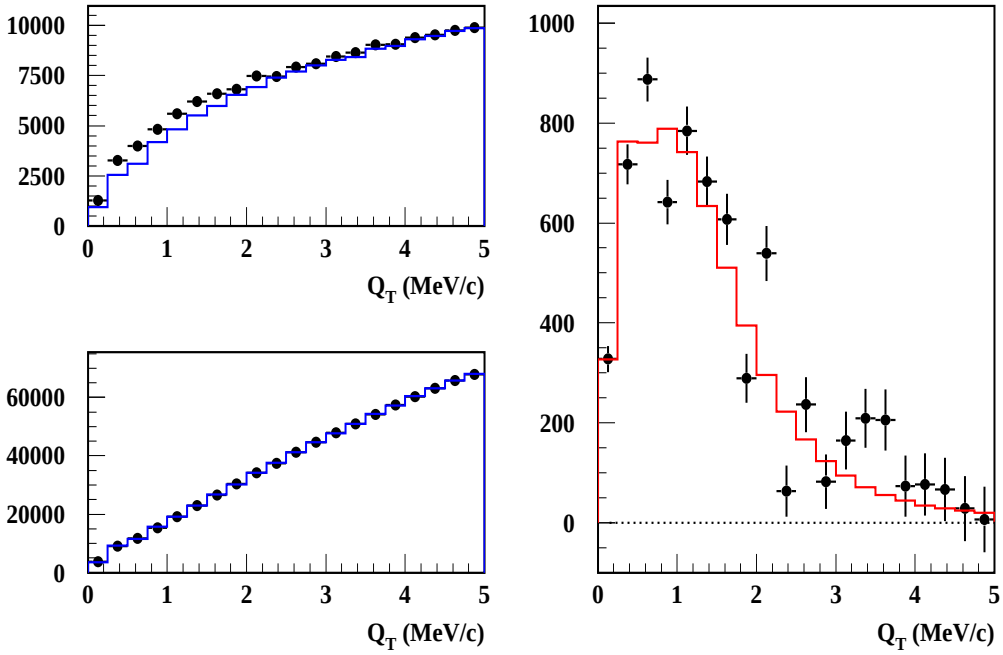

Figure 9.5: *Two-dimensional fit projection onto Q_T. The data are shown separately for $Q_L < 2\ MeV/c$ and $Q_L > 2\ MeV/c$ (left plots). The difference between prompt data (dots) and Monte Carlo (blue line), which corresponds to transverse pionium signal, is plotted (right) and compared with the pionium atom Monte Carlo (red line).*

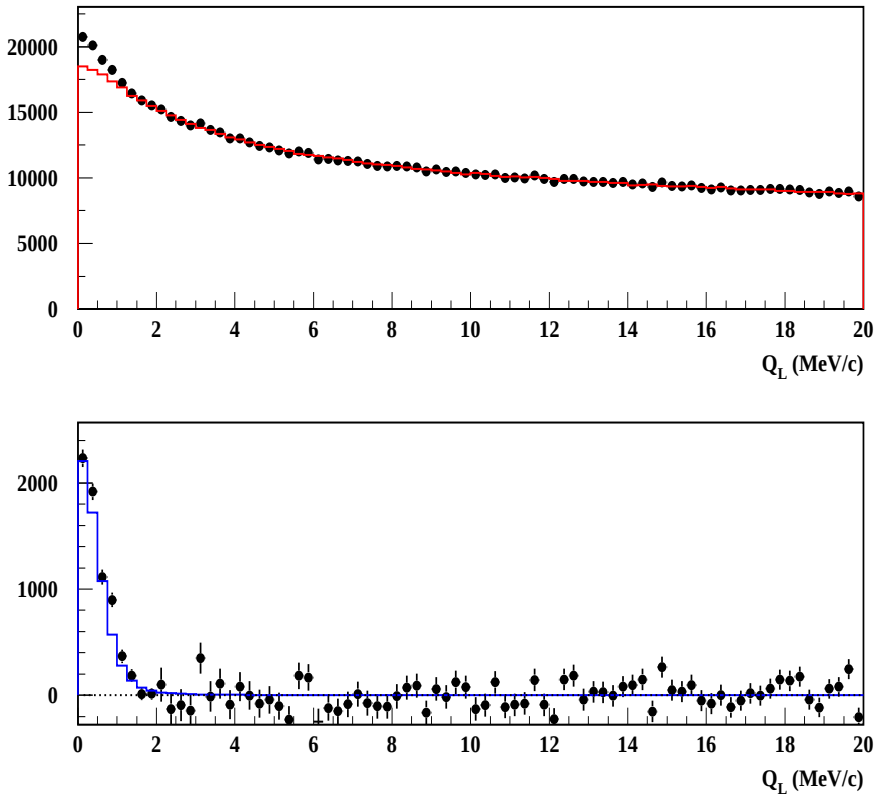

Figure 9.6: *Two-dimensional fit projection onto Q_L. The difference between prompt data (dots) and Monte Carlo (blue line) , which corresponds to pionium signal, is plotted at the bottom, where the signal is compared with the pionium atom Monte Carlo (red line).*

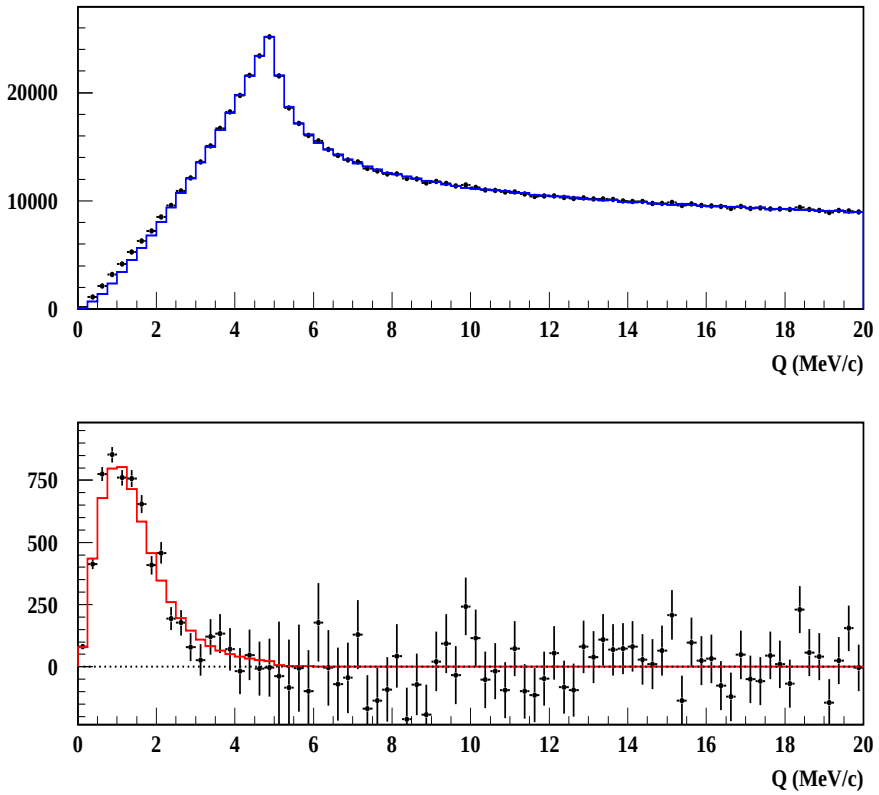

Figure 9.7: *Two-dimensional fit projection onto Q. The difference between prompt data (dots) and Monte Carlo (blue line) , which corresponds to pionium signal, is plotted at the bottom. The signal is compared with the pionium atom Monte Carlo (red line).*

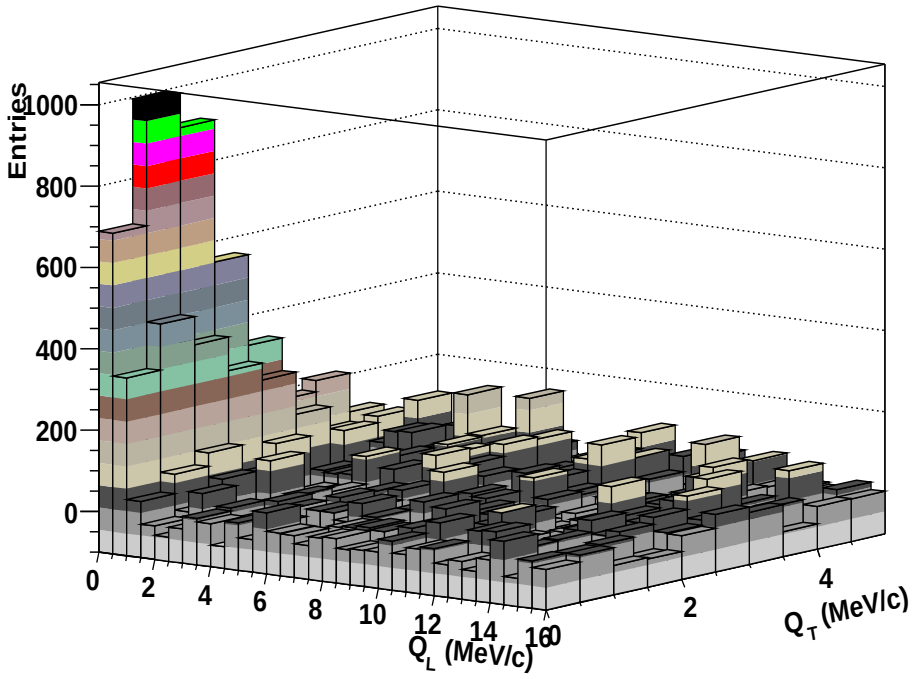

Figure 9.8: *Lego plot showing pionium break-up in* $(Q_T, Q_L = |Q_Z|)$ *plane*

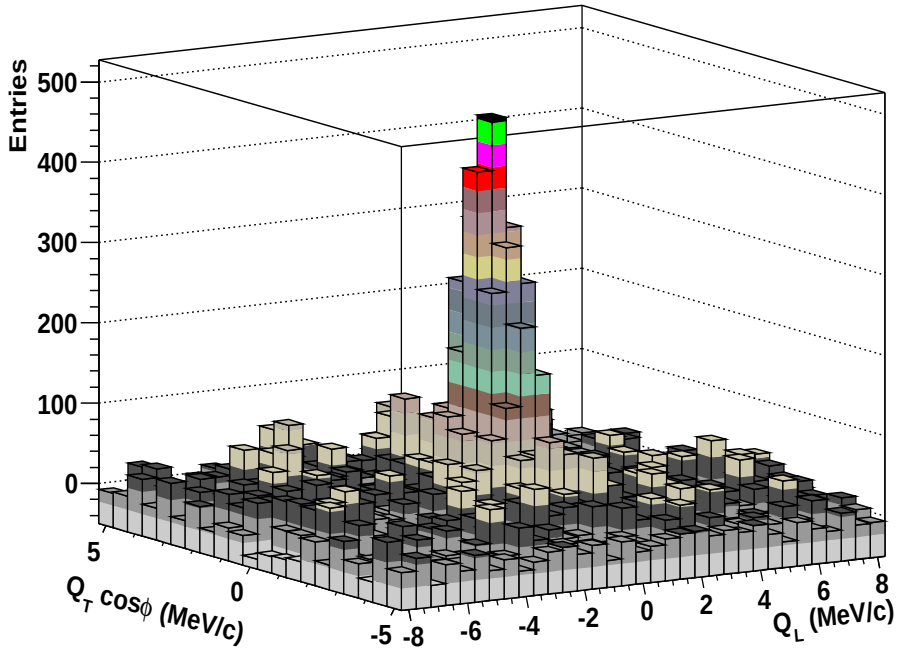

Figure 9.9: *Lego plot showing pionium break-up in (Q_{xy}, Q_L) plane. The transverse component $Q_{xy} = Q_T\ cos\phi$ is defined as the product of the measured Q_T value times the cosine of a random azimuth.*

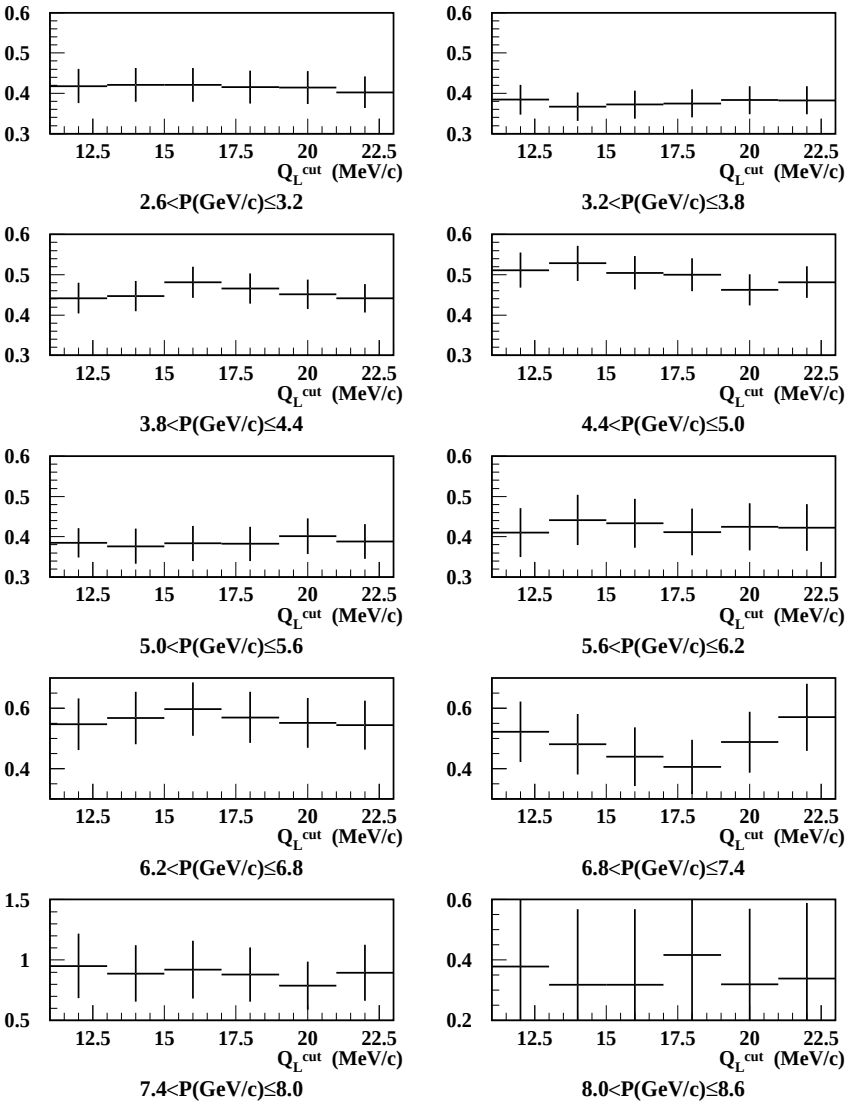

Figure 9.10: *Measured values of P_{Br} as function of Q_L upper limit in the fit (Q_L^c) for the ten momentum intervals.*

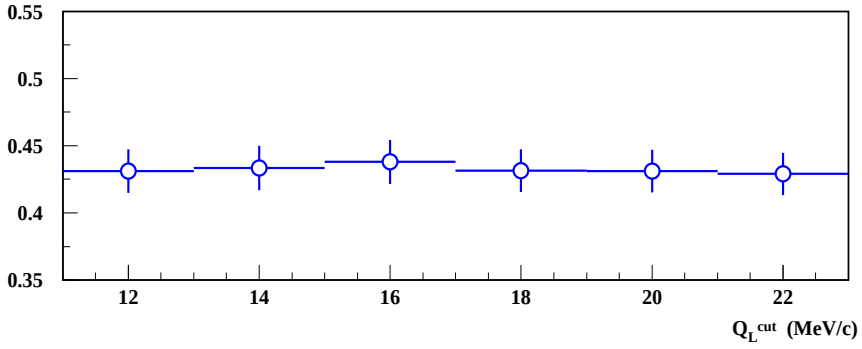

Figure 9.11: *Measured values of statistical average of momentun intervals of P_{Br} as function of Q_L upper limit in the fit (Q_L^c).*

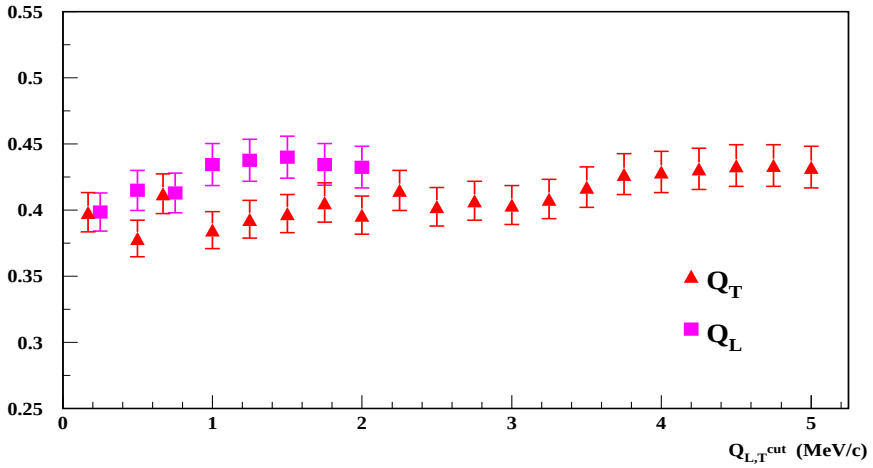

Figure 9.12: *Measured break-up probability as function of Q_L and Q_T cuts.*

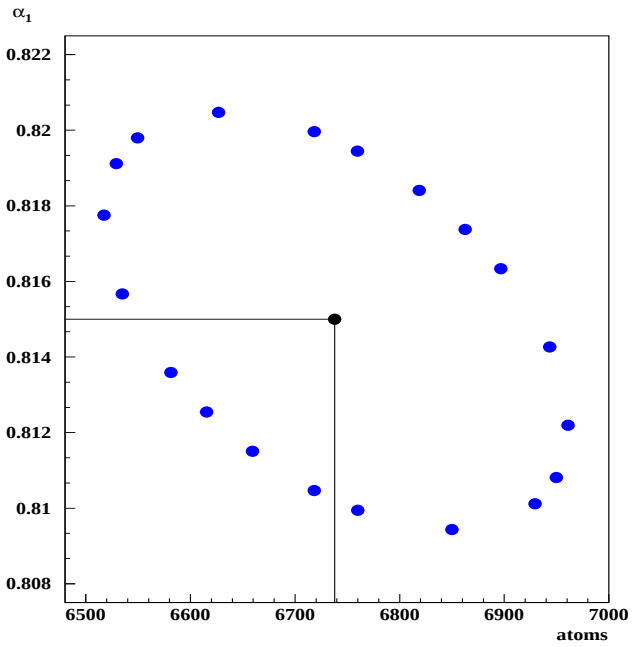

Figure 9.13: *1σ contour plot calculated by MINOS program for α_1 and the number of atoms N_A found by the global 2D-fit, showing statistical errors and correlation.*

9.3 Systematic error

We have studied the magnitude and sign of possible systematic errors in the measurement of break-up probability P_{Br}, related to imperfect simulation of detector response and to other effects. The most significant contributions we found are the following:

- knowledge of average multiple scattering angle in upstream detectors
- correction for non-uniformity of Q_L trigger acceptance
- simulation of MSGC background
- simulation of pionium atom signal
- simulation of Q_T spectrum
- finite-size effects and η' / ω contamination

The total radiation length of upstream detectors is known with $\pm$1.5% precision and has been the subject of a detailed study [62]. Furthermore, its contribution to Q_T resolution is much reduced by the exclusive utilization of MSGC/GEM signals in the final track fitting. Note that the X and Y planes (located closest to the target foil) are essentially free of multiple scattering in the spectrometer. A $\pm$1.5% variation of the average θ_{MS} angle produces a negligible change in the Monte Carlo spectrum of pionium. A maximum uncertainty of $\Delta P_{Br} = \pm 0.003$ is attributed to this particular source.

Results have shown that the Q_L trigger acceptance correction determined from accidental pairs works well in describing correctly the Coulomb spectrum. Having used the full sample of accidental pairs for Ni 2001, we are probably still limited by statistics (specially at large momentum) for a precision knowledge of this correction, and there we find one source of systematic error. From variations of the correction structure, compatible with the accidentals pattern, we estimate $\Delta P_{Br} = \pm 0.007$ as a maximum possible shift of P_{Br}.

MSGC background has also been the subject of very detailed study . The probability of noise hits entering the real tracks is known very precisely, as

figure 6.4 shows. We assign a maximum systematic error to this concept of $\Delta P_{Br} = \pm 0.006$. Momentum resolution of the spectrometer was determined rather accurately using small Q_T Λ pairs and the Monte Carlo simulation was cross-checked according to it. We think this work is behind the good agreement between the pionium Monte Carlo and the experimental signal in figure 9.6. We assign a very small error to the fact that we use this Monte Carlo to guide the 2D fit, since the hypothesis is well consistent with the data.

Simulation of SFD signals (including PSC) and background has been optimized according to the work in [77], and it has little influence on the final Q_T spectrum. SFD inefficiency, on the other hand, has been accurately determined by means of MSGC/GEM detector [71]. It contributes to the observed rate of single-track events, but the analysis of the Q_T spectrum in the region $Q_L > 2\ MeV/c$ provides a good handle to reduce this particular simulation uncertainty. We assign a global ± 0.003 maximum systematic error coming from imperfect simulation of the Q_T spectrum, and double-track resolution.

Finally, we have incorporated to our analysis a correction to the P_{Br} measurement originated from the effect of large-size resonances η' and ω, as well as finite-size nuclear effects [63] on the Coulomb spectrum [64]. This correction is based on a 1% η' and 19% ω contamination, determined by with the UrQMD Monte Carlo, and on parametrizations of nuclear size, cross-checked with real $\pi^+\pi^+$ data from the spectrometer [78]. The systematic error we associate with this correction comes from a ± 25% uncertainty in the production of ω resonance, which is the dominant effect.

Without knowledge of correlations between the above sources of systematic error, we have convoluted them by generating random numbers with squared-pulse shape probability distributions, the width being determined by the contents of the second column in table 9.5. A gaussian fit to the resulting distribution provides a 1σ equivalent to the combined systematic error of ± 0.009 wich can be added in quadrature to the statistical error, for the sake of synthesis. The resulting P_{br} measurement is then 0.432 $\pm$ 0.016 (stat) $\pm$ 0.009 (syst) = 0.432 $\pm$ 0.018.

A contamination of K^+K^- pairs in the 2001 $\pi^+\pi^-$ data sample has been studied [79] and it appears to be $(2.38 \pm 0.35) \times 10^{-3}$ at $p = 2.9\ GeV/c$. The Coulomb spectrum of K^+K^- is known and this may originate a small correction to τ_{1s} with, negative sign. Another small correction (with positive sign) is also being considered, due to a slight lower Z contamination in the target foil. The overall systematic uncertainty is not expected to increase significantly, as the result of both studies.

Table 9.5: *Estimated contributions to systematic error in average break-up probability measurement. Last row indicates total systematic error equivalent to 1σ, under the assumption of uncorrelated effects.*

Simulation error	ΔP_{Br} extreme values
Multiple scattering ($\pm 1.5\%$)	± 0.003
Q_L trigger acceptance	± 0.007
MSGC background	± 0.006
Atom signal shape	± 0.002
Double-track resolution	± 0.003
Finite-size correction ($\pm 25\%$ ω)	± 0.003
Total 1σ equivalent	± 0.009

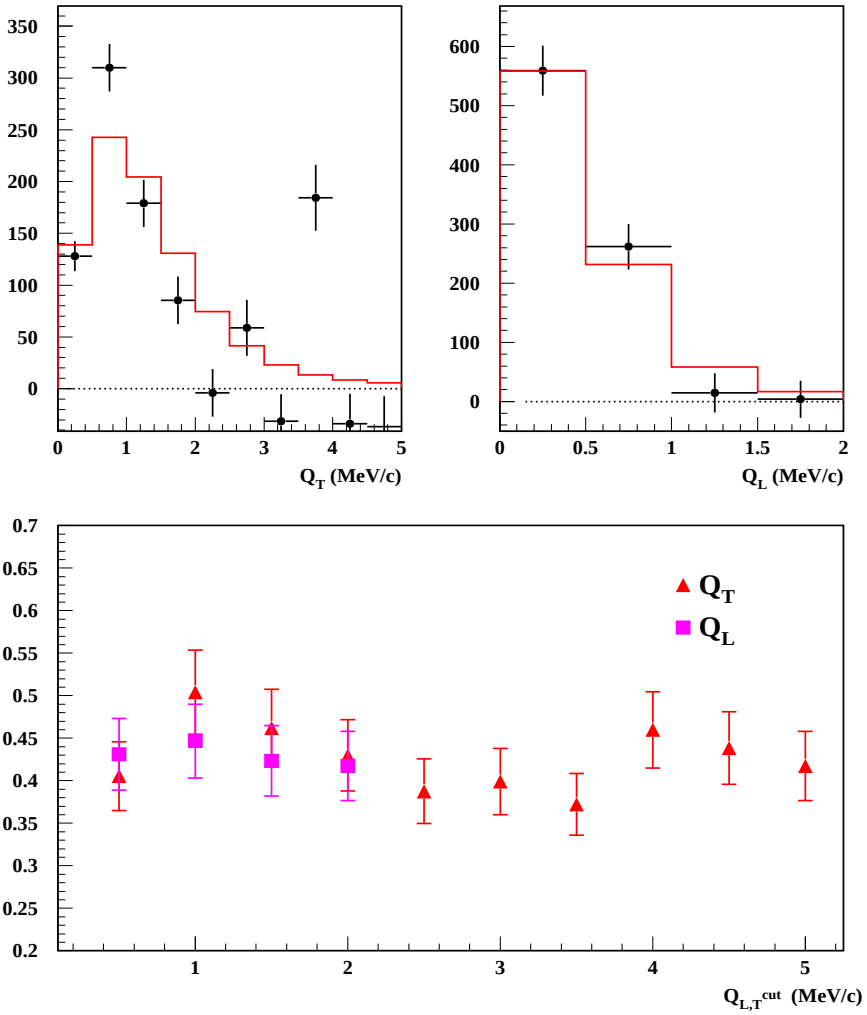

Figure 9.14: *Fit results for a $\pi^+\pi^-$ momentum interval $2.6 < p < 3.2$ GeV/c in lab-frame. a) Transverse (Q_T) and longitudinal (Q_L) projections of the atom signal found in the extrapolation region ($Q_L < 2$ MeV/c) after subtraction of the Monte Carlo prediction with pionium component removed (top). b) Differences in Q_L spectrum between the Monte Carlo prediction and the prompt data (center). c) Values of break-up probability determined for different integration upper limits (Q_T^u, Q_L^u) to define the atom signal (bottom).*

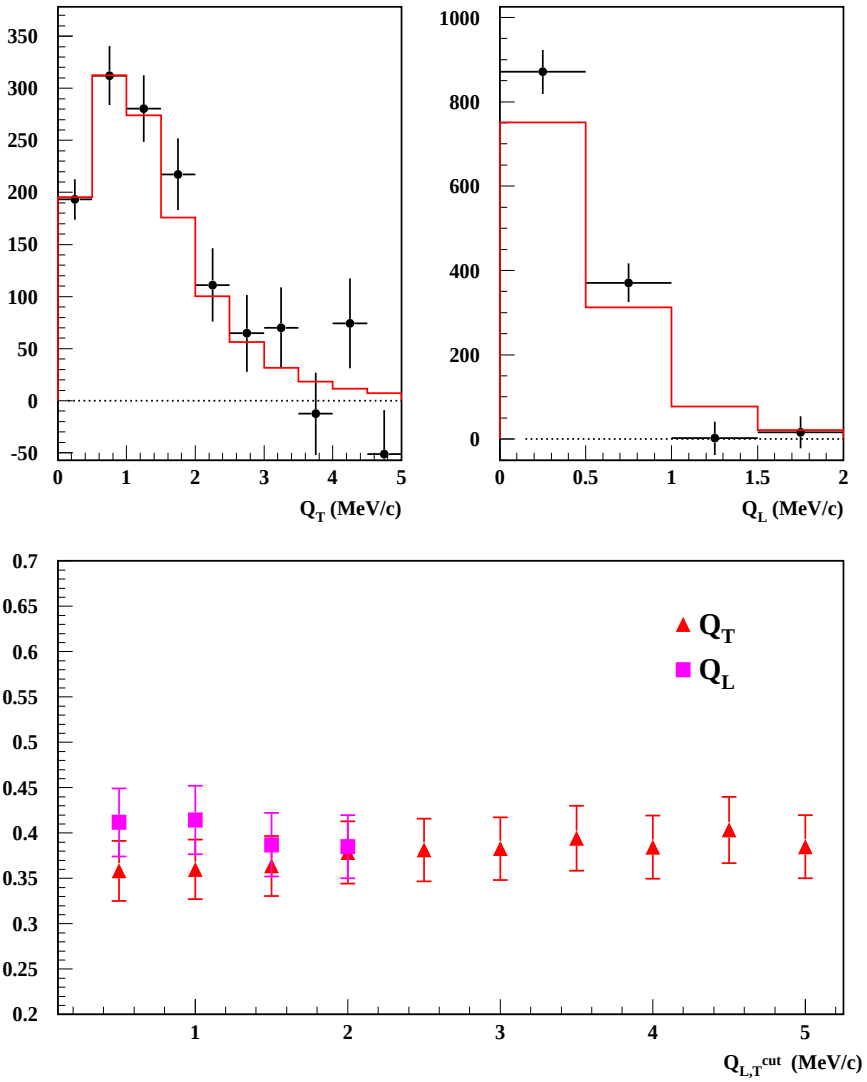

Figure 9.15: *Fit results for a $\pi^+\pi^-$ momentum interval $3.2 < p < 3.8\, GeV/c$ in lab-frame. Caption is identical to figure 9.14.*

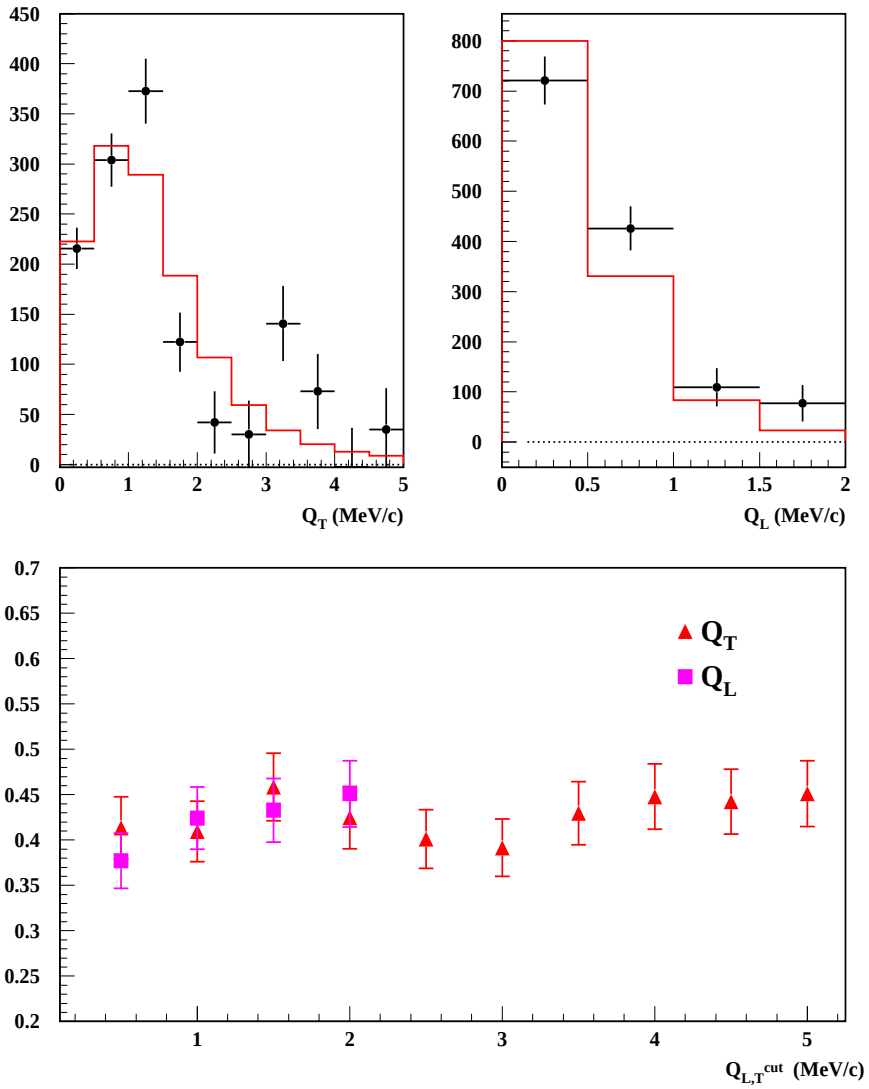

Figure 9.16: *Fit results for a $\pi^+\pi^-$ momentum interval $3.8 < p < 4.4\, GeV/c$ in lab-frame. Caption is identical to figure 9.14.*

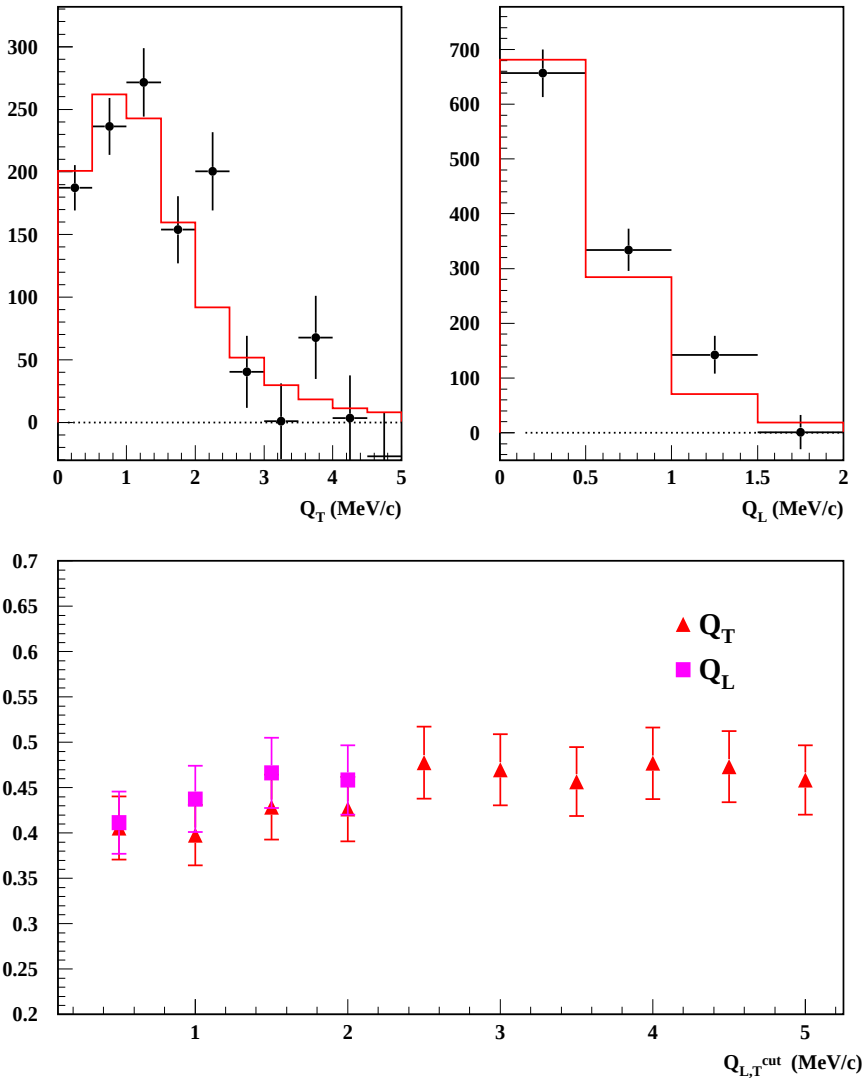

Figure 9.17: *Fit results for a $\pi^+\pi^-$ momentum interval $4.4 < p < 5.0\ GeV/c$ in lab-frame. Caption is identical to figure 9.14.*

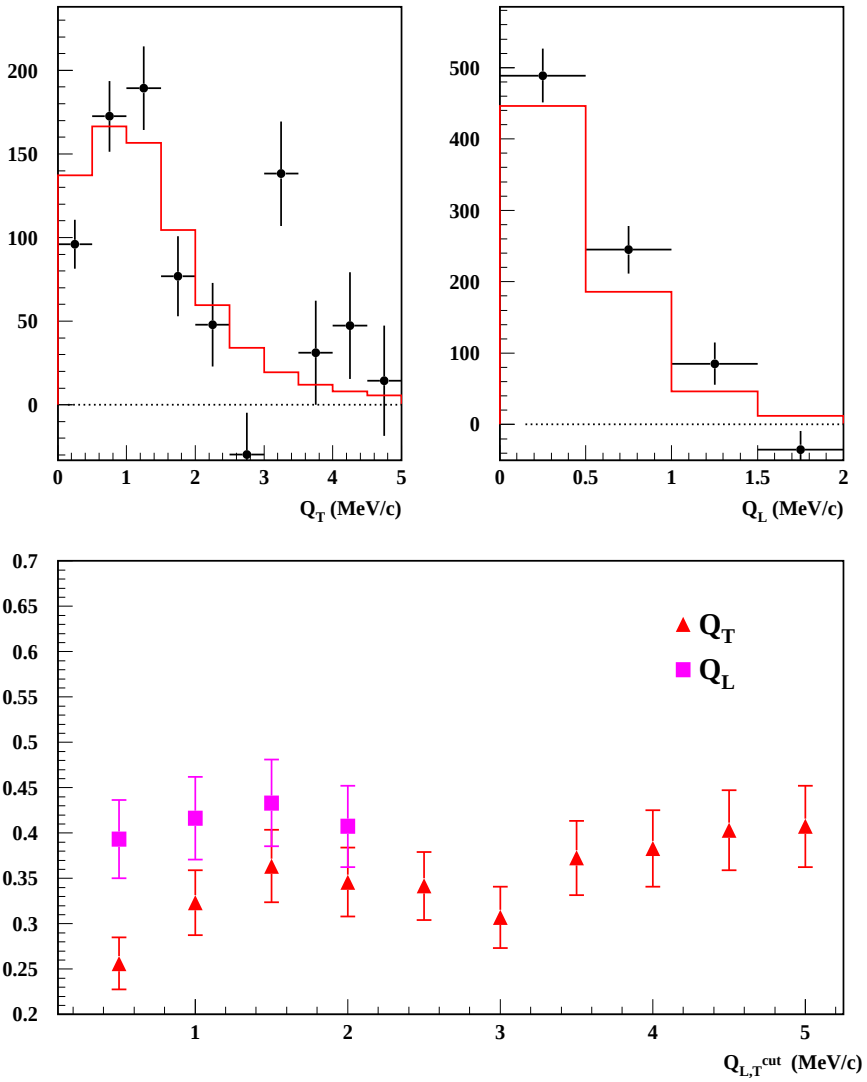

Figure 9.18: *Fit results for a $\pi^+\pi^-$ momentum interval $5. < p < 5.6\ GeV/c$ in lab-frame. Caption is identical to figure 9.14.*

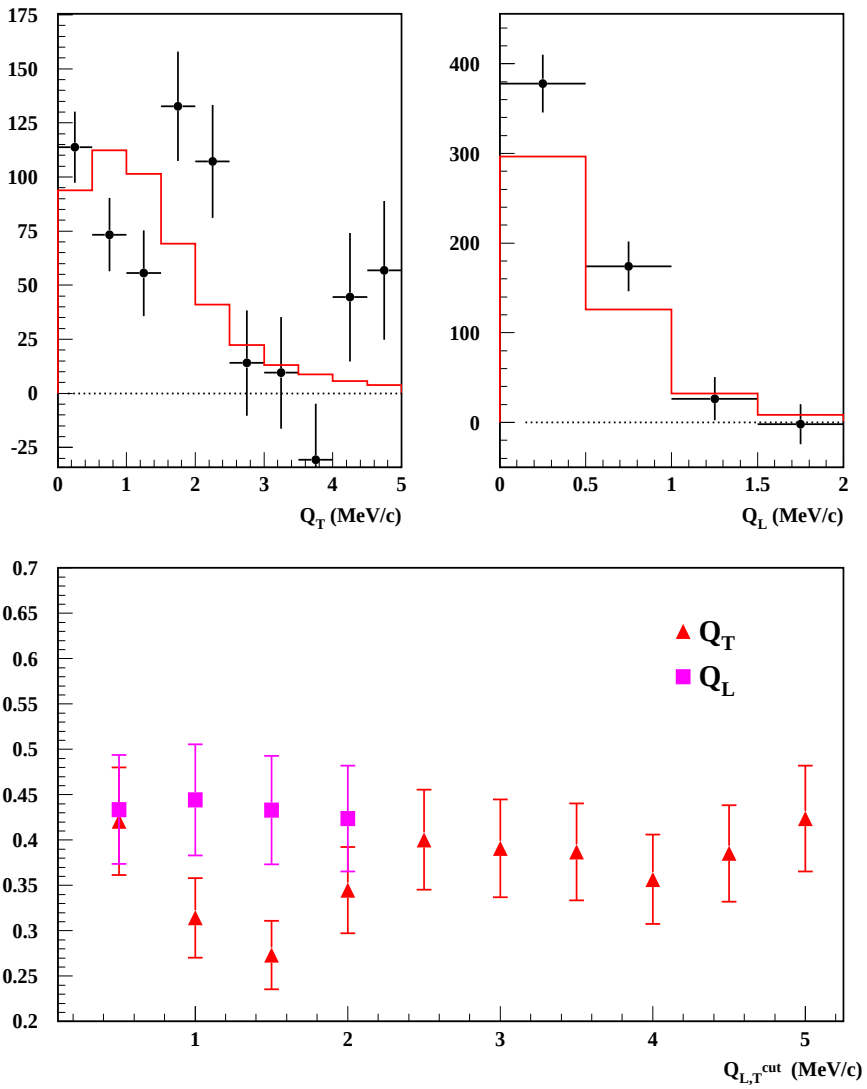

Figure 9.19: *Fit results for a $\pi^+\pi^-$ momentum interval $5.6 < p < 6.2\, GeV/c$ in lab-frame. Caption is identical to figure 9.14.*

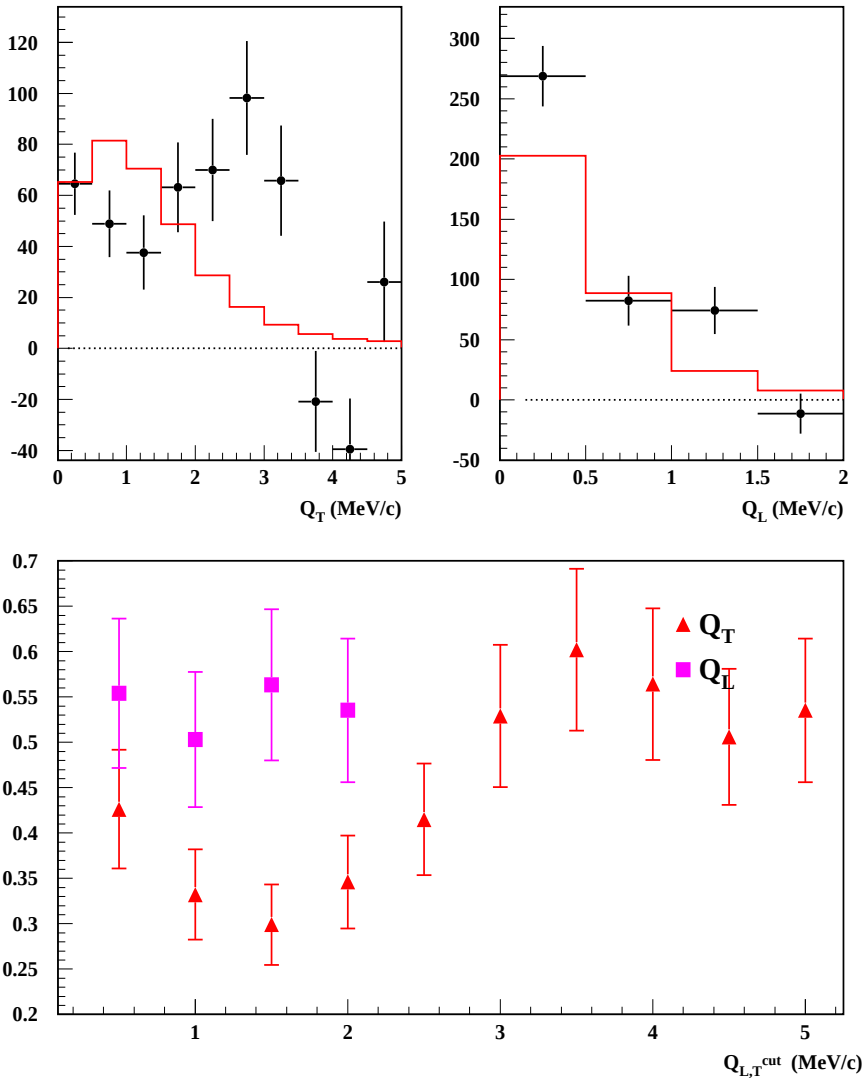

Figure 9.20: *Fit results for a $\pi^+\pi^-$ momentum interval $6.2 < p < 6.8\ GeV/c$ in lab-frame. Caption is identical to figure 9.14.*

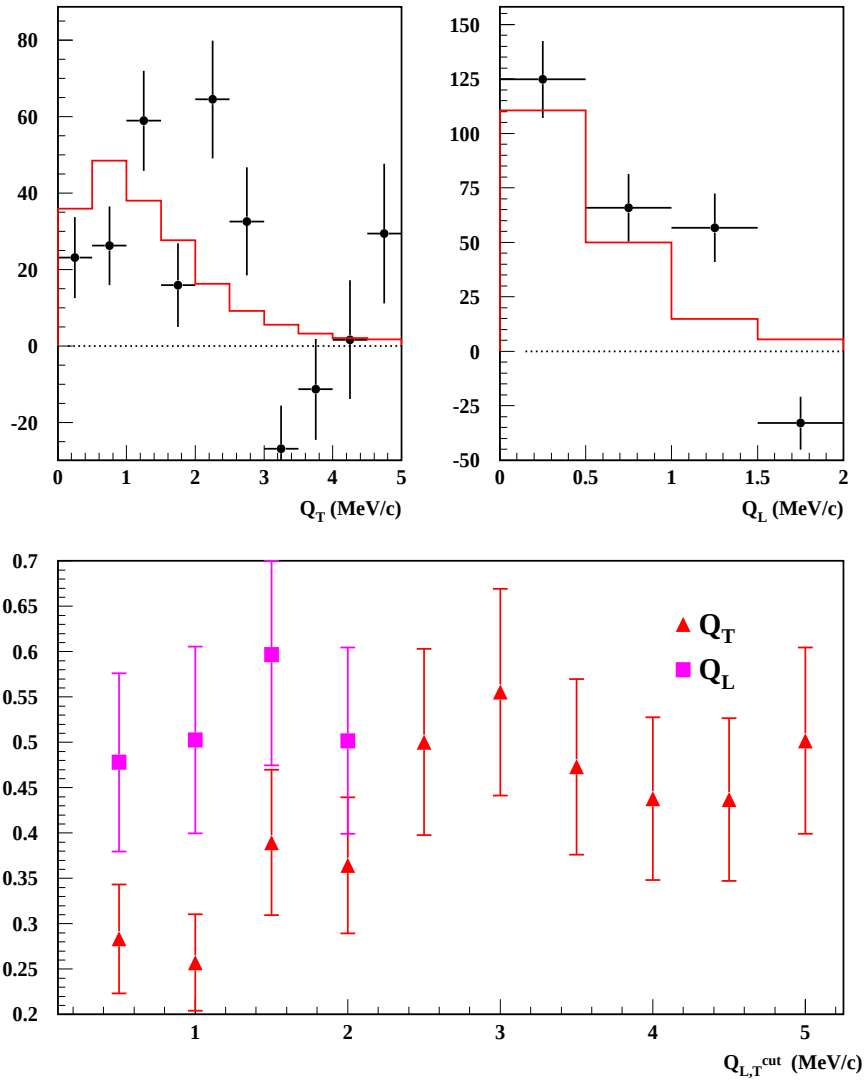

Figure 9.21: *Fit results for a $\pi^+\pi^-$ momentum interval $6.8 < p < 7.4\, GeV/c$ in lab-frame. Caption is identical to figure 9.14.*

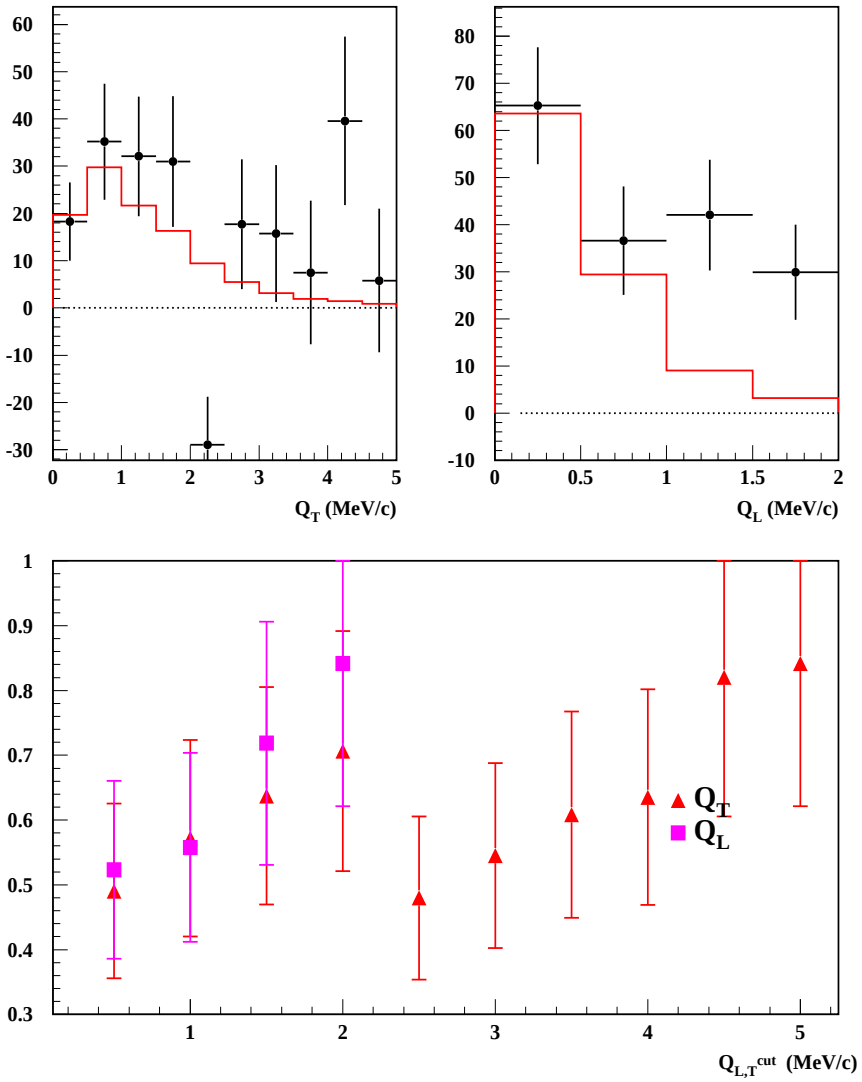

Figure 9.22: *Fit results for a $\pi^+\pi^-$ momentum interval $7.4 < p < 8.0\ GeV/c$ in lab-frame. Caption is identical to figure 9.14.*

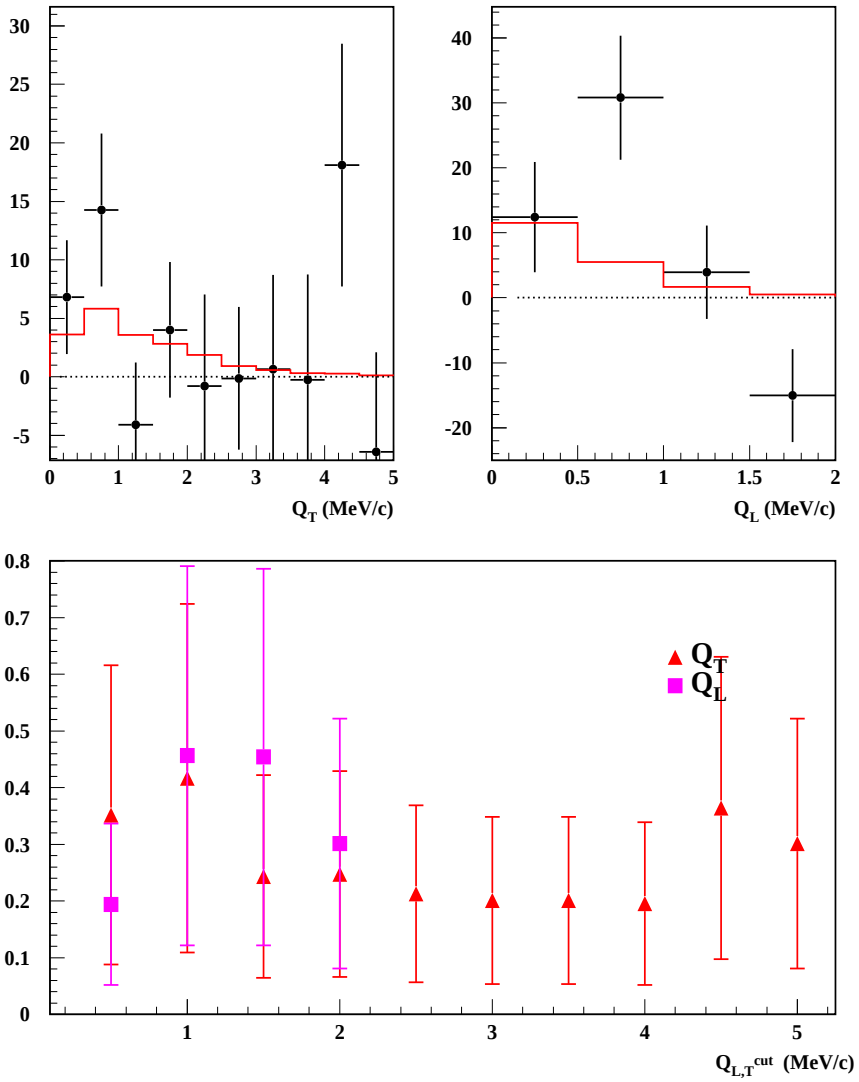

Figure 9.23: *Fit results for a $\pi^+\pi^-$ momentum interval $8.0 < p < 8.6\ GeV/c$ in lab-frame. Caption is identical to figure 9.14.*

Chapter 10

Summary of results and conclusions

The work presented in this thesis has been devoted, on the instrumental side, to the construction and installation for the DIRAC spectrometer at CERN of a tracking detector, the MSGC/GEM, that has been essential for the unambiguous measurement of $\pi^+\pi^-$ transverse momentum in the high radiation enviroment of p-Ni collisions at $p = 24\ GeV/c$.

As main physics output from this work, it is presented here a precision measurement of Pionium Lifetime in 1s state following the extrapolation method originally proposed by the DIRAC collaboration to CERN in 1994.

The measurement includes a detailed assesment of systematic and statistical errors, with the result:

$$\tau_{1S} = 2.58\ ^{+0.26}_{-0.22}(stat)\ ^{+0.15}_{-0.14}(syst)$$

A quadrature of both sources of error yields the combined result :

$$\tau_{1S} = 2.58\ ^{+0.30}_{-0.26}$$

which is close to the original objetive of the experiment to attain a 10% error in this important physics observable.

The precision of our result for pionium lifetime has required to apply a small correction (with negative sign) due to the effect of finite nuclear size and ω and η' resonances, as explained in chapter 10.

There are still two effects that might eventually require appplication of small corrections to the measurement, with known sign, that are being investigated at the moment of writing this thesis. These are a possible contamination of K^+K^- in the $\pi^+\pi^-$ sample, and the chemical composition of the target foil, which includes a fraction of lighter elements ($Z < 26$). The correction sign is known (negative in the former case, positive in the latter), and once the study of the magnitude is completed, the total systematic error is not expected to increase significantly.

The achieved pionium lifetime result can be converted into a measurement of the s-wave amplitude difference [4] by means of the expression 1.5, with the result:

$$|a_0 - a_2| = 0.280 \ {}^{+\ 0.016}_{-\ 0.014}\ M_\pi^{-1} = (0.280 \pm 0.015)\ M_\pi^{-1}$$

Bibliography

[1] S. Weinberg, Physica A 96, 327 (1979).

[2] G. Colangelo, J. Gasser and H. Leutwyler, Nucl. Phys. B603, 125 (2001).

[3] J. Uretsky and J. Palfrey, Phys. Rev. 121, 1798 (1961).

[4] J. Gasser, V. E. Lyubovitskij, A. Rusetsky and A. Gall, Phys. Rev. D64, 016008 (2001).

[5] G. Colangelo, J. Gasser and H. Leutwyler, Phys. Rev. Lett. 86, 5008 (2001).

[6] M. Knecht, et al., Nucl. Phys. B 457, 513 (1995).

[7] J. Nieves and E. Ruiz-Arriola, Eur. Phys. J. A8, 377 (2000).

[8] J. R. Peláez and F. J. Ynduráin, Physical Review D71, 074016 (2005).

[9] R. Lednicky, Proceedings of the HadAtom 99 Workshop, BUTP-99/26 (1999).

[10] L. Nemenov, Sov. J. Nucl. Phys. 41, 629 (1985). Yad. Fiz. 41, 2015 (1985).

[11] B. Adeva, et al., DIRAC proposal, CERN/SPSLC 95-1, SPSLC/P 284 (1994).

[12] O. E. Gorchakov et al., Yad. Fiz. 63, 1936 (2000).

[13] Schumann M, et al., J. Phys. B: 35 2683 (2002).

[14] H. W. Hammer et al., Eur. Phys. J. A6, 115 (1999).

[15] Gillespie, G. H., Phys. Rev. A18, 1967 (1978).

[16] L. G. Afanasyev and A. V. tarasov, Yad. Fiz. 59, 2212 (1996). Phys. At. Nucl. 61, 1517 (1998).

[17] C. Santamarina, M. Schumann, L. G. Afanasyev, T. Heim, J. Phys. B 36, 4273 (2003).

[18] K. G. Denisenko and S. Mròwczyński, Phys. Rev. D 36, 1529 (1987).

[19] A. V. Tarasov and I. U. Khristova, JINR-P2-91-10 (1991).

[20] T. Heim, et al., J. Phys. B 34, 3763 (2001).

[21] B. Adeva et al., [DIRAC collaboration], Phys. Lett. B619, 50 (2005).

[22] B. Adeva et al., [DIRAC collaboration], Nucl. Instr. Meth. A515, 467 (2003).

[23] K. Brown, D. Carey, C. Iselin, F. Rothacker., CERN-80-04 (1980).

[24] I.A. Kurochkin, DIRAC note 96-07 (1996) (http://dirac.web.cern.ch/DIRAC/i_notes.html).

[25] V. Agoritsas et al., Nucl. Instr. and Meth., A411, 17-30 (1998).

[26] A. Gorin et al., Nucl. Instr. and Meth., A452, 280-288 (2000).

[27] O. Vázquez Doce, Presentation in DIRAC analysis meeting, unpublished.

[28] A. Romero, Ph.D. Thesis, Universidad de Santiago de Compostela, in preparation.

[29] V. Brekhovskikh et al., DIRAC note 2002-09 (2002).

[30] G. Bitsadze, et al., Nucl. Instr. Meth. A533 353 (2004).

[31] Millipore paper type HAWP pore size 0.45 made by MILLIPORE Corp., Bedford, Ma 01730 USA.

[32] M. Gallas, et al., DIRAC Note 98-06 (1998).

[33] L. Afanasyev, V. Karpukhin, NIM A492 351 (2002).

[34] B. Adeva et al., Nucl. Inst. and Meth. A491, 41 (2002).

[35] M. Bragadireanu et al., NIM 426, 254 (1999).

[36] M. Pentia, Gh. Caragheorgheopol, M. Ciobanu, D. Pop and C. Rusu, DIRAC note 99-03 (1999).

[37] A. Lanaro, DIRAC Note 02-02 (2002).

[38] L. Afanasyev et al., NIM A491, 376 (2002).

[39] A. Kulikov, M. Zhabitsky, Nucl. Instr. Meth. A527, 591 (2004).

[40] L. Afanasyev, M. Gallas, V. Karpukhin and A. Kulikov, NIM A479, 407 (2002).

[41] P. Kokkas, M. Steinacher, L. Tauscher and S. Vlachos, NIM A471, 358 (2001).

[42] F.R. Leimgruber et al., NIM A365, 198 (1995).

[43] G.D. Badhwar, S.A. Stephens, R.L. Golden Phys Rev. D15, 820 (1977).

[44] A. Lanaro, DIRAC Note 01-01 (2001).

[45] V. Karpukhin, A. Kulikov, V. Olshevsky, S. Trusov. Preprint JINR E10-2003-2, Dubna, 2003. Submitted to NIM.

[46] FERA. Application Note AN-4004A, LeCroy Corporation.

[47] F. Gomez, P. Vazquez, DIRAC Note 00-01 (2000).

[48] V. Karpukhin, A. Kulikov, Preprint JINR E10-2001-2 (2001).

[49] V.G. Olshevsky, S.V. Trusov, NIM A469, 216 (2001).

[50] G. Charpak et al., Nucl. Instr. and Meth. 62 (1968).

[51] A. Oed, Nucl. Instr. and Meth. A263, 351. (1988).

[52] T. Nuñez Pardo de Vera, Ph.D. Thesis, Universidad de Santiago de Compostela (1999).

[53] C. Buttner et al., NIM A409, 1-3, 79-83 (1998).

[54] P. Vázquez, Ph.D. Thesis, Universidad de Santiago de Compostela (2000).

[55] F. Sauli, NIM A386, 531 (1997).

[56] R. Horisberger et al., NIM A326, 92 (1993).

[57] L. Landau, J. Phys 8, 201 (1944).

[58] P. Zrelov and V. Yazkov, DIRAC Note 98-08 (1998).

[59] "Dixitos", CESGA magazine (www.cesga.es), January 2006.

[60] C. Santamarina, Ph.D. Thesis, Universidad de Santiago de Compostela (2001).

[61] A. D. Sakharov, Zh. Eksp. Teor. Fiz 18, 631 (1948).

[62] B. Adeva, A. Romero and O. Vázquez Doce, DIRAC Note 05-16 (http://dirac.web.cern.ch/DIRAC/i_notes.html)

[63] R. Lednicky, *nucl-th/0501065*.

[64] R. Lednicky, V. L. Lyuboshitz, Sov. J. Nucl. Phys. 35, 1316 (1982).

[65] C. Santamarina *et al.*, *J. Phy. B* **36**, 4273 (2003).

[66] I. Amirkhanov et al., Phys. Lett. B452, 155 (1999).

[67] S. Trusov, DIRAC Note 02-10 (2002).

[68] D. Drijard, M. Hansroul, V. Yazkov, http://www.cern.ch/dirac/ariane.html

[69] V. Yazkov, http://dirac.web.cern.ch/DIRAC/pre-sel.html

[70] B. Adeva et al., [DIRAC collaboration], J. Phys. G: Nucl. Part. Phys. 30, 1929 (2004).

[71] B. Adeva, A. Romero, O. Vázquez Doce, DIRAC Note 05-11 (2005).

[72] Particle Data Group Collaboration. (http://pdglive.lbl.gov/).

[73] F. James, http://wwwasdoc.web.cern.ch/wwwasdoc/minuit.minmain.html

[74] P. Kokkas, DIRAC Note 04-04 (2004).

[75] L. Afanasyev et al., Phys. At. Nucl. 60 938 (1997).

[76] L. Afanasyev et al., Physics of Atomic Nuclei, Vol. 60, No. 6, 938 (1997).

[77] V. Yazkov, DIRAC Note 05-04 (2005).

[78] J. Smolik., Doctoral Thesis, Faculty of Physics and Mathematics Charles University, Prage (2005).

[79] B. Adeva, A. Romero, O. Vázquez Doce, DIRAC Note 06-08 (2006).